

Titre: Active Backscattering Positioning System Using Innovative
Harmonic Oscillator Tags for Future Internet of Things: Theory and
Experiments
Title:

Auteur: Kuangda Wang
Author:

Date: 2020

Type: Mémoire ou thèse / Dissertation or Thesis

Référence: Wang, K. (2020). Active Backscattering Positioning System Using Innovative
Harmonic Oscillator Tags for Future Internet of Things: Theory and Experiments
Citation: [Thèse de doctorat, Polytechnique Montréal]. PolyPublie.
<https://publications.polymtl.ca/3731/>

 **Document en libre accès dans PolyPublie**
Open Access document in PolyPublie

URL de PolyPublie:
PolyPublie URL: <https://publications.polymtl.ca/3731/>

**Directeurs de
recherche:** Ke Wu
Advisors:

Programme: génie électrique
Program:

UNIVERSITÉ DE MONTRÉAL

ACTIVE BACKSCATTERING POSITIONING SYSTEM USING INNOVATIVE
HARMONIC OSCILLATOR TAGS FOR FUTURE INTERNET OF THINGS:
THEORY AND EXPERIMENTS

KUANGDA WANG

DÉPARTEMENT DE GÉNIE ÉLECTRIQUE
ÉCOLE POLYTECHNIQUE DE MONTRÉAL

THÈSE PRÉSENTÉE EN VUE DE L'OBTENTION
DU DIPLÔME DE PHILOSOPHIE DOCTOR
(GÉNIE ÉLECTRIQUE)

DÉCEMBRE 2018

UNIVERSITÉ DE MONTRÉAL

ÉCOLE POLYTECHNIQUE DE MONTRÉAL

Cette thèse intitulée:

ACTIVE BACKSCATTERING POSITIONING SYSTEM USING INNOVATIVE
HARMONIC OSCILLATOR TAGS FOR FUTURE INTERNET OF THINGS:
THEORY AND EXPERIMENTS

présenté par : WANG Kuangda

en vue de l'obtention du diplôme de : Philosophiae Doctor

a été dûment accepté par le jury d'examen constitué de :

M. FRIGON Jean-François, Ph. D., président

M. WU Ke, Doctorat, membre et directeur de recherche

M. AKYEL Cevdet, D. Sc. A., membre

M. KISHK Ahmed, Ph. D., membre externe

DEDICACE

To my parents,

To my girlfriend Alice Zhan,

To Canadian taxpayers.

ACKNOWLEDGMENT

I would like to express my utmost respect and acknowledge to my Ph.D. advisor, Prof. Ke Wu, for offering me the opportunity to join his great research group, for lending me his wisdom and vision, and for providing me countless support during my whole endeavor. This work could not be accomplished without his guidance, patience, and tolerance.

I would also like to express my sincere gratitude to Prof. Anthony Ghiotto and Prof. Simon Hemour. Anthony's ideas and hardworking attitude have been always inspiring me. Simon had guided me step by step at the beginning of research and we had many wonderful times of brainstorming. Many thanks to my old friend, schoolmate, colleague and partner Dr. Fang Zhu, who has been always trustworthy whenever I need help in design and experiments. I would like to thank Dr. Jianfeng Gu, whose cross-disciplinary expertise was irreplaceable for a work of the system.

I truly appreciate the excellent technical support team of the Poly-Grames Research Center including Mr. Jules Gauthier, Mr. Traian Antonescu, Mr. Steve Dubé, Mr. Maxime Thibault, and Mr. Jean-Sébastien Décarie. They not only provided me with the finest work and support but also helped me to master useful skills. I am grateful to Madam Rachel Lortie, secretary of our research center for being extremely patient, helpful and understanding. I would also thank Dr. David Dousset, who was always around me when I ran into trouble.

I am also indebted to my colleagues and friends Dr. Yangping Zhao, Prof. Tarek Djerafi, Dr. Sulav Adhikari, Dr. Jaber Moghaddasi, Dr. Peng Chu, Dr. Lei Guo, Prof. Haiyan Jin and Dr. Fengchao Ren for advice and contribution to my work and this thesis.

My special thanks go to the members of the examination jury, who took their time to read the thesis and provided very valuable comments.

Last but not least, I would like to extend my gratitude to my parents, who raised and educated me. Their support is beyond what I can imagine.

RÉSUMÉ

D'ici 2020, l'Internet des objets (IoT) permettra probablement de créer 25 milliards d'objets connectés, 44 ZB de données et de débloquer 11 000 milliards de dollars d'opportunités commerciales. Par conséquent, ce sujet a suscité d'énormes intérêts de recherche dans le monde académique entier. L'une des technologies clés pour l'IoT concerne le positionnement physique intérieur précis. Le principal objectif dans ce domaine est le développement d'un système de positionnement intérieur avec une grande précision, une haute résolution, un fonctionnement à plusieurs cibles, un faible coût, un faible encombrement et une faible consommation d'énergie. Le système de positionnement intérieur conventionnel basé sur les technologies de Wi-Fi ou d'identification par radiofréquence (RFID) ne peut répondre à ces exigences. Principalement parce que leur appareil et leur signal ne sont pas conçus spécialement pour atteindre les objectifs visés. Les chercheurs ont découvert qu'en mettant en œuvre de différents types de modulation sur les étiquettes, le radar à onde continue (CW) et ses dérivés deviennent des solutions prometteuses. Les activités de recherche présentées dans cette thèse sont menées dans le but de développer des systèmes de positionnement en intérieur bidimensionnel (2-D) à plusieurs cibles basées sur des étiquettes actives à rétrodiffusion harmonique avec une technique à onde continue modulée en fréquence (FMCW). Les contributions de cette thèse peuvent être résumées comme suit:

Tout d'abord, la conception d'un circuit actif harmonique, plus spécifiquement une classe d'oscillateurs harmoniques innovants utilisée comme composant central des étiquettes actives dans notre système, implique une méthodologie de conception de signal de grande taille et des installations de caractérisation. L'analyseur de réseau à grand signal (LSNA) est un instrument émergent basé sur les fondements théoriques du cadre de distorsion polyharmonique (PHD). Bien qu'ils soient disponibles dans le commerce depuis 2008, des organismes de normalisation et de recherche tels que l'Institut national des normes et de la technologie (NIST) des États-Unis travaillent toujours à la mise au point d'un standard largement reconnu permettant d'évaluer et de comparer leurs performances. Dans ce travail, un artefact de génération multi-harmonique pour la vérification LSNA est développé. C'est un dispositif actif capable de générer les 5 premières harmoniques d'un signal d'entrée avec une réponse ultra-stables en amplitude et en phase, quelle que soit la variation de l'impédance de la charge.

Deuxièmement, un oscillateur harmonique à boucle de rétroaction innovant avec un effet de traction réduit est proposé et conçu avec le modèle non linéaire à paramètre-X d'un amplificateur

extrait à l'aide d'un LSNA vérifié dans notre laboratoire. Les émetteurs de radiofréquence (RF) à faible coût d'activation-désactivation (OOK) utilisent généralement des oscillateurs modulés pour alimenter directement une antenne d'émission. Sans mécanisme d'isolation utilisé dans le système, tel qu'un amplificateur tampon, la variation d'impédance externe ou l'injection de signal peut provoquer un décalage de fréquence porteuse, connu sous le nom d'effet d'attraction de l'oscillateur. Notre oscillateur harmonique proposé utilise les effets synergiques de l'unilatéralité d'un amplificateur et la propriété de séparation des harmoniques d'un diplexeur pour créer une condition d'auto-isolation. Nous appelons ce type d'oscillateur l'oscillateur harmonique auto-isolé (SIHO). Des expériences ont montré que la topologie SIHO non seulement facilite la conception d'oscillateurs à haute fréquence, mais aussi offre plus de 15 fois la réduction de l'effet de tirage.

Troisièmement, à la suite de la démonstration initiale d'un SIHO, son principe de fonctionnement est étudié théoriquement en profondeur au moyen de modèles équivalents de circuit et de la technique des paramètre-X. Les expressions sous forme fermée des impédances actives et passives équivalentes sous la variation de l'impédance de charge ou injection de signal sont dérivées. La conception de circuits actifs non linéaires est souvent une tâche compliquée et repose fortement sur des modèles précis de signaux de grande taille de transistor, tels que le modèle à paramètre-X. Comme solution alternative à la conception de circuits non linéaires, un système de mesure et conception harmoniques (HMD) est proposé dans ce travail, qui illustre le concept d'une automatisation de la conception de circuits non linéaires sans modèle basée sur l'optimisation expérimentale. À titre d'exemple, un prototype SIHO à 4 GHz avec une efficacité dc-RF de 28% est conçu par une telle plate-forme matérielle.

Quatrièmement, un radiateur harmonique auto-isolé fonctionnant à une fréquence de 28 GHz est proposé et démontré. Il peut être utilisé pour l'identification et le positionnement à ondes millimétriques (mmW). Selon son fonctionnement, le dispositif équivaut à la combinaison d'une SIHO et d'une antenne à guide d'onde intégré au substrat (SIW) chargée par résonateur diélectrique (DR). Cependant, l'interconnexion de blocs de construction à mmW et au-delà entraîne généralement une perte d'insertion (IL) élevée. Le radiateur intégré proposé jette un pont entre la division artificielle de la fonction ou de l'opération. Une structure harmonique diplexeur-résonateur-antenne est conçue pour permettre le filtrage à la fréquence fondamentale, rayonnant à la fréquence du 2^e harmonique et créant naturellement un isolement entre elles. Basé sur cette structure, le radiateur conçu bénéficie des avantages d'une efficacité élevée et d'un faible effet de

traction. Par rapport à sa contrepartie fondamentale, la traction et l'injection sont atténuées respectivement de 10 et de 17 fois.

Cinquièmement, une modélisation du système et des techniques innovantes de post-traitement de séries chronologiques sont proposées pour le positionnement actif 2D multi-cibles en intérieur. L'architecture matérielle est basée sur le principe d'un oscillateur commuté verrouillé par injection (SILO) et de radar FMCW, qui a été étudié par d'autres chercheurs. La technique conventionnelle de post-traitement dans le domaine fréquentiel utilisant une transformation de Fourier rapide (FFT) rencontre généralement un compromis entre la résolution, la quantité cible, le rapport signal-sur-bruit (SNR) et d'autres spécifications critiques, ce qui rend difficile son adaptation à de nombreuses applications. La nouvelle technique développée comporte un algorithme ESPRIT basé sur la décomposition en valeurs singulières (SVD) et la technique de diagonalisation matricielle utilisant le pseudo-inverse de Moore-Penrose pour l'estimation de l'ordre des modèles, ainsi que les extractions de l'heure d'arrivée (TOA) et de la direction d'arrivée (DOA). Avec des simulations et des démonstrations expérimentales, la précision et la résolution sont supérieures à celles des méthodes conventionnelles.

Enfin, un système de positionnement par rétrodiffusion harmonique à multi-cibles avec étiquettes actives (HPS-AT) utilisant le SIHO est inventé et présenté. Les étiquettes utilisées pour notre précédent système de positionnement à cibles multiples sont basées sur un oscillateur à boucle de réaction à signal fondamental. Ainsi, l'émission et la réception de la station de base (BS) et de l'étiquette partagent la même bande de fréquence. Une telle architecture matérielle présente un nombre d'inconvénients, à savoir une auto-ingérence inévitable et la dispersion de grappes, une forte interférence mutuelle entre plusieurs étiquettes, l'effet de traction d'étiquettes, etc. Le HPS-AT développé peut parfaitement résoudre ces problèmes en exploitant les harmoniques. En outre, l'architecture peut économiser 50% de bande passante absolue pour la même résolution de gamme. Le modèle de signal est étudié et les spécifications détaillées des étiquettes et des BS, leur conception et leur intégration sont présentées. Les résultats expérimentaux dans des environnements intérieurs riches en réflexion ont démontré le concept et la conception.

Le HPS-AT est une intégration complète des travaux théorique, technologique et technique tout au long de cette thèse. Sa version mmW avec étiquette intégrée par CMOS et une conception plus mature des BS est sur le point d'aller. Il finira par devenir un candidat très compétitif pour la solution de prise de conscience de position omniprésente pour la prochaine génération d'IoT.

ABSTRACT

By 2020, the internet of things (IoT) will probably enable 25 billion connected objects, create 44 ZB data and unlock 11 trillion US dollar business opportunities. Therefore, this topic has been attracting tremendous research interests in the entire academic world. One of the key enabling technologies for IoT is concerned with accurate indoor physical positioning. The development of such an indoor positioning system with high accuracy, high resolution, multitarget operation, low cost, small footprint, and low power consumption is the major objective in this area. The conventional indoor positioning system based on WiFi or radiofrequency identification (RFID) technology cannot fulfill these requirements mainly because their device and signal are not purposely designed for achieving the targeted goals. Researchers have found that by implementing different types of modulation on the tags, continuous-wave (CW) radar and its derivatives become promising solutions. The research activities presented in this Ph.D. thesis are carried out towards the goal of developing multitarget two-dimensional (2-D) indoor positioning systems based on harmonic backscattering active tags together with a frequency-modulated continuous-wave (FMCW) technique. Research contributions of this thesis can be summarized as follows:

First of all, the design of a harmonic active circuit, more specifically, a class of innovative harmonic oscillators used as the core component of active tags in our system, involves a large signal design methodology and characterization facilities. The large signal network analyzer (LSNA) is an emerging instrument based on the theoretical foundation for the Poly-Harmonic Distortion (PHD) framework. Although they have been commercially available since 2008, standard and research organizations such as the National Institute of Standards and Technology (NIST) of the US are still working towards a widely-recognized standard to evaluate and cross-reference their performances. In this work, a multi-harmonic generation artifact for LSNA verification is developed. It is an active device that can generate the first 5 harmonics of an input signal with ultra-stable amplitude and phase response regardless of the load impedance variation.

Secondly, an innovative harmonic feedback-loop oscillator with a reduced pulling effect is proposed and designed with the X-parameter nonlinear model of an amplifier extracted using a verified LSNA in our lab. Low-cost on-off keying (OOK) radiofrequency (RF) transmitters usually employ modulated oscillators to feed a transmitting antenna directly. If there is no isolation mechanism used in the system such as buffer amplifier, external impedance variation or signal injection may cause a carrier frequency shift, which is known as the pulling effect of oscillator.

Our proposed harmonic oscillator utilizes the synergetic effects of the unilaterality of an amplifier and the harmonics-separation property of a diplexer to create a self-isolation condition. We call such a class of oscillators as the self-isolated harmonic oscillator (SIHO). It has been verified by experiments that, the SIHO topology not only makes the design of high-frequency oscillators easier but also enjoys more than 15 times of pulling effect reduction.

Third, following the initial demonstration of an SIHO, its operation principle is theoretically studied in-depth through equivalent circuit models and X-parameter technique. The closed-form expressions of equivalent active and passive impedances under a load impedance variation or signal injection are derived. From the expressions, a physical insight of the pulling effect is gained and critical parameters affecting the pulling figure are identified. The design of nonlinear active circuits is usually a complicated task and highly relies on accurate large signal models of transistor such as X-parameter model. As an alternative solution of nonlinear circuit design, a harmonic-measurement-and-design (HMD) system is proposed in this work, which demonstrates the concept of a model-free nonlinear circuit design automation based on the experimental optimization. As an example, an SIHO prototype at 4 GHz with 28% dc-to-RF conversion efficiency is designed by such a hardware platform.

Fourth, a self-isolated harmonic radiator operating at 28 GHz frequency is proposed and demonstrated. It can be applied for millimeter-wave (mmW) identification and positioning. Judging from its operation, the device is equivalent to the combination of an SIHO and a dielectric resonator (DR) loaded substrate integrated waveguide (SIW) antenna. However, building block interconnects at mmW and beyond usually result in a high insertion loss (IL). The proposed integrated radiator bridges the artificial division of function or operation. A harmonic diplexer-resonator-antenna structure is designed to enable filtering at the fundamental frequency, radiating at the 2nd harmonic frequency and naturally creating an isolation between them. Based on this structure, the designed radiator enjoys the advantages of high efficiency and low pulling effect. Compared with its fundamental counterpart, the load pulling and injection pulling are mitigated by 10 and 17 times, respectively.

Fifth, system modeling and innovative time-series post-processing techniques are proposed for multitarget active 2-D indoor positioning. The hardware architecture is based on the principle of a switched injection locked oscillator (SILO) and FMCW radar, which has been investigated by other researchers. Conventional frequency domain post-processing technique using a fast Fourier transformation (FFT) usually encounters a compromise among the resolution, target quantity,

signal-to-noise ratio (SNR) and other critical specifications, making it difficult to be adapted to many applications. The developed new technique features a joint singular value decomposition (SVD) based ESPRIT algorithm and a matrix diagonalization technique using Moore-Penrose pseudoinverse for the model order estimation as well as the time-of-arrival (TOA) and direction-of-arrival (DOA) extractions. With simulations and experimental demonstrations, the accuracy and resolution are shown to be superior to those of the conventional methods.

Finally, a multitarget harmonic backscattering positioning system with active tags (HPS-AT) using the SIHO is invented and presented. The tags used for our previous multitarget positioning system are based on fundamental-signal feedback-loop oscillator. So, the transmitting and receiving of both the base station (BS) and tag share the same frequency band. Such a hardware architecture has a number of drawbacks, namely unavoidable self-interference and cluster scattering, strong mutual-interference among multiple tags, load and injection pulling of tags, and so on. The developed HPS-AT can perfectly overcome these problems by leveraging the harmonics. In addition, the architecture can save 50% absolute bandwidth for the same resolution of range. Signal model is studied, and detailed tag and BS specifications, design and integration schemes are presented. Experimental results in reflection-rich indoor environments have demonstrated the concept and design.

The HPS-AT is a complete integration of the theoretical, technological and engineering works throughout this thesis. Its mmW version with CMOS integrated tag and more mature BS design is on the way. It will eventually become a very competitive candidate for ubiquitous position awareness solution for future generation IoT.

TABLE OF CONTENTS

DEDICACE.....	III
ACKNOWLEDGMENT.....	IV
RÉSUMÉ.....	V
ABSTRACT	VIII
TABLE OF CONTENTS	XI
LIST OF TABLES	XVI
LIST OF FIGURES.....	XVII
LIST OF ACRONYMS AND ABBREVIATIONS.....	XXVI
LIST OF APPENDICES	XXX
CHAPTER 1 INTRODUCTION.....	1
1.1 A Survey of Wireless Positioning Technology	1
1.2 Harmonic Wireless System and Devices	4
1.3 Motivation and Objectives	5
1.4 Thesis Organization.....	5
CHAPTER 2 ARTICLE 1: MULTIARMONIC GENERATOR FOR LARGE-SIGNAL- NETWORK-ANALYZER VERIFICATION	11
2.1 Design Requirements and Proposed Scheme	14
2.2 Circuit Design and Implementation	16
2.3 Measurement, Evaluation and Discussion	19
2.4 Summary	23
2.5 Acknowledgement.....	23
CHAPTER 3 ARTICLE 2: HARMONIC FEEDBACK-LOOP OSCILLATOR FOR PULLING EFFECT REDUCTION AND IMPROVED PHASE NOISE	25
3.1 Introduction	25

3.2	Operating Principle and Design Considerations	26
3.2.1	Principle of the harmonic feedback-loop oscillator	27
3.2.2	Diplexer design and oscillator simulation	27
3.3	Measurements and Discussions	29
3.4	Conclusion	32
3.5	Acknowledgement	33
CHAPTER 4 ARTICLE 3: LARGE SIGNAL MODELING AND EXPERIMENTAL DESIGN AUTOMATION OF SELF-ISOLATED HARMONIC OSCILLATOR FOR PULLING EFFECT REDUCTION		34
4.1	Introduction	34
4.2	Operation Principle and Equivalent Circuit	37
4.2.1	Review and comparison of the operation principle of SIHO and fundamental oscillators	37
4.2.2	Equivalent circuit development	39
4.2.3	Operation principle with negative resistance model	42
4.3	SIHO Modeling Based on X-Parameters	44
4.3.1	PHD model and X-parameter formulations	45
4.3.2	SIHO large signal modeling based on X-parameters	47
4.3.3	Large signal analysis of fundamental oscillator based on X-parameters	53
4.3.4	Injection locking of SIHO and fundamental oscillator	54
4.4	Design Theory, Methodology, Implementation and Model Verification	55
4.4.1	Microstrip diplexer design	55
4.4.2	Transistor characterization and SIHO design setup	58
4.4.3	HMD system calibration	61
4.4.4	Synthesis and screening of transistor waveform towards a feasible SIHO design	62
4.4.5	Experimental optimization of transistor waveform	66

4.4.6	Closed-form design of SIHO input matching network	68
4.4.7	Summary of experimental design procedure.....	71
4.4.8	Design example, model validation and discussions	72
4.5	Conclusion.....	84
4.6	Acknowledgement.....	85
CHAPTER 5 ARTICLE 4: A MILLIMETER-WAVE SELF-ISOLATED HARMONIC ACTIVE RADIATOR FOR IDENTIFICATION, SENSING, TRACKING AND COMMUNICATION APPLICATIONS.....		86
5.1	Introduction	86
5.2	Concept and Operation Principle	89
5.2.1	Partially-air-filled SIW cavity as resonator, diplexer, and antenna	90
5.2.2	Dependency of resonating frequency on dimensions and structure, and cavity design procedure.....	95
5.3	Fabricated Prototype, Tuning Technique and the Characterizations	104
5.3.1	Frequency and power post-tuning technique	104
5.3.2	Experimental characterizations of self-isolated active harmonic radiator prototype	106
5.3.3	Pulling effect mitigation experimental comparison with a fundamental frequency output active radiator.....	110
5.4	Conclusion.....	114
CHAPTER 6 ARTICLE 5: A MULTITARGET ACTIVE BACKSCATTERING 2-D POSITIONING SYSTEM WITH SUPERRESOLUTION TIME SERIES POST-PROCESSING TECHNIQUE		115
6.1	Introduction	115
6.2	System Architecture and Signal Model.....	118
6.2.1	Transmitted FMCW interrogation waveform	119
6.2.2	Backscattered signal from active targets.....	120

6.2.3	Received waveforms by base station	121
6.2.4	Discussion	124
6.3	Algorithm Development of Model Order Detection and Parameter Estimation.....	125
6.3.1	Principle of matrix construction and solution	125
6.3.2	Algorithm for model order estimation	127
6.3.3	Matrix stacking and joint SVD technique	128
6.3.4	Joint estimation of the TOA and DOA.....	129
6.4	System Performance Analysis and Simulation	132
6.4.1	Conventional FFT enabled FMCW and SILO positioning system	132
6.4.2	Effect of unsynchronized sampling	135
6.4.3	Validate the proposed algorithm and comparison with the FFT technique by simulations	136
6.5	Experimental Demonstration and Measurement Results	141
6.5.1	Base station and target demonstrator	141
6.5.2	Indoor experiments and measured results	145
6.5.3	Outdoor experiments and measured results	149
6.6	Conclusion.....	152
6.7	Acknowledgment	153
CHAPTER 7	A MULTITARGET HARMONIC-BACKSCATTERING POSITIONING SYSTEM WITH ACTIVE TAGS BASED ON SELF-ISOLATED HARMONIC OSCILLATOR.....	154
7.1	System Architecture and Signal Model.....	154
7.1.1	Architecture and advantages	154
7.1.2	Signal model and operation principle.....	157
7.2	Hardware Design of System Demonstrator.....	160
7.2.1	Frequency planning and link budget	160

7.2.2	Tag analysis and schematic	165
7.2.3	Tag components and complete design	167
7.2.4	BS front-end analysis and schematic	174
7.2.5	BS front-end filters and complete design.....	175
7.2.6	BS antennas and replaceable transition.....	181
7.3	Measurement and System Demonstration.....	185
7.3.1	Function measurement of tag and BS front-end.....	185
7.3.2	Positioning test in two indoor scenarios.....	190
CHAPTER 8	GENERAL DISCUSSIONS	199
CHAPTER 9	CONCLUSIONS AND FUTURE WORK	202
9.1	Conclusions	202
9.2	Prospects of Future Work.....	204
REFERENCES	206
APPENDICES	220

LIST OF TABLES

Table 2.1: Output Phasors Measured by an Agilent PNA-X NVNA.....	22
Table 2.2: The Calculated FOM.....	22
Table 4.1: Frequency Pulling Comparison of the Two Types of Oscillators.....	44
Table 4.2: Exemplary X-Parameter S and T Matrices of the Gain Block.....	79
Table 5.1: Performance Summary and Comparison with Published Active Radiators and Oscillators	110
Table 5.2: Performance Summary of the Harmonic and Fundamental Active Radiators	112
Table 7.1: System Demonstrator Link Budget and Key Specs	164
Table 7.2: Parameters of the Experimental Setup	191
Table 7.3: Result of the First Test Scenario with a Single Target	193
Table 7.4: RMSE of the Second Test Scenario with a Single Target	196
Table 9.1: Comparison of the Fundamental and Harmonic Positioning Systems Developed in this Thesis	203

LIST OF FIGURES

Figure 1.1: Active backscattering positioning system diagram illustrating the organization of chapters and the main contribution of the thesis.	10
Figure 2.1: The incident and scattered waves in a two-port nonlinear network mapping function contain fundamental and harmonic tones [53].	12
Figure 2.2: The block diagram of the proposed round-robin device. The arrows on top of each power marker indicate the signal content at that point.....	15
Figure 2.3: The ADS schematic and momentum combined simulation for an Avago HSMS8101 Schottky diode with input/output filtering and matching.....	17
Figure 2.4: Simulated and measured spectra of HSMS8101 Schottky diode with matching stubs.	17
Figure 2.5: The fabricated round-robin device. A JQL 2~10GHz isolator is added between the power amplifier and output variable attenuator.	18
Figure 2.6: The measured output spectra of the round-robin device. The input power is marked on the left of each curve.	19
Figure 2.7: Loading conditions for wave data measurement and FOM calculation are selected. Γ is frequency dependent and its values for 2 GHz and 10 GHz are shown.....	20
Figure 2.8: Load dependent wave data measurement setup of the round-robin device. The load impedances of Fig. 2.7 are presented to the output port of the round-robin. The coupling port of the 20-dB coupler is connected to the PNA-X.....	22
Figure 3.1: A conventional feedback-loop oscillator design.....	26
Figure 3.2: The proposed harmonic feedback-loop oscillator.....	27
Figure 3.3: The proposed diplexer: (a) layout; (b) simulated and measured S-parameters; (c) and (d) electric field distributions.	28
Figure 3.4: Simulated results of the proposed harmonic feedback-loop oscillator: (a) output spectrum with 50 Ω load; (b) frequency pulling.	29
Figure 3.5: The harmonic (a) and fundamental (b) feedback-loop oscillators.....	29

Figure 3.6: Measured results of both oscillators with 50 Ω load: output spectrum of (a) the harmonic and (b) the fundamental feedback-loop oscillators; phase noise of (c) the harmonic and (d) the fundamental feedback-loop oscillators.....	30
Figure 3.7: Load-pull measurement results: (a), (c) and (e) are the output frequency, power and phase noise variation of the fundamental feedback-loop oscillator; (b), (d) and (f) are those of the harmonic feedback-loop oscillator.	31
Figure 3.8: Comparison of the frequency pulling effects between the harmonic feedback-loop oscillator and the fundamental feedback-loop oscillator with and without 3 dB attenuator. .	32
Figure 4.1: (a) SIHO with a feedback-loop structure [91], (b) targeted frequency response of the diplexer.	38
Figure 4.2: (a) Fundamental oscillator, (b) frequency response of the resonator.	39
Figure 4.3: (a) Equivalent circuit of diplexer in SIHO, (b) equivalent circuit of resonator in the fundamental oscillator.	40
Figure 4.4: The frequency domain nonlinear circuit model of a gain.....	41
Figure 4.5: Complete equivalent circuit of the SIHO and the fundamental oscillator.....	42
Figure 4.6: Schematic of active subnetwork impedance derivation.....	43
Figure 4.7: Incident and scattered power waves of two-port nonlinear network mapping functions with the fundamental and harmonic tones [104].	45
Figure 4.8: Relation between the voltage/current waveforms of a gain block and the virtual source/load.	48
Figure 4.9: Equivalent circuit of SIHO employing X-parameters as the nonlinear model of the gain block.	49
Figure 4.10: Equivalent circuit of fundamental oscillator employing X-parameters as the nonlinear model of the gain block.	53
Figure 4.11: (a) One of the fabricated microstrip diplexers, and (b) simulated electric field intensity distribution of the first two resonant modes.....	56
Figure 4.12: Measured S-parameters of (a) fabricated diplexers with various value of parameter x , and (b) the fabricated diplexer with $x = 0.406$ mm.	57

Figure 4.13: (a) Schematic and (b) photo of the HMD system.	59
Figure 4.14: Schematic of SIHO for linear analysis and design.	63
Figure 4.15: Schematic of input matching network design.	69
Figure 4.16: (a) The fabricated SIHO with replacement diplexers of different values of parameter x , and (b) the open-loop SIHO for equivalent circuit building and X-parameter extraction.	72
Figure 4.17: Test setups for (a) power and efficiency measurement, (b) load pulling measurement, and (c) injection pulling measurement.	73
Figure 4.18: Measured results with a $50\ \Omega$ load of (a) spectrum of the first three harmonics, and (b) phase noise of the 2 nd harmonic output.	74
Figure 4.19: Transistor drain voltage and current waveforms synthesized by the experimental design procedure and obtained by measuring the SIHO prototype.	74
Figure 4.20: dc to 2 nd harmonic efficiency from the experimental design with respect to (a) source reflection coefficients at the 2 nd harmonic frequency, (b) load reflection coefficient at the fundamental frequency and (c) load reflection coefficient at the 2 nd harmonic frequency.	75
Figure 4.21: SIHO load pulling measurement results of the frequency shift and phase noise with diplexers of different x of (a) & (b) 0.406 mm, (c) & (d) 0.457 mm, (e) & (f) 0.356 mm, (g) & (h) 0.559 mm, (i) & (j) 0 mm and (k) & (l) -0.254 mm.	76
Figure 4.22: SIHO injection pulling measurement results with different value of x	77
Figure 4.23: Gain block X-parameter measurement (a) photo of the setup and (b) schematic of the configuration.	78
Figure 4.24: SIHO load pulling simulation results of frequency shift with diplexers of different isolations at $2f_0$ of (a) -46 dB, (b) -38 dB, (c) -35 dB, (d) -31 dB, (e) -28 dB, and (f) -22 dB.	80
Figure 4.25: (a) Equivalent circuit parameters of the diplexer, (b) variation of normalized transformer ratio versus to 2 nd harmonic isolation, and (c) S_{11} variations of the passive impedance in the SIHO equivalent circuit subject to load reflection coefficient points of Fig. 4.21, around the fundamental resonant frequency.	81

Figure 4.26: Model-predicted SIHO load pulling results of frequency shift with duplexers of different isolations at $2f_0$ of (a) -46 dB, (b) -38 dB, (c) -35 dB, (d) -31 dB, (e) -28 dB and (f) -22 dB.	82
Figure 4.27: Model-predicted SIHO load pulling results of frequency shift as the load impedance of the gain block at the 2^{nd} harmonic sweeps across the entire Smith chart.	83
Figure 4.28: Model-predicted SIHO load pulling results of the overall frequency shift as different X-parameter elements are independently attenuated or amplified.	83
Figure 5.1: The proposed self-isolated harmonic active radiator and the correspondences of its diplexer with the one based on microstrip line in [91].	89
Figure 5.2: Normalized intrinsic resonating frequencies of the first few modes of the rectangular and circular dielectric-filled SIW cavities.	90
Figure 5.3: The electric fields magnitude and surface current vectors of (a) TM_{010} mode, and (b) TM_{110} mode of the circular cavity. The proposed air-filled region and the radiation slot are also displayed.	92
Figure 5.4: The electric field vector of (a) TM_{010} mode and (b) TM_{110} mode of a regular circular cavity; and of (c) TM_{010} mode and (d) TM_{110} mode of a partially-air-filled circular cavity, at the AA' cutting in Fig. 5.3.	93
Figure 5.5: The assembly diagram of the fabricated tri-function SIW cavity with multilayer PCB process. (a) the top side with microstrip feeding lines; (b) the bottom side with radiation slot.	94
Figure 5.6: Ratio of the first two resonating mode frequencies and variation of the TM_{010} mode frequency (unit: GHz)	95
Figure 5.7: The simulated reflection coefficient at P2 of the designed tri-function SIW cavity. ..	96
Figure 5.8: The electric field magnitude and vector of the first three modes, (a) TM_{010} , (b) TM_{110} and (c) hybrid, of the tri-function SIW cavity.	96
Figure 5.9: (a) The simulated reflection coefficient at P2 of the designed SIW cavity without a radiation slot; (b) and (c) The electric field magnitude and vector of TM_{010} and TM_{110} modes of the designed SIW cavity without a slot.	98

Figure 5.10: (a) A dielectric resonator is attached to the slot; (b) The simulated reflection coefficients at P2 of the designed tri-function SIW cavity with dielectric loading; (c) The electric field vectors of the cavity with ϵ_r changed from 1 to 6.	99
Figure 5.11: (a) The top and (b) the bottom side photo of the fabricated tri-function SIW cavity prototype with dielectric resonator loading. (c) The prototype with the based and connectors assembled, and covered with microwave absorber material.	101
Figure 5.12: The simulated and measured S-parameters of the finalized tri-function SIW cavity design.	102
Figure 5.13: The simulated and measured gain of the finalized tri-function SIW cavity design.	102
Figure 5.14: The simulated E-plane gain with different size of the ground plane.	103
Figure 5.15: (a) The front and (b) the back sides of the fabricated self-isolated harmonic active radiator.	104
Figure 5.16: (a) and (b) are the photo and the simulation model of the cavity of the active radiator with tuning pins.	105
Figure 5.17: (a) The simulated S21 and S22 curves versus different pin insertion depth; (b) The frequency and power tuning setup.	106
Figure 5.18: The measurement setup for characterization of the active radiator prototype.	107
Figure 5.19: (a) The measured spectrum in the boresight of the DUT; (b) The measured phase noise of the DUT.	108
Figure 5.20: (a) The measured EIRP pattern in the E-plane and H-plane; (b) The TRP estimated by subtracting the gain curve from the EIRP curve.	109
Figure 5.21: The fabricated active radiator with fundamental frequency output at 28.24 GHz, based on a partially-air-filled SIW cavity.	111
Figure 5.22: Measurement setups of (a) load pulling test and (b) injection pulling test.	111
Figure 5.23: Measured normalized frequency and phase noise pulling of the harmonic radiator and the fundamental frequency radiator as the dielectric or the copper bar is positioned at different distance from the dielectric resonator.	113

Figure 5.24: Measured normalized frequency of the signal from the active radiators with respect to the injection signal frequency.	113
Figure 6.1: (a) System architecture and (b) Rx antennae array.	118
Figure 6.2: Backscattered waveform from the k th target.	120
Figure 6.3: Timing diagram of the sampled baseband signal.	123
Figure 6.4: The real part of the baseband spectrum of the SILO positioning system with one target. The carrier frequency of the target is assumed to be the center frequency of the interrogation chip signal.	132
Figure 6.5: Simulated spectrum and time-domain waveforms of the baseband: (a), (c) and (d) are the spectrum of the un-filtered, 20 MHz low pass filtered and 5 MHz low pass filtered baseband; (b), (d) and (e) are the time-domain waveform of the un-filtered, 20 MHz low pass filtered and 5 MHz low pass filtered baseband.	134
Figure 6.6: (a) Time-domain pulse in baseband and (b) its corresponding frequency-domain signal obtained by FFT.	135
Figure 6.7: Simulated curves of the TOA estimation error due to unsynchronized sampling through both the FFT method and the proposed method.	136
Figure 6.8: (a) Targets configuration for simulation; (b) Calculated and simulated CRLB and RMSE curves for radial distance estimations.	137
Figure 6.9: Calculated and simulated CRLB and RMSE curves for the DOA estimations.	138
Figure 6.10: Calculated and simulated CRLB and RMSE curves for the vector estimations.	138
Figure 6.11: Simulated 2-D position estimations with different target spacing at 10 dB SNR, using the proposed algorithms.	139
Figure 6.12: Resolution test of the FFT method at modulation frequency at (a) 1 MHz, (b) 5 MHz, (c) 10 MHz and (d) 20 MHz.	140
Figure 6.13: Description of the base station (a) system architecture and (b) fabricated demonstrator.	141
Figure 6.14: Fabricated active backscattering target demonstrator. (a) Front side and (b) back side.	142

Figure 6.15: (a) Antennae structure for the base station and the targets, (b) S-parameters of a pair of Tx and Rx antennae and (c) radiation patterns.	144
Figure 6.16: (a) The indoor measurement environment, (b) the layout plan of the test points and (c) the measurement setup.	145
Figure 6.17: (a) A snapshot of the I/Q waveforms of a target at 4 m/13.238°. (b) An indoor interference waveform recorded in baseband. (c) The I ₁ spectrum of the target at 4 m/13.238°.	147
Figure 6.18: Measured (a) distance and (b) angle of the indoor test.	148
Figure 6.19: Measurement results for two targets located at (a) 4 m/−6.619° and 4 m/6.619° as well as (b) 4 m/−13.238° and 4 m/0°.	149
Figure 6.20: (a) The outdoor measurement environment and (b) the layout plan of the test points.	150
Figure 6.21: Measured (a) distance and (b) angle of the outdoor test.	151
Figure 6.22: Measurement results for two targets located at (a) (−1.2 m, 4.8 m) and (0 m, 7.2 m) as well as (b) (−1.2 m, 4.8 m) and (0 m, 4.8 m).	152
Figure 7.1: A simplified schematic of the proposed HPS-AT. The BS has one Tx and J Rx's, and the active tags are based on SIHO with fundamental signal injection phase-locking and on/off modulation.	155
Figure 7.2: Illustrative waveforms of the k th tag: (a) received periodical chirp signal from the BS, (b) fundamental oscillation signal of SIHO phase-locked to signal in (a), and (c) 2nd harmonic of signal in (b), which is transmitted towards the BS.	158
Figure 7.3: Occupied frequencies in 4 GHz ~ 15 GHz band around the location of indoor HPS-AT demonstration.	161
Figure 7.4: Tag output spectrum with 5 MHz modulation frequency and 8 ns rise/fall time. Carrier frequency is normalized to 1 GHz.	161
Figure 7.5: (a) Proposed frequency planning of the BS front-end demonstrator. (b) Output spectrum of the Tx mixer in the BS front-end. (c) Output spectrum of the IF mixer of the Rx in the BS front-end.	163

Figure 7.6: (a) Operation principle of active tag with a switched SIHO, antennas, and switch-signal generator. (b) Timing diagram of switch control signals.	165
Figure 7.7: Layout of switch circuits on an HPS-AT tag.	167
Figure 7.8: Measured S-parameters of loop switch at (a) Switch I is at on-state and Switch II is at off-state; (b) Switch I is at off-state and Switch II is at on-state; (c) Both Switch I and Switch II are at on-state.	168
Figure 7.9: Layout and dimensions of tag input filters following the LNA.	169
Figure 7.10: Simulated and measured S-parameters of (a) BPF a, and (b) BPF a cascaded with notch filter a and notch filter b.	170
Figure 7.11: Perspective view and dimensions of Rx and Tx antennas of an HPS-AT tag.	170
Figure 7.12: (a) Measured S11 of Rx and Tx antennas of tag. (b) radiation patterns of Rx antenna. (c) radiation patterns of Tx antenna.	171
Figure 7.13: Simplified schematic of switch-signal generator of tag.	172
Figure 7.14: Photos of the PCB and complete unit of a tag for HPS-AT.	173
Figure 7.15: Detailed schematic and chain budget of the proposed BS Front-end.	174
Figure 7.16: (a) Layout of BPF3 with dimensions. (b) Simulated and measured S-parameters of BPF3.	176
Figure 7.17: (a) Layout of BPF4 with dimensions. (b) Simulated and measured S-parameters of BPF4.	177
Figure 7.18: (a) Layout of BPF5 with dimensions. (b) Simulated and measured S-parameters of BPF5.	178
Figure 7.19: (a) Layout of LPF in BPF6 with dimensions. (b) Simulated and measured S-parameters of LPF of (a) and BPF6.	179
Figure 7.20: Photo of the fabricated filters for BS front-end.	180
Figure 7.21: Photo of the BS front-end prototype.	180
Figure 7.22: Aperture feed patch array antenna for BS Tx, (a) structure and dimensions, (b) S11, and (c) radiation pattern.	181

Figure 7.23: SIW slot array antenna for BS Rx, (a) structure and dimensions, (b) S11, and (c) radiation pattern.....	182
Figure 7.24: (a) Fabricated antennas assembled on a BS front-end demonstrator. (b) SIW replaceable transition to an Rx antenna with 90° bend or to an SMA connector. (c) Structure and dimensions of an SIW transition between thin and thick SIW units using an impedance matching wedge. (d) Measured S-parameters of two test interface blocks in back-to-back connection, and thin to thick SIW transition followed by a 90° bend.	184
Figure 7.25: (a) OTA measured waveform of a tag. (b) Close-in view of a pulse in the measured waveform.....	185
Figure 7.26: OTA measured output spectrum of a TUT under frequency pulling test. The TUT is in continuous-wave mode, subject to signal injection with different frequency.....	186
Figure 7.27: Phase locking test results of a TUT. Waveforms of a tag are OTA measured with an injection signal at 6.5 GHz and with power of (a) -74 dBm, (b) -64 dBm, (c) -54 dBm, (d) -44 dBm, (e) -34 dBm, (f) -29 dBm, and (g) -16 dBm.	188
Figure 7.28: Output spectrum of Tx of the BS demonstrator.....	189
Figure 7.29: Baseband spectrum of Rx when RF input power is (a) -72.5 dBm, and (b) -44.5 dBm.	190
Figure 7.30: (a) Photo of the first test environment and setup. (b) Layout plan and target distribution. (c) Error bar of angle and range measurements.	192
Figure 7.31: (a) A snapshot of the baseband I/Q waveforms related to a tag at position No. 12. (b) Spectrum of the recorded baseband I_1 signal during a chirp period.	194
Figure 7.32: (a) Photo of the second test environment and setup. (b) Layout plan and target distribution. (c) Error bar of angle and range measurement.	195
Figure 7.33: (a) A snapshot of baseband I/Q waveforms related to a tag at position 2_8. (b) Spectrum of the recorded baseband I_1 signal during a chirp period.	197
Figure 8.1: (a) The perspective view of an SIW liquid crystal phase shifter. (b) The fabricated assembly showing the liquid crystal cell and electrode.	200
Figure 8.2: A waveform of mmW switched SIHO on CMOS technology.	200

LIST OF ACRONYMS AND ABBREVIATIONS

2-D	Two-dimensional
3-D	Three-dimensional
5G	5 th generation
ADC	Analog-to-digital converter
ADS	Advanced Design System
AM	Amplitude modulated
AR	Augmented reality
AWG	Arbitrary waveform generator
BPF	Band-pass filter
BS	Base station
CDMA	Code Division Multiple Access
CRLB	Cramer-Rao lower bound
CW	Continuous wave
DAR	Distributed-active-radiator
DDS	Direct digital synthesizer
DOA	Direction-of-arrival
DR	Dielectric resonator
DRA	Dielectric resonator antenna
DUT	Device under test
EIRP	Equivalent isotropic radiated power
ET	Extraction tone
FCC	Federal Communications Commission
FFT	Fast Fourier transform
FMCW	Frequency-modulated continuous-wave

FOM	Figure of merit
HMD	Harmonic-measurement-and-design
HMFCW	Heuristic multi-frequency continuous-wave
HPF	High-pass filter
HPR	Harmonic phase reference
HPS-AT	Harmonic-backscattering positioning system with active tags
I/Q	In-phase and quadrature
IF	Intermediate frequency
IL	Insertion loss
IM	Intermodulation product
IoS	Internet of Space
IoT	Internet of Things
LNA	Low noise amplifier
LO	Local oscillation
LPF	Low-pass filter
LS	Least-squares
LSNA	Large signal network analyzer
MCU	Micro-controlling-unit
MIMO	Multi-input and multi-output
MMIC	Millimeter-wave integrated circuit
mmW	Millimeter-wave
MSL	Microstrip line
NF	Noise figure
NIST	National Institute of Standards and Technology
NLTL	Nonlinear-transmission-line

NVNA	Nonlinear vector network analyzer
OOK	On-off keying
Op-Amp	Operational amplifier
OTA	Over-the-air
OWF	OpenWave Forum
PA	Power amplifier
PCB	Printed circuit board
PD	Pin diode
PHD	Poly-Harmonic Distortion
PLL	Phase-locked-loop
PSO	Particle swarm optimization
Q factor	Quality factor
RF	Radio frequency
RFID	Radio frequency identification
RMSE	Root-mean-square-error
Rx	Receiving channel
SIHO	Self-isolated harmonic oscillator
SILO	Switched injection-locked oscillator
SIR	Stepped-impedance resonator
SIW	Substrate integrated waveguide
SNR	Signal to noise ratio
SoC	System-on-chip
SPDT	Single-pole-double-throw
SVD	Singular value decomposition
TOA	Time-of-arrival

TOF	Time-of-flight
TRP	Total radiated power
TUT	Tag-under-test
Tx	Transmitting channel
UWB	Ultra-wideband
VCO	Voltage controlled oscillator
VNA	Vector network analyzer
VR	Virtual reality
WLAN	Wireless local area network

LIST OF APPENDICES

Appendix A – Publications and patents.....	220
--	-----

CHAPTER 1 INTRODUCTION

About two decades ago, people realized that future wireless should be more than just a simple upgrade of the data rate, many additional features like positioning are required to enable people to benefit from wireless services in a much more convenient and efficient way [1, 2]. From then on, wireless technology has steadily evolved from the 2nd to 4th generation. Unfortunately, the improvements of the basic infrastructure are still limited to a relatively narrow scope of the data rate. As the 5th generation (5G) wireless is becoming even closer to a reality, once again people start to imagine a world with truly ubiquitous connectivity [3, 4], not only between people to people, but also embracing all types of objects, empowered with smartness [5-8], enabled by sensing, location awareness, communication, computing and machine learning. The internet of things (IoT) and related future wireless systems are designed in support of the hardware, software and function fusion of communication, sensing and powering. One of the critical enabling technologies is accurate indoor and outdoor physical positioning, which allows the real-time tracking of objects. Location awareness helps the nodes of an autonomous network to effectively interact and cooperate with each other and to discover the value of data. Different applications of wireless positioning technology can be found in logistics, manufacturing, healthcare, security, virtual reality (VR)/augmented reality (AR), and so on.

1.1 A Survey of Wireless Positioning Technology

A large number of publications and documents have already contributed to the understanding of different types of wireless positioning technology for different applications [9-12]. A straightforward way is to use the received signal strength [13, 14], which is reversely proportional to the square of distance in the perfect and ideal situation. This technology is mostly used with wireless local area network (WLAN) and commercially available terminals like mobile phone. With the most sophisticated algorithms, single-digit meter of accuracy can be achieved.

Generally speaking, systems based on geometry information (e.g. measuring the direction-of-arrival (DOA)) and systems based on propagation time (e.g. measuring the time-of-arrival (TOA)) are the two broad categories of remote or wireless positioning systems that can achieve a decimeter magnitude of accuracy. Geometry-information-based systems need a number of distributed base station (BS) with prior-known coordinates for angle detection, from which the distance is calculated through trigonometry. The most commonly used positioning techniques based on

propagation time are related to GPS, Galileo, GLONASS, and Bei-Dou systems. They are all self-positioning oriented, which means the BSs (e.g. satellites) broadcast reference signals to let any person or object equipped with dedicated receivers to get their own coordinates based on measuring the time differences. Ultra-wideband (UWB) positioning technology utilizes very short electromagnetic wave pulses (< 1 ns) to measure the time-of-flight (TOF) of an echo signal with a centimeter level high accuracy [15, 16]. But they usually have a limited range of coverage.

Absolute or relative time synchronization depending on specific architectures is required for a time-based system. The well-known and widely deployed frequency-modulated continuous-wave (FMCW) radar is a typical round-trip TOF positioning concept [17-19]. It has a relative time synchronization requirement fulfilled by the base station generating a highly linear and precise modulated waveform, which can easily be realized with voltage-controlled oscillator (VCO) or direct digital synthesizer (DDS) techniques [20]. Many researchers have been focusing on the development of derivatives of the FMCW system, thereby attempting to make breakthroughs with regards to larger range, lower bandwidth, higher sensitivity, multitarget identification and immunity to multipath. The essentials of some of these works can be concluded as adding modulation capabilities to the targets [21-23]. This move would be able to avoid low-frequency noise and passive clutter scattering. Moreover, data can be modulated on the backscattered signal of the targets. However, a major drawback is related to a heavy burden of dynamic range on the amplification stages of the targets and a limited link gain improvement. The signal has to travel through the round-trip distance, and the link loss is thus proportional to the 4th power of distance. Researchers have also successfully implemented the concept of multi-input and multi-output (MIMO) to realize a super-resolution FMCW system for dense multipath environment [24].

Recently, an FMCW concept with harmonic frequency diversity in down-link (BS to tag) and up-link (tag to BS) has been proposed [25]. The authors of this work use a 24 GHz wide locking-range divider-by-10 as a positioning tag. The BS is a modified FMCW radar in which the mixer in the receiver uses a transmitted chirp signal divided by 10. Due to the wide locking range and excellent sensitivity of the divider, the tag can tightly track the frequency of the interrogation signal and backscatter an echo with a fixed amplitude. In this way, the dynamic issue related to the 4th power of distance free space loss is greatly mitigated. However, from the resolution point of view, assuming the 24 GHz interrogation signal has a bandwidth of BW , such a system is equivalent to a conventional FMCW radar with $BW/10$ bandwidth because of the operation of frequency dividing.

Instead of dividing the frequency, some other researchers have exploited the harmonic generation of tags in the development of positioning systems [26-31]. Among them, D. Psychoudakis et al. developed an ultra-small tag with Minkowski loop around a Schottky diode, which works with an FMCW radar of doubled demodulation frequency as the BS [26]. By doing so, the problem of BS-related self-interference issue is solved. But there is a severe problem of sensitivity caused by the high conversion loss of the tag. In [27], the tag still uses a diode to generate harmonics, while the radar BS uses a pulse pseudorandom code as the transmitted interrogation signal, thereby greatly improving the sensitivity. Y. Ma et al. developed a heuristic multi-frequency continuous-wave (HMFCW) scheme with harmonic tags based on a nonlinear-transmission-line (NLTL) [28]. Compared with tags based on a single diode, NLTL tags have conversion loss and bandwidth advantages. The phase ambiguity issue with a CW radar is solved by a heuristic multi-frequency method. This work achieved an outstanding millimeter level accuracy in a space less than 1 square meter. However, to achieve two-dimensional (2-D) or three-dimensional (3-D) positioning, multiple BS receivers need to be deployed around the region of coverage. Since there is an absence of modulation capability on the tag, data transmission or object identification is impossible. In [29] and [30], the authors further empowered the NLTL tag with Code Division Multiple Access (CDMA) coding so as to achieve a multitarget processing capability in real-time.

In recent years, a new positioning scheme based on switched injection locked oscillator (SILO) has been brought to light. As it has been discussed in the literature [31-34], it extends the concept of conventional FMCW system and exhibits the advantages of simple structure, high precision, long range, and less sensitive to clutter as well as the feasibility of simultaneous data transmission. It can be regarded as a discrete form of conventional FMCW radar. Since the signal out of the target is spontaneous rather than a modulated/doubled/amplified duplicate of the interrogation signal, the link loss is solely proportional to the 2nd power of distance. For such a system, a fast Fourier transform (FFT) is usually employed to convert the baseband into the frequency-domain and calculate the range. Such a frequency-domain technique maintains a significant accuracy as long as only one single target is in the range of detection. As more targets come into play, their modulation frequency has to be appropriately staggered such that their corresponding characteristic peaks in the spectrum can be differentiated and the spectrum leakage issue can be minimized. At the same time, the pulse width of the targets has to be narrow enough for an increased peak sharpness so as to guarantee a low mean error [35] as well as to avoid a multitarget overlapping.

However, a reduced pulse width would lower down the duty cycle and in turn the signal to noise ratio (SNR).

1.2 Harmonic Wireless System and Devices

Besides the systems utilizing harmonics for extra performance improvements in wireless positioning as mentioned above, there are other scenarios in which harmonic signals provide favorable features. P. Cheong et al. investigated a nonlinear communication system through a harmonic diversity [36]. Instead of transmitting and receiving a single sideband of the up/down converted signal, their proposed communication scheme takes advantages of harmonic mixing products concurrently. This move is equivalent to the use of multiple channels with a single transceiver. Therefore, the SNR is multiplied with a minimum power consumption overhead. They have resolved the issue of a phase shift difference for different channels and successfully combined the information at the receiver by controlling the phase of local oscillator (LO). In sensing applications, the movement or vibration of the sensor itself may destroy an extremely weak signal. Researchers have attempted to look for different techniques to mitigate this issue, but generally with an increase of system complexity, cost, and power consumption. F. Zhu et al. proposed and demonstrated a vital sign sensor using the fundamental and 2nd harmonic signal of a VCO concurrently to cancel the radar platform vibration [37].

The harmonic phenomenon, no matter how strong or negligible, is the nature of all semiconductor and other nonlinear/active devices. People have been making all their efforts to understand, model and harness harmonics for improved circuit performance and functionality. The large signal network analyzer (LSNA) and X-parameters in this connection, have been attracting much attention of researchers and engineers in nonlinear device modeling and circuit design [38-40]. The X-parameter is an extension of the most widely used tool – the S-parameter. However, it is far less mature, and many activities are going on for its standardization, characterization and verification [41-43]. Nevertheless, many nonlinear circuit designs have been done with X-parameters, such as oscillator [44, 45], power detector [46], power amplifier [47], and so on. Moreover, it is an effective tool for device modeling [48-51]. Although the X-parameters are usually regarded as a black box method due to the complexity, they can be mapped to describe circuit behavior and physical insights. However, for the best of our knowledge, only few pieces of literature use the X-parameter in an analytical way [48, 49].

1.3 Motivation and Objectives

From our search and examination of the background and state-of-the-art positioning technology, it seems that a backscattering positioning system with modulated active tags and harmonic frequency diversity has not existed so far. It is expected to combine numerous advantages, namely long range, high accuracy and resolution, immune to self- and mutual- interference, cluster resistant, large equivalent bandwidth and easy to integrate. Moreover, we need to consider application scenarios in which tags are subject to foreign object in proximity or high-density spectrum, thus resulting in load pulling or injection pulling. Therefore, the objective of this thesis research from theory to engineering and from component to system includes the following aspects:

- First, we propose, study and demonstrate a new class of harmonic oscillator addressing the issue of pulling effect.
- Second, we develop accurate modeling technique and design methodology for analysis and design of the innovative harmonic oscillator.
- Third, we develop signal modeling and baseband post-processing algorithms for an active backscattering positioning system based on SILO principle, towards multitarget operation and superresolution. Simulation and experiments need to be used to verify the results.
- Fourth, we develop and demonstrate an active backscattering positioning system with harmonic frequency diversity, in which a tag is based on the proposed harmonic oscillator, using developed post-processing techniques.

1.4 Thesis Organization

This thesis is organized in an articles-based format. Chapter 2 to Chapter 6 present the contents of three published articles and two submitted articles. The content of Chapter 7 is an article that is ready for submission, in which the proposed and disclosed device and system are pending for patent filing. In the above-mentioned articles, the Ph.D. candidate has made principle contributions and is also the principal author. The general discussions of Chapter 8 reflect some other published works related to the theme of the present thesis, in which the Ph.D. candidate is the principal or secondary contributor. The chapters organization which explains the process of this research work and the coherence of those articles in connection with the objective of the research is detailed follows:

Chapter 1: Introduction

This chapter introduces wireless positioning technologies and applications, reviews the state-of-the-art and summarize existing problems and our motivation for the development of this highly original research project and related demonstrations in this area. It also introduces the background and our motivation of analysis and design of nonlinear circuits, explaining how it is relevant and important to the proposed system architecture. This chapter also explains the organically arranged structure of the thesis.

Chapter 2 Article 1: Multiharmonic Generator for Large-Signal-Network-Analyzer Verification

by Kuangda Wang, Sulav Adhikari, Anthony Ghiotto and Ke Wu, in *IEEE Microwave Magazine*, 2014.

This chapter serves as the foundation work of harmonic measurement and design techniques used throughout this thesis. An LSNA round-robin verification artifact is designed and characterized. It is a robust harmonic generation device that receives a monotone as the input signal with a frequency of 2 GHz and a power from -20 dBm to 10 dBm. The device output is required to deliver the 1st to 5th harmonics of the input one each with a power gain/loss within a single digit dB. The developed device is subject to a load pull test, from which a figure of merit (FOM) defined as the standard deviation of the output wave vectors under different loading conditions is calculated. This work won the first prize of IMS2013 student design competition coordinated by NIST.

Chapter 3 Article 2: Harmonic Feedback-Loop Oscillator for Pulling Effect Reduction and Improved Phase Noise by Kuangda Wang, Anthony Ghiotto and Ke Wu, in *2014 IEEE MTT-S International Microwave Symposium*, 2014.

In this chapter, a novel feedback-loop oscillator architecture that features low pulling effect and low phase noise is proposed. The loop of the proposed oscillator uses a diplexer to replace the resonator to achieve an effect of separating the fundamental and 2nd harmonic signal. Since the gain block in the loop operates under a deeply saturated, strong nonlinear condition, circuit design and optimization are based on its X-parameter, which is measured with a calibrated and verified LSNA. Due to its performance advantages of low pulling effect and harmonic output, the proposed oscillator is an excellent choice for building a tag designated for a harmonic positioning system. An exemplary oscillator design with a 5.8 GHz output is fabricated, measured and shown to be 15~20 times superior over a conventional fundamental oscillator related to the pulling effect.

Chapter 4 Article 3: Large Signal Modeling and Experimental Design Automation of Self-Isolated Harmonic Oscillator for Pulling Effect Reduction by Kuangda Wang, Anthony Ghiotto, Fang Zhu and Ke Wu, in *IEEE Transactions on Microwave Theory and Techniques*, 2018.

In this chapter, the operating principle and mechanism of the pulling effect of the proposed novel harmonic oscillator are investigated, with equivalent circuit and matrix manipulations on X-parameters. From the analysis, it can be found that a self-isolation property is created by a joint effect of the gain block and the diplexer of the loop. Therefore, the device is named as a self-isolated harmonic oscillator (SIHO). Besides the modeling, a design automation methodology and hardware system not only for the SIHO but also benefits any nonlinear circuit design is proposed and demonstrated. System calibration, waveform measurement & optimization, parameter screening, and harmonic impedance matching are all formulated and can be executed automatically. Compared with simulation with software packages, synthesizing a nonlinear circuit with the proposed system does not require an accurate large signal transistor model but can provide a more predictable result. An SIHO designed by this system has a 16.6 dBm output power, 4 GHz output frequency, 28% dc to RF conversion efficiency and -136.5 dBc/Hz phase noise at 1 MHz offset. Such a prototype is used to verify the developed SIHO model by comparing the measured and model-predicted frequency shift subject to a load variation. It has been identified that to mitigate the pulling effect of an SIHO, a diplexer with high isolation and a gain block with weak conversion between the fundamental and 2nd harmonic signal at its output terminal have to be selected.

Chapter 5 Article 4: A Millimeter-Wave Self-Isolated Harmonic Active Radiator for Identification, Sensing, Tracking and Communication Applications by Kuangda Wang, Anthony Ghiotto, Lei Guo, Fang Zhu, and Ke Wu, in *IEEE Transactions on Antennas and Propagation*, 2018.

An SIHO-antenna integration is one more step towards a harmonic tag for the active backscattering positioning system to be highlighted in this thesis research. This chapter demonstrates such a concept of a function and structure fusion over the mmW band, in which signal interconnection between blocks with long transmission lines is usually inefficient. Instead of using a microstrip line (MSL) diplexer for fundamental and 2nd harmonic signal separation as an SIHO, the proposed harmonic active radiator takes advantage of a unified diplexer-resonator-antenna structure based on an orthogonally feed dual mode, partially air-filled SIW resonator with high quality factor (Q-factor). A low load pulling effect is still preserved and the generated 2nd harmonic signal can be radiated concurrently through a slot on the broadside of the cavity, which only couples to the 2nd order mode. Resonator mode frequency tuning techniques including an adjustment of the air-filled

region and dielectric resonator (DR) loading on the radiating slot are implemented. The fabricated radiator prototype has an equivalent isotropic radiated power (EIRP) of 15 dBm at 28.15 GHz with a phase noise of -108 dBc/Hz at 1 MHz offset. Another active radiator is designed and fabricated for comparison. Because it has an inline feeding of the diplexer-resonator-antenna as the only structural difference to the proposed radiator, it will oscillate and radiate both at 28 GHz. Dielectric and metal strips approaching the radiating elements are used to emulate the load pulling effect while injection pulling test is carried out by illuminating the active radiators with a horn antenna attached to a signal generator. As a result, the proposed harmonic active radiator has made 10 and 17 times reduction of load pulling and injection pulling, respectively. This work was filled as a US provisional patent.

Chapter 6 Article 5: A Multitarget Active Backscattering 2-D Positioning System with Superresolution Time Series Post-Processing Technique by Kuangda Wang, Jian-Feng Gu, Fengchao Ren and Ke Wu, in *IEEE Transactions on Microwave Theory and Techniques*, 2017.

This chapter is an invited paper in IEEE T-MTT. It presents the theoretical foundation and experimental verification of the signal model and innovative post-processing algorithms of a multitarget active backscattering positioning system based on the hardware architecture of a SILO and FMCW radar. Classical algorithms used by other researchers for this type of hardware architecture are based on an FFT, which has been proven to be fast, accurate and easy to realize if only one target is considered. As more targets are involved, a lot of compromises has to be made to ensure the function of the system. This chapter overcomes certain drawbacks and improves the system performance with time domain post-processing technique features a joint singular value decomposition (SVD) based ESPRIT algorithm and a matrix diagonalization technique using Moore-Penrose pseudoinverse for model order estimation as well as the TOA/DOA extraction. Performance advantages are verified by simulations and experiments with the developed BS and tag prototype. In spite of the achievements, there are still some drawbacks with the system that hinder a robust application in real environments, which are inherent to the hardware architecture. With this in mind, we have made further advancements in the next chapter.

Chapter 7 A Multitarget Harmonic-Backscattering Positioning System with Active Tags Based on Self-Isolated Harmonic Oscillator

This chapter invents and presents a new hardware system for the multitarget active backscattering indoor positioning that incorporates harmonic tags based on the developed SIHO. The same post-

processing algorithms as what has been described in Chapter 6 are implemented. Therefore, the work in this chapter bridges the hardware and algorithm aspects and results in a system with highly preferred features and performance. The key innovation is using fundamental and harmonic bands as down- and up-link respectively between a BS and tags. This is achieved by using a switched phase locked SIHO as the backscattering tag and using a chirp signal frequency doubling in the BS. By doing so, the primary issue of self-interference on both tags and BS and mutual-interference among tags are completely suppressed. Cluster scattering, which may get overlapped with a useful signal is mitigated. Another valuable feature of the system is a saving of 50% bandwidth for the same resolution requirement. And a reduced pulling effect of tags is certainly maintained. Signal model of the entire system is studied and proven to have equivalence to a fundamental system (the one in Chapter 6) with a doubled bandwidth. The design of such a harmonic system is presented as a tutorial, which consists of frequency planning, link budget, BS chain budget, conception and components design of tag and BS, as well as system integration. The developed tag and BS are tested and studied independently. Two indoor scenarios with different multipath characteristics are selected for the final positioning test and evaluation. This work is subject to a patent pending.

Chapter 8: General Discussions

This chapter makes general discussion on some other aspects in our published papers related to the theme of the thesis that is not covered by the first few chapters. It includes system re-configurability, other applications of the harmonic techniques and additional comments about positioning system signal processing.

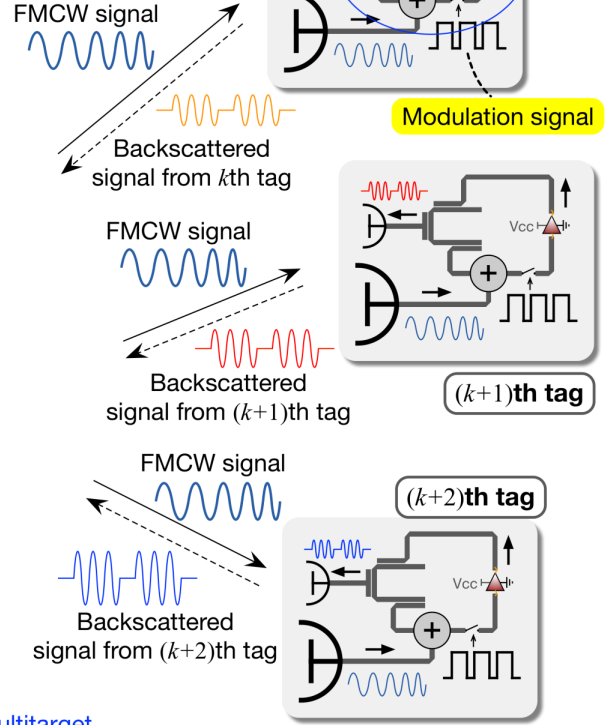
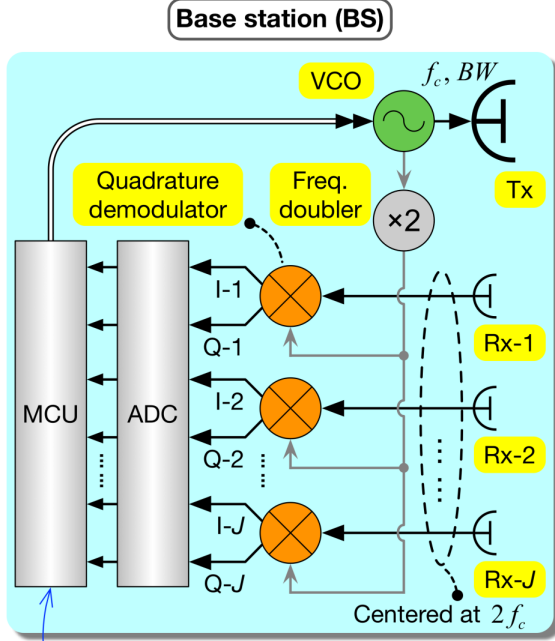
Chapter 9: Conclusions and Future Works

This chapter concludes the results of research and demonstration in this thesis, introduces some on-going extension works and discusses the prospects of promising directions of related future work.

To summarize, the contents of Chapter 2 to Chapter 7 and the main contribution of this thesis can be reflected by Fig. 1.1.

1. Verification artifact for nonlinear device characterization (**Chapter 2**)
2. Experimental verification of SIHO pulling effect reduction (**Chapter 3**)
3. Theory, modeling and design technique of SIHO (**Chapter 4**)
4. Self-isolated harmonic radiator (SIHO and antenna fusion) for tags of millimeter-wave positioning system (**Chapter 5**)

SIHO



5. Time domain signal post-processing technique of multitarget active backscattering positioning system and experimental verification (**Chapter 6**)
6. Complete active backscattering positioning system using tags based on SIHO: theory and experiments (**Chapter 7**)

Figure 1.1: Active backscattering positioning system diagram illustrating the organization of chapters and the main contribution of the thesis.

CHAPTER 2 ARTICLE 1: MULTIARMONIC GENERATOR FOR LARGE-SIGNAL-NETWORK-ANALYZER VERIFICATION

Co-authored by Sulav Adhikari, Anthony Ghiotto, and Ke Wu

Published in « *IEEE Microwave Magazine* », 2014.

Since S-parameters [52] were first used to describe linear microwave circuits in the 1960s, circuit designers, software developers and instrument manufacturers have gradually come to the agreement on this ‘black-box’ representation, resulting in significant advancements in modeling, simulation, and measurement. As a mathematical language of high frequency signal transmission and scattering, S-parameter stands for a unified form of the linear characteristics of microwave networks in the frequency domain. Subsequently, the vector network analyzer (VNA) was invented as the principal instrument to measure S-parameters and characterize the linear behavior of devices and components including small signal active circuits.

As high frequency electronics are considered to operate in a nonlinear regime, designers and developers are in urgent need of not only a similar ‘black-box’ model that contains nonlinear information but also a nonlinear VNA (NVNA) or large-signal network analyzer (LSNA) to be able to conveniently build such a model through measurement or experimental parameter extractions. For example, in conventional RF oscillator design, S-parameters are used to determine the transistor’s unstable region and to carry out impedance matching. This is a popular method because, first, sometimes the transistor is low noise oriented and only linear model is provided by the manufacturer. Second, this method is simple and effective although strictly speaking, the oscillating transistor works under a nonlinear condition where the S-parameter is invalid. But such a design method has many limitations as it cannot guarantee the frequency accuracy or predict the output power. Therefore, researchers and practitioners have been looking for the nonlinear counterpart of S-parameters, which, as a design protocol, could render the entire nonlinear circuit design workflow more efficient and accurate. Then, the oscillator designers only need to measure the transistor’s nonlinear parameter and accomplish the design with compatible simulation software.

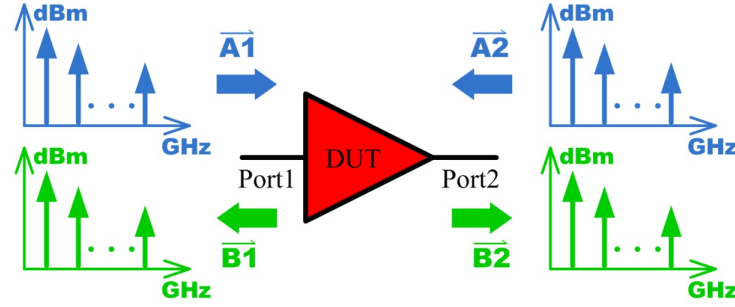


Figure 2.1: The incident and scattered waves in a two-port nonlinear network mapping function contain fundamental and harmonic tones [53].

Such a ‘black-box’ model should be different from the conventional nonlinear models including empirical and physics-based models and the models based on load-pull measured figure of merits (FOMs) [54]. The first type of model makes use of the knowledge of the device physics and an array of measured data. Model parameters are adjusted to curve-fit with the data. Existing models cannot adapt to the needs of new devices, which demand different and more sophisticated models, naturally resulting in higher costs and more effort. With the assistance of automated active load-pull systems, the second type of models are easier to obtain but are only applicable to specific conditions under which measurements are conducted. Generally, they can only reveal part of the nonlinear property such as efficiency of power amplifier (PA) versus load impedance. Nonetheless, the load-pull model seems to gain ground in connection with a new type of models that will be introduced below.

The initial effort of a ‘black-box’ type of nonlinear modeling was made by Hewlett-Packard’s Microwave Technology Center (now Agilent Technologies Inc.) in the early 1990s. In the mid 2000’s, the Poly-Harmonic Distortion (PHD) framework based on a Ph.D. student’s work was proposed [55-57]. This model is derived from Volterra theory when the various Volterra Gain functions are linearized relative to the finite number of weak harmonic tones [58]. In other words, the devices under test (DUTs) to be modeled are assumed to responds to the large drive signal in a nonlinear way, but to the additional small harmonic signals in a linear way. Such a power restriction to the harmonic tones is the limitation of the PHD model and is of great importance in understanding derivative models and measurement approaches. But it is shown that such an assumption is well approximated by different classes of power amplifiers and other common nonlinear circuits [59]. As a result, the DUTs are represented by a series of mapping functions in

the frequency domain to relate the input and output waves (containing fundamental and harmonic tones), as shown in Fig. 2.1 [53]. The magnitude and phase information extracted from those functions enables the description of complete time domain I/O waveforms.

Under this framework, X-parameter [53], which is a registered trademark of Agilent, has been developed. Together with X-parameter, Agilent PNA-X series NVNAs were put into the market and Advanced Design System (ADS) software was also updated in support of X-parameter models in the simulation. Besides Agilent, some other corporations have also used the PHD model to develop their own practical nonlinear modeling, simulation and measurement techniques. Rohde & Schwarz, for example, cooperated with NMDG, a company which was created by a former employee of HP/Agilent and is now part of National Instrument. They developed ZVA and ZVT series LSNAs. In parallel, the OpenWave Forum (OWF) with founding members of Anritsu, AWR, Rohde & Schwarz, Tektronix, HFE, NMDG and Mesuro was formed to collaborate, create and promote a unified and transparent data exchange format for large signal simulations, measurements and modeling [60].

Unlike S-parameters that only need relative amplitude and phase between input and output tones at certain frequencies, the nonlinear models based on the PHD framework or the OWF framework require not only the absolute amplitude of the input and output tones at fundamental and harmonic frequencies but also the cross frequency relative phase between the input and output tones at fundamental and harmonic frequencies. The accuracy of measuring absolute amplitudes and relative phases determines the nonlinear instrument's performance and reliability.

One of the key components determining the NVNAs' or LSNAs' accuracy is the harmonic phase reference generator (HPR or comb generator). The accuracy of the HPRs used in today's LSNAs is traceable to the electro-optic sampling oscilloscope at the National Institute of Standards and Technology (NIST) [38, 61, 62]. There is still a lack of a universal standard at NIST that could identify the measurement errors of LSNAs and evaluate the instruments' ability of resolving the amplitude and phase of signals.

The NVNA user's forum of the ARFTG conference in 2011 discussed the system verification of NVNAs or LSNAs. Mesuro proposed several ways and one of them is the round-robin device that can be seen as a standard nonlinear device and circulated among different systems in different labs [63]. Furthermore, Mesuro mentioned that such a round-robin device was highly desirable but was not readily available in the market. In the discussion of NVNA calibration, verification and

traceability during that conference, attendees talked about the necessity of a round-robin device. National labs have also been searching for ways to improve the NVNA's calibration, verification and traceability. All in all, vendors and labs have shared a common view that a round-robin device (different from HPR) is needed [64].

The harmonic contents of nonlinear device response can be influenced by its input and output termination impedance. The reason is the altered input/output incident waves which are the consequences of changed termination will result in the variation of output signal in a nonlinear way. However, for error diagnostic purposes, the round-robin device should always be able to generate a constant output signal under different fundamental and harmonic termination impedances and input power. The round-robin device has its own harmonic fingerprint that can be extracted accurately by a national lab (such as NIST). Then, NVNAs and LSNAs are set to measure the round-robin device. The instruments' errors should be identified by comparing the data they have measured with the fingerprint. If one instrument's measured data is coincident with the fingerprint, the instrument's accuracy is traceable to the national lab.

During the 2012 IEEE Microwave Theory and Techniques Society (MTT-S) International Microwave Symposium (IMS2012) in Montreal, a new topic of student design competition entitled 'Development of a Large-Signal-Network-Analyzer Round-Robin Artifact' was added, leading to significant interests and fruitful results. It was promoted by NIST and sponsored by the Microwave Measurement Committee in the MTT-S. Again, during IMS2013 in Seattle, this design competition was scheduled with extra technical requirements including a larger input power range and also overall power gain restrictions. This article presents the winning project of this year's student design competition.

2.1 Design Requirements and Proposed Scheme

The main requirements of the competition are listed below:

- (1) The input tone is at 2 GHz.
- (2) The device should create a fundamental and four harmonic tones at the output of the device.
- (3) The output fundamental and harmonic phasors should be insensitive to the load mismatch for which the reflection coefficients are limited to $|\Gamma_L(n\omega_0)| < 0.5$ for $1 \leq n \leq 5$.
- (4) The device can function with input signal power between -20 dBm and 10 dBm.

- (5) The output power of each tone must be between the input signal level and the input signal level+15 dB.
- (6) Each output tone should change at least 20 dB as the input signal change between -20 dBm to 10 dBm.
- (7) No more than two dual polarity power supplies (20 V, 1 A).

Based on the aforementioned competition rules, the amplitudes of the output tones are considered first in the design. It is known that any microwave nonlinear element can be used to generate harmonic tones. Under a large input monotone condition, most of the nonlinear components such as diodes and transistors generate a spectrum such that the higher the harmonic order, the lower the power level. The difference of amplitude between the fundamental and 5th harmonic tones could be as high as 40 dB. As implied by the design rules, the difference of amplitude between the first five tones must be within 15 dB. As such, a flat output spectrum (the fundamental and harmonic tones have the same amplitude) is targeted in the design.

In order to achieve a flat output spectrum, appropriate input/output filtering and termination of nonlinear element are required. Since the nonlinear behavior strongly depends on input power, an appropriate power control scheme is needed to keep the nonlinear element's input power independent from the variation of the round-robin's input power (from -20 dBm to 10 dBm as required by the rules).

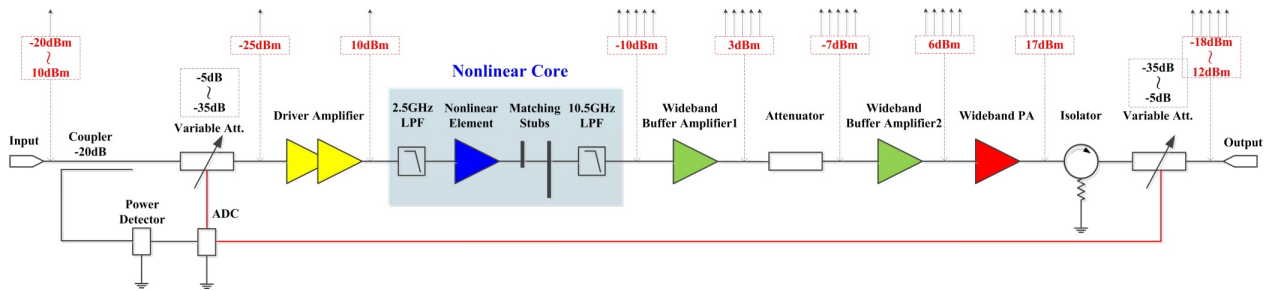


Figure 2.2: The block diagram of the proposed round-robin device. The arrows on top of each power marker indicate the signal content at that point.

The nonlinear element and its input/output filtering/termination circuit constitute the nonlinear core of the round-robin. Furthermore, two issues have to be considered. First, its delivered power will be much lower than the input; second, its generated flat spectrum is probably very sensitive to the load. To overcome these two hurdles, multiple stages of buffer amplifiers and power amplifiers are needed. Those amplifiers must work under a strictly linear condition so as to provide isolation.

Otherwise, the harmonic tones they generate will distort the flat spectrum and increase the sensitivity of the output signal with the load. Finally, the system block diagram is developed as shown in Fig. 2.2.

As the input power changes from -20 dBm to 10 dBm as shown on the left side of Fig. 2.2, the input/output variable attenuations change from 5 dB to 35 dB and 35 dB to 5 dB respectively (the attenuator used has a 5 -dB nominal insertion loss). In this way, the portion between the two variable attenuators, especially the nonlinear core, is driven under a constant power level and the final output power closely follows the input power. The two variable attenuators are controlled by the input power through a 20 -dB coupler, logarithmic power detector and analog-to-digital converter (ADC).

2.2 Circuit Design and Implementation

From the left to the right side in Fig. 2.2, the design of the entire round-robin device is explained as follows.

The variable attenuators at the input and output are Hittite HMC939LP4E 5-bit wideband digital attenuators having a nominal 1.0 -dB step. The input variable attenuator is controlled by the ADC so that its output signal power is locked at around -25 dBm, independent of the input power level. This -25 dBm signal is much lower than the required power (about 10 dBm) to drive the nonlinear element. So, two Avago VMMK-3803 LNAs are cascaded and used as driver amplifiers. One VMMK-3803 LNA has 17.5 dB small signal gain at 2 GHz and 11 dBm output P1dB under 5 -V drain voltage.

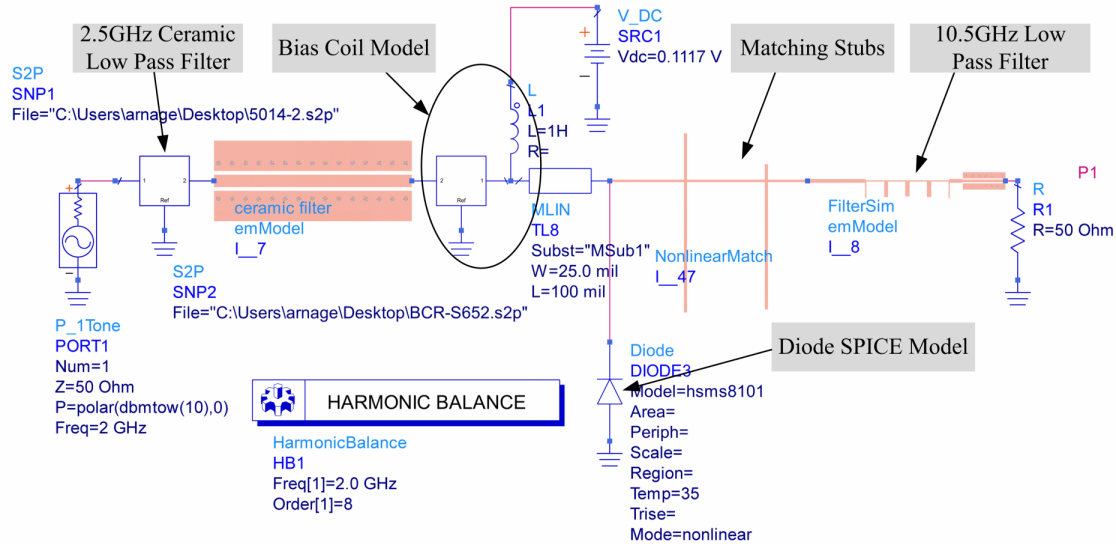


Figure 2.3: The ADS schematic and momentum combined simulation for an Avago HSMS8101 Schottky diode with input/output filtering and matching.

Before the nonlinear element, a 2.5 GHz ceramic low pass filter is used for two purposes. First, it prevents the harmonic tones generated by the driver stage from entering the nonlinear element. Second, it prevents the harmonic tones generated by the nonlinear element from changing the operating characteristics of the driver amplifier. After the nonlinear element, a 10.5 GHz microstrip open stub low pass filter is used to reduce the level of harmonic tones higher than 10 GHz and avoid pushing the following amplifiers into compression state. The layout of this filter can be seen in Fig. 2.3 and Fig. 2.5.

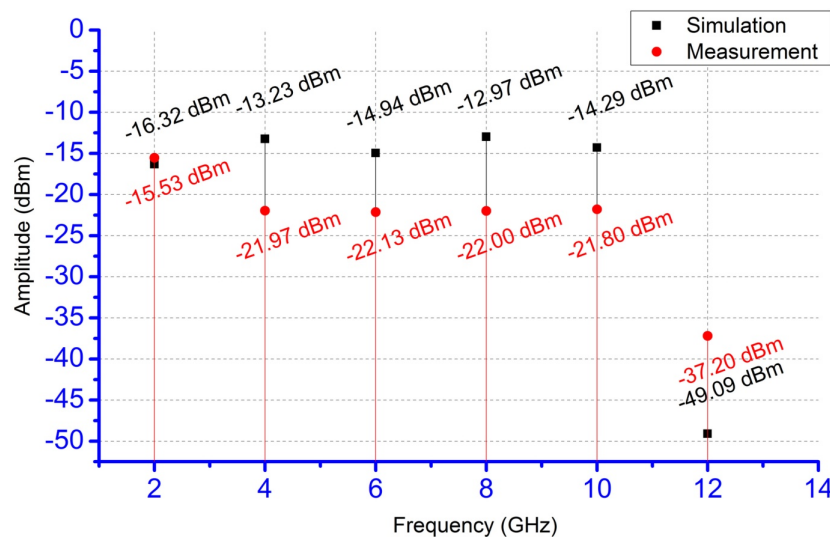


Figure 2.4: Simulated and measured spectra of HSMS8101 Schottky diode with matching stubs.

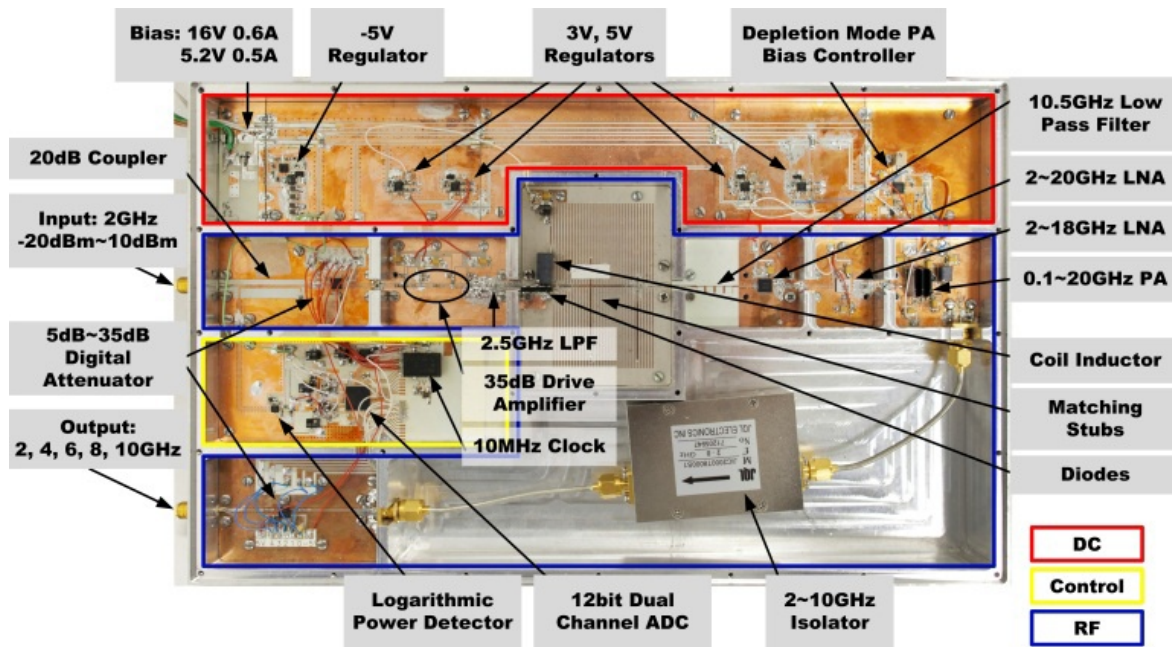


Figure 2.5: The fabricated round-robin device. A JQL 2~10GHz isolator is added between the power amplifier and output variable attenuator.

The nonlinear element selected is an Avago HSMS8101 Schottky diode whose SPICE model is used for the simulation. The ADS schematic and momentum combined simulation is shown in Fig. 2.3. The length and position of the matching stubs are obtained by optimization. Simulated and measured output spectra are shown in Fig. 2.4. The fabricated device is shown in the center portion of Fig. 2.5.

Measured results in Fig. 2.4 do not include the two low pass filters. This is probably the cause for the difference between simulation and measurement. From both simulation and measurement, it is found that by tuning the bias voltage and adding more diodes in parallel, the relative amplitude between output tones can be adjusted.

Then the first and second buffer amplifiers selected are Hittite HMC462LP5E and HMC606LC5. They have 15 dBm output power at 1 dB compression point and about 13 dB small signal gain within the working frequency range. The optional fixed value attenuator between these two buffers is a pi-attenuator which may be used to adjust the power level. The wideband power amplifier is a Hittite HMC998LP5E. It has 31 dBm output power and 11 dB linear gain. This PA is used to satisfy the output power level requirement. Since five tones with similar power level are processed by the three amplifiers, at least 7 dB (five times in linear scale) power back-off is necessary for them to

work in the linear region. The final two components are a wideband isolator and the output variable attenuator which is also controlled by the ADC.

The power budget is also shown in Fig. 2.2. Ideally, the overall power gain is about 2 dB regardless of the input power. Referring to the S12 of the buffer amplifiers, the power amplifier and the isolator and taking into account the attenuators, the overall isolation is more than 139 dB at 10 GHz and more than 180 dB at 2 GHz.

To increase stability and also to reduce noise, HMC860LP3E regulator chips and HMC980LP4E active bias chip are used to bias the preamplifiers, nonlinear device, buffer amplifiers, digital attenuators and power amplifier. Also, TPS63700 dc-dc inverter from Texas Instruments (TI) is used to supply -5 V for the digital attenuator.

The controller is composed of a logarithmic power detector (TI LMV221SD) and a dual channel 12-bit A/D converter (Analog Devices AD9238). A 10-MHz clock is provided to the ADC. Reference voltages are carefully tuned so that the full span of the ADC is utilized. Finally, each module is fabricated and tested separately. The final device is shown in Fig. 2.5.

2.3 Measurement, Evaluation and Discussion

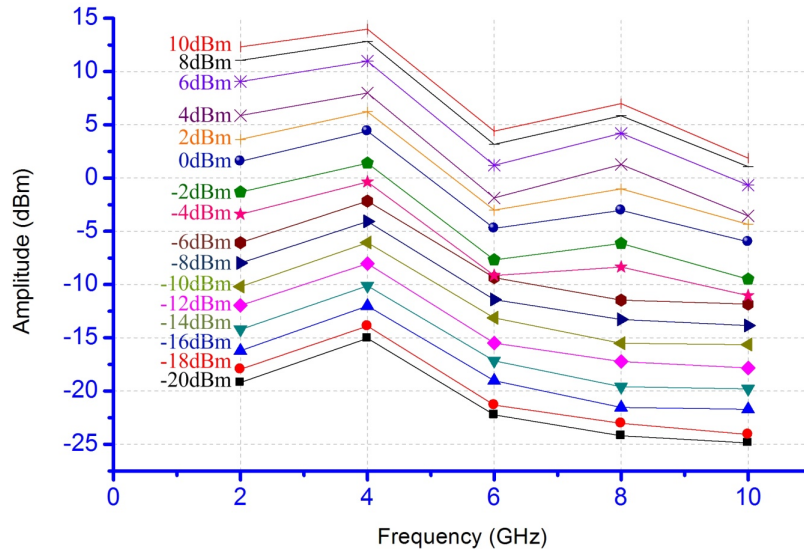


Figure 2.6: The measured output spectra of the round-robin device. The input power is marked on the left of each curve.

A series of measurements are performed to verify the performances of the round-robin device. First of all, output spectrum measurement is conducted under different input power level to confirm that the device is working properly. The measured results are illustrated in Fig. 2.6. The output spectrum curves with lower than -6 dBm input power and higher than -4 dBm input power have slightly different shapes. The first reason is that the output voltage signal of the power detector is not strictly logarithmic. The second is the drifting of ADC's reference voltages.

It is obvious that the spectra in Fig. 2.6 are not as flat as the simulated and measured ones in Fig. 2.4 and that the weakest tones are lower than the input power. The first reason is that the insertion loss of the variable attenuators has different value at different frequency. The second is that the frequency dependent insertion loss of the total transmission line from the input to the output is not taken into account in the power budget. The third is that the buffers and PA still generate harmonic tones although power back-off is performed. For the on-site demonstration during the competition, an extra PA was added outside the round-robin to make sure the output power satisfies the rules. After the competition, it was suggested that PA be removed since for actual LSNA verification such an output spectrum is fully acceptable.

The next step is to calculate the round-robin's FOM and evaluate its performance. First, the phasors of each output tone for different loads have to be extracted from the B2 wave (refer to Fig. 2.1), which can be obtained from the wave data of the round-robin. So, the load dependent wave data measurements have to be conducted with LSNA.

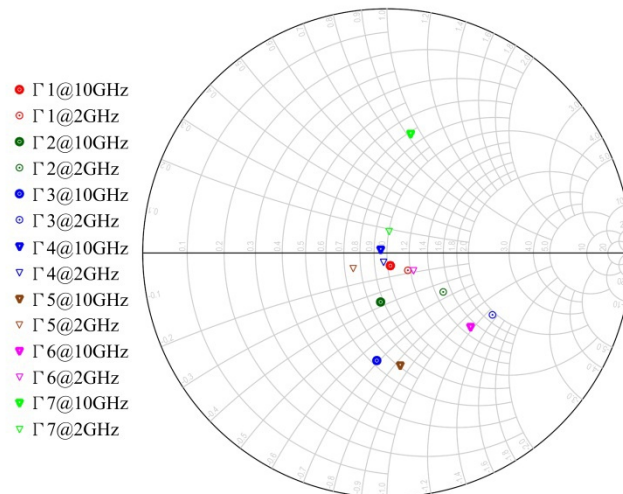


Figure 2.7: Loading conditions for wave data measurement and FOM calculation are selected. Γ is frequency dependent and its values for 2 GHz and 10 GHz are shown.

Different load impedances are established using a load tuner, fixed value attenuators, short/match terminations and a 20-dB wideband directional coupler. The selected loads are shown in Fig. 2.7. $\Gamma_1 \sim \Gamma_3$ are established by short terminated 10 dB, 6 dB and 3 dB attenuators which provide almost a constant reflection amplitude for each tone. $\Gamma_4 \sim \Gamma_7$ are established with Focus CCMT-4020-TC-JS load-pull tuner terminated with 50Ω . The phases of $\Gamma_5 \sim \Gamma_7$ at 2 GHz are distributed equally on the Smith chart. For any frequency between 2 GHz~10 GHz, $|\Gamma| < 0.5$ is guaranteed. The load dependent wave data measurement setup is shown in Fig. 2.8. Agilent N5247A PNA-X NVNA is used.

The FOM defined by the rules is a standard deviation that describes the variation of the phasors of the first N tones ($N=5$) of the transmitted waves (B_2) for the M loading conditions ($M=7$). The B_2 waves are first processed by phase alignment for all the tones and all the loading conditions:

$$\angle \widetilde{B_2}(n\omega, \Gamma_m) = \angle B_2(n\omega, \Gamma_m) - n\angle A_1(\omega, \Gamma_m) \text{ and } |\widetilde{B_2}(n\omega, \Gamma_m)| = |B_2(n\omega, \Gamma_m)|. \quad (1.1)$$

Following this, FOM is defined in the form of a standard deviation:

$$\text{FOM} = \sqrt{\frac{1}{N \times M} \sum_{n=1}^N \sum_{m=1}^M \frac{|\widetilde{B_2}(n\omega, \Gamma_m) - \overline{B_2}(n\omega)|^2}{|\overline{B_2}(n\omega)|^2}} \text{ with } \overline{B_2}(n\omega) = \frac{1}{M} \sum_{m=1}^M \widetilde{B_2}(n\omega, \Gamma_m). \quad (1.2)$$

For each input power, the FOM is calculated. The smaller the resulting FOM in these measurements with different output loads, the higher the rating for the round-robin device. In the measurement, three input powers -20 dBm, 0 dBm and 10 dBm are used.

In Table 2.1, the measured phasors for each loading condition, harmonic index and input power are listed. Taking a look at the column corresponding to $n=1$, the phasors for -20 dBm input power are close to each other throughout all the values of m . So, it can be seen that the output signal is insensitive to the variation of load impedance. In Table 2.2 the FOMs for $\Gamma_1 \sim \Gamma_3$, $\Gamma_4 \sim \Gamma_7$ and $\Gamma_1 \sim \Gamma_7$ are calculated. In order to compare with the performance of our joint winning project in IMS2012 [65], we remeasured the round-robin device of IMS2012 with the same setup and loading conditions $\Gamma_1 \sim \Gamma_3$. The calculated FOM is 0.0557, higher than the values in Table 2.2 for $\Gamma_1 \sim \Gamma_3$. This demonstrates the progress achieved this year.

Table 2.1: Output Phasors Measured by an Agilent PNA-X NVNA.

$B2(n\omega, \Gamma_m)$	Input Power	$n=1$	$n=2$	$n=3$	$n=4$	$n=5$
$m=1$	-20dB	$2.41e-4+i2.72e-4$	$-7.09e-4-i5.84e-5$	$-2.08e-4-i1.61e-4$	$6.07e-6-i3.41e-4$	$-2.35e-4-i1.07e-4$
	0dBm	$1.30e-3+i1.53e-3$	$-3.90e-3-i6.62e-4$	$-1.10e-3-i9.17e-4$	$4.23e-4-i2.00e-3$	$-1.10e-3-i8.77e-4$
	10dBm	$5.50e-3+i6.10e-3$	$-1.48e-2-i2.80e-3$	$-4.60e-3-i2.50e-3$	$2.30e-3-i8.00e-3$	$-3.10e-3-i3.40e-3$
$m=2$	-20dB	$2.45e-4+i2.75e-4$	$-7.08e-4-i7.69e-5$	$-2.16e-4-i1.66e-4$	$4.93e-6-i3.54e-4$	$-2.45e-4-i1.09e-4$
	0dBm	$1.30e-3+i1.50e-3$	$-3.90e-3-i7.63e-4$	$-1.10e-3-i9.49e-4$	$3.64e-4-i2.00e-3$	$-1.10e-3-i9.32e-4$
	10dBm	$5.60e-3+i6.10e-3$	$-1.48e-2-i3.30e-3$	$-4.60e-3-i2.60e-3$	$2.00e-3-i8.30e-3$	$-3.20e-3-i3.60e-3$
$m=3$	-20dB	$2.51e-4+i2.77e-4$	$-7.03e-4-i1.06e-4$	$-2.27e-4-i1.77e-4$	$-1.86e-5-i3.69e-4$	$-2.56e-4-i1.22e-4$
	0dBm	$1.30e-3+i1.50e-3$	$-3.90e-3-i8.82e-4$	$-1.20e-3-i1.00e-3$	$2.67e-4-i2.10e-3$	$-1.20e-3-i1.00e-3$
	10dBm	$5.60e-3+i6.00e-3$	$-1.48e-2-i4.00e-3$	$-4.70e-3-i2.70e-3$	$1.30e-3-i8.90e-3$	$-3.20e-3-i3.90e-3$
$m=4$	-20dB	$2.36e-4+i2.70e-4$	$-7.14e-4-i4.75e-5$	$-2.04e-4-i1.58e-4$	$1.44e-5-i3.44e-4$	$-2.33e-4-i1.03e-4$
	0dBm	$1.30e-3+i1.50e-3$	$-3.90e-3-i6.27e-4$	$-1.10e-3-i8.89e-4$	$4.69e-4-i1.90e-3$	$-1.10e-3-i8.53e-4$
	10dBm	$5.50e-3+i6.20e-3$	$-1.48e-2-i2.60e-3$	$-4.60e-3-i2.40e-3$	$2.60e-3-i7.60e-3$	$-3.10e-3-i3.30e-3$
$m=5$	-20dB	$2.35e-4+i2.67e-4$	$-7.21e-4-i7.68e-5$	$-1.87e-4-i1.63e-4$	$1.35e-6-i3.17e-4$	$-2.53e-4-i1.26e-4$
	0dBm	$1.30e-3+i1.50e-3$	$-4.00e-3-i7.56e-4$	$-1.00e-3-i8.99e-4$	$4.03e-4-i1.80e-3$	$-1.10e-3-i1.00e-3$
	10dBm	$5.40e-3+i6.20e-3$	$-1.51e-2-i3.30e-3$	$-4.40e-3-i2.30e-3$	$1.90e-3-i6.60e-3$	$-3.00e-3-i3.90e-3$
$m=6$	-20dB	$2.40e-4+i2.74e-4$	$-7.45e-4-i6.03e-5$	$-1.98e-4-i1.42e-4$	$4.42e-5-i3.44e-4$	$-2.33e-4-i1.31e-4$
	0dBm	$1.30e-3+i1.50e-3$	$-4.10e-3-i6.63e-4$	$-1.10e-3-i8.04e-4$	$7.02e-4-i1.90e-3$	$-9.85e-4-i1.10e-3$
	10dBm	$5.50e-3+i6.20e-3$	$-1.56e-2-i2.70e-3$	$-4.60e-3-i2.20e-3$	$3.80e-3-i7.20e-3$	$-2.70e-3-i3.70e-3$
$m=7$	-20dB	$2.33e-4+i2.75e-4$	$-6.89e-4-i3.69e-5$	$-1.86e-4-i1.57e-4$	$4.22e-5-i3.35e-4$	$-2.09e-4-i9.48e-5$
	0dBm	$1.30e-3+i1.60e-3$	$-3.80e-3-i5.97e-4$	$-1.00e-3-i8.69e-4$	$6.76e-4-i1.90e-3$	$-9.45e-4-i7.65e-4$
	10dBm	$5.50e-3+i6.30e-3$	$-1.42e-2-i2.50e-3$	$-4.50e-3-i2.30e-3$	$3.60e-3-i6.80e-3$	$-2.80e-3-i2.90e-3$

Table 2.2: The Calculated FOM.

Input Power=-20dBm			Input Power=0dBm			Input Power=10dBm		
$\Gamma_1 \sim \Gamma_3$	$\Gamma_4 \sim \Gamma_7$	$\Gamma_1 \sim \Gamma_7$	$\Gamma_1 \sim \Gamma_3$	$\Gamma_4 \sim \Gamma_7$	$\Gamma_1 \sim \Gamma_7$	$\Gamma_1 \sim \Gamma_3$	$\Gamma_4 \sim \Gamma_7$	$\Gamma_1 \sim \Gamma_7$
0.031	0.053	0.058	0.032	0.059	0.063	0.039	0.068	0.077

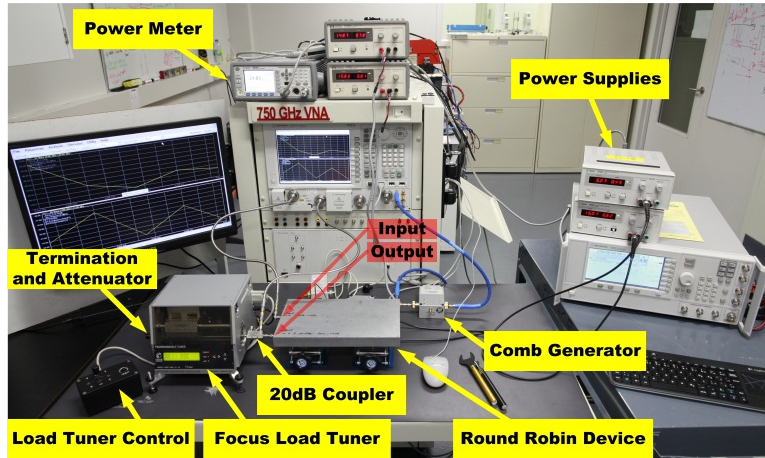


Figure 2.8: Load dependent wave data measurement setup of the round-robin device. The load impedances of Fig. 2.7 are presented to the output port of the round-robin. The coupling port of the 20-dB coupler is connected to the PNA-X.

2.4 Summary

This article briefly introduced the history and presented principles of new nonlinear models and the evolution of LSNAs or NVNAs. In addition, the demand for a round-robin device that can be used to verify different LSNAs or NVNAs is analyzed. With such an objective and the design requirement of IMS2013 student design competition ‘Development of a Large-Signal-Network-Analyzer Round-Robin Artifact’ in mind, the simulation, design, measurement and discussion are presented in detail.

As a verification device that will be used as a standard, temperature stability is one of the critical performances. During the tuning and measurement, it is found that the stability of the reference voltage for the ADC is not satisfactory. Its variation comes from both the inevitable changing of the bias for the entire device and temperature. To solve this problem, two ultra-stable voltage reference chips from Analog Device are used. Due to time limitation, it is not shown in this article. Furthermore, the following work will be carried out for improvements. First of all, the output voltage variations of the voltage regulators and bias controllers will be evaluated under different bias voltage and temperature. Second, all sections of the RF part such as attenuators, driver amplifiers, nonlinear core, buffer amplifiers, power amplifier and RF power detector will be evaluated with bias voltage and temperature variation. These results will indicate the source of instability of the entire circuit. Third, the output signal variation will be tracked after the device is turned on so as to check the effect of the warm-up process. Finally, environmental temperature range, overall bias range and warm-up time will be provided to users.

In addition, one effect that limits the device’s performance is the distortion introduced by the buffer amplifiers and power amplifier. With single input tone, P1dB indicates the amplifier’s linear working condition. But for our design, in which the amplifiers process five tones altogether, further measurements should be conducted to determine the linear working condition.

Although a substantial amount of further work is required to improve the performances, our design has been considered as the most attractive one and will be provided to NIST for further evaluation and eventually it may become a standard device.

2.5 Acknowledgement

The authors wish to acknowledge the assistance and support of the IMS2013 student design competition coordinators Dr. Rashaunda Henderson and Dr. Jon Martens. They also acknowledge

Dr. Dylan Williams, from NIST, for valuable design advices. The authors would like to thank the always supportive technicians of our Poly-Grames Research Center: Jules Gauthier, Traian Antonescu, Steve Dubé, and Maxime Thibault for their outstanding fabrication and assembling work. Also, the authors are obliged to Hittite Microwave Corporation, Analog Devices, Rogers Corporation and Coilcraft for sample support. Finally, the authors are grateful to Anritsu Company for generous financial support.

CHAPTER 3 ARTICLE 2: HARMONIC FEEDBACK-LOOP OSCILLATOR FOR PULLING EFFECT REDUCTION AND IMPROVED PHASE NOISE

Co-authored by Anthony Ghiotto, and Ke Wu

Published in « *2014 IEEE MTT-S International Microwave Symposium* », 2014.

Abstract—A diplexer-based harmonic feedback-loop oscillator concept is presented and demonstrated at 5.8 GHz. Without additional complexity, the diplexer together with an RF amplifier creates isolation between nonlinear feedback-loop dynamics and second harmonic signal component that is directed to the output. As a result, the load pulling effect is reduced as well as the phase noise performance is improved with reference to its fundamental feedback-loop counterpart. Load-pull measured results ($VSWR \leq 9$) are observed follows: 1) load dependent frequency drift is significantly reduced from $-19\text{‰} \sim 15\text{‰}$ to $-0.75\text{‰} \sim 1.06\text{‰}$; 2) phase noise at 1 MHz offset is improved by 15 dB; and 3) output power is slightly affected only.

Index Terms—Oscillator, feedback-loop, harmonics, pulling effect, phase noise.

3.1 Introduction

Power oscillators are frequently used in on-off keying (OOK) transmitters for active RFID tags [66]. Within the architecture of such transmitters, base-band signal pulses switch a power oscillator which directly feeds the antenna. Compared with heterodyne transmitter, they exhibit a simpler structure and a higher power efficiency. The feedback-loop oscillator is one of the popular structures [67]. It is not only low-cost and simple to implement but its performance can also be highly appreciable. One conventional design scheme is illustrated in Fig. 3.1. As suggested by the Barkhausen criterion [68], the circuit begins to oscillate at frequency f_0 as long as the loop gain is higher than 0dB and loop phase delay is multiples of 360 degrees at f_0 . In addition, any type of resonator such as dielectric resonator or substrate integrated waveguide (SIW) cavity can be integrated in the loop and act as filter to improve the frequency stability and phase noise performances.

A major concern with feedback-loop oscillator and other types of free running oscillator is the output signal deviation subject to both load impedance variation [69] and external signal injection [70]. Moreover, observed phase noise performance cannot satisfy many application requirements.

Such fundamental drawbacks have propelled the invention and development of phase-locked-loop (PLL) techniques. In the design of active or self-powered RFID tags, however, PLLs significantly decrease the overall efficiency and increase the circuit complexity. Without a PLL circuitry, the pulling effect introduces frequency drift and power decreasing that may result in communication interruption.

In order to resolve such dilemmas, a novel feedback-loop oscillator architecture that features low pulling effect and low phase noise is proposed in this work. With the resonance and coupling structure replaced by a diplexer, the proposed oscillator isolates the feedback-loop oscillating at the fundamental frequency from the output port that delivers the second harmonic signal. In this way, the impact of a load variation on the nonlinear dynamics of the feedback-loop is reduced. Measured results indicate a significant improvement in terms of frequency stability with loading variation and also phase noise reduction.

3.2 Operating Principle and Design Considerations

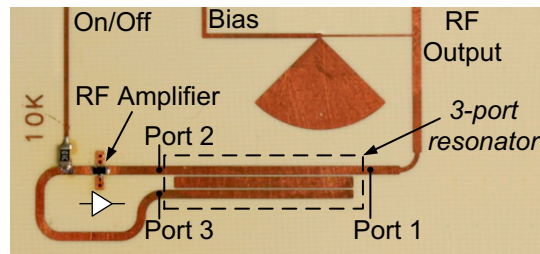


Figure 3.1: A conventional feedback-loop oscillator design.

When the load of an oscillator deviates from the value of the output port impedance, signal reflection takes place at the output port. Due to the reciprocity of a 3-port resonator as shown in Fig. 3.1, the reflection results in a single injection into the feedback-loop. Consequently, the nonlinear working condition of the RF amplifier is changed, and both the frequency and amplitude of the output signal are altered.

One approach to mitigating such a problem is adding an attenuator between the output port and the load in order to reduce the reflection and in turn the alteration of working condition [65]. However, this is at the expense of output power decrease and noise degradation. Another way is to establish isolation between the oscillating and external circuits with a nonreciprocal device [71]. Nevertheless, it would significantly increase the circuit complexity, size and cost.

3.2.1 Principle of the harmonic feedback-loop oscillator

Fig. 3.2 illustrates the proposed scheme of the harmonic feedback-loop oscillator. The diplexer in the circuit exhibits its first pass-band between port 2 and port 3 at frequency f_0 for which the loop phase delay is designed as $n \cdot 360^\circ$. Its second pass-band is designed at exactly $2f_0$ between port 1 and port 2. Port 1 and port 3 have high rejection at frequency f_0 and $2f_0$, respectively. Moreover, the isolation between port 1 and port 3 should be as high as possible to prevent signals at f_0 or $2f_0$ transmitting between them. With such a diplexer, the relative independence of the feedback-loop is established. The second harmonic signal at $2f_0$ generated by the nonlinear RF amplifier is directed to the output through the second pass-band of the diplexer. In order to briefly explain the pulling effect reduction, an ideal unilateral RF amplifier and an infinite isolation between port 1 and port 3 are assumed for simplicity of discussion. Once the output load impedance is changed in this case, the reflected signal at $2f_0$ can only reach the output terminal of the RF amplifier through the second pass-band between port 1 and port 2. The diplexer together with the RF amplifier prevents the reflected signal from getting involved in the nonlinear feedback-loop dynamics, which primarily determines the oscillating frequency.

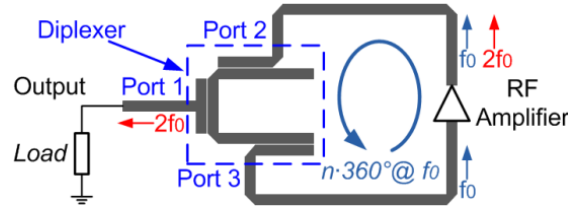


Figure 3.2: The proposed harmonic feedback-loop oscillator.

3.2.2 Diplexer design and oscillator simulation

Fig. 3.3 shows the diplexer design. The selected substrate is Rogers RT/duroid® 6002 with 0.508mm thickness. The diplexer consists of a folded $\lambda/4$ microstrip resonator at $f_0 = 2.9$ GHz and three coupled ports. The first and second resonant modes (at about 2.9 GHz and 5.8 GHz respectively) are used. The position and strength of the couplings are calculated and optimized. At port 2, strong couplings to both modes are realized. At port 1, the coupling with respect to the first mode is suppressed and to the second mode is enhanced and vice versa at port 3. Due to the shortening effect, the resonant frequency of the second mode is not exactly twice that of the first one. As explained in [72], this can be overcome by tuning the ratio between widths w_1 and w_2 , which are shown in Fig. 3.3 (a). The port impedance is designed to be 50 Ω .

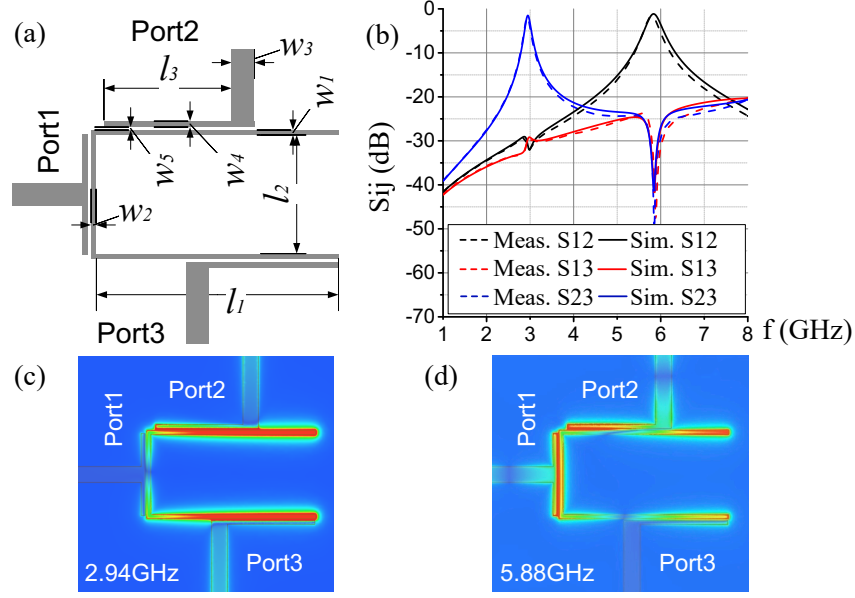


Figure 3.3: The proposed diplexer: (a) layout; (b) simulated and measured S-parameters; (c) and (d) electric field distributions.

Finally, the structural dimensions (in mm) are: $l_1=13.35$, $l_2=6.5$, $l_3=7.09$, $w_1=0.323$, $w_2=0.32$, $w_3=1.27$, $w_4=0.323$, $w_5=0.15$ (w_3 , w_4 and w_5 also apply to the corresponding dimensions for port 1 and port 3). As shown in Fig. 3.3 (b), measured S-parameters are in agreement with simulated counterparts, showing pass-bands at 2.94 GHz and 5.88 GHz with insertion loss of about 1.5 dB. The loaded Q factor at 2.94 GHz is about 28. Over 30 dB isolation between port 1 and port 3 is observed at f_0 and $2f_0$. Electric field distributions of the two modes are shown in Fig. 3.3 (c) and (d).

With the measurement results of the diplexer and the nonlinear model (X-parameters) of the RF amplifier, the oscillator is simulated with Advanced Design System (ADS). Pulling effect is also simulated with load reflection coefficient (Γ_l) uniformly distributed in the $VSWR \leq 9$ circle of the Smith chart. As shown in Fig. 3.4, the oscillator has an output signal running at 5.78 GHz with 7.05 dBm power. The frequency variation is about 1.4‰ with the load impedance variation.

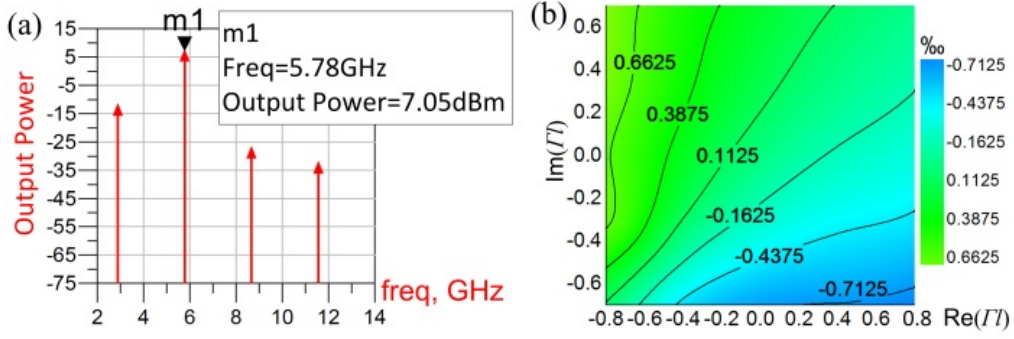


Figure 3.4: Simulated results of the proposed harmonic feedback-loop oscillator: (a) output spectrum with 50 Ω load; (b) frequency pulling.

3.3 Measurements and Discussions

The proposed harmonic feedback-loop oscillator is fabricated on the same substrate for the diplexer. In order to demonstrate the improvement, a conventional fundamental feedback-loop oscillator at the same frequency is also designed and serves as a reference. They are both shown in Fig. 3.5.

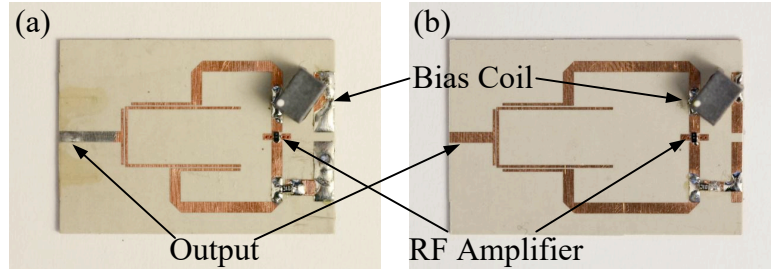


Figure 3.5: The harmonic (a) and fundamental (b) feedback-loop oscillators.

The fundamental feedback-loop oscillator is designed by symmetrically arranging the coupling ports to realize pass-bands between each pair of the three ports for both the first and second resonant modes. The loop phase delay is carefully tuned so as to satisfy the oscillation start-up condition only at the second mode frequency (5.8 GHz). The selected RF amplifier model is Avago VMMK-2303. From 1 GHz to 6 GHz, it has a linear gain of about 14 dB, an output P1dB of 9 dBm and isolation of about 20 dB.

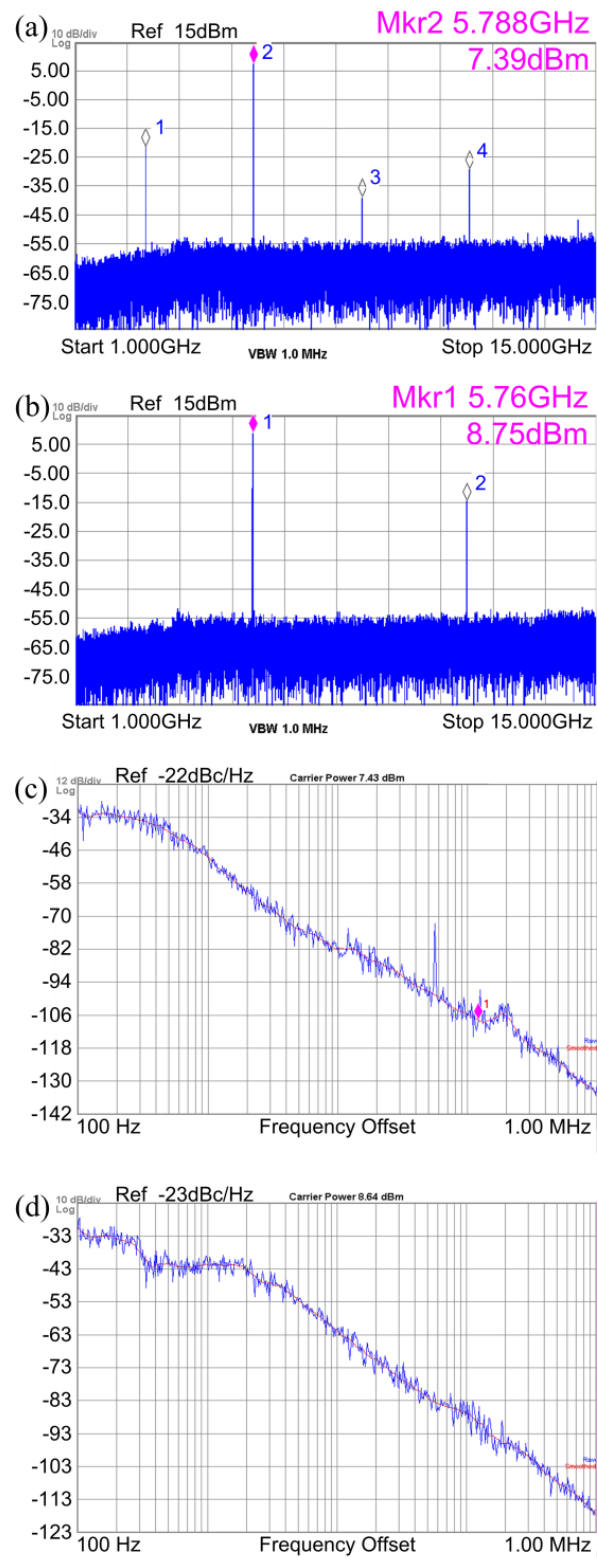


Figure 3.6: Measured results of both oscillators with 50 Ω load: output spectrum of (a) the harmonic and (b) the fundamental feedback-loop oscillators; phase noise of (c) the harmonic and (d) the fundamental feedback-loop oscillators.

Measured results with matched output load ($50\ \Omega$) are shown in Fig. 3.6. The harmonic feedback-loop oscillator has 1.4 dB lower output power than its fundamental counterpart. Its fundamental tone is about 30 dB lower than the second harmonic component. The fundamental scheme does not have any signal component around 2.9 GHz. Moreover, the phase noise at 1 MHz offset of the harmonic feedback-loop oscillator is -133.5 dBc/Hz and that of the fundamental scheme is -117.8 dBc/Hz.

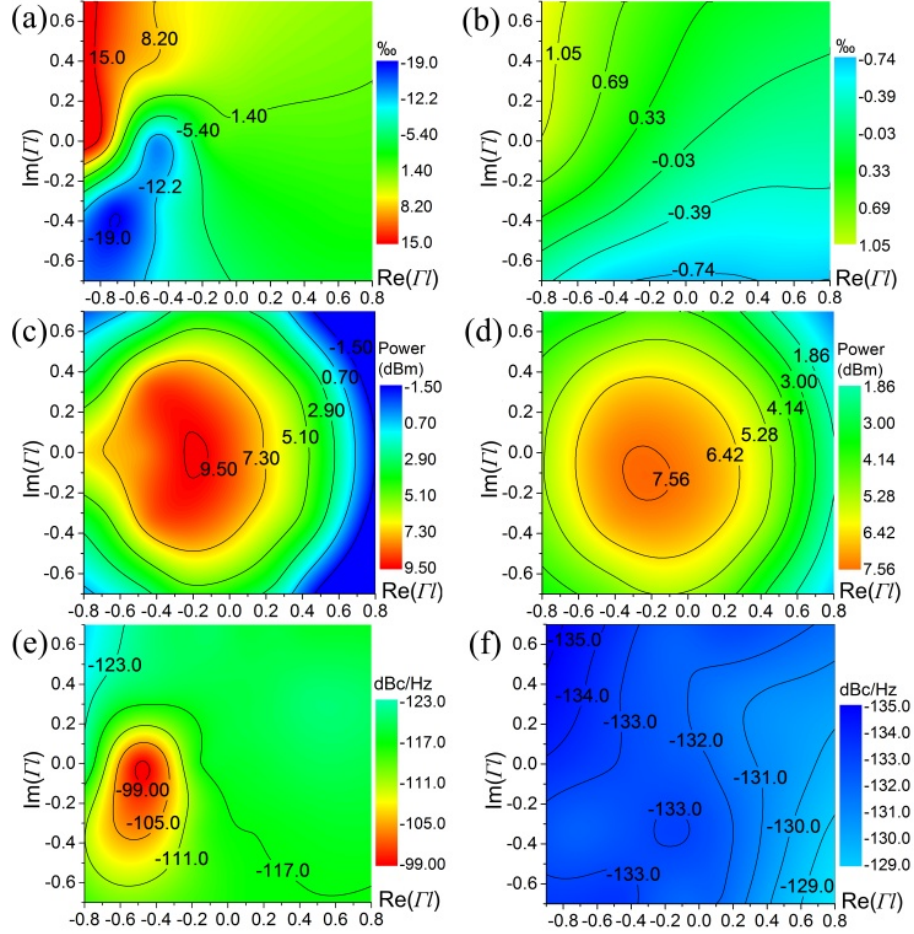


Figure 3.7: Load-pull measurement results: (a), (c) and (e) are the output frequency, power and phase noise variation of the fundamental feedback-loop oscillator; (b), (d) and (f) are those of the harmonic feedback-loop oscillator.

Fig. 3.7 displays the load-pull measurement results carried out with the impedance distribution used in the simulation. The relative output frequency variations shown in Fig. 3.7 (a) and (b) are normalized to their $50\ \Omega$ -loaded frequency. Obviously, the frequency stability is significantly improved with the new technique. The measured frequency variation of the harmonic feedback-

loop oscillator is about 1.8%, coincident with the simulation result. As shown in Fig. 3.7 (c) and (d), the power variation of the harmonic feedback-loop oscillator is about half that of the fundamental one. The difference between the maximum output powers of the two oscillators is about 2 dB. The improvement of the phase noise value and its stability subject to load variation is observed in Fig. 3.7 (e) and (f).

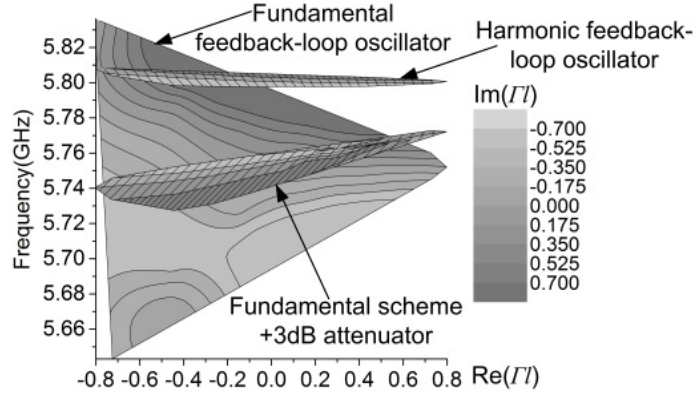


Figure 3.8: Comparison of the frequency pulling effects between the harmonic feedback-loop oscillator and the fundamental feedback-loop oscillator with and without 3 dB attenuator.

On top of these advantages of the proposed harmonic feedback-loop oscillator, its drawback of power decrease is worth discussing. Therefore, a trivial testing is carried out by connecting a 3-dB attenuator between the fundamental feedback-loop oscillator and the variable load. This method reduces the loading effect by 6 dB and the output power by 3 dB. Fig. 3.8 shows the overall comparison of the frequency pulling. The harmonic feedback-loop oscillator still preserves the superiority. In addition, using the attenuator does not have any positive impact on the phase noise improvement.

3.4 Conclusion

On the basis of the operating principle of feedback-loop oscillator, theoretical and experimental studies of the proposed harmonic feedback-loop oscillator are presented in this paper. It is shown that a significant improvement in terms of pulling effect and phase noise has been achieved by using the proposed harmonic technique as opposed to the conventional fundamental scheme. In circumstances where complex modulation schemes or high efficiency coding are not used such as RFID tags, this design could be used without other frequency stabilization devices (such as PLLs).

In addition, it is possible to improve the performance of other oscillator architectures with the harmonic technique.

3.5 Acknowledgement

The authors would like to acknowledge the assistance and support from Traian Antonescu and Maxime Thibault, the technicians of our Poly-Grames Research Center, for their outstanding fabrication and assembling work. Also, the authors are grateful to Rogers Corporation for free sample support.

CHAPTER 4 ARTICLE 3: LARGE SIGNAL MODELING AND EXPERIMENTAL DESIGN AUTOMATION OF SELF-ISOLATED HARMONIC OSCILLATOR FOR PULLING EFFECT REDUCTION

Co-authored by Anthony Ghiotto, Fang Zhu, and Ke Wu

Accepted by « *IEEE Transactions on Microwave Theory and Techniques* », 2018.

Abstract—A class of self-isolated harmonic oscillator (SIHO) has been successfully demonstrated in the form of a feedback-loop structure. The SIHO is able to significantly reduce the pulling effect without involving extra circuit complexity such as buffer amplifier. In this paper, the operation principle of the SIHO is theoretically studied through equivalent circuit models and X-parameter technique. Closed-form expressions are derived to represent the respective active and passive equivalent impedances of SIHO subnetworks perturbed by varied load and injected signal. For the purpose of comparison, a feedback-loop oscillator delivering the fundamental tone is studied. Such a modeling technique reveals the physical principle and behavior parameters that have impact on the pulling effect. For the SIHO design and model verification, a harmonic-measurement-and-design (HMD) system is proposed, thus demonstrating the concept of a nonlinear circuit design automation based on the experimental optimization. An SIHO delivering a 4 GHz signal is designed by such a hardware platform, without relying on circuit simulation software packages or a prior knowledge of the large signal model of transistors. The SIHO prototype has a 16.6 dBm output power, 28% dc-RF efficiency and -136.5 dBc/Hz phase noise at 1 MHz offset. The SIHO circuit model is validated with the measured X-parameters.

Index Terms—Diplexer, experimental design automation, feedback-loop, harmonic oscillator, isolation, large signal model, pulling effect, X-parameter.

4.1 Introduction

The research and development on cost- and power consumption-sensitive RF and microwave transceivers and transponders are getting even more attractive in recent years with the emerging prospect of future wireless infrastructures (e.g. 5G cellular) featuring ubiquitous sensing, positioning, powering and communication [3, 73-76]. Without the integration of phase-locked loops (PLLs) or other frequency stabilization circuitries, which may give rise to power penalty and system complexity, free-running oscillators may suffer from severe pulling effects due to self or

external interference and degrade system performance [77-79]. Especially in the case of an active radio frequency identification (RFID) transponder where the oscillators directly feed antenna with a modulated signal [80, 81], a pulling effect will then change the transponder carrier frequency, reduce the output power, deteriorate the phase noise and even interrupt the data transmission. Recently, an emerging integrated active radiator array technology [82-84] presents a remarkable efficiency, power and function over millimeter-wave (mmW) and THz bands. A key factor that makes these efficient and simple structure arrays possible is that the designers abandon the popular PLL and only employ an inter-coupling between the elements to enhance the stability. Still, the pulling effect should be handled so that these arrays can be applied under complex conditions. Note that reciprocal antenna and matching networks may inherently transfer a free space impedance variation, which is caused by transponder position alteration or foreign object in proximity (e.g. on wearable devices), to the oscillating circuit.

Plenty of techniques have been implemented to mitigate the pulling effect and its impact on the communication and radar systems. In the case of amplitude modulated (AM) scheme, a power amplifier (PA) can be inserted between the antenna and the oscillator to create an isolation [85]. For low-frequency signal synthesizing, local oscillation (LO) signal at frequency f_0 can be generated from a source of frequency nf_0 followed by a $1/n$ frequency divider to minimize the pulling [86]. Careful component design in an oscillator may cancel the external interference and reduce the pulling effect [87]. Researchers have also proposed an approach combining an open-loop digital predistortion, a second-point voltage-controlled oscillator (VCO) modulation and an inner self-injection technique to suppress impairments introduced by the pulling effect of the LO and the distortion of the PA [77]. Besides that, an EVM degradation caused by the LO pulling originated from a self-interference can be reduced by an automated digital controlled delay circuit [78]. These techniques either sacrifice the phase noise performance or increase the system design complexity.

Pulling effect generally includes load pulling and injection pulling. Conventional push-push harmonic oscillators can reduce the former one. This is because the signal output at the fundamental frequency f_0 is canceled, reflection from the load at f_0 is zero regardless of the load impedance [88, 89]. However, since the two sub-oscillators are not perfectly matched, output at f_0 always exists in reality. Therefore, the circuit is not protected against a varied reflection of this leakage signal when the load impedance changes. Moreover, a push-push oscillator cannot reduce the injection pulling because its active devices are directly exposed to the injection signal. At its output frequency $2f_0$,

any load-reflected or externally injected signal is only attenuated by 3 dB at the output power combiner before it disturbs the oscillating mechanism.

To the best of our knowledge, there is no oscillator architecture available so far providing inherent pulling resistant characteristics. Actually, the intrinsic pulling signal path in a conventional microwave oscillator structure that delivers a fundamental frequency signal (hereinafter referred to as the fundamental oscillator) cannot be strongly blocked since the bidirectional property of transistors facilitates feedback, which has to be maintained or even enhanced for sufficient instability [90]. In [91], a self-isolated harmonic oscillator (SIHO) is presented in the form of a feedback-loop structure at 5.8 GHz. Instead of using a nonreciprocal device such as amplifier or circulator to isolate the oscillator's output port from the load, such an SIHO structure takes advantage of the unilaterality of a gain block inside the feedback-loop, which has not been exploited by the fundamental oscillator structures. The self-isolation is achieved by embedding a microstrip harmonic diplexer in the loop. As a result, a nonreciprocal path is established through which the oscillating signal is converted to its 2nd harmonic and propagates to the load. Compared to the fundamental oscillator structures, the SIHO makes it feasible to separate and independently control the feedback signal path and the pulling signal path, thanks to synergetic effects of the unilaterality of a gain block and harmonics-separation property of a diplexer. Simulation and measured results have shown that the range of a normalized frequency drift within certain load reflection coefficient (pulling figure) is reduced by more than 15 times. In the same way, the injection pulling can be mitigated too. In [92], the same principle is demonstrated with a diplexer designed on the basis of a substrate integrated waveguide (SIW) loaded with multiple complementary split-ring resonators. Due to the quality-factor (Q-factor) advantage of such a diplexer and the lower flicker noise of SiGe HBT technology, this design exhibits a lower phase noise. In [93], a mmW harmonic radiator using the same self-isolation principle is demonstrated. The radiation property is directly achieved by a diplexer at $2f_0$ without a dedicated antenna, thereby resulting in a size and efficiency advantage. Compared to a fundamental frequency radiator, the load pulling and injection pulling factors are reduced by 10 and 17 times, respectively.

In [91], the operation principle is qualitatively explained. However, complete model and theory are necessary to describe the behavior of SIHO under pulling. The theoretical contribution made by Adler [94] and Razavi [70] has provided significant theoretical insights and intuitive understandings of oscillator injection pulling and locking. However, their models are mainly based

on linear or weak nonlinear assumption and cannot be applied to the SIHO that works in a strong nonlinear condition and efficiently delivers a 2nd harmonic as the output.

Obregon and Khanna presented an analytical derivation of the pulling figure of negative resistance oscillators, taking into full consideration of nonlinearity [69]. However, their model cannot be adopted for the SIHO for two reasons. First, the 1st order Taylor approximation is presumed, thus implying a limited valid region of impedance offset; Second, the resulting pulling figure is related to a nonlinear-index of the negative resistance at oscillating frequency and amplitude, but such an index does not have a significant physical meaning.

This work proposes and utilizes a frequency domain nonlinear behavior model of the gain block: the X-parameters [53]. This not only facilitates the mathematical manipulation but also takes complete parasitic effects into consideration.

In Section 4.2, the operation principle of the SIHO is reviewed, analyzed and compared with reference to its fundamental counterpart based on the equivalent circuit models. In Section 4.3, an X-parameter model is implemented to formulate the gain block, which comprises a biased transistor and its matching networks. Subsequently, the equivalent circuit models of two oscillators are divided into active and passive portions and their respective impedances are derived. Steady-state oscillation condition is given by the zero-loop-impedance criteria. The physical insight of load pulling and injection pulling of the SIHO and the fundamental oscillator is discussed. Section 4.4 presents the SIHO design methodology and experimental validations of the proposed model with fabricated prototypes. A hardware platform is demonstrated for automated experimental design, which saves the efforts of accurately characterizing a nonlinear device and greatly shortens the design cycle. Section 4.5 concludes this work.

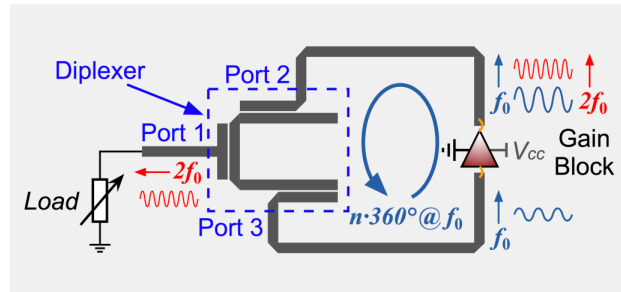
4.2 Operation Principle and Equivalent Circuit

4.2.1 Review and comparison of the operation principle of SIHO and fundamental oscillators

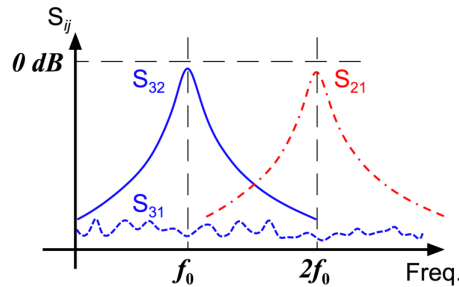
Fig. 4.1 (a) illustrates the SIHO schematic realized with a feedback-loop structure. The diplexer not only acts as a filter at frequency f_0 between port 2 and port 3 in a fundamental oscillator [67] but also transfers a harmonic signal at frequency $2f_0$ between port 2 and port 1. The closed loop is carefully adjusted to exhibit an $n \cdot 360^\circ$ phase at f_0 to satisfy the oscillation start-up condition [68]. Moreover, a high isolation between port 1 and port 3 is important at both frequencies. The

frequency response of the diplexer that meets the above requirements is sketched in Fig. 4.1 (b). Such a closed-loop circuit oscillates at f_0 . Due to the nonlinearity of the gain block, abundant harmonic signals are generated, among which the second one is directed to the load through the pass-band between port 2 and port 1. Since virtually all the generated signal at f_0 is fed to the input of the gain block, the SIHO has the maximum possible driving level among all the oscillator structures, which is beneficial to the phase noise performance [95].

The pulling effect reduction characteristic of the SIHO is explained by assuming that the diplexer and the gain block have a sufficient isolation. Actually, by using a SIW technology, the isolation of diplexers can reach more than 50 dB [96, 97]. On the other hand, the isolation of the gain block can be enhanced up to 40 dB using neutralization networks [98]. In case that the load impedance of the SIHO deviates from the value at which the diplexer and the SIHO are designed, reflected signal at $2f_0$ can only reach the output terminal of the gain block due to the diplexer's isolation property. Then it will be either absorbed by the gain block's output port or reflected back to port 1, instead of joining nonlinear oscillating dynamics. Although the gain block is under a large signal drive at f_0 , it can still be closely modeled using a linear superposition principle at $2f_0$ [99]. It means that the gain block is much less sensitive to the harmonic load pulling compared to the fundamental one.



(a)



(b)

Figure 4.1: (a) SIHO with a feedback-loop structure [91], (b) targeted frequency response of the diplexer.

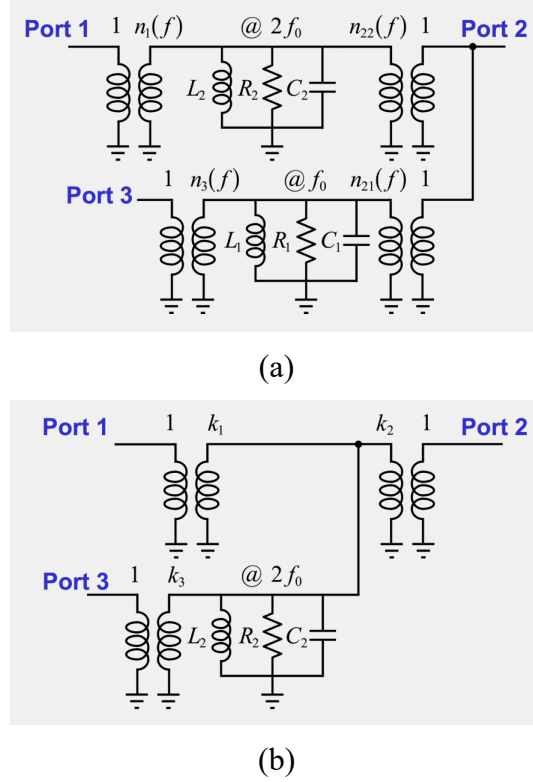


Figure 4.3: (a) Equivalent circuit of diplexer in SIHO, (b) equivalent circuit of resonator in the fundamental oscillator.

The diplexer is composed of two parallel RLC tanks representing the two resonant modes, corresponding to the two pass-bands at f_0 and $2f_0$ respectively as shown in Fig. 4.3 (a). Since the two intrinsic resonant modes are orthogonal with each other, it can be assumed that they do not have direct couplings in the circuit. If the fundamental resonant mode is supported by a half wavelength transmission line, the lumped elements can be expressed as [101, 102]:

$$\begin{aligned}
 R_1 &\approx \frac{2Z_0}{\alpha_1 \lambda_g}, \quad C_1 \approx \frac{\pi}{2Z_0 \omega_0}, \quad L_1 \approx \frac{1}{\omega_0^2 C_1}, \\
 R_2 &\approx \frac{2Z_0}{\alpha_2 \lambda_g}, \quad C_2 \approx \frac{\pi}{2Z_0 \omega_0}, \quad L_2 \approx \frac{1}{4\omega_0^2 C_2}.
 \end{aligned} \tag{4.1}$$

In these expressions, Z_0 is the characteristic impedance of the transmission line, which is assumed to be nondispersive, λ_g is the guided wavelength of the fundamental mode, α_1 and α_2 are the attenuation factors at the two frequencies and $\omega_0 = 2\pi f_0$. These expressions are derived from the intrinsic resonant modes. Therefore, approximate symbols are used to account for the loading and shortening effects in the loaded resonators.

The field distributions of a microstrip diplexer in [91] at the two resonant frequencies suggest that the couplings between the port terminals and each of the two modes are different. Therefore, transformer ratios n_1 , n_{21} , n_{22} , and n_3 in Fig. 4.3 (a) are frequency-dependent. At f_0 , n_{22} takes a much smaller value than others so that port 2 will see a high impedance towards the top branch and establishes a pass-band only to port 3 through the bottom branch. Similarly, at $2f_0$, n_{21} takes a much smaller value than others and port 2 establishes a pass-band only to port 1 through the top branch. The resonator of Fig. 4.3 (b) is simply composed of one RLC tank resonating at $2f_0$ and transformers. Ratios k_1 , k_2 and k_3 have the same magnitude around $2f_0$.

The gain block, realized as a matched transistor, is represented by voltage controlled current sources in parallel at the fundamental and each of the harmonics, as shown in Fig. 4.4. As a frequency domain model, the parasitic effects are embodied in the current/voltage (I/V) dependency. The amplitude and phase of each current source are determined by the driving voltage phasors as well as the loading conditions.

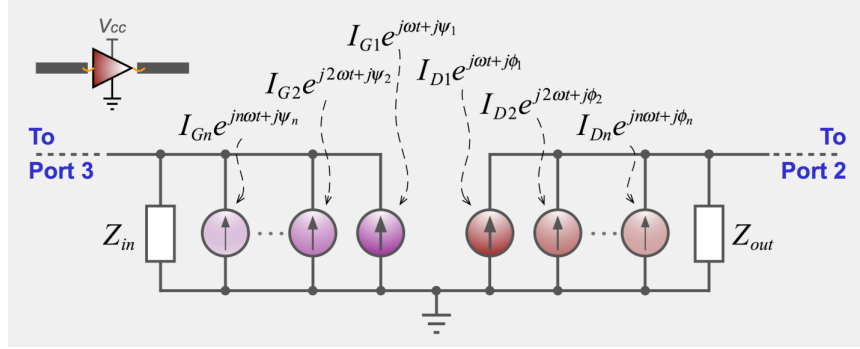


Figure 4.4: The frequency domain nonlinear circuit model of a gain

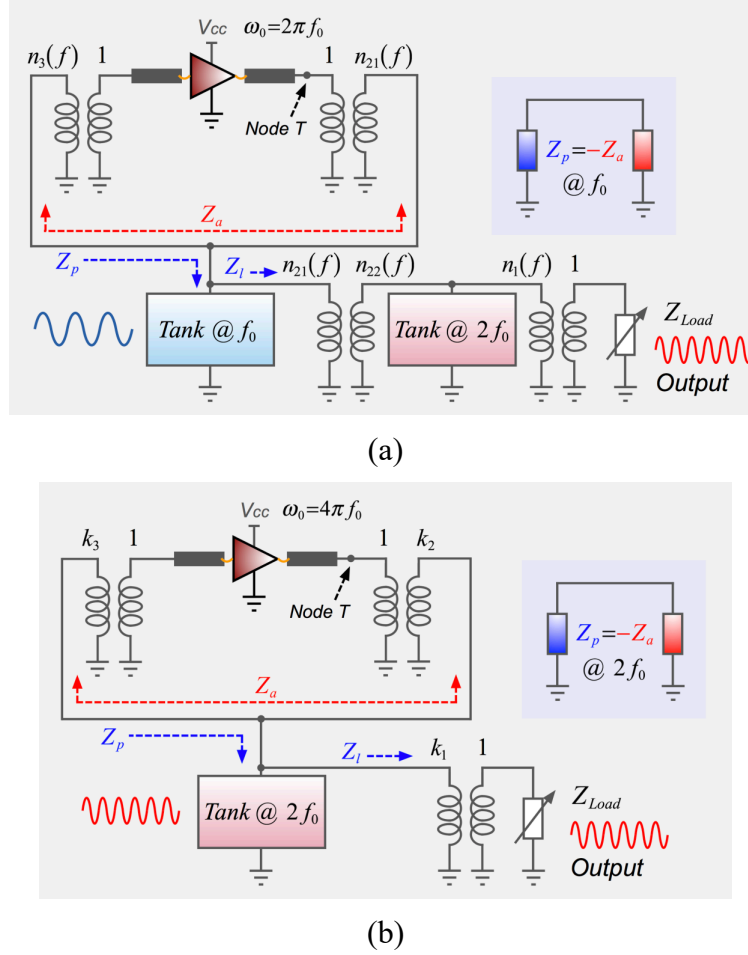


Figure 4.5: Complete equivalent circuit of the SIHO and the fundamental oscillator.

Combining the equivalent circuit of the gain block with that of the diplexer or the resonator, complete equivalent circuits of the SIHO and the fundamental oscillator are illustrated in Fig. 4.5. It should be noted that the fundamental frequency of the SIHO and the fundamental oscillator are f_0 and $2f_0$, respectively.

4.2.3 Operation principle with negative resistance model

Using the equivalent circuits of Fig. 4.5, the operation principle can be presented in the manner of a negative resistance oscillator model.

First of all, the circuit model shown in Fig. 4.5 (a) is examined. By dividing the circuit into active and passive subnetworks with their respect impedance of Z_a and Z_p , the oscillation condition at f_0 is fulfilled if $Z_a + Z_p = 0$ at f_0 . Furthermore, the load branch with an impedance of Z_l can be considered as two impedances Z_{l1} and Z_{l2} in parallel whose values are defined as:

$$\begin{cases} Z_{l1}(f) = Z_l(f), f \leq 1.5f_0, \\ Z_{l1}(f) = +\infty, f > 1.5f_0. \end{cases} \quad (4.2)$$

$$\begin{cases} Z_{l2}(f) = +\infty, f \leq 1.5f_0, \\ Z_{l2}(f) = Z_l(f), f > 1.5f_0. \end{cases} \quad (4.3)$$

On the other hand, referring to Fig. 4.6, the impedance of the active subnetwork of the SIHO around f_0 can be calculated using a test voltage $V_0 e^{j\omega t}$:

$$Z_a(f) = \frac{V_0 e^{j\omega t}}{I_1 e^{j\omega t} + I'_1 e^{j\omega t}} = 1 / \left[\frac{G_{in} - G_{G1}}{n_3^2(f)} + \frac{G_{out} - G_{D1}}{n_{21}^2(f)} \right], \quad (4.4)$$

in which $G_{G1} = n_3(f) \cdot I_{G1} e^{j\psi_1} / V_0$ and $G_{D1} = n_{21}(f) \cdot I_{D1} e^{j\phi_1} / V_0$ are the large signal equivalent conductance at the input and output generator of the gain block.

Secondly, through the examination of Fig. 4.5 (b), the active subnetwork impedance of the fundamental oscillator can be also expressed in the form of equation (4.4) provided that f is around $2f_0$. The passive subnetwork is simply the tank and the load impedances in parallel.

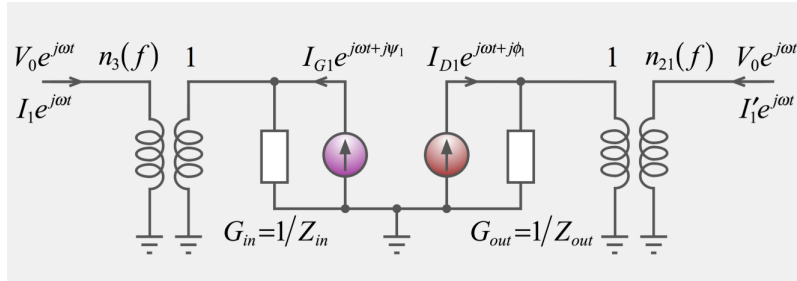


Figure 4.6: Schematic of active subnetwork impedance derivation.

The load perturbation can be modeled as an impedance ΔZ_{Load} in parallel with Z_{Load} . The resulting perturbation to the gain block can be inspected at *Node T* of both circuits. For the SIHO, an extra shunt impedance $\Delta Z_{Load} \cdot n_1^2(f) / n_{22}^2(f)$ at *Node T* can be found, whereas for the fundamental oscillator, the extra shunt impedance is $\Delta Z_{Load} \cdot k_1^2 / k_2^2$. Since $n_1^2(f) / n_{22}^2(f) \gg 1$ and $k_1^2 / k_2^2 \approx 1$ around their respective oscillating frequencies of the two oscillators, G_{G1} and G_{D1} of the fundamental oscillator is subject to a much stronger load variation compared to those of the SIHO. At their respective oscillating frequencies, the physical meaning of n_1^2 / n_{22}^2 and k_1^2 / k_2^2 is the strength of isolation. For the SIHO, although the change of the load impedance at $2f_0$ seen by

the gain block is $\Delta Z_{Load} \cdot n_1^2(f)/n_{22}^2(f) \approx \Delta Z_{Load}$, the harmonic pulling effect is much weaker than the fundamental counterpart as stated in section 4.2.1.

Then, the passive subnetworks subject to a load perturbation is considered. Any load impedance in the upper half plane of the Smith chart can be represented as a parallel resistor and inductor (R, L) and in the lower half as a parallel resistor and capacitor (R, C). Taking the first case (R, L) as an example, the normalized resonant frequency of *Tank* @ f_0 of the SIHO is as follows, if there is an extra shunt inductance ΔL :

$$f'_0/f_0 \approx \sqrt{\frac{L_1 + \Delta L \cdot n_1^2(f_0) \cdot n_{21}^2(f_0)/n_{22}^2(f_0)}{\Delta L \cdot n_1^2(f_0) \cdot n_{21}^2(f_0)/n_{22}^2(f_0)}} \quad (4.5)$$

And the normalized resonant frequency of *Tank* @ $2f_0$ of the fundamental oscillator is:

$$2f'_0/2f_0 \approx \sqrt{\frac{L_1/4 + \Delta L \cdot k_1^2}{\Delta L \cdot k_1^2}} \quad (4.6)$$

Since $n_{21}^2(f_0)/n_{22}^2(f_0) \gg 4$ and $k_1 \approx n_1(f_0)$, the frequency pulling attributed to the passive subnetwork of the SIHO is smaller than that of the fundamental oscillator.

As a summary, the frequency pulling caused by the active and passive subnetwork perturbations is listed and compared in Table 4.1.

Table 4.1: Frequency Pulling Comparison of the Two Types of Oscillators

Factor Type	Active at fundamental	Active at 2 nd harmonic	Passive	Total
SIHO	—	—	—	—
Fundamental	■	—	■	■

4.3 SIHO Modeling Based on X-Parameters

From the analysis conducted in the previous section, it can be found that a rigorous mathematical expression can hardly be developed mainly because of the limitation of the large signal modeling

technique, which is not able to provide explicit dependencies of conductance G_{G1} and G_{D1} on the driving and loading conditions of a gain block.

Traditionally, behavior models of nonlinear RF devices are widely used in the time domain and frequency domain circuit simulators. However, attempting to manipulate the behavior models in an analytical form is infeasible and will definitely result in extremely complicated transcendental equations.

In the frequency domain, the Poly-Harmonic Distortion (PHD) model is a very powerful tool in accounting for the harmonic dependencies in a matrix form (X-parameters) [40, 55, 56]. It has been successfully implemented for nonlinear circuit modeling and designing workflows, supported by the Keysight nonlinear vector network analyzer (nonlinear VNA or NVNA) and advanced design system (ADS) [44, 45, 103]. As presented in these three papers, one of the benefits of the PHD model is the support of analytical derivations like the scattering parameter (S-parameter). In this section, the SIHO-related large signal modeling is improved using the X-parameter model.

4.3.1 PHD model and X-parameter formulations

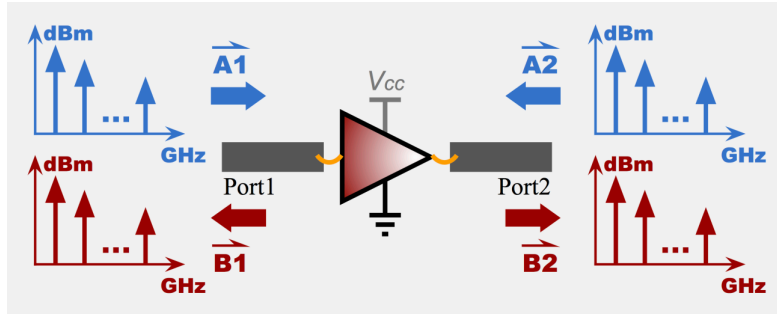


Figure 4.7: Incident and scattered power waves of two-port nonlinear network mapping functions with the fundamental and harmonic tones [104].

Generally, a two-port nonlinear device (e.g. a transistor or an amplifier) in operation has its incident and scattered power waves at each port and each harmonic with fundamental frequency f , as shown in Fig. 4.7. These waves can be related to each other by a set of nonlinear mapping functions as follows:

$$\begin{aligned} b_{1m} &= F_{1m}(V_{CC}, a_{11}, a_{12}, \dots, a_{1n}, \dots, a_{1N}, a_{21}, a_{22}, \dots, a_{2n}, \dots, a_{2N}), \\ b_{2m} &= F_{2m}(V_{CC}, a_{11}, a_{12}, \dots, a_{1n}, \dots, a_{1N}, a_{21}, a_{22}, \dots, a_{2n}, \dots, a_{2N}), \end{aligned} \quad (4.7)$$

and

$$\begin{aligned}\mathbf{A1} &= [a_{11}, a_{12}, \dots, a_{1N}]^T, \quad \mathbf{A2} = [a_{21}, a_{22}, \dots, a_{2N}]^T, \\ \mathbf{B1} &= [b_{11}, b_{12}, \dots, b_{1M}]^T, \quad \mathbf{B2} = [b_{21}, b_{22}, \dots, b_{2M}]^T.\end{aligned}\tag{4.8}$$

In these definitions, n and m are the harmonic indices for the \mathbf{A} and \mathbf{B} waves, respectively. Among all the waves, a_{11} is the large driving signal at the fundamental frequency that sets the operating condition of the device. Linearization of the mapping functions subject to each of the wave components at the vicinity of a_{11} gives rise to the following linear functions, in which k and i are the port indices for the \mathbf{A} and \mathbf{B} waves, respectively:

$$b_{im} = \sum \left[X_{im, kn}^{(S)} P^{m-n} a_{kn} + X_{im, kn}^{(T)} P^{m+n} a_{kn}^* \right]. \tag{4.9}$$

In this equation, P is the absolute phase of the a_{11} wave, which is usually selected as the phase reference so that P can be set as zero (so a_{11} becomes a real positive number) without losing generality. The existence of complex conjugate term a_{kn}^* is because F_{im} is a nonanalytic nonlinear function for [56]. The S terms $X_{im, kn}^{(S)}$ and T terms $X_{im, kn}^{(T)}$ are collectively referred to as the generalized X-parameters, by analogy with the generalized S-parameters [68]. If the device approaches linear operation, the S terms for the second and higher harmonics and all the T terms become zero so that the X-parameters are reduced to S-parameters. Equation (4.9) can be rewritten in a matrix form:

$$\mathbf{B} = \mathbf{X}^{(S)} \cdot \mathbf{A} + \mathbf{X}^{(T)} \cdot \mathbf{A}^*, \tag{4.10}$$

in which

$$\mathbf{A} = \begin{bmatrix} \mathbf{A2} \\ \mathbf{A1} \end{bmatrix}, \quad \mathbf{B} = \begin{bmatrix} \mathbf{B2} \\ \mathbf{B1} \end{bmatrix},$$

$$\mathbf{X}^{(S)} = \begin{bmatrix} X_{21,21}^{(S)} & X_{21,22}^{(S)} & \cdots & X_{21,2N}^{(S)} & X_{21,11}^{(S)} & X_{21,12}^{(S)} & \cdots & X_{21,1N}^{(S)} \\ X_{22,21}^{(S)} & X_{22,22}^{(S)} & \cdots & X_{22,2N}^{(S)} & X_{22,11}^{(S)} & X_{22,12}^{(S)} & \cdots & X_{22,1N}^{(S)} \\ \vdots & \vdots & \ddots & \vdots & \vdots & \vdots & \ddots & \vdots \\ X_{2M,21}^{(S)} & X_{2M,22}^{(S)} & \cdots & X_{2M,2N}^{(S)} & X_{2M,11}^{(S)} & X_{2M,12}^{(S)} & \cdots & X_{2M,1N}^{(S)} \\ X_{11,21}^{(S)} & X_{11,22}^{(S)} & \cdots & X_{11,2N}^{(S)} & X_{11,11}^{(S)} & X_{11,12}^{(S)} & \cdots & X_{11,1N}^{(S)} \\ X_{12,21}^{(S)} & X_{12,22}^{(S)} & \cdots & X_{12,2N}^{(S)} & X_{12,11}^{(S)} & X_{12,12}^{(S)} & \cdots & X_{12,1N}^{(S)} \\ \vdots & \vdots & \ddots & \vdots & \vdots & \vdots & \ddots & \vdots \\ X_{1M,21}^{(S)} & X_{1M,22}^{(S)} & \cdots & X_{1M,2N}^{(S)} & X_{1M,11}^{(S)} & X_{1M,12}^{(S)} & \cdots & X_{1M,1N}^{(S)} \end{bmatrix},$$

$$\mathbf{X}^{(T)} = \begin{bmatrix} X_{21,21}^{(T)} & X_{21,22}^{(T)} & \cdots & X_{21,2N}^{(T)} & X_{21,11}^{(T)} & X_{21,12}^{(T)} & \cdots & X_{21,1N}^{(T)} \\ X_{22,21}^{(T)} & X_{22,22}^{(T)} & \cdots & X_{22,2N}^{(T)} & X_{22,11}^{(T)} & X_{22,12}^{(T)} & \cdots & X_{22,1N}^{(T)} \\ \vdots & \vdots & \ddots & \vdots & \vdots & \vdots & \ddots & \vdots \\ X_{2M,21}^{(T)} & X_{2M,22}^{(T)} & \cdots & X_{2M,2N}^{(T)} & X_{2M,11}^{(T)} & X_{2M,12}^{(T)} & \cdots & X_{2M,1N}^{(T)} \\ X_{11,21}^{(T)} & X_{11,22}^{(T)} & \cdots & X_{11,2N}^{(T)} & X_{11,11}^{(T)} & X_{11,12}^{(T)} & \cdots & X_{11,1N}^{(T)} \\ X_{12,21}^{(T)} & X_{12,22}^{(T)} & \cdots & X_{12,2N}^{(T)} & X_{12,11}^{(T)} & X_{12,12}^{(T)} & \cdots & X_{12,1N}^{(T)} \\ \vdots & \vdots & \ddots & \vdots & \vdots & \vdots & \ddots & \vdots \\ X_{1M,21}^{(T)} & X_{1M,22}^{(T)} & \cdots & X_{1M,2N}^{(T)} & X_{1M,11}^{(T)} & X_{1M,12}^{(T)} & \cdots & X_{1M,1N}^{(T)} \end{bmatrix}.$$

\mathbf{A}^* is the complex conjugate of \mathbf{A} . Equation (4.10) can be further written in a square matrix form:

$$\tilde{\mathbf{B}} = \mathbf{X}^{(ST)} \cdot \tilde{\mathbf{A}}, \quad (4.11)$$

in which

$$\tilde{\mathbf{A}} = \begin{bmatrix} \mathbf{A} \\ \mathbf{A}^* \end{bmatrix}, \quad \tilde{\mathbf{B}} = \begin{bmatrix} \mathbf{B} \\ \mathbf{B}^* \end{bmatrix}, \quad \mathbf{X}^{(ST)} = \begin{bmatrix} \mathbf{X}^{(S)} & \mathbf{X}^{(T)} \\ \mathbf{X}^{(T)*} & \mathbf{X}^{(S)*} \end{bmatrix}.$$

4.3.2 SIHO large signal modeling based on X-parameters

Assuming the target SIHO design has a fundamental frequency f_0 , around which the X-parameters of the gain block are extracted. The SIHO real fundamental oscillating frequency is f_r and $f_r = f_0$ when a pulling does not exist. The X-parameter measurement procedure of a nonlinear device makes use of extraction tones (ETs) with lower power (e.g. 16 dB lower than the a_{11} wave power) to perform phase sweep measurements at the fundamental and each of the harmonic frequencies, under a large signal (a_{11} wave) driving. So, the X-parameters are valid within a certain source and load impedance region around the point where the device measurement is performed. The size of the region depends on the level of the ETs, which is constrained by the linearization accuracy requirement of equation (4.9). Such an impedance-independent (region-limited) X-parameter model has been used to robustly predict large signal responses [44, 45, 55] and to design nonlinear circuits although the size of the valid region varies for different devices and is not very well characterized in the literature. Therefore, in order to utilize an X-parameter model, the impedance termination and driving level in the real operating condition need to be identified as close as possible. And also, a pre-match is necessary before experimentally extracting valid X-parameters of a transistor.

From alternative point of view, the real operating conditions of a nonlinear device embedded in a circuit is described by the voltage and current waveforms at each port and each harmonic, from which the virtual source and load can be determined, as shown in Fig. 4.8.

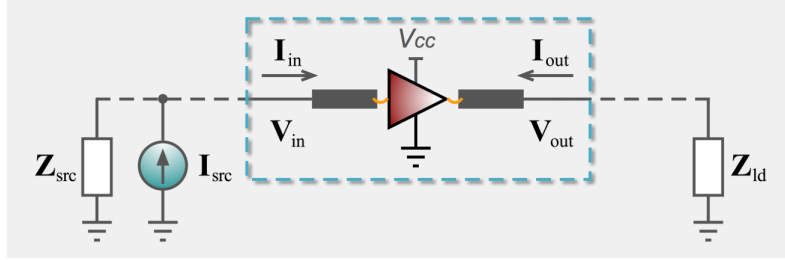


Figure 4.8: Relation between the voltage/current waveforms of a gain block and the virtual source/load.

A nonlinear gain block operating in an oscillator with certain input and output waveforms can be replaced into a virtual source and load environment whose parameters are defined with the following equations:

$$Z_{ld} = -V_{out}/I_{out}, \quad I_{src} = I_{in} + V_{in}/Z_{src}. \quad (4.12)$$

It can be found that the virtual load impedance is completely determined by the output voltage and current, but the virtual source cannot be determined since two unknowns (I_{src} and Z_{src}) are involved. Without losing generality, all the elements of Z_{src} are selected to be $50 \, \Omega$ so I_{src} can be determined. In this way, the input/output reference impedances of the X-parameters of the gain block can be selected as $50 \, \Omega$ and Z_{ld} . Moreover, since the harmonic signals are either weakly generated or significantly attenuated by the filter of the feedback-loop of an oscillator, the harmonic level in I_{in} and V_{in} are much lower than the fundamental ones. Therefore, it is valid to ignore the harmonic components in the large driving signal I_{src} and set the phase of I_{src} to zero, when extracting the X-parameters of the gain block.

The incident and scattered power waves for all the ports and harmonics are related to the terminal voltage and current in a matrix form as follows:

$$\tilde{\mathbf{A}} = \tilde{\mathbf{G}} \cdot (\tilde{\mathbf{V}} + \tilde{\mathbf{Z}} \cdot \tilde{\mathbf{I}}), \quad \tilde{\mathbf{B}} = \tilde{\mathbf{G}} \cdot (\tilde{\mathbf{V}} - \tilde{\mathbf{Z}}^* \cdot \tilde{\mathbf{I}}), \quad (4.13)$$

in which

$$\tilde{\mathbf{G}} = \left(\sqrt{8 \operatorname{Re}(\tilde{\mathbf{Z}})} \right)^{-1},$$

If Z_l (so that both Z_{l1} and Z_{l2}) is subject to a load pulling, but not strongly enough to force the gain block leaving the valid region of the X-parameters, the load impedance and impedance matrix change from \mathbf{Z}_{ld} and $\tilde{\mathbf{Z}}$ to \mathbf{Z}'_{ld} and $\tilde{\mathbf{Z}}'$, respectively. Then the gain block terminal voltage and current are related to the test current sources by:

$$\tilde{\mathbf{I}} = \mathbf{N} \cdot \mathbf{I}_s - (\tilde{\mathbf{Z}}')^{-1} \cdot \tilde{\mathbf{V}}, \quad (4.16)$$

in which

$$\mathbf{N} = \text{diag} \left[n_{21}(f_r), n_{21}(2f_r), \dots, n_{21}(Nf_r), n_3(f_r), n_3(2f_r), \dots, n_3(Nf_r), \right. \\ \left. n_{21}(f_r), n_{21}(2f_r), \dots, n_{21}(Nf_r), n_3(f_r), n_3(2f_r), \dots, n_3(Nf_r) \right],$$

$$\mathbf{I}_s = \begin{bmatrix} I_{S2}(f_r), \overbrace{0, 0, \dots, 0}^{N-1}, I_{S1}(f_r), \overbrace{0, 0, \dots, 0}^{N-1}, \\ I_{S2}(f_r), \overbrace{0, 0, \dots, 0}^{N-1}, I_{S1}(f_r), \overbrace{0, 0, \dots, 0}^{N-1} \end{bmatrix}^T.$$

Substituting (4.16) into (4.14) and defining $\tilde{\mathbf{V}}_s = \mathbf{N} \cdot \tilde{\mathbf{V}}$, which is the voltage at the test current source output:

$$\left[\mathbf{1} - \tilde{\mathbf{X}}^{(\text{ST})} + \tilde{\mathbf{Z}}^* \cdot (\tilde{\mathbf{Z}}')^{-1} + \tilde{\mathbf{X}}^{(\text{ST})} \cdot \tilde{\mathbf{Z}} \cdot (\tilde{\mathbf{Z}}')^{-1} \right] \cdot \mathbf{N}^{-1} \cdot \tilde{\mathbf{V}}_s = (\tilde{\mathbf{Z}}^* + \tilde{\mathbf{X}}^{(\text{ST})} \cdot \tilde{\mathbf{Z}}) \cdot \mathbf{N} \cdot \mathbf{I}_s. \quad (4.17)$$

$$\left(\begin{bmatrix} \frac{Z_{ld1}^* + Z_{ld1}}{Z_{ld1} \cdot n_{21}(f_r)} \\ \frac{2}{n_3(f_r)} \end{bmatrix} + \begin{pmatrix} \tilde{X}_{21,22}^{(\text{S})} & \tilde{X}_{21,22}^{(\text{T})} \\ \tilde{X}_{11,22}^{(\text{S})} & \tilde{X}_{11,22}^{(\text{T})} \end{pmatrix} \begin{pmatrix} \alpha_{ld2} & 0 \\ 0 & \alpha_{ld2}^* \end{pmatrix} \begin{pmatrix} \frac{V_{22}}{V_1 \cdot n_{21}(2f_r)} \\ \frac{V_{22}^*}{V_1 \cdot n_{21}(2f_r)} \end{pmatrix} \right) = \begin{pmatrix} (Z_{ld1}^* + Z_{ld1} \tilde{X}_{21,21}^{(\text{S})} + Z_{ld1}^* \tilde{X}_{21,21}^{(\text{T})}) \cdot n_{21}(f_r) & 50 \cdot (\tilde{X}_{21,11}^{(\text{S})} + \tilde{X}_{21,11}^{(\text{T})}) \cdot n_3(f_r) \\ (Z_{ld1} \tilde{X}_{11,21}^{(\text{S})} + Z_{ld1}^* \tilde{X}_{11,21}^{(\text{T})}) \cdot n_{21}(f_r) & 50 \cdot (\tilde{X}_{11,11}^{(\text{S})} + \tilde{X}_{11,11}^{(\text{T})} + 1) \cdot n_3(f_r) \end{pmatrix} \begin{pmatrix} \frac{I_{S2}}{V_1} \\ \frac{I_{S1}}{V_1} \end{pmatrix}, \quad (4.18)$$

$$\mathbf{K} + \mathbf{X} \cdot \boldsymbol{\alpha} \cdot \mathbf{P} = \mathbf{Q} \cdot \mathbf{E}, \quad (4.18.1)$$

$$\begin{pmatrix} \frac{Z_{ld2}^*}{Z'_{ld2}} + 1 + \tilde{X}_{22,22}^{(\text{S})} \alpha_{ld2} & \tilde{X}_{22,22}^{(\text{T})} \alpha_{ld2}^* \\ \tilde{X}_{22,22}^{(\text{T})*} \alpha_{ld2} & \frac{Z_{ld2}}{Z'^*_{ld2}} + 1 + \tilde{X}_{22,22}^{(\text{S})*} \alpha_{ld2}^* \end{pmatrix} \begin{pmatrix} \frac{V_{22}}{V_1 \cdot n_{21}(2f_r)} \\ \frac{V_{22}^*}{V_1 \cdot n_{21}(2f_r)} \end{pmatrix} = \begin{pmatrix} (Z_{ld1} \tilde{X}_{22,21}^{(\text{S})} + Z_{ld1}^* \tilde{X}_{22,21}^{(\text{T})}) \cdot n_{21}(f_r) & 50 \cdot (\tilde{X}_{22,11}^{(\text{S})} + \tilde{X}_{22,11}^{(\text{T})}) \cdot n_3(f_r) \\ (Z_{ld1} \tilde{X}_{22,21}^{(\text{T})*} + Z_{ld1}^* \tilde{X}_{22,21}^{(\text{S})*}) \cdot n_{21}(f_r) & 50 \cdot (\tilde{X}_{22,11}^{(\text{S})*} + \tilde{X}_{22,11}^{(\text{T})*}) \cdot n_3(f_r) \end{pmatrix} \begin{pmatrix} \frac{I_{S2}}{V_1} \\ \frac{I_{S1}}{V_1} \end{pmatrix}, \quad (4.19)$$

$$\mathbf{S} \cdot \mathbf{P} = \mathbf{R} \cdot \mathbf{E}. \quad (4.19.1)$$

Equations (4.18) and (4.19) can be extracted from (4.17). Their symbolic forms are written as equations (4.18.1) and (4.19.1). $\tilde{X}_{im,kn}^{(\text{S})}$, $\tilde{X}_{im,kn}^{(\text{T})}$ and their conjugates are from the $\tilde{\mathbf{X}}^{(\text{ST})}$ matrix. V_1 is

the fundamental frequency voltage at the test current source as shown in Fig. 4.9. α_{ld2} is the 2nd harmonic load impedance pulling ratio:

$$\alpha_{ld2} = Z_{ld2} / Z'_{ld2} - 1. \quad (4.20)$$

The equivalent admittance of the upper portion with the gain block in the SIHO at the fundamental frequency can be obtained by solving equations (4.18) and (4.19) together:

$$1/Z_a(f_r) = [1, 1] \cdot (\mathbf{Q} - \mathbf{X} \cdot \boldsymbol{\alpha} \cdot \mathbf{S}^{-1} \cdot \mathbf{R})^{-1} \cdot \mathbf{K}. \quad (4.21)$$

The equivalent admittance of the lower portion at the fundamental frequency can be expressed as:

$$1/Z_p(f_r) = j2\pi f_r C_1 + \frac{1}{j2\pi f_r L_1} + \frac{1}{R_1} + \frac{1}{Z_{l1}(f_r)} - \frac{1}{50 \cdot n_3^2(f_0)} - \frac{1}{Z_M(f_0) \cdot n_{21}^2(f_0)}. \quad (4.22)$$

Equations (4.21) and (4.22) can be solved simultaneously to get the pulled oscillating frequency f_r , output power at $2f_r$, and other variables that are swept in the X-parameter measurement. The phase noise variation can be also predicted based on the Q-factor dependence. When α_{ld2} is zero, which means no pulling exists, equations (4.21) and (4.22) are reduced to:

$$1/Z_a(f_0) = [1, 1] \cdot \mathbf{Q}^{-1} \cdot \mathbf{K}, \quad (4.23)$$

$$1/Z_p(f_0) = \frac{1}{R_1} + \frac{1}{Z_{l1}(f_0)} - \frac{1}{50 \cdot n_3^2(f_0)} - \frac{1}{Z_M(f_0) \cdot n_{21}^2(f_0)}. \quad (4.24)$$

The physical insight of the pulling effect can be gained from the following aspects:

- (1) The impedance Z_p of the linear subnetwork deviates from the designed value due to the pulling effect around f_0 , which changes the shunt impedance $Z_{l1}(f)$. To reduce the effect, the only choice is to enhance the isolation of the diplexer at the target fundamental frequency f_0 , so that $Z_{l1}(f)$ gets more amplification and has less effect on Z_p .
- (2) When the norm of matrix $\boldsymbol{\alpha}$ is reduced, the shift of the impedance Z_a gets weaker, and equation (4.21) is reduced to equation (4.23).
- (3) Matrix \mathbf{S} relates to the 2nd harmonic reflection coefficients at the output of the gain block. If the reflection gets strong enough such that the norm of \mathbf{S}^{-1} is reduced, the 2nd harmonic

signal injection into the output of the gain block as a result of the load impedance variation is weaker, so that the perturbation on the oscillating dynamics is smaller.

- (4) Matrix \mathbf{X} relates to the conversion rate of the incident 2nd harmonic signal at port 2 of the gain block to the fundamental signal output at both ports. Apart from the reflected portion of the 2nd harmonic injection at port 2, the remaining portion cannot perturb the oscillating dynamics unless it is converted into the fundamental signal for which the oscillation condition is established. As such, the smaller the norm of \mathbf{X} is, the weaker the shift of impedance Z_a will be.
- (5) The elements in \mathbf{R} matrix are proportional to the conversion rate of the fundamental frequency signal to the 2nd harmonic. A smaller norm of \mathbf{R} means a weaker nonlinearity of the gain block and certainly a weaker pulling effect at the 2nd harmonic frequency. The first and second columns are respectively proportional to the rate of conversion from the incident fundamental tone at port 2 and port 1 to the 2nd harmonic output at port 2. Therefore, smaller $\tilde{X}_{22,21}^{(S)}$ and $\tilde{X}_{22,21}^{(T)}$ parameters and larger $\tilde{X}_{22,11}^{(S)}$ and $\tilde{X}_{22,11}^{(T)}$ parameters will potentially result in a high harmonic output efficiency and low pulling effect.
- (6) The isolation of the diplexer around $2f_0$ affects the performance of the upper portion subnetwork. This effect can be modeled by substituting the element $Z_M(2f_0)$ with $Z_M(2f_0)n_{21}^2(2f_0)/n_{21}'^2(2f_0)$ in \mathbf{Z}_M , in which n_{21}' is the ratio of the corresponding transformer of a diplexer which has a different isolation around $2f_0$. As the isolation becomes weaker at this frequency, $n_{21}'(2f_0)$ gets larger and $n_{21}' \approx n_{21}$ around other harmonics. This implies the load of the gain block around $2f_0$ in an SIHO is pulled towards the $(-1, 0)$ point of the Smith chart where the gradient of the frequency variation is larger. This phenomenon is illustrated in Section 4.4.8.

The equivalent admittance of the lower portion at the fundamental frequency can be expressed as:

$$1/Z_p(2f_r) = j4\pi f_r C_2 + \frac{1}{j4\pi f_r L_2} + \frac{1}{R_2} - \frac{1}{50 \cdot k_3^2} - \frac{1}{Z_M(2f_0) \cdot k_2^2} . \quad (4.29)$$

The operation frequency of the oscillator can be obtained from equations (4.28) and (4.29). The physical meaning of the pulling effect on the fundamental oscillator can be understood by observing equation (4.26). A load variation will produce an extra reflected signal phasor superposed with the original one. The phasor will be distributed to both the input and output of the gain block. The portion to the output will not take effect in pulling only with the condition that $\hat{\mathbf{X}}$ is a zero matrix, which means the gain block is unidirectional and perfectly matched at the output. This condition can be hardly satisfied by a compressed gain block. The portion to the input will always take effect because $\hat{\mathbf{K}}$ contains the perturbed impedance Z'_{ld1} .

The right-hand-sides of equations (4.18) and (4.26) share the same expression. Comparing the left-hand-side term \mathbf{K} with $\hat{\mathbf{K}}$ implies that the fundamental oscillator pulling cannot be sufficiently reduced no matter how sophisticated the design is, because the interference inevitably joins the loop through the mainstream. The term $\hat{\mathbf{P}}$ of (4.26) relates to the resonator design and cannot be adjusted independently. The term \mathbf{X} of (4.18) relates to the harmonic conversion performance, which is a secondary effect compared to the co-frequency reflection and conversion effects represented by $\hat{\mathbf{X}}$.

4.3.4 Injection locking of SIHO and fundamental oscillator

In case that the SIHO is locked to an external injection signal around the frequency $2f_0$, its steady-state can still be interpreted with the equivalent circuit in Fig. 4.9 except that the impedance $Z_{l1}(f)$ will not be affected. The external signal injection can be modeled by a perturbation on $Z_{l2}(f)$ around $2f_0$. The steady-state frequency can be solved from equations (4.21) and (4.22). The steady-state of the injection pulling for the fundamental oscillator can be described by the circuit of Fig. 4.10, with the $Z_i(f)$ perturbed around $2f_0$.

Quantitatively comparing the lock ranges of the oscillators can be carried out by estimating the maximum phase shift induced by the injection signal [70]. For the SIHO and the fundamental oscillator, their respective maximum phase shifts are:

$$|\mathbf{E} - \mathbf{E}_0|/|\mathbf{E}_0| = |\mathbf{X} \cdot \boldsymbol{\alpha} \cdot \mathbf{P}|/|\mathbf{K}_0|, \quad (4.30)$$

and

$$|\hat{\mathbf{E}} - \hat{\mathbf{E}}_0|/|\hat{\mathbf{E}}_0| = (|\hat{\mathbf{K}} - \hat{\mathbf{K}}_0| + |\hat{\mathbf{X}} \cdot \hat{\boldsymbol{\alpha}} \cdot \hat{\mathbf{P}}|)/|\hat{\mathbf{K}}_0|. \quad (4.31)$$

It can be seen that with the same relative injection amplitude and a lower energy conversion from the 2nd to the fundamental tone at the output of the gain block, the SIHO will have less phase shift to be compensated by the tank. Therefore, a smaller lock range can be expected from the SIHO, compared to the fundamental oscillator.

4.4 Design Theory, Methodology, Implementation and Model Verification

In this section, the design theory and methodology of SIHO are presented with an exemplary prototype oscillating at 2 GHz and efficiently delivering a 4 GHz signal. In section 4.4.1, a diplexer is designed and tested. From section 4.4.2 to 4.4.7, an automated experimental design setup, named as the harmonic-measurement-and-design (HMD) system is proposed and studied comprehensively in terms of hardware configuration, waveform measurement principle, calibration procedure, design screening and optimization methods, and matching network design formulas. In section 4.4.8, the designed SIHO is fabricated and tested. The X-parameters of the gain block are experimentally extracted and the proposed SIHO circuit model is verified by both simulation and measurement. In the context, maximum 3 harmonics including the fundamental tone are considered. All the waves, reflection coefficients, and S-parameters in this section are normalized to 50 Ω except otherwise stated.

4.4.1 Microstrip diplexer design

Similar diplexers as what is shown in [91] are designed at $f_0 = 2$ GHz and fabricated on Rogers RT/duroid® 6002 substrates with 0.508 mm thickness. One of the devices is shown in Fig. 4.11 (a), in which dimensions are marked. With a fine-tuning and optimization, the designed diplexers can achieve both high Q-factor and good impedance matching. Fig. 4.11 (b) illustrates the simulated electric field intensity of the first two resonant modes, which support the pass-bands of the fundamental frequency at 2 GHz and the 2nd harmonic frequency at 4 GHz, respectively.

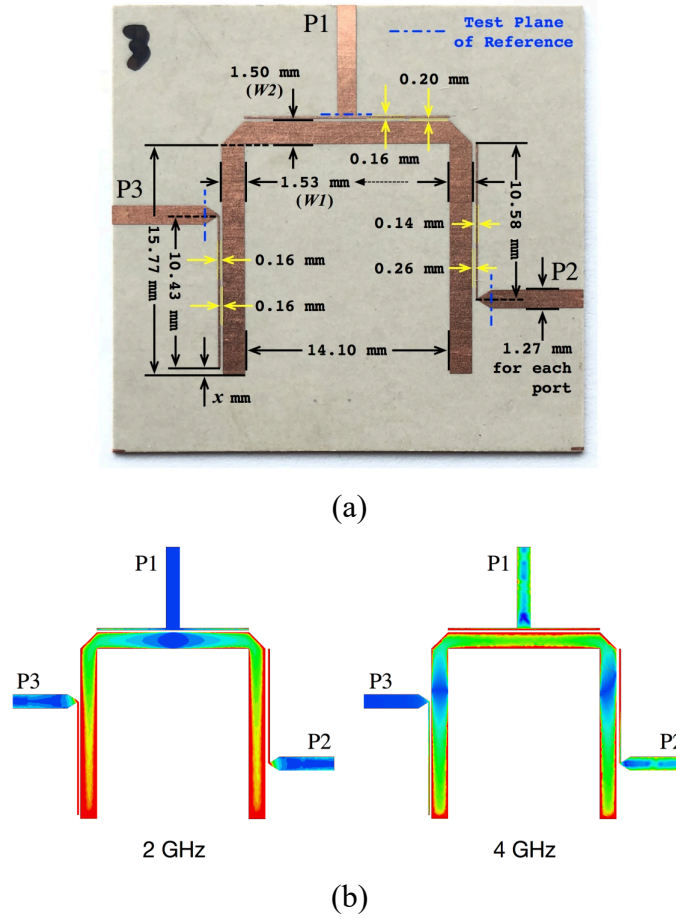
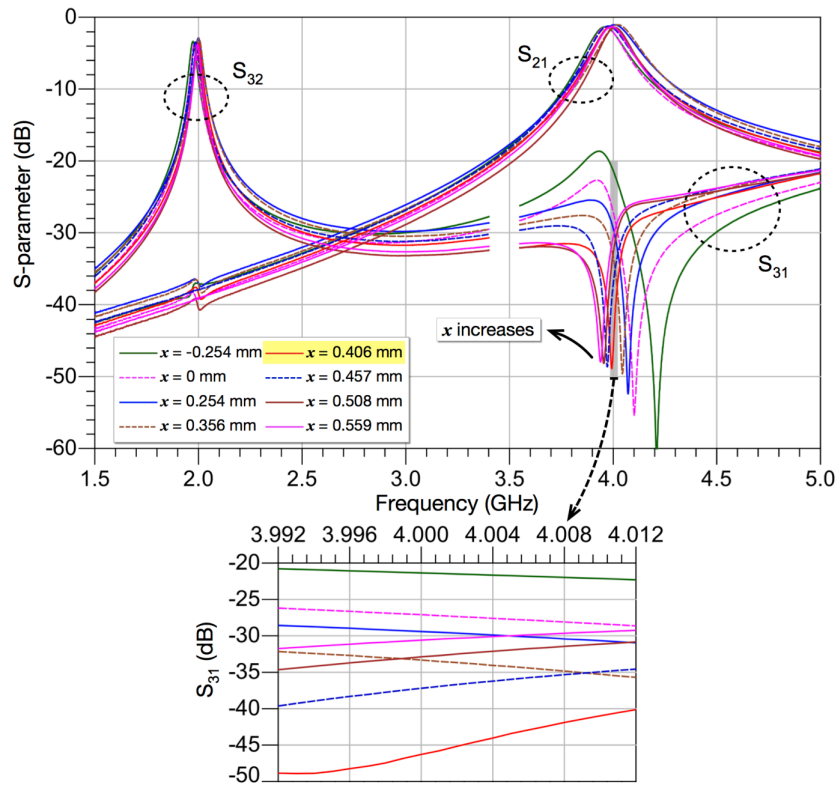


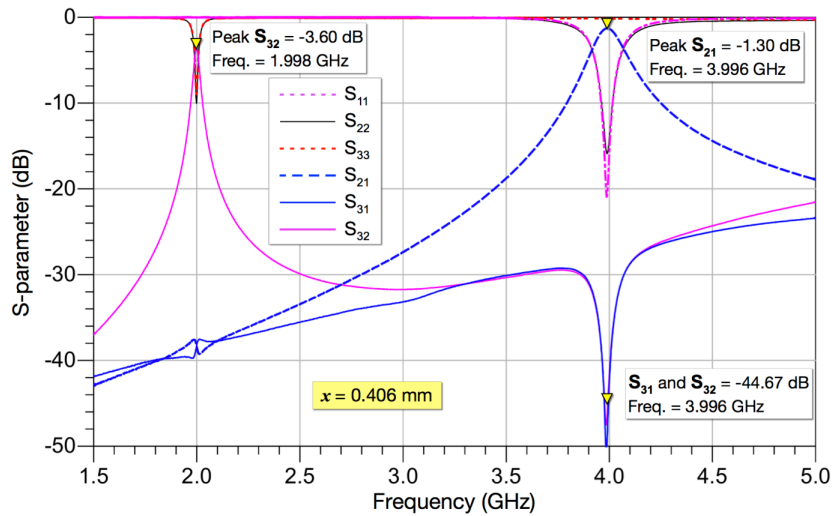
Figure 4.11: (a) One of the fabricated microstrip diplexers, and (b) simulated electric field intensity distribution of the first two resonant modes.

The diplexer structure is based on a folded dual-mode microstrip resonator. The pass-band frequency accuracy and isolation are the critical specifications, which are impacted by physical parameters $W2/W1$ and length x , respectively. It is important to tune $W2/W1$ such that the ratio between the 2nd and the 1st resonant frequencies is 2, using a step impedance technique reported in [72]. By changing x , the position of P3 is changed with respect to the electric field notch of the 2nd resonant mode, such that the frequency of the transmission zero is changed, which can be explained by Fig. 4.11 (b). Fig. 4.12 (a) shows the measured S-parameters of the diplexers with different length x . As x is increased, the frequency of the maximum isolation between P1 and P3 is reduced. This is because as P3 is shifted farther from the end of the resonator, the minimum coupling happens at a lower frequency. The diplexer with $x = 0.406$ mm is selected for the SIHO design, whose maximum isolation almost happens at the 2nd pass-band frequency of 3.996 GHz, which is

exactly a double of that of the 1st one. The full S-parameters are shown in Fig. 4.12 (b). The loaded Q-factor which has a major effect on the phase noise is about 65.



(a)



(b)

Figure 4.12: Measured S-parameters of (a) fabricated duplexers with various value of parameter x , and (b) the fabricated duplexer with $x = 0.406$ mm.

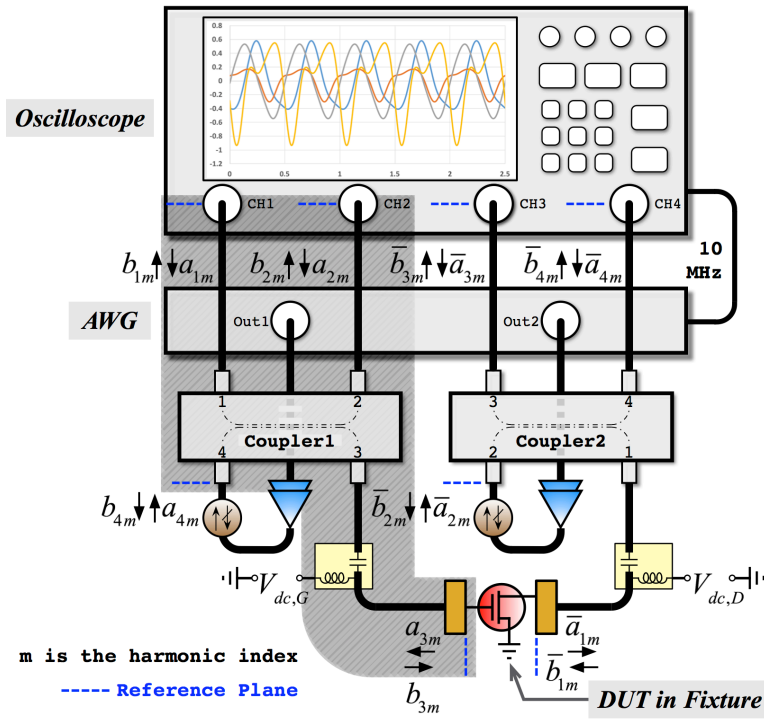
4.4.2 Transistor characterization and SIHO design setup

An ATF-541M4 low-noise enhanced E-pHEMT from Broadcom Inc. is selected in building the SIHO. It has 17.5 dB associated gain and 21.4 dBm OP1dB at 2 GHz, and it is usually applied for low noise or driver amplifier design in the frequency range of 450 MHz to 6 GHz. This transistor is intended for small signal and linear operations and no reliable large signal model is available from the vendor. The transistor is positioned in the design with a common source configuration.

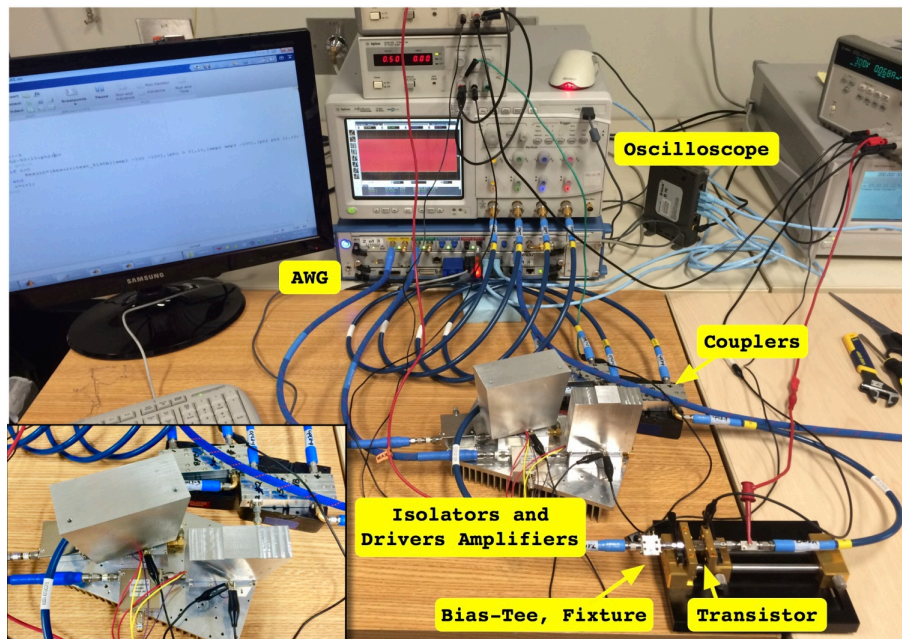
Usually, this kind of strong nonlinear circuit design heavily relies on an accurate and verified nonlinear model and exhaustive source- and load-pull simulations [105]. But such a model is not always available, especially for low power transistors and certain technology nodes. As stated in section 4.3.2, to adopt the X-parameter model in circuit synthesizing, the impedance terminations (sometimes far from the NVNA port impedance) and input power level at each harmonic close to the real operating conditions need to be identified a priori, which also involves a blind searching through source- and load-pull measurements. As harmonics are involved, the impedance searching procedure may become extremely time-consuming.

To overcome these problems, an HMD system as shown in Fig. 4.13 (a) and (b) is proposed and implemented as a unified solution for the automated experimental design of an SIHO. It is composed of an oscilloscope, an arbitrary waveform generator (AWG), wideband directional couplers, driver amplifiers, isolators, bias-Tees, fixtures, and a program for calibration, control, and optimization. Even without any sophisticated nonlinear transistor model, the system is able to directly synthesize and optimize the waveforms of a transistor in a hardware setup, which is assisted with calibration and control software that selects the feasible design, matches the device & components and evaluates the final performance as if the transistor is autonomously operating in a real SIHO.

The HMD system is waveform-design-oriented, contrary to the impedance-searching-oriented harmonic active source- and load-pull system used to synthesize various load impedances under which the optimal response of a nonlinear device is captured [106-111]. Similar hardware setups for active harmonic source- and load-pull measurements have been reported. Among these papers, [108-111] report similar hardware setups. It can be seen that as commercially available AWG and oscilloscope now approach 100 GSa/s sampling rate and beyond, a lot of tasks can be accomplished without investing on a dedicated active load-pull system.



(a)



(b)

Figure 4.13: (a) Schematic and (b) photo of the HMD system.

Two tasks are performed iteratively by the HMD system, namely to measure the transistor response under different source & load conditions, and to evolve a circuit design automatically. For each

test, the two output channels of the AWG generate waveforms with fully controlled amplitude and phase at the fundamental and harmonic frequencies. With a series of tests and searching controlled by the program, the real optimal waveforms presented at the input and output pins of the transistor as if it is operating in an actual SIHO can be directly synthesized and measured.

Measurement of the waveforms is carried out with the oscilloscope, couplers, and connected accessories. The relations between the a_{im} and b_{im} ($i=1$ to 3 is the port index, and m is the harmonic index) waves at the reference planes as shown in Fig. 4.13 (a) can be expressed as:

$$b_{1m} = S_{11m}a_{1m} + S_{12m}a_{2m} + S_{13m}a_{3m} + S_{14m}a_{4m}, \quad (4.32.1)$$

$$b_{2m} = S_{21m}a_{1m} + S_{22m}a_{2m} + S_{23m}a_{3m} + S_{24m}a_{4m}, \quad (4.32.2)$$

$$b_{3m} = S_{31m}a_{1m} + S_{32m}a_{2m} + S_{33m}a_{3m} + S_{34m}a_{4m}, \quad (4.32.3)$$

in which S_{ijm} is the S-parameter at the m^{th} harmonic for coupler 1 extended with cables, bias-Tees and test fixture to the marked reference planes (refer to the shaded area). A TRL calibration with customized standards is used to measure S_{ijm} . Since $a_{im} = b_{im}\Gamma_{im}$, and $b_{im} = V_{im}/(10\Gamma_{im} + 10)$, in which Γ_{im} and V_{im} ($i=1$ to 2) are the input reflection coefficient and the measured voltage wave of the port of the i^{th} oscilloscope channels, a_{3m} and a_{4m} can be solved from equations (4.32.1) and (4.32.2). Then, from equation (4.32.3), b_{3m} can be calculated. After applying the same mathematical manipulations to the S-parameters for coupler 2 (for which the correspondence symbols are added with bars) extended with cables, bias-Tees and test fixture, the incident and reflected waves for both the input and output of the transistor at the fundamental and harmonic frequencies are expressed as equation (4.33).

$$a_{3m} = \frac{V_{1m}(\Gamma_{1m}S_{14m}S_{21m} + S_{24m} - \Gamma_{1m}S_{11m}S_{24m})/(\Gamma_{1m} + 1)}{10(-S_{14m}S_{23m} + S_{13m}S_{24m})} + \frac{V_{2m}S_{14m}(-1 + \Gamma_{2m}S_{22m})/(\Gamma_{2m} + 1) - V_{2m}\Gamma_{2m}S_{12m}S_{24m}/(\Gamma_{2m} + 1)}{10(-S_{14m}S_{23m} + S_{13m}S_{24m})}, \quad (4.33.1)$$

$$b_{3m} = \frac{S_{31m}V_{1m}\Gamma_{1m}}{10\Gamma_{1m} + 10} + \frac{S_{32m}V_{2m}\Gamma_{2m}}{10\Gamma_{2m} + 10} + \begin{pmatrix} S_{33m} & S_{34m} \end{pmatrix} \begin{pmatrix} S_{13m} & S_{14m} \\ S_{23m} & S_{24m} \end{pmatrix}^{-1} \begin{pmatrix} \frac{V_{1m} - V_{1m}S_{11m}\Gamma_{1m}}{10\Gamma_{1m} + 10} - \frac{V_{2m}S_{12m}\Gamma_{2m}}{10\Gamma_{2m} + 10} \\ \frac{V_{2m} - V_{2m}S_{22m}\Gamma_{2m}}{10\Gamma_{2m} + 10} - \frac{V_{1m}S_{21m}\Gamma_{1m}}{10\Gamma_{1m} + 10} \end{pmatrix}, \quad (4.33.2)$$

$$\bar{a}_{1m} = \frac{V_{3m}(\Gamma_{3m}\bar{S}_{32m}\bar{S}_{43m} + \bar{S}_{42m} - \Gamma_{3m}\bar{S}_{33m}\bar{S}_{42m})/(\Gamma_{3m} + 1)}{10(-\bar{S}_{32m}\bar{S}_{41m} + \bar{S}_{31m}\bar{S}_{42m})} + \frac{V_{4m}\bar{S}_{32m}(-1 + \Gamma_{4m}\bar{S}_{44m})/(\Gamma_{4m} + 1) - V_{4m}\Gamma_{4m}\bar{S}_{34m}\bar{S}_{42m}/(\Gamma_{4m} + 1)}{10(-\bar{S}_{32m}\bar{S}_{41m} + \bar{S}_{31m}\bar{S}_{42m})}, \quad (4.33.3)$$

$$\bar{b}_{1m} = \frac{\bar{S}_{13m}V_{3m}\Gamma_{3m}}{10\Gamma_{3m} + 10} + \frac{\bar{S}_{14m}V_{4m}\Gamma_{4m}}{10\Gamma_{4m} + 10} + \begin{pmatrix} \bar{S}_{11m} & \bar{S}_{12m} \end{pmatrix} \begin{pmatrix} \bar{S}_{31m} & \bar{S}_{32m} \\ \bar{S}_{41m} & \bar{S}_{42m} \end{pmatrix}^{-1} \begin{pmatrix} \frac{V_{3m} - V_{3m}\bar{S}_{33m}\Gamma_{3m}}{10\Gamma_{3m} + 10} - \frac{V_{4m}\bar{S}_{34m}\Gamma_{4m}}{10\Gamma_{4m} + 10} \\ \frac{V_{4m} - V_{4m}\bar{S}_{44m}\Gamma_{4m}}{10\Gamma_{4m} + 10} - \frac{V_{3m}\bar{S}_{43m}\Gamma_{3m}}{10\Gamma_{3m} + 10} \end{pmatrix}. \quad (4.33.4)$$

4.4.3 HMD system calibration

The results above rely on the accuracy of the S-parameters and reflection coefficients of the couplers, accessories and oscilloscope ports, as well as the amplitude and timing accuracy of the voltage wave measurement. Therefore, the HMD system has to be calibrated at all the frequencies of interest before synthesizing and measuring the transistor waveform. During the calibration, all the instruments are synchronized with 10 MHz signal. The complete calibration procedure includes:

- (1) Calibrate a VNA with two-port vector calibration and source power calibration.
- (2) Measure the port input reflection coefficient Γ_{im} of each channel of the oscilloscope with the calibrated VNA, at each scale setting of the channels and each harmonic. Measure the S-parameters of the couplers, cables, bias-Tees and test fixture with the VNA, and calculate the S_{ijm} parameters.
- (3) Calculate the ratio between the real signal amplitude and the nominal signal amplitude measured by the oscilloscope. To this end, firstly use the oscilloscope to get the nominal amplitude of the power-calibrated VNA output signal. Then Γ_{im} is used to correct the VNA output power to get the real amplitude on the oscilloscope ports. The ratio at each scale setting of a channel and at each harmonic is tabularized for correcting the measured signal.
- (4) The phase of the signal measured by the oscilloscope changes when different scales of the oscilloscope channels are set. The phase vs. scale table has to be built for each harmonic to correct the measured signal.
- (5) Measure the phase shift between each two of the oscilloscope channels at different harmonics and different scales. This is achieved by replacing the transistor under test with

characterized open or short standards. With equation (4.32), the following function can be derived:

$$\begin{pmatrix} -\Gamma_{1m} S_{11m} b_{1m} + b_{1m} \\ -\Gamma_{1m} S_{21m} b_{1m} \\ -\Gamma_{1m} S_{31m} b_{1m} \end{pmatrix} = \begin{pmatrix} \Gamma_{2m} S_{12m} b_{2m} & \Gamma_{Lm} S_{13m} & S_{14m} \\ \Gamma_{2m} S_{22m} b_{2m} - b_{2m} & \Gamma_{Lm} S_{23m} & S_{24m} \\ \Gamma_{2m} S_{32m} b_{2m} & \Gamma_{Lm} S_{33m} - 1 & S_{34m} \end{pmatrix} \begin{pmatrix} \delta_{21m} \\ b_{3m} \delta_{31m} \\ a_{4m} \delta_{41m} \end{pmatrix} \quad (4.34)$$

In this function, a_{im} and b_{im} are nominal waves measured by the oscilloscope, and Γ_{Lm} is the reflection coefficient of the open or short standard, all at the m^{th} harmonic. $a_{im}\delta_{im}$ and $b_{im}\delta_{im}$ are the real waves on the oscilloscope ports, and $\delta_{ijm} = \delta_{im}/\delta_{jm} \cdot \delta_{21m}$ can be solved from this function, and the phase shift between channels 1 and 2 can be obtained by taking its angle. Similarly, δ_{43m} can be obtained with the same setup, whereas δ_{31m} and δ_{42m} can be obtained by switching the cable connections on channels 2 and 3 of the oscilloscope.

4.4.4 Synthesis and screening of transistor waveform towards a feasible SIHO design

For each test, the stimulations from the AWG, the waves at the input and output of the transistor, the voltage and current of the gate and drain are recorded, analyzed and screened, so that the AWG can adjust its output to optimize the synthesized waves of the transistor to guarantee the start-up of the SIHO, and for better output power, efficiency, noise and other specifications. Such an optimization procedure will also generate the design guidelines and key parameters of the matching circuit.

The criteria for screening the synthesized waves and the methodology of designing an SIHO can be derived using a linear analysis with the schematic shown in Fig. 4.14. The loop of the SIHO includes an output matched diplexer, a transistor, and its input matching block, and the symbols of their scattering matrices are marked beside them respectively. A typical gain block as shown in Fig. 4.1 (a) cannot be explicitly found in Fig. 4.14 because the matching circuits of the transistor are repositioned for simplification. Since the diplexer presents a pass-band at the fundamental frequency between its port P2 and P3, any matching circuit at the output of the transistor taking effect at that frequency can be moved to the input side. The same can be assumed for the 3rd harmonic frequency because the diplexer is based on an open resonator, which has parasitic resonances around odd harmonics. The transistor output matching at the 2nd harmonic frequency is

placed at the output of the SIHO without loss of generality because of the pass-band between port P1 and P2. Due to the isolating characteristic of the diplexer, the matchings at the fundamental and the 2nd harmonic frequencies, which are the most critical ones for the SIHO, can be designed individually. This feature provides significant convenience for design and tuning. It should be noted that such a design strategy assumes that the diplexer has low-loss and is sufficiently matched to 50 Ω at each of the ports and respective pass-bands. If the matching is poor, a delay line between the output of the transistor and P2 of the diplexer may be used to extend the feasible domain of design. A virtual coupler is inserted between the input matching and the transistor only for evaluating the closed-loop gain at the start-up of the SIHO. Its 4 \times 4 scattering matrix S_{vc} has $S_{vc,12m} = S_{vc,23m} = S_{vc,41m} = 1$ (for $m=1$ to 3) and $S_{vc,21m} = 1$ (for $m=2$ to 3), whereas the rest of its elements are zeros [112].

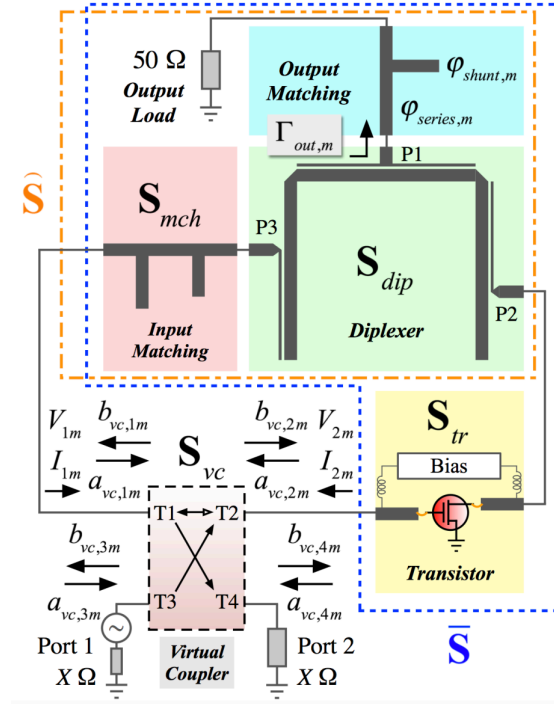


Figure 4.14: Schematic of SIHO for linear analysis and design.

With a specific set of waves (a_{3m}, b_{3m}) and $(\bar{a}_{1m}, \bar{b}_{1m})$ of a test at the input and output of the transistor given by equation (4.33), and the dc power consumed by the transistor, some preliminary judgement can be pronounced: 1) the gate and the drain must have a net input power and a net output power respectively at the fundamental frequency, which is expressed as $|b_{31}|^2 - |a_{31}|^2 > 0$ and $|\bar{a}_{11}|^2 - |\bar{b}_{11}|^2 > 0$; 2) there should be a net output power from the drain at the 2nd harmonic frequency,

so $|\bar{a}_{12}|^2 - |\bar{b}_{12}|^2 > 0$; 3) as the only generator in an autonomous circuit, the transistor should have a net power output at each harmonic, that is $|\bar{a}_{1m}|^2 + |a_{3m}|^2 - |\bar{b}_{1m}|^2 - |b_{3m}|^2 > 0$ for any $m=1$ to 3; 4) the total AC output power should be less than the total dc input power: $\sum_{m=1}^3 [|\bar{a}_{1m}|^2 + |a_{3m}|^2 - |\bar{b}_{1m}|^2 - |b_{3m}|^2] < P_{dc}$.

If all these conditions are satisfied, the output matching is designed firstly, although the feasibility of the waves for a standalone SIHO needs a further evaluation. At the 2nd harmonic frequency, P3 of the diplexer is significantly isolated from the other two ports, between which an independent subnetwork of \mathbf{S}_{dip} can be defined by terminating P3 with a 50Ω load and noted as $\mathbf{S}_{dip12} = [S_{dip,ijm}]$, ($i, j=1$ to 2 and $m=2$). Therefore, the output matching block can be designed without any knowledge of the input matching block at this frequency. To match the measured waves, the output reflection coefficient at P1 and the 2nd harmonic frequency has to be:

$$\Gamma_{out,2} = \frac{\bar{b}_{12} - \bar{a}_{12} S_{dip,222}}{S_{dip,112} (\bar{b}_{12} - \bar{a}_{12} S_{dip,222}) + \bar{a}_{12} S_{dip,122} S_{dip,212}}, \quad (4.35)$$

whose modulus must be less 1 for passivity. Since the output matching only matters for the 2nd harmonic frequency, a single open stub matching circuit with 50Ω lines is selected for simplicity, as shown in Fig. 4.14. With $\Gamma_{out,2}$, the initial guess of the electric length of the shunt section and the series section at the 2nd harmonic frequency can be obtained, by assuming they are lossless:

$$\varphi_{shunt,2} = \text{atan} \left(2|\Gamma_{out,2}| / \sqrt{1 - |\Gamma_{out,2}|^2} \right), \quad (4.36.1)$$

$$\varphi_{series,2} = \text{atan} \left[\text{Re} \left(\frac{Z_{out,2} - 50 + jZ_{out,2} \tan \varphi_{shunt,2}}{50j - jZ_{out,2} - 50 \tan \varphi_{shunt,2}} \right) \right], \quad (4.36.2)$$

in which $Z_{out,2} = 50(1 + \Gamma_{out,2}) / (1 - \Gamma_{out,2})$. To get the accurate physical length L_{shunt} and L_{series} of the shunt and series sections, the frequency-dependent propagation constant γ_m of a 50Ω line has to be extracted with multilayer method [105, 113]. Then L_{shunt} and L_{series} can be obtained by the quasi-newton optimization method, with the initial values of $\varphi_{shunt,2} / \text{Im}(\gamma_2)$ and $\varphi_{series,2} / \text{Im}(\gamma_2)$, respectively.

Secondly, with the designed output matching network, the scattering matrix of the output matched diplexer between P3 and P2 can be calculated, which is noted as $\mathbf{S}_{dip32} = [S_{dip32,ijm}]$, ($i, j=1$ to 2 and

$m=1$ to 3). On the other hand, the passive section of the loop, i.e. the cascade of the input matching and the diplexer, whose scattering matrix is noted as $\hat{\mathbf{S}} = [\hat{S}_{ijm}]$, ($i, j=1$ to 2 and $m=1$ to 3), is related to the waves of the transistor by:

$$\begin{pmatrix} b_{3m} \\ \bar{b}_{1m} \end{pmatrix} = \begin{pmatrix} \hat{S}_{11m} & \hat{S}_{12m} \\ \hat{S}_{21m} & \hat{S}_{22m} \end{pmatrix} \begin{pmatrix} a_{3m} \\ \bar{a}_{1m} \end{pmatrix}. \quad (4.37)$$

Since $\hat{S}_{12m} = \hat{S}_{21m}$, $\hat{\mathbf{S}}$ can be represented as:

$$\hat{\mathbf{S}} = \frac{1}{\bar{a}_{1m}} \begin{pmatrix} \bar{a}_{1m} \hat{S}_{11m} & b_{3m} - \hat{S}_{11m} a_{3m} \\ b_{3m} - \hat{S}_{11m} a_{3m} & \bar{b}_{1m} - (b_{3m} - \hat{S}_{11m} a_{3m}) a_{3m} / \bar{a}_{1m} \end{pmatrix}. \quad (4.38)$$

And with a known \mathbf{S}_{dip32} , \mathbf{S}_{mch} can be derived using a transmission matrix theory. At each harmonic, there must be at least one value of \hat{S}_{11m} in the Smith chart to ensure both \mathbf{S}_{mch} and $\hat{\mathbf{S}}$ are passive and reciprocal.

Thirdly, the loop-gain at the fundamental frequency G_1 needs to be examined. With reference to the virtual coupler ports, G_1 is represented as the ratio between the output wave from T4 and the input wave generated by a test source into T3:

$$G_1 = \frac{b_{vc,41}}{a_{vc,31}} = \frac{V_{11} + X \cdot I_{11}}{V_{21} - X \cdot I_{21}}, \quad (4.39)$$

in which V_{i1} , I_{i1} ($i=1$ to 2) are the terminal voltage and current at T1 and T2 of the coupler, and X is the reference impedance of \mathbf{S}_{vc} , as well as the waves $a_{vc,im}$ and $b_{vc,im}$ ($i=1$ to 4 and $m=1$ to 3) of the coupler. On the other hand, the definition of $\bar{\mathbf{S}} = [\bar{S}_{ijm}]$, which is $\hat{\mathbf{S}}$ cascaded with the scattering matrix of the reversed transistor, suggests that:

$$V_{11} + 50 \cdot I_{11} = \bar{S}_{111} (V_{11} - 50 \cdot I_{11}) + \bar{S}_{121} (V_{21} - 50 \cdot I_{21}), \quad (4.40.1)$$

$$V_{21} + 50 \cdot I_{21} = \bar{S}_{211} (V_{11} - 50 \cdot I_{11}) + \bar{S}_{221} (V_{21} - 50 \cdot I_{21}). \quad (4.40.2)$$

And since $b_{vc,11} = a_{vc,21}$,

$$V_{11} - X \cdot I_{11} = V_{21} + X \cdot I_{21}. \quad (4.40.3)$$

$$G_1 = \frac{2500(1+\bar{S}_{111}-\bar{S}_{121}\bar{S}_{211}+\bar{S}_{221}+\bar{S}_{111}\bar{S}_{221})-100[1+\bar{S}_{121}(\bar{S}_{211}-2)-\bar{S}_{111}\bar{S}_{221}]}{2500(1+\bar{S}_{111}-\bar{S}_{121}\bar{S}_{211}+\bar{S}_{221}+\bar{S}_{111}\bar{S}_{221})+100[1+\bar{S}_{211}(\bar{S}_{121}-2)-\bar{S}_{111}\bar{S}_{221}]} X - \frac{(-1+\bar{S}_{111}+\bar{S}_{121}\bar{S}_{211}+\bar{S}_{221}-\bar{S}_{111}\bar{S}_{221})X^2}{(-1+\bar{S}_{111}+\bar{S}_{121}\bar{S}_{211}+\bar{S}_{221}-\bar{S}_{111}\bar{S}_{221})X^2} \quad (4.41)$$

With equations (4.39) and (4.40), the loop-gain can be derived and expressed by equation (4.41). The necessary condition on which oscillation can start is that G_1 has to be a real value and larger than 1, for a certain real impedance X . Moreover, the loop-gain at the 2nd and 3rd harmonic frequencies should also be checked with a similar equation to ensure no parasitic harmonic oscillation exists.

Fourthly, every test of the transistor that can pass these bars is related to three Smith chart regions, each of which filled with screened \hat{S}_{1m} ($m=1, 2$ or 3). From the region of \hat{S}_{112} , the maximum available output power and efficiency for the test can be found. First, for each \hat{S}_{112} in that region, the scattering matrix of the input matching block can be determined. Second is to design the output single open stub matching circuit, whose scattering matrix can be derived from its transmission matrix having the form of:

$$\begin{pmatrix} \cosh(\gamma_2 L_{series}) + \sinh(\gamma_2 L_{series}) \tanh(\gamma_2 L_{shunt}) & 50 \sinh(\gamma_2 L_{series}) \\ \frac{\sinh(\gamma_2 L_{series}) + \cosh(\gamma_2 L_{series}) \tanh(\gamma_2 L_{shunt})}{50} & \cosh(\gamma_2 L_{series}) \end{pmatrix}$$

Then, the scattering matrix $\hat{S} = [\hat{S}_{ij}]$ ($i, j=1$ to 3) of the three-port network formed by cascading the input and output matching blocks and the diplexer can be calculated. Therefore, the total power delivered to the output load is $P_L = |\bar{a}_{12}\hat{S}_{12} + a_{32}\hat{S}_{13}|^2$. With the dc voltage and current of the test, the total efficiency E_{tot} can be obtained.

4.4.5 Experimental optimization of transistor waveform

To perform the second function of an HMD system, namely the experimental optimizations of a design towards maximum output power or efficiency, the following function is defined first:

$$J = f(V_g, V_d, A_{1,1}, \theta_{1,1}, A_{1,2}, \theta_{1,2}, \dots, A_{2,1}, \theta_{2,1}, A_{2,2}, \theta_{2,2}, \dots), \quad (4.42)$$

in the initial steps, and the 3rd harmonic can be included after local optimum is found. The first-order partial derivative of function f is approximated by its partial difference quotient. If tuning is performed in advance to get a setting of dc bias and AWG waveforms such that an acceptable performance is reached, the design can be evolved to a local optimal one with the conjugate

gradient method, which is used in this work. Otherwise, if there is no workable initial design or global optimum in a large feasible region is desired, a more sophisticated method such as the particle swarm optimization (PSO) method [114] should be considered. The main optimization procedure in this work is as follows:

- (1) Assuming the variables of function (4.42) at the k^{th} step is $\mathbf{x}^{(k)} = [V_g^{(k)}, V_d^{(k)}, A_{1,1}^{(k)}, \theta_{1,1}^{(k)}, A_{1,2}^{(k)}, \theta_{1,2}^{(k)}, \dots, A_{2,1}^{(k)}, \theta_{2,1}^{(k)}, A_{2,2}^{(k)}, \theta_{2,2}^{(k)}, \dots]$, and $\mathbf{x}^{(0)}$ is the initial value.
- (2) The direction-of-search of the first step is defined by the gradient of function f at $\mathbf{x}^{(0)}$: $\mathbf{d}^{(0)} = \nabla f(\mathbf{x}^{(0)})$. So $\mathbf{x}^{(1)} = \mathbf{x}^{(0)} + \lambda^{(0)} \mathbf{d}^{(0)}$, in which $\lambda^{(0)}$ is determined by a one-dimensional search that maximize $f(\mathbf{x}^{(1)})$.
- (3) The directions-of-search for the following steps are the conjugate directions: $\mathbf{d}^{(k+1)} = \nabla f(\mathbf{x}^{(k+1)}) + \beta^{(k)} \mathbf{d}^{(k)}$, in which $\beta^{(k)} = \frac{|\nabla f(\mathbf{x}^{(k+1)})|^2}{|\nabla f(\mathbf{x}^{(k)})|^2}$. So $\mathbf{x}^{(k+2)} = \mathbf{x}^{(k+1)} + \lambda^{(k+1)} \mathbf{d}^{(k+1)}$, the step $\lambda^{(k+1)}$ is obtained by one-dimensional search. The criteria discussed in section 4.4.4 need to be considered for each step. As $|\nabla f(\mathbf{x}^{(k+1)})|$ is smaller than a pre-defined threshold, or the criteria cannot be satisfied with a nonzero $\lambda^{(k+1)}$, the optimization can be terminated.

The initial value $\mathbf{x}^{(0)}$ whose largest harmonic index is limited to 2 can be found with the following principles. Different from conventional power oscillators that are designed based on the PA configurations [105, 115, 116], the gain block in an SIHO is usually subject to a deeper saturation and exhibits close to 0 dB of gain at the fundamental frequency. It is because at this frequency, the passive part of the SIHO conserves the energy, with only a minor portion consumed by 1 to 2 dB metal, dielectric and radiation losses. Therefore, the AWG channel 1 output power at the fundamental frequency should be tuned such that $|\bar{a}_{11}|^2 + |a_{31}|^2 - |\bar{b}_{11}|^2 - |b_{31}|^2$ is approximately equal to the passive loss.

An SIHO can be regarded as a frequency doubler whose fundamental driving signal is self-sufficient. Therefore, to enhance the output power and efficiency, a 2nd harmonic signal reflector should be established at the input of the transistor [117-121]. As such, the AWG channel 1 output power and phase at the 2nd harmonic frequency should be adjusted to obtain a total reflection looking outwards the gate and a constructive interference at the drain of the transistor.

Moreover, the transistor is designed to operate in the class E mode from which the best fundamental tone to 2nd harmonic conversion efficiency can be expected [122-124]. To this end, the initial gate bias is set near the pinch-off voltage. The drain of the transistor is biased at about 1/3 of its peak voltage [125], which is limited by the saturated output power and the maximum allowed input power.

4.4.6 Closed-form design of SIHO input matching network

The input matching as shown in Fig. 4.14 for an optimized SIHO design is a harmonic matching network. In principle, it has to be designed to achieve a designated full two-port performance characterized by S_{mch} for each harmonic. Usually in other types of microwave circuit (such as PA) design, only certain reflection coefficient at each harmonic needs to be synthesized [125]. To develop a methodology with closed-form expressions such that the design can be automated, two assumptions have to be made. First, the network at each harmonic is lossless. If the calculated S_{mch} in certain bias and waveform setup turns out to be very lossy, it implies that the selected SIHO can be significantly improved by re-running the optimization procedure with a different initial value. Second, the amplitude of the reflection coefficient looking into P3 of the diplexer at the 2nd harmonic frequency is close to 1. This can be fulfilled as long as the diplexer based on the proposed topology is properly designed. Considering both assumptions, the amplitude of the reflection coefficient seen by the transistor's gate at the 2nd harmonic frequency should be close to 1, which fulfills the required signal reflector.

The selected matching network topology is shown in Fig. 4.15. It comprises microstrip open stubs and delay lines, grouped in a T-network M1, a PI-network M3 and a delay section M2. The line dispersion is ignored so the characteristic impedance Z_i ($i=1$ to 7) is constant for all frequencies. θ_i is the electrical length at the 3rd harmonic frequency. M2, M3 and M1 together present S_{mch} for the fundamental and 3rd harmonic frequencies, and S_{11} of S_{mch} at the 2nd harmonic frequency is presented at the indicated position in the figure and denoted as Γ_2 . It is unnecessary to fully synthesize S_{mch} at the 2nd harmonic frequency because the loop is opened by the isolation property of the diplexer at this frequency, where the transmission of the matching network is not critical for the operation. Any two-port lossless reciprocal network at one frequency has 3 degrees of freedom [68], and a reflection coefficient with unit amplitude has 1, therefore the totally 14 degrees of

freedom of the matching network topology is more than enough, and the redundant ones provide convenience and flexibility to the design.

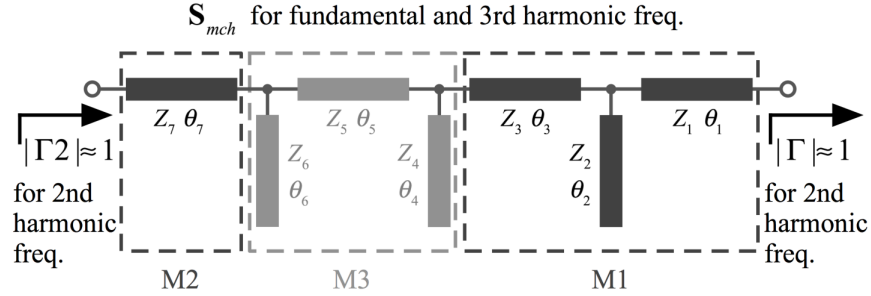


Figure 4.15: Schematic of input matching network design.

In M1, θ_i ($i=1$ to 3) takes 2π or 4π such that this network is transparent for the 3rd harmonic. In M3, θ_6 takes $3\pi/4$ or $9\pi/4$, such that Γ_2 is only determined by M2, in which Z_7 is arbitrarily selected as 50Ω . Therefore, θ_7 can be determined as: $\theta_7 = 1.5 \arctan[(1 + \Gamma_2)/j(1 + \Gamma_2)]$.

The transmission matrix of any two-port lossless reciprocal network has real-valued elements A and D and imaginary-valued elements B and C , so the following two transmission matrices for lossless networks are prepared first:

$$\mathbf{T}_1 = \begin{pmatrix} \bar{A}_1 & j\bar{B}_1 \\ j\bar{C}_1 & \bar{D}_1 \end{pmatrix} \doteq \frac{1}{\text{Re}(A_1)\text{Re}(D_1) + \text{Im}(B_1)\text{Im}(C_1)} \begin{pmatrix} \text{Re}(A_1) & j\text{Im}(B_1) \\ j\text{Im}(C_1) & \text{Re}(D_1) \end{pmatrix}, \quad (4.43.1)$$

$$\mathbf{T}_3 = \begin{pmatrix} \bar{A}_3 & j\bar{B}_3 \\ j\bar{C}_3 & \bar{D}_3 \end{pmatrix} \doteq \frac{1}{\text{Re}(A_3)\text{Re}(D_3) + \text{Im}(B_3)\text{Im}(C_3)} \begin{pmatrix} \text{Re}(A_3) & j\text{Im}(B_3) \\ j\text{Im}(C_3) & \text{Re}(D_3) \end{pmatrix}. \quad (4.43.2)$$

Therefore, \mathbf{T}_i approximates $\begin{bmatrix} A_i & B_i \\ C_i & D_i \end{bmatrix}$, the transmission matrix of \mathbf{S}_{mch} for the fundamental tone ($i=1$) or the 3rd harmonic ($i=3$).

Defining the transmission matrix of M3 at the 3rd harmonic frequency as \mathbf{T}_{M3} , it can be found that:

$$\mathbf{T}_{M3} = \begin{pmatrix} \cos\theta_5 - \frac{Z_5 \sin\theta_5 \tan\theta_4}{Z_4} & jZ_5 \sin\theta_5 \\ / & \cos\theta_5 - \frac{Z_5 \sin\theta_5 \tan\theta_6}{Z_6} \end{pmatrix} = \begin{pmatrix} \cos\theta_7 & 50j \sin\theta_7 \\ 0.02j \sin\theta_7 & \cos\theta_7 \end{pmatrix}^{-1} \mathbf{T}_3 \quad (4.44)$$

The lower left element of \mathbf{T}_{M3} is ignored because for any reciprocal network, the element C in its transmission matrix can be expressed as $(AD-1)/B$. Therefore,

$$Z_5 \sin\theta_5 = \bar{B}_3 \cos\theta_7 - 50\bar{D}_3 \sin\theta_7, \quad (4.45.1)$$

$$\cos\theta_5 - \sin\theta_5 \tan\theta_4 Z_5/Z_4 = \bar{A}_3 \cos\theta_7 + 50\bar{C}_3 \sin\theta_7, \quad (4.45.2)$$

$$\cos\theta_5 - \sin\theta_5 \tan\theta_6 Z_5/Z_6 = 0.02\bar{B}_3 \sin\theta_7 + \bar{D}_3 \cos\theta_7. \quad (4.45.3)$$

In equation (4.45.1), if $\bar{B}_3 \cos\theta_7 - 50\bar{D}_3 \sin\theta_7 = 0$, simply extend θ_7 by 1.5π . So that $Z_5 = (\bar{B}_3 \cos\theta_7 - 50\bar{D}_3 \sin\theta_7)/\sin\theta_5$. θ_5 can be arbitrarily selected only to ensure Z_5 is positive. Then, if θ_4 and θ_6 are also selected with care, Z_4 and Z_6 can be solved from equations (4.45.2) and (4.45.3), respectively.

Similarly, defining the transmission matrix of M1 at the fundamental frequency as \mathbf{T}_{M1} , it can be found that:

$$\mathbf{T}_{M1} = \begin{pmatrix} \cos\frac{\theta_5}{3} - \frac{Z_5 \sin\frac{\theta_5}{3} \tan\frac{\theta_6}{3}}{Z_6} & -jZ_5 \sin\frac{\theta_5}{3} \\ / & \cos\frac{\theta_5}{3} - \frac{Z_5 \sin\frac{\theta_5}{3} \tan\frac{\theta_4}{3}}{Z_4} \end{pmatrix} \cdot \begin{pmatrix} \cos\frac{\theta_7}{3} & -50j \sin\frac{\theta_7}{3} \\ -\frac{j}{50} \sin\frac{\theta_7}{3} & \cos\frac{\theta_7}{3} \end{pmatrix} \mathbf{T}_1 = \begin{pmatrix} \hat{A}_1 & j\hat{B}_1 \\ j\hat{C}_1 & \hat{D}_1 \end{pmatrix}. \quad (4.46)$$

Expanding \mathbf{T}_{M1} , the following functions can be obtained:

$$\hat{A}_1 = \frac{1}{4} - \frac{3\Lambda_3}{4\Lambda_1} + \frac{3\Lambda_3}{8\Lambda_2}, \quad (4.47.1)$$

$$\hat{B}_1 = -\frac{3\Lambda_3}{8} - \frac{3\Lambda_1}{8} - \frac{9\Lambda_1\Lambda_3}{16\Lambda_2}, \quad (4.47.2)$$

$$\hat{D}_1 = \frac{1}{4} - \frac{3\Lambda_1}{4\Lambda_3} + \frac{3\Lambda_1}{8\Lambda_2}, \quad (4.47.3)$$

in which $\Lambda_1 = Z_1 / \sin \frac{\theta_1}{3}$, $\Lambda_2 = Z_2 / \tan \frac{\theta_2}{3}$ and $\Lambda_3 = Z_3 / \sin \frac{\theta_3}{3}$. As the results:

$$\Lambda_1 = 2(\hat{D}_1 - 1) / 3\hat{C}_1, \quad (4.48.1)$$

$$\Lambda_2 = \frac{(\hat{A}_1 - 1)(\hat{D}_1 - 1)}{\hat{C}_1(4\hat{A}_1\hat{D}_1 - \hat{A}_1 - \hat{D}_1 - 2)}, \quad (4.48.2)$$

$$\Lambda_3 = 2(\hat{A}_1 - 1) / 3\hat{C}_1. \quad (4.48.3)$$

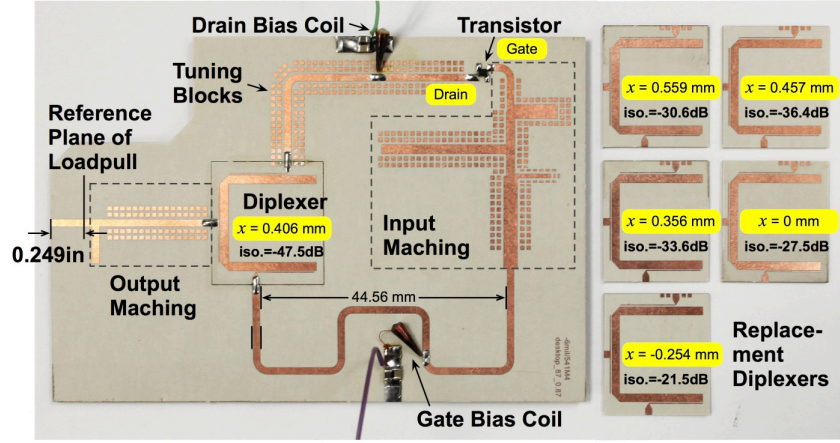
Then select θ_i ($i=1$ to 3) as 2π or 4π to ensure positive Z_i ($i=1$ to 3) can be obtained.

From the characteristic impedance and electrical length of the ideal microstrip lines, the real dimensions can be obtained and further optimized.

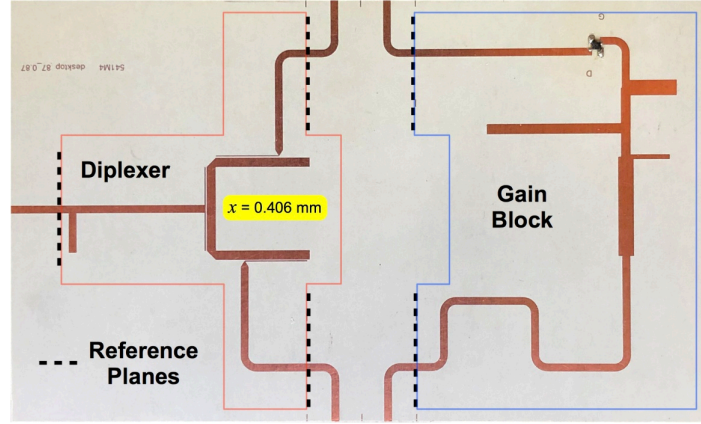
4.4.7 Summary of experimental design procedure

- (1) Design and characterize a diplexer at the targeted frequency f_0 and based on a selected topology.
- (2) Select a transistor as the active device according to the targeted frequency and the output power. The initial bias, input/output power, and AWG setup are estimated based on the transistor specification and operating class.
- (3) The HMD system set up and calibration are carried out following the steps in section 4.4.2 and 4.4.3.
- (4) The experimental optimization of the transistor waveform is carried out with the conjugate gradient method of section 4.4.5 or other methods. During the iteration steps, the waveform is measured with equation (4.33) and the screening is performed following the steps in section 4.4.4.
- (5) The matching network is designed to achieve the optimized waveform with equation (4.36) and the equations developed in section 4.4.6.

4.4.8 Design example, model validation and discussions



(a)



(b)

Figure 4.16: (a) The fabricated SIHO with replacement diplexers of different values of parameter x , and (b) the open-loop SIHO for equivalent circuit building and X-parameter extraction.

The designed and fabricated SIHO prototype is shown in Fig. 4.16 (a). Its open-loop version for circuit model building and X-parameter extraction is shown in Fig. 4.16 (b). The reference planes are defined by TRL calibration. The circuits are on the same substrate as what is used in section 4.4.1. Replacement diplexers with different values of parameter x so as to achieve different isolations at the 2nd harmonic frequency (values are marked aside) according to Fig. 4.12 are also fabricated. The test setup shown in Fig. 4.17 (a) is used to characterize the SIHO output power and efficiency. The used power meter and power sensor are ML2438A and MA2474A both from Anritsu. It can be seen that an output power of 16.62 dBm and a dc drain current of 47 mA with 3.48 V voltage are measured, resulting in an efficiency of 27.9%. Fig. 4.17 (b) and (c) are the setups

of load pulling and injection pulling measurement. The load impedance synthesized by the tuner is calibrated to the reference plane as indicated in Fig. 4.16 (a). About -5 dBm injection monotone is received by the SIHO through the coupler. Fig. 4.18 (a) and (b) are the spectrum and phase noise both measured by the setup in Fig. 4.17 (b), when $50\ \Omega$ load is set. The fundamental tone and the 3rd harmonic are about 28 dB and 55 dB lower than the 2nd harmonic, which is at 3.996 GHz. The phase noise of the 2nd harmonic at 1 MHz offset is -136.5 dBc/Hz. The measured and HMD-synthesized waveforms corresponding to the SIHO prototype at the drain of the transistor are shown in Fig. 4.19. The voltage waveform is measured by a calibrated high impedance probe connected to an oscilloscope. The dotted-line current waveform is obtained from voltage waveforms measured at several different points on the transmission line between the drain and the diplexer, provided that the propagation constant and the characteristic impedance of the line can be determined a priori. The synthesized waveform presents the features of a class E operation but contains a higher proportion of the 2nd harmonic. Fig. 4.20 illustrates the contour of the dc-RF efficiency with respect to the source and load reflection coefficients. Fig. 4.20 (a) proves the efficiency gain from the 2nd harmonic reflector at about 35° . Fig. 4.20 (b) implies that multiple local optimal solutions exist due to the involved multiple harmonics.

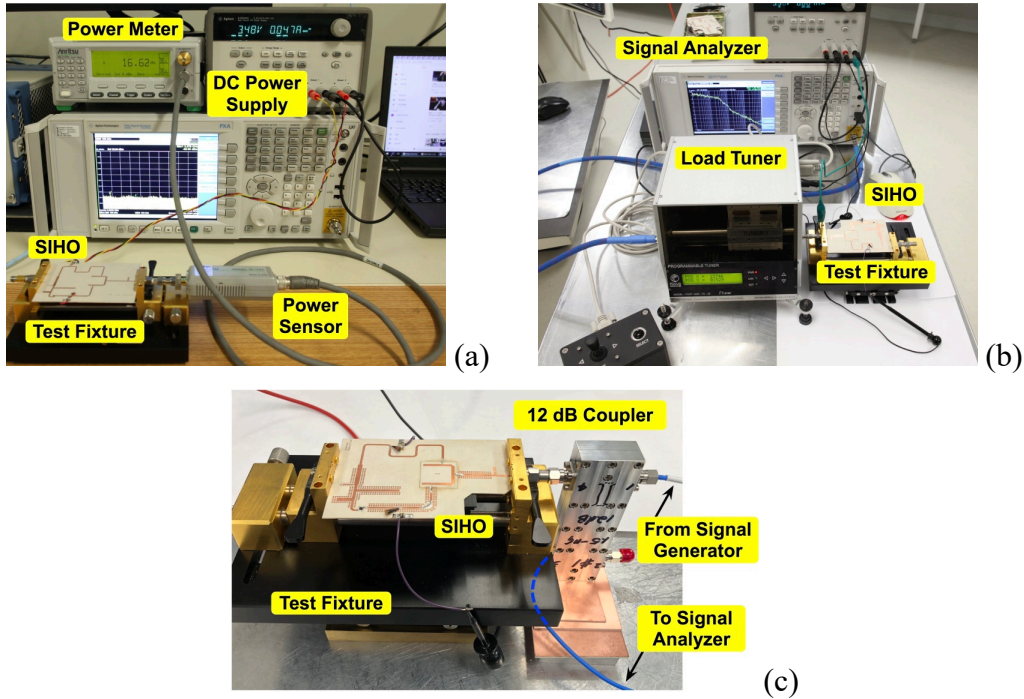


Figure 4.17: Test setups for (a) power and efficiency measurement, (b) load pulling measurement, and (c) injection pulling measurement.



Figure 4.18: Measured results with a 50 Ω load of (a) spectrum of the first three harmonics, and (b) phase noise of the 2nd harmonic output.

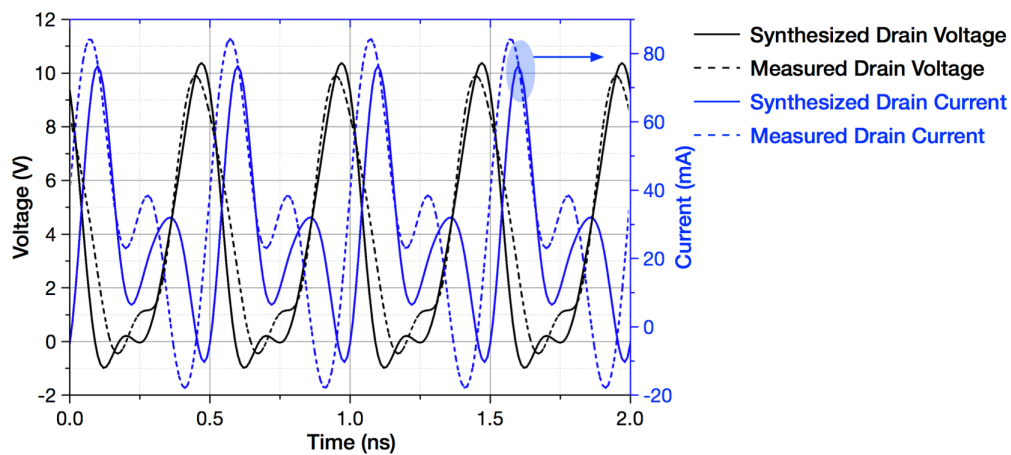


Figure 4.19: Transistor drain voltage and current waveforms synthesized by the experimental design procedure and obtained by measuring the SIHO prototype.

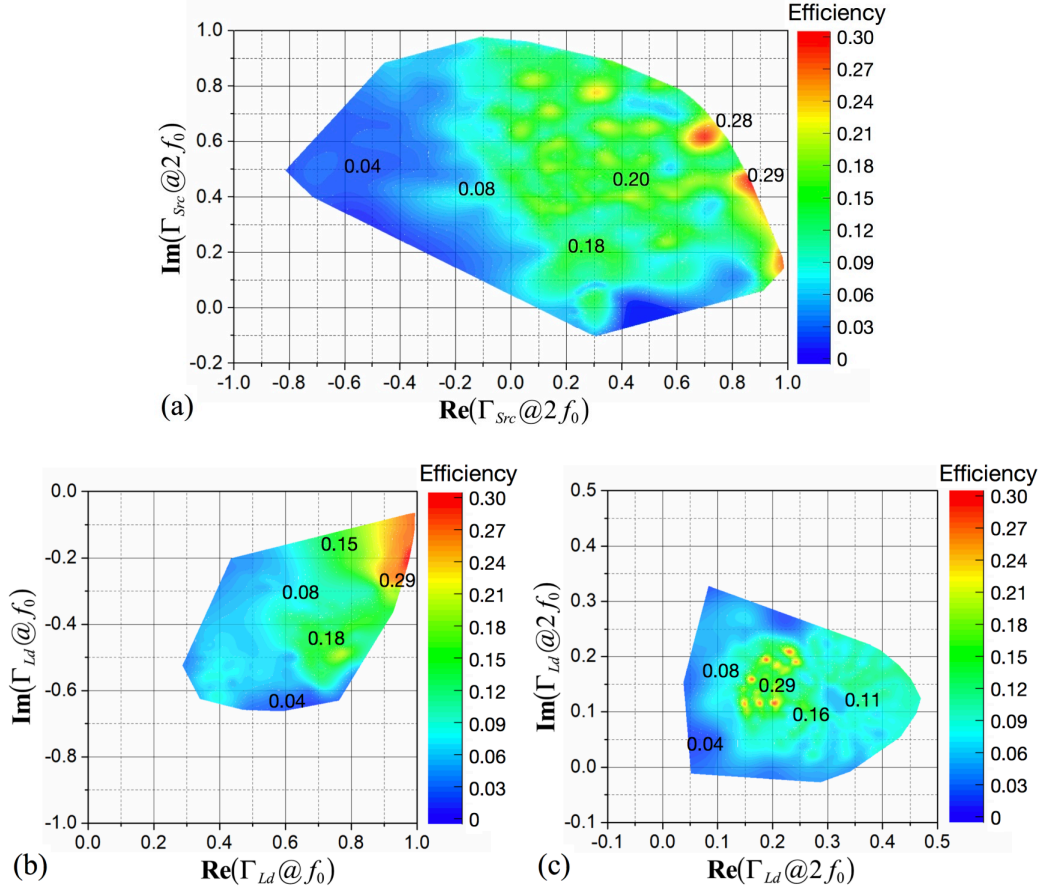


Figure 4.20: dc to 2nd harmonic efficiency from the experimental design with respect to (a) source reflection coefficients at the 2nd harmonic frequency, (b) load reflection coefficient at the fundamental frequency and (c) load reflection coefficient at the 2nd harmonic frequency.

Fig. 4.21 illustrates the SIHO output frequency and phase noise measurement results for each of the diplexers with respect to the load impedance distribution. The circles in the Γ_{Load} plane represent the SIHO load reflection coefficients where the measurements are performed. It can be found that as the isolation of the diplexers gets weaker, the ranges of the frequency and phase noise change become larger. Fig. 4.22 shows the injection pulling results of the SIHO with each of the diplexers. The x-axis is the real injection frequency and the y-axis is the output frequency variation normalized to the output frequency without an injection signal. The increasing portion of each curve represents that the SIHO is locked to the injection signal. It can also be seen that with a diplexer of stronger isolation, the locking range becomes smaller.

Figure 4.21: SIHO load pulling measurement results of the frequency shift and phase noise with duplexers of different x of (a) & (b) 0.406 mm, (c) & (d) 0.457 mm, (e) & (f) 0.356 mm, (g) & (h) 0.559 mm, (i) & (j) 0 mm and (k) & (l) -0.254 mm.

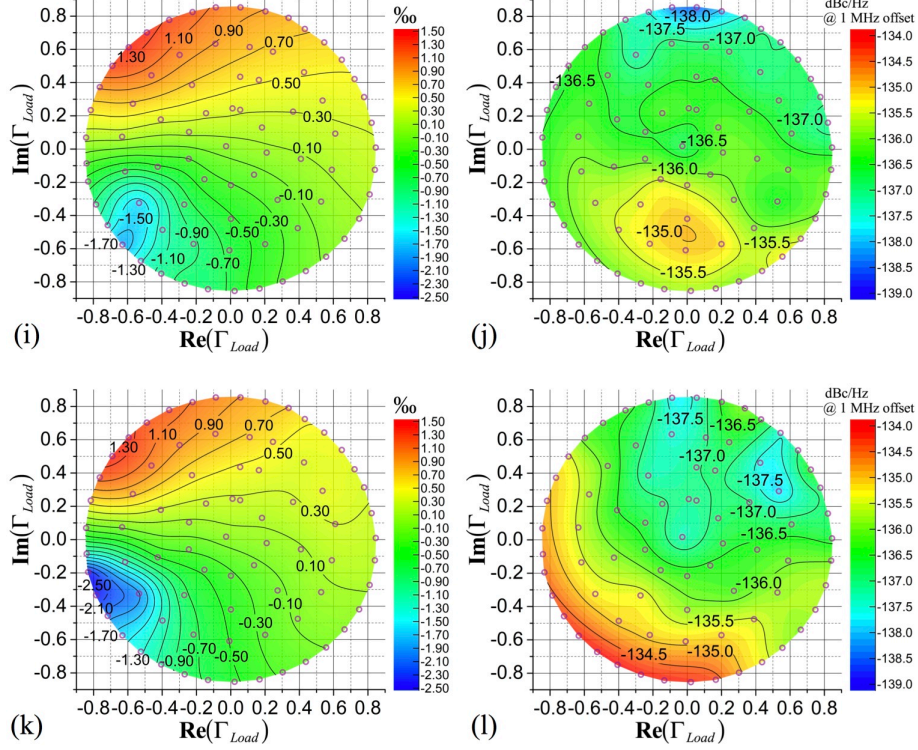
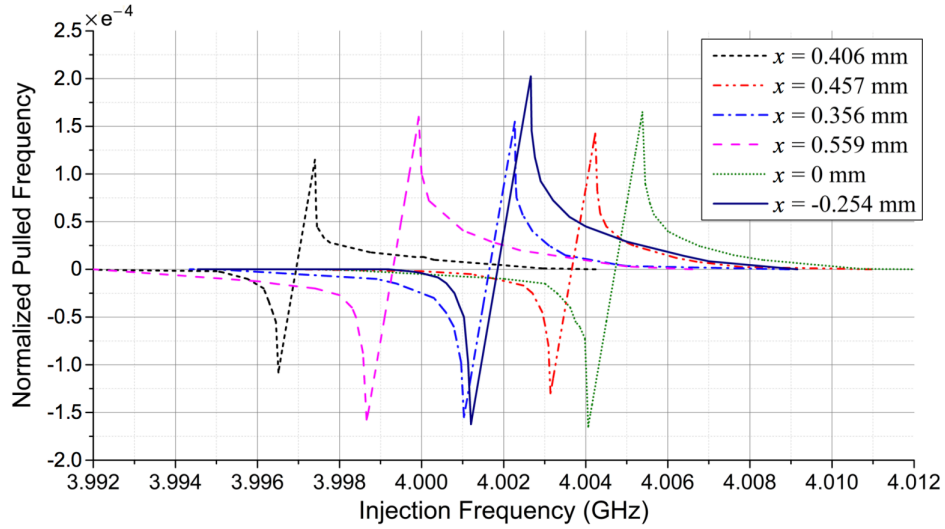


Figure 4.21 (cont.)

Figure 4.22: SIHO injection pulling measurement results with different value of x .

To further study and validate the SIHO model, the X-parameter of the gain block in Fig. 4.16 (b) is experimentally extracted with the setup in Fig. 4.23 (a). The setup has a high-power configuration with pre-amplifiers and its detailed schematic is shown in Fig. 4.23 (b). Measured exemplary S and T matrices with a fundamental driving level of 17 dBm at 1.998 GHz and the same bias condition as used by the SIHO prototype is listed in Table 4.2. With the measured X-parameters and the full-

wave simulated duplexers of different isolations, the SIHO load pulling frequency shift is simulated in Keysight ADS, for the same load impedance distribution used in the measurement. The results are shown in Fig. 4.24. Since the measured X-parameters do not include noise parameters, the phase noise is not simulated.

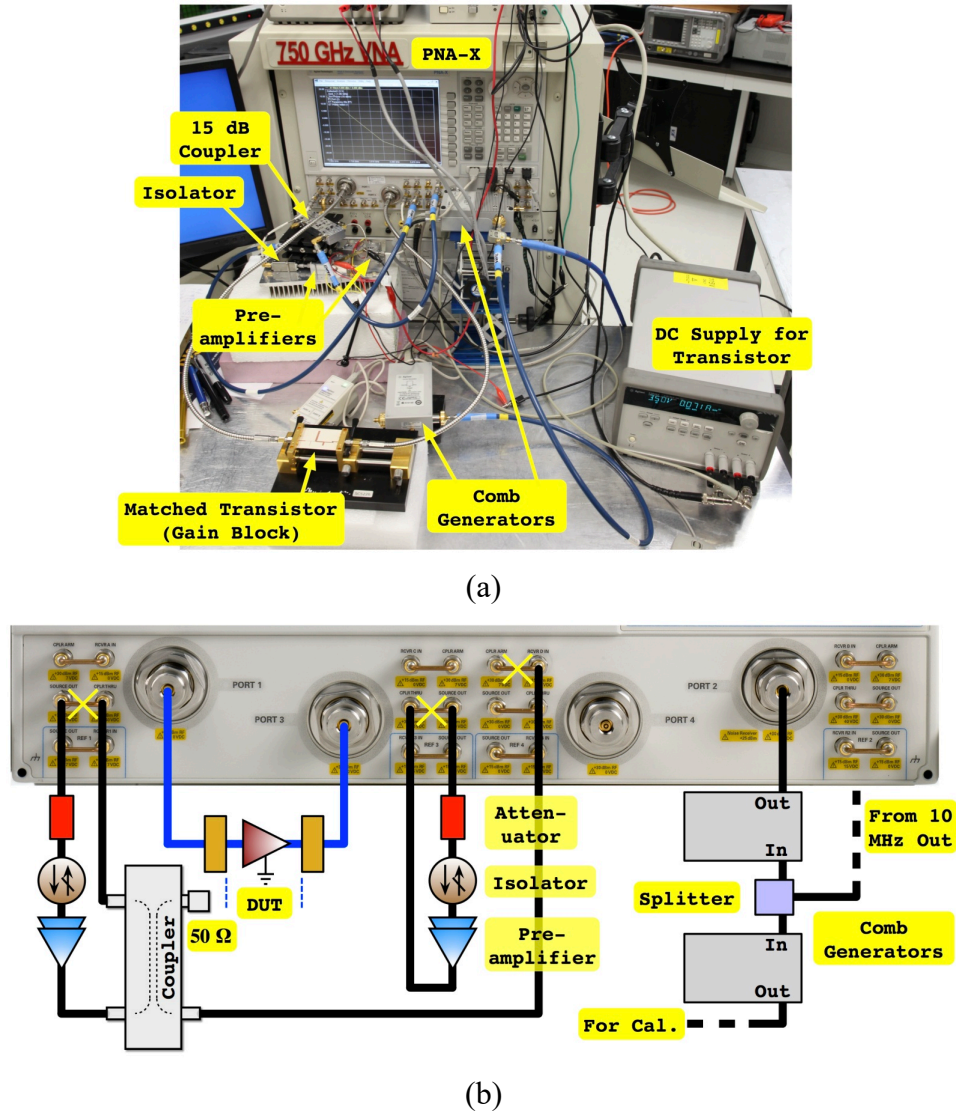


Figure 4.23: Gain block X-parameter measurement (a) photo of the setup and (b) schematic of the configuration.

Table 4.2: Exemplary X-Parameter S and T Matrices of the Gain Block

$\mathbf{X}^{(S)}$	0.22+0.44i	0.06+0.22i	-0.06-0.03i	1.41-0.71i	0.53-0.24i	0.01-0.01i
	-0.31-0.02i	0.07-0.40i	0.26-0.22i	0.15-0.20i	0.57-0.53i	-0.03-0.02i
	-0.09-0.05i	0.26+0.32i	-0.09+0.29i	-0.04+0.24i	0.01+0.04i	-0.01+0.01i
	0.01-0.02i	$2e^{-3}+0.01i$	$0.01-2e^{-3}i$	0.43+0.79i	$-0.03+4e^{-3}i$	$2e^{-3}-5e^{-4}i$
	0.01-0.01i	0.01-0.05i	0.01+0.02i	0.01-0.02i	-0.86-0.26i	$-3e^{-3}+8e^{-4}i$
	$7e^{-4}-4e^{-4}i$	$-2e^{-3}-8e^{-4}i$	$0.01-9e^{-4}i$	$3e^{-4}-4e^{-4}i$	$-0.01+2e^{-3}i$	0.83+0.09i
$\mathbf{X}^{(T)}$	0.15-0.08i	-0.03-0.04i	0.08-0.06i	0	-0.15-0.01i	$3e^{-3}+0.01i$
	0.01-0.07i	$-3e^{-3}-3e^{-3}i$	-0.01-0.01i	0	0.08-0.14i	$2e^{-3}+4e^{-3}i$
	-0.03+0.04i	0.03+0.03i	-0.01+0.04i	0	0.07-0.10i	-0.01+0.01i
	$-4e^{-3}-2e^{-3}i$	$4e^{-3}+0.01i$	$-3e^{-3}-9e^{-4}i$	0	$-2e^{-3}+2e^{-3}i$	$9e^{-5}+4e^{-4}i$
	$1e^{-3}-1e^{-3}i$	$-5e^{-3}-4e^{-3}i$	$2e^{-3}-2e^{-3}i$	0	$5e^{-3}+3e^{-3}i$	$-1e^{-5}-6e^{-5}i$
	$1e^{-4}-1e^{-4}i$	$-2e^{-4}-1e^{-4}i$	$-1e^{-5}-2e^{-4}i$	0	$7e^{-5}+6e^{-4}i$	$-4e^{-6}-6e^{-5}i$

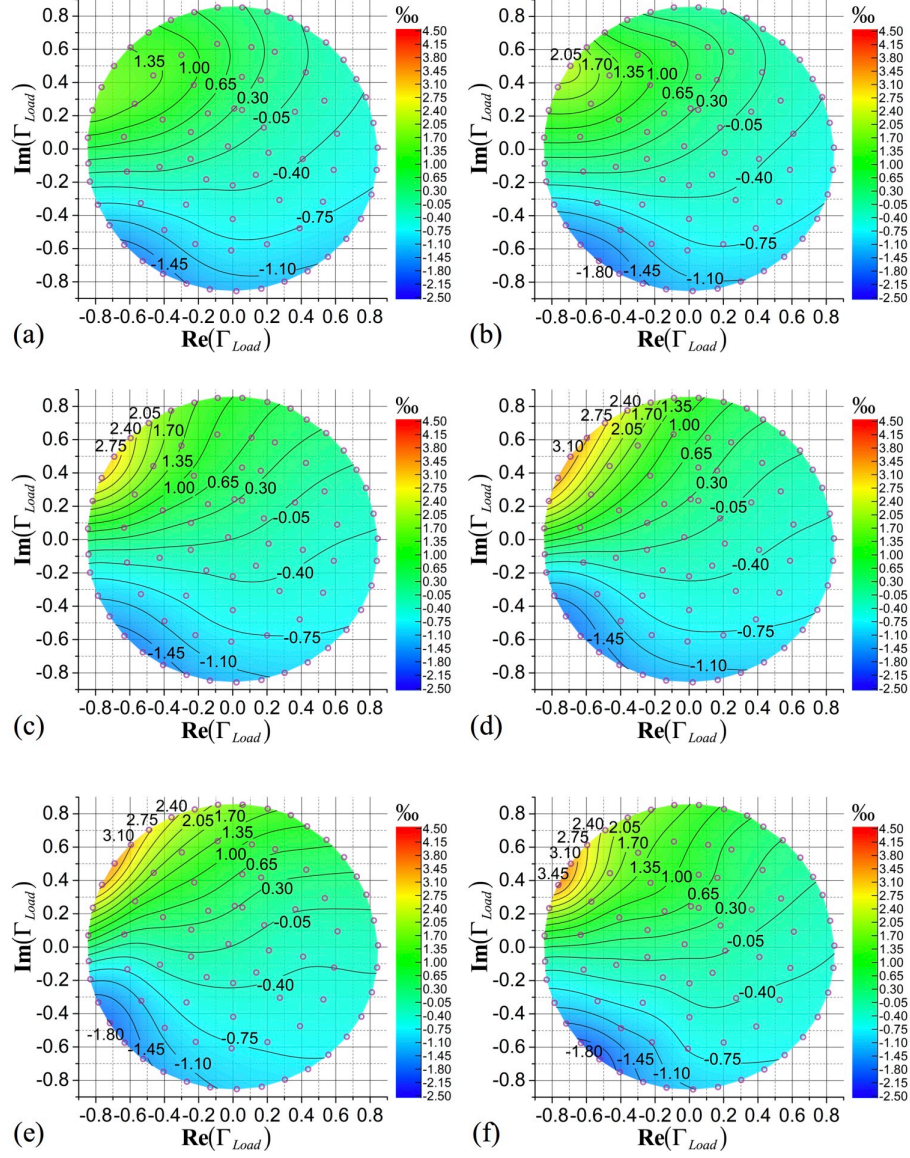


Figure 4.24: SIHO load pulling simulation results of frequency shift with duplexers of different isolations at $2f_0$ of (a) -46 dB, (b) -38 dB, (c) -35 dB, (d) -31 dB, (e) -28 dB, and (f) -22 dB.

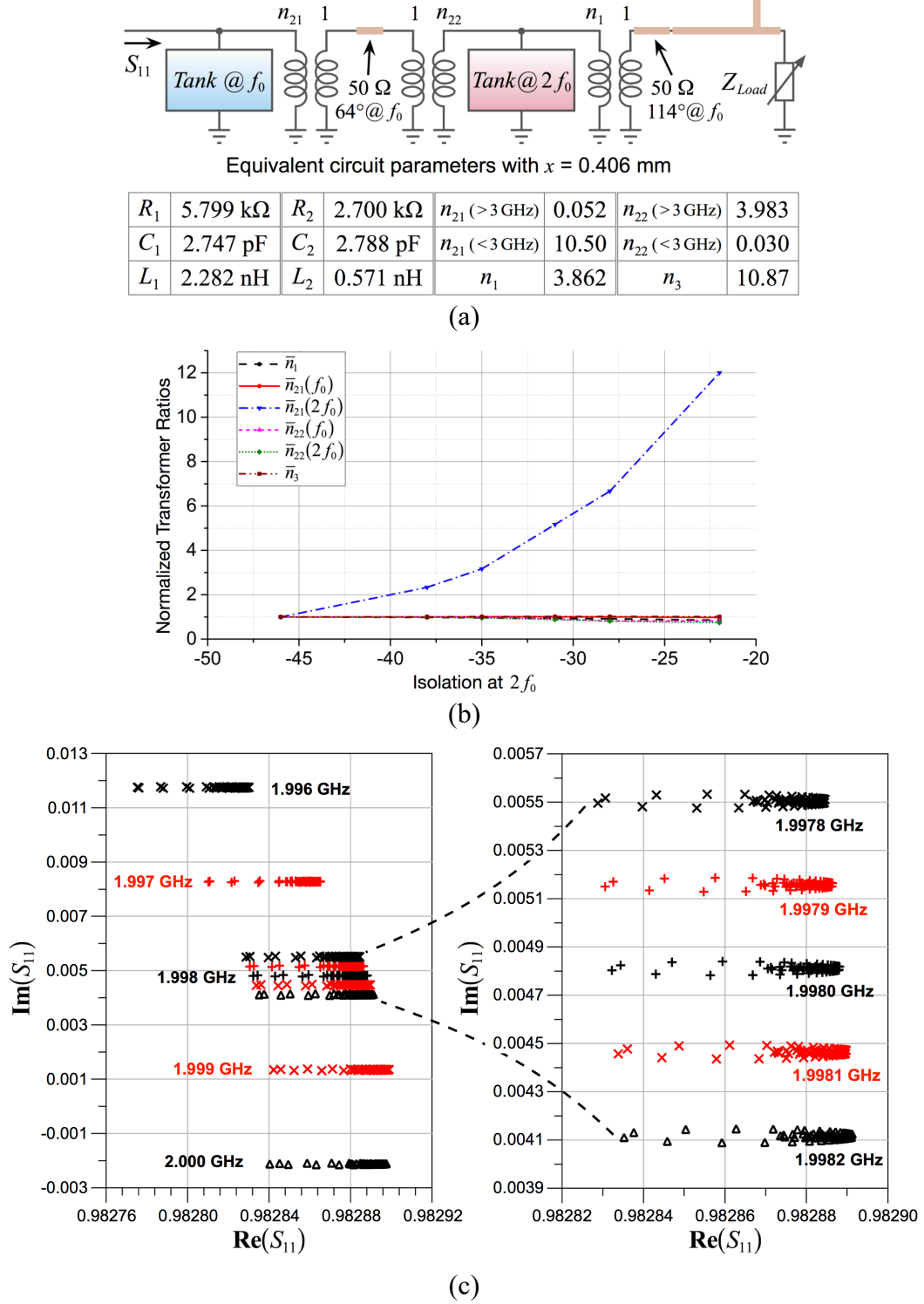


Figure 4.25: (a) Equivalent circuit parameters of the diplexer, (b) variation of normalized transformer ratio versus to 2nd harmonic isolation, and (c) S_{11} variations of the passive impedance in the SIHO equivalent circuit subject to load reflection coefficient points of Fig. 4.21, around the fundamental resonant frequency.

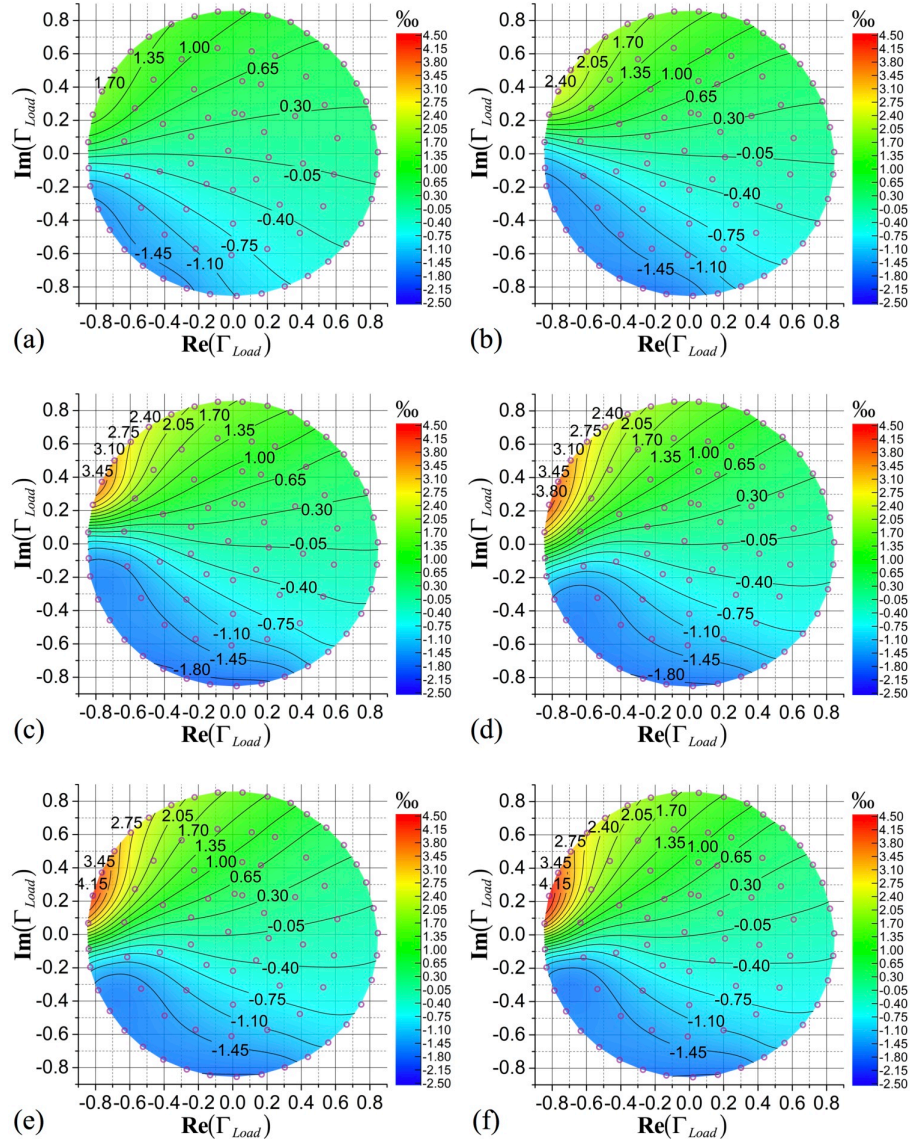


Figure 4.26: Model-predicted SIHO load pulling results of frequency shift with duplexers of different isolations at $2f_0$ of (a) -46 dB, (b) -38 dB, (c) -35 dB, (d) -31 dB, (e) -28 dB and (f) -22 dB.

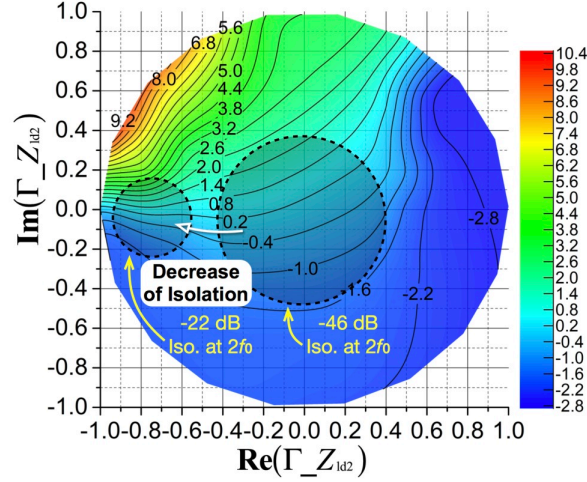


Figure 4.27: Model-predicted SIHO load pulling results of frequency shift as the load impedance of the gain block at the 2nd harmonic sweeps across the entire Smith chart.

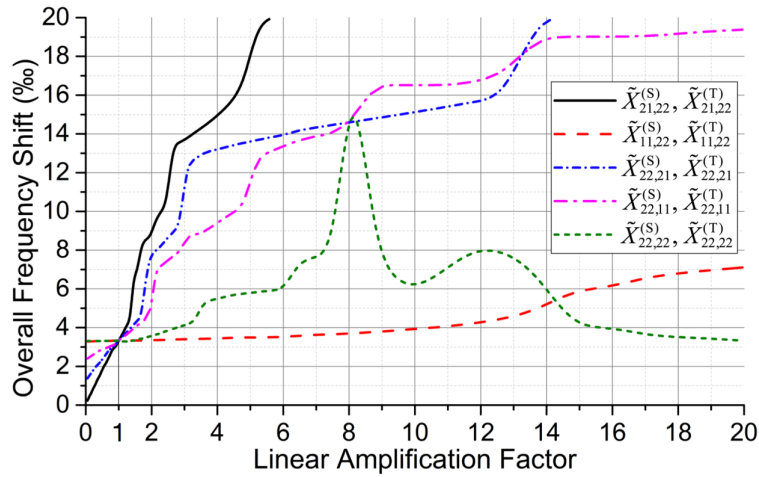


Figure 4.28: Model-predicted SIHO load pulling results of the overall frequency shift as different X-parameter elements are independently attenuated or amplified.

Fig. 4.25 (a) summarizes the parameters of the SIHO passive part equivalent circuit corresponding to the diplexer with $x=0.406$ mm. Two sections of delay lines are inserted to balance the phase of the diplexer. Fig. 4.25 (b) shows the transformer ratio variations versus the change of isolation at $2f_0$. They are normalized to the ones in Fig. 4.25 (a). It can be seen the key factor is $n_{21}(2f_0)$ and the rest are almost constant. As the load impedance changes in the same range as in the load pulling measurement, the equivalent circuit S_{11} around the fundamental resonance changes, as shown in Fig. 4.25 (c). It can be seen that the load pulling to the passive circuit will introduce no more than

0.05‰ of frequency shift, which is negligible compared to the SIHO overall operating frequency shift of about 2‰, as shown in Fig. 4.21 (a).

On the other hand, the load pulling as a result of the change of the equivalent admittance calculated by equation (4.21) is shown in Fig. 4.26, with the same load impedance distribution used in the measurement and the equivalent circuit parameters extracted from diplexers with different isolations. The results predicted by the circuit model have a strong correlation with the simulated results of Fig. 4.24. Fig. 4.27 is a model-predicted frequency variation as the load impedance of the gain block at $2f_0$ sweeps across the entire Smith chart. It also shows that as $n'_{21}(2f_0)$ increases (isolation decreases) the region of the actual Z_{ld2} variation shrinks and moves towards the ‘open’ side due to the decrease of $Z_M(2f_0)n_{21}^2(2f_0)/n_{21}'^2(2f_0)$, referring to Fig. 4.9. Since the gradient of frequency variation is larger at the ‘open’ side, the decreased isolation still results in a larger overall frequency pulling. Fig. 4.28 shows the effect of some of the X-parameter elements on the frequency pulling, as discussed in section 4.3.2. The overall frequency shift in this figure is limited to 2%, which is the frequency range of the measured X-parameter. The overall frequency pulling increases monotonically as the increase of the amplitude of the S and T terms for (i, m, k, n) equals to (2, 1, 2, 2), (1, 1, 2, 2), (2, 2, 2, 1) or (2, 2, 1, 1). For the case of (2, 2, 2, 2), the frequency pulling decreases as the S and T terms are amplified by more than 12. This is due to the existence of the term $Z_{ld2}^*/Z_{ld2}' + 1$ and its conjugate in matrix **S** of equation (4.19). This figure implies that the conversion rate between the 1st and the 2nd harmonics at the output of the gain block are the major contributors to the pulling effect. In other words, if the output of the gain block has no response to any incident signal, the pulling effect of an SIHO vanishes.

4.5 Conclusion

In this paper, an analytical modeling technique of the SIHO based on the X-parameter model is proposed and studied, focusing on the frequency pulling effect. The feedback-loop structure of the SIHO is represented by a lumped element circuit model with active and passive subnetworks for which equivalent impedances are expressed in closed-forms. As a comparison, the conventional feedback-loop oscillator delivering a fundamental frequency signal is modeled and studied in the same manner. Both the load impedance variation and the signal injection are considered and their impact on the output frequency is evaluated. The study identifies key factors of both the gain block and the diplexer, which cause the pulling effect.

An HMD system which can be used for the automated experimental design of transistor-based nonlinear circuit is proposed. Its operating principle, hardware configuration, calibration technique, and design & optimization procedures are reported. Following the experimental optimization, the matching network design can be also automated using the formulas developed in this work. The HMD system can be generalized and implemented for a large variety of nonlinear microwave circuit design, especially when accurate active device model is lacking. Experimental and simulation results are presented to validate the SIHO modeling techniques and the conclusions drawn from the theory.

4.6 Acknowledgement

The authors would like to thank Keysight Technology for providing AWG and technical assistance for the measurements. The authors would also like to acknowledge Traian Antonescu, Steve Dubé and Jules Gauthier of the Poly-Grames Research Center of Polytechnique Montréal for their outstanding fabrication works and technical support.

CHAPTER 5 ARTICLE 4: A MILLIMETER-WAVE SELF-ISOLATED HARMONIC ACTIVE RADIATOR FOR IDENTIFICATION, SENSING, TRACKING AND COMMUNICATION APPLICATIONS

Co-authored by Anthony Ghiotto, Lei Guo, Fang Zhu, and Ke Wu

Submitted to « *IEEE Transactions on Antennas and Propagation* », 2018.

Abstract—A harmonic active radiator with self-isolation property operating around 28 GHz is proposed, investigated and demonstrated in this work. The active radiator takes advantages of the harmonic feedback-loop oscillator principle, which enjoys the superiority of simple structure, harmonic output and pulling effect mitigation, thanks to the inherent self-isolation property of the proposed loop structure. A partially-air-filled dual-mode substrate integrated waveguide (SIW) cavity structure is designed and implemented as part of the active radiator to realize the functionalities of resonator, diplexer, and antenna concurrently. The whole circuit oscillates at fundamental frequency f_0 and the generated 2nd harmonic signal at $2f_0$ is radiated through a slot etched on the broadside of the SIW cavity. A dielectric resonator is coupled to the slot for both tuning the 2nd mode frequency of the cavity and enhancing the antenna bandwidth. A circuit prototype is fabricated and tested. The measured results show a maximum equivalent isotropic radiated power of 15 dBm at 28.15 GHz and a phase noise of -108 dBc/Hz at 1 MHz offset. The load pulling and injection pulling are reduced by a factor of 10 and 17, respectively, compared with an active radiator transmitting the fundamental frequency signal around 28 GHz. Such a compact circuit structure is a good candidate for low-cost millimeter-wave (mmW) Internet of Things (IoT) applications in connection with identification, sensing, tracking and communication, especially when realized with mmW integrated circuit chip technologies.

Index Terms—Active radiator, air-filled substrate integrated waveguide (SIW), antenna, dielectric resonator, pulling effect, harmonic oscillator, self-isolation.

5.1 Introduction

Free running oscillator is one of the core components of active radio frequency identification (RFID) tags, which enables the wireless functions of sensing, positioning, powering and communication [75, 76, 126]. As ubiquitous connectivity becomes the focus of the future wireless technology, critical characteristics including minimized footprint, reduced cost, low latency, rich storage, high data rate and superior positioning accuracy have to be achieved by next generation RFID tags. The industry and academia have come to a general consensus that the millimeter-wave (mmW)

technology is arguably the only choice for achieving all these merits because of its abundant spectrum resources and short wavelength. In 2016, the Federal Communications Commission (FCC) of the United States opened up 11 GHz of high frequency spectrum for the 5th generation (5G) wireless applications, including an 850 MHz band at 28 GHz [127]. Similar spectrum regulation policies have also been stated in other countries and regions.

In spite of the advantages of mmW, many challenges remain to be addressed and in what area further research is needed. First of all, mmW signal is difficult to generate directly due to the f_{max} limitation of semiconductor technologies, so that frequency multiplying techniques [128-131] and harmonic extraction techniques [132-136] have widely been adopted. The former scheme shows a better flexibility and the signal quality depends on the low frequency sources which drive the frequency multipliers. However, the latter solution, exempted from explicit multiplier, is more favorable in terms of performance and power consumption. Secondly, reducing the transistor count, power consumption and system cost is particularly desired by mmW IC designers. In addition, the interconnects among mmW components are usually lossy and bandwidth-limited. Therefore, the concept of building block co-design, such as active antenna [137-140], filter antenna (filtenna) [141-144], and self-oscillating mixer [145, 146], are introduced to bridge the artificial function divisions and also to mitigate performance bottlenecks. Active radiator or oscillator antenna is another co-design example that has received much attention in recent years [147-152]. The resonate type of antenna is reused as a tank of the oscillator to gain the efficiency and reduce the circuit size. F. Giuppi *et al.* demonstrated a substrate integrated waveguide (SIW) cavity backed voltage controlled oscillator (VCO) antenna in X band [148]. Its active circuit and related radiation structure are placed back-to-back on the two broadsides of an SIW cavity. Such a topology enables a more compact and efficient implementation than those with the active and passive parts located separately. In [149-151], T. G. Ma *et al.* proposed ring, semi-ring and monopole loaded semi-ring, based self-oscillating active antennas with frequency and/or pattern agilities. In these works, the microstrip ring structures act as both the feedback-loop and the radiation elements. PIN diodes at different locations on the rings are used to reconfigure working modes of the structures, which shows different radiation properties. Because of limited quality factor (Q factor) of the passive structures, the phase noise is relatively poor. The oscillator phase noise can be improved by implementing a high Q factor dielectric resonator antenna (DRA) as the tank, as reported in [152]. That paper not only demonstrated a regular DRA loaded active radiator, but also proposed a hollow DRA inside which the active circuit is placed for shielding and to achieve a reduced footprint.

Another particular advantage of the active radiators is pronounced in connection with arrays. Usually, the feeding structures of antenna arrays are complex for design and often introduce unwanted couplings with radiation elements. Especially as frequency goes higher, the spacing between elements is reduced proportionally, there is hardly any space for the integration of the feeding network. In this case, the compact active radiators can be used as an alternative technique to constitute arrays without feeding structures. Moreover, beam steering can be achieved by using the inter-element coupling mechanism [153]. In recent years, researchers studied the optimal surface current distribution for efficient on-chip mm-/THz-wave generation and radiation using a group of distributed-active-radiators (DARs), which realizes signal generation, multiplication, filtering and radiation in a single structure [154-156]. By forming a closed loop with dual-rings and introducing cross-coupled transistor pairs in a distributive way, the structure can sustain oscillation at a certain frequency and radiate at only the 2nd harmonic frequency in the far field. A coupled array of DARs also shows a beamforming capability. This concept allows the on-chip surface current flow to be reconfigured at a scale much less than the wavelength, thanks to a tiny footprint of the active and passive parts on silicon, and a fine manipulation of the field is achieved towards a maximized radiation efficiency. P. Nazari *et al.* proposed a similar active radiator on chip, which is based on an octagonal-cavity backed antenna with eight feeding points. For each adjacent pair of feeding points, a section of amplifier with a progressive phase is inserted between them to form a closed loop [157]. The cavity exhibits high Q factor by preventing the substrate leakage. Thus, a low phase noise signal generation and radiation are achieved at 114 GHz.

Free running active radiators suffer from obvious pulling effect as its load impedance varies [69] or as an external signal is injected [70]. This phenomenon would result in a shifted frequency and a deteriorated phase noise, which may interrupt communications. This gets even more severe as these circuits operate in crowded frequency bands, and/or when they are implemented with wearable and implantable devices because of body touch. Our previous work [91] studied a new feedback-loop structure that self-isolates the load impedance variation and the external signal injection from the oscillating dynamics. Based on that, a harmonic oscillator is designed. The frequency pulling is reduced by 20 times and the phase noise is improved, compared with a conventional feedback-loop oscillator.

In this work, a harmonic active radiator exploiting the same self-isolation principle is proposed and studied. An SIW cavity with two perpendicular microstrip line feedings and a slot etched on the broadside of the cavity constitutes a resonator, diplexer, and antenna in one. The feedback-loop is

composed of a low noise amplifier (LNA) as well as the cavity through its low frequency port and the common port. The loop oscillates at fundamental frequency f_0 and only the 2nd harmonic signal at $2f_0$ is radiated through the slot. The air-filled SIW [158-160] and the dielectric loading techniques are both used to adjust the first two resonating frequencies of the cavity. The prototype has an f_0 at about 14 GHz so that it can be applied to 28 GHz band mobile 5G devices, particularly low-cost Internet of Things (IoT) chips.

This paper is organized as follows. Section 5.2 elucidates the structure of the self-isolated harmonic active radiator, explains its operating principle, analyzes the tri-function SIW cavity and the effects of the air-filled region as well as the dielectric loading on the filtering and radiation performance. A complete procedure of designing the SIW cavity is summarized, followed by an experimental verification. The fabricated prototype is shown in Section 5.3 together with a post-tuning technique. The measurement results of the radiation power, pattern and the phase noise are presented. Performance is summarized and compared with published works. Another active radiator having fundamental frequency output based on a similar air-filled-SIW cavity structure is developed. Comparative load and injection pulling measurements with the two active radiators are performed to demonstrate the pulling effect mitigation performance of the proposed self-isolated harmonic active radiator. Finally, conclusions are drawn in Section 5.4.

5.2 Concept and Operation Principle

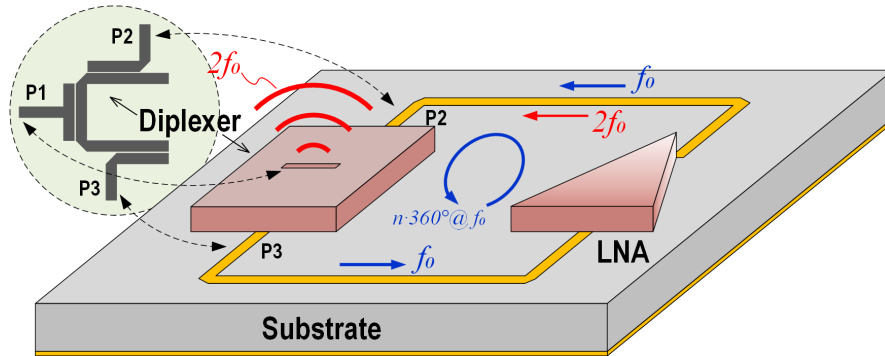


Figure 5.1: The proposed self-isolated harmonic active radiator and the correspondences of its diplexer with the one based on microstrip line in [91].

The harmonic feedback-loop oscillator in the previous work [91] has a diplexer whose common port P2 presents two narrow passbands at f_0 and $2f_0$, respectively. The loop oscillates at f_0 and the 2nd harmonic signal generated by the LNA nonlinearity is directed to the load through high

frequency port P1, while the fundamental frequency signal is fed to the input of the LNA via low frequency port P3. As illustrated in Fig. 5.1, the harmonic active radiator proposed in this work uses a diplexer that has port correspondences with that in [91]. Instead of directing the 2nd harmonic signal to the following circuit block through the 50 Ω high frequency port, it transmits the harmonic signal to the free space efficiently as an antenna. At the same time, the isolation property of the original planar diplexer must be preserved to prevent the oscillation dynamics at f_0 from being pulled by external injection signals or by certain close-in foreign objects.

5.2.1 Partially-air-filled SIW cavity as resonator, diplexer, and antenna

SIW has been enjoying its huge popularity over the past decades thanks to its combined advantages of both non-planar metallic waveguide and planar transmission lines. SIW's characteristics of low loss, self-shielding, low-cost and low profile make it an irreplaceable choice for circuit design and system integration on printed circuit board (PCB) and other processing techniques at the mmW frequency and beyond [138, 161]. Therefore, SIW cavity is selected to design the tri-function structure of the proposed active radiator. Fig. 5.2 illustrates the intrinsic resonating frequencies of the first few resonating modes of the rectangular and circular dielectric-filled SIW cavities, normalized by their respective lowest resonating frequencies. The analytical expressions are given by equation (5.1) and (5.2).

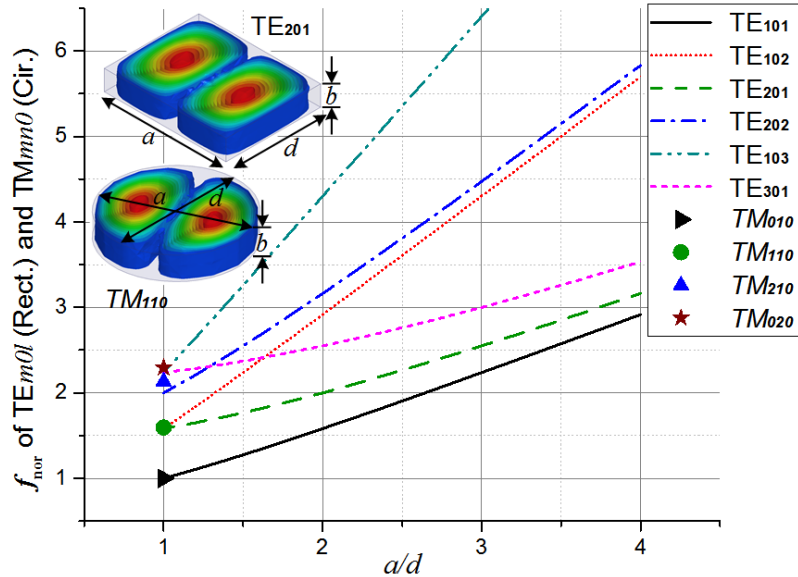


Figure 5.2: Normalized intrinsic resonating frequencies of the first few modes of the rectangular and circular dielectric-filled SIW cavities.

For the TE_{m0l} mode of the rectangular SIW cavity:

$$f_{nor} = \sqrt{m^2 + (la/d)^2} / \sqrt{1 + (a/d)^2}, \quad (5.1)$$

in which m and l are the number of variations of mode in the length (of a) and the width (of d) directions of the cavity. And for the TM_{mn0} mode of the circular SIW cavity ($a = d$):

$$f_{nor} = p_{mn} / p_{01}, \quad (5.2)$$

in which m and n are the number of variations of mode around the circumference and in the radial direction, respectively. The parameter p_{mn} is the n th root of the first kind Bessel function $J_m(x)$, whose values are given in mathematical tables [68]. Since the cavities are based on SIW on thin PCB, the modes with variations in the thickness direction are ignored.

The objective is to find two modes of an SIW cavity that present intrinsic frequencies with a ratio close to 2 between them. For the rectangular SIW cavity, first, the TE_{102} and TE_{103} modes are not selected as operational modes because of a large aspect ratio of their mode profile. In real structures, a slight field deviation of such two modes from their theoretical distributions may result in the excitation of spurious modes. The TE_{202} mode is also avoided since it can be easily contaminated by the TE_{102} mode, which not only has a close frequency but is also difficult to suppress separately even with carefully designed feeding structures. For the TE_{301} mode, a small a/d makes it easily contaminated by the TE_{202} mode, while a large a/d makes its frequency close to that of the TE_{101} and TE_{201} modes and away from the frequency-doubling-relation with them. Therefore, the TE_{101} and TE_{201} modes at $a/d = 1$ are selected for the rectangular SIW cavity. Similarly, for the circular SIW cavity ($a/d = 1$), the TM_{010} mode and TM_{110} mode are selected. In terms of the frequency ratio, $f_{TE201}/f_{TE101} = 1.58$ for the square cavity and $f_{TM110}/f_{TM010} = 1.59$ for the circular cavity.

The Q factor of the TE_{m0l} mode of the square cavity and the TM_{mn0} mode of the circular cavity is expressed as:

$$Q = \left(\frac{1}{\tan \delta} + \frac{2R_s}{k\eta b} + \frac{4R_{s1}}{k\eta a} \right)^{-1}, \quad (5.3)$$

in which $\tan \delta$ is the dielectric loss tangent; R_s and R_{s1} are the surface resistance of the copper foil of the PCB and the copper plating of the metalized slots, respectively; k and η are the wave number and the wave impedance of the dielectric media at the resonating frequency. It can easily be found

that if the TE_{101} and TM_{010} modes of the two respective cavities on the same PCB have the same resonating frequency, the length a of the square one is smaller than the diameter a of the circular counterpart. By referring to equation (5.3), one can determine that the circular cavity has a higher Q factor. This conclusion also applies to the TE_{201} and TM_{110} mode of the two cavities.

Therefore, the circular cavity has superiorities in both Q factor and frequency ratio. Its symmetry also provides more flexibilities in feeding structure design and circuit layout. Other cavity shapes are not considered for the simplicity of design and fabrication.

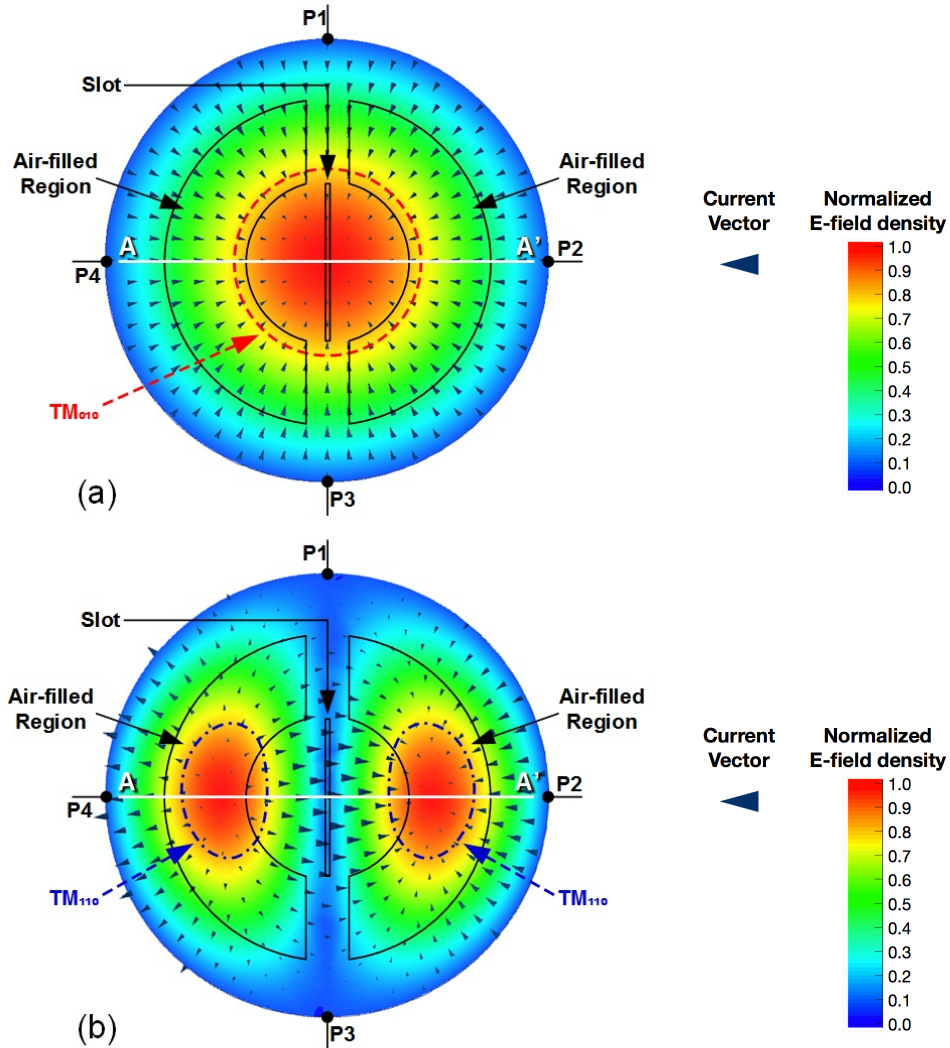


Figure 5.3: The electric fields magnitude and surface current vectors of (a) TM_{010} mode, and (b) TM_{110} mode of the circular cavity. The proposed air-filled region and the radiation slot are also displayed.

Fig. 5.3 presents the electric field magnitude and surface current vectors of the TM_{010} and TM_{110} modes of a circular cavity. The outlines of the regions, where the energy of the two modes is concentrated, are indicated with dashed line and dashed line with dots. To adjust $f_{TM_{110}}/f_{TM_{010}}$ to 2, it is necessary to reduce the effective permittivity of the TM_{110} mode concentrated region, but with minimized influences on the TM_{010} mode. As such, a pair of air-filled regions as shown in Fig. 5.3 is implemented. By removing the substrate in those regions, the resonating frequencies of both of the modes are increased, but their ratio changes regarding the shapes, sizes, and locations of the regions. A detailed explanation of the fabrication process of such an air-filled SIW structure with multilayer PCB was explained in [159]. Fig. 5.4 shows the electric field vector of the two modes in a regular circular cavity and the partially-air-filled circular cavity at the AA' cutting of Fig. 5.3, generated by the eigenmode simulator of ANSYS HFSS. It can be seen that the TM_{110} mode is more significantly affected by the air-filled region.

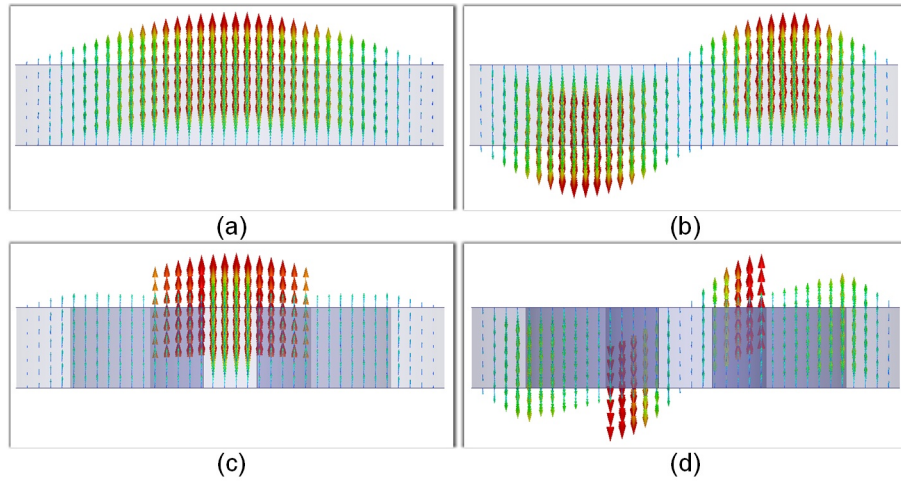


Figure 5.4: The electric field vector of (a) TM_{010} mode and (b) TM_{110} mode of a regular circular cavity; and of (c) TM_{010} mode and (d) TM_{110} mode of a partially-air-filled circular cavity, at the AA' cutting in Fig. 5.3.

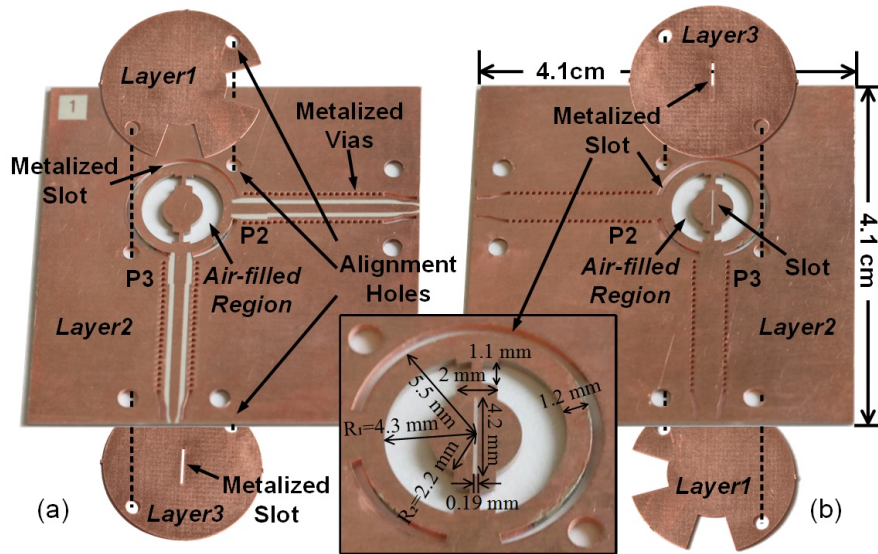


Figure 5.5: The assembly diagram of the fabricated tri-function SIW cavity with multilayer PCB process. (a) the top side with microstrip feeding lines; (b) the bottom side with radiation slot.

A slot on the broadside of the cavity and between the air-filled regions will cut the surface current of the TM_{110} mode, with minimum effect on that of the TM_{010} mode. Therefore, it only couples to the TM_{110} mode and can be regarded as an efficient slot antenna when an appropriate length and width are selected. Four symmetrically located feeding points where microstrip lines can be connected are shown in Fig. 5.3. Among them, P1 and P3 have electrical coupling only to the TM_{010} mode, while P2 and P4 couple to both modes. Thus, by selecting any two adjacent feeding points (e.g. P2 and P3), a tri-function cavity is formed. P2 is the common port and P3 is the low frequency port in this case. Moreover, isolation is created between P3 and the free space at both of the two resonating modes.

The top and bottom sides of the designed and fabricated prototype of the cavity as a resonator, diplexer, and antenna concurrently are shown in Fig. 5.5 (a) and Fig. 5.5 (b), respectively. The structure is designed to have a passband from P2 to P3 at about 14 GHz using the TM_{010} mode. The key dimensions are displayed in the lower center. The procedure of determining those dimensions are discussed in Section 5.2.2. The microstrip feeding lines and the radiation slots are placed on the opposite sides of Layer 2, which is based on a Rogers RT/duriod 6002 high frequency substrate with a thickness of 0.508 mm. Instead of putting them on the same side, such an arrangement reduces the coupling of the radiated signal to the low frequency port P3, and also ensures a reduced parasitic radiation from the microstrip line and the feeding structure. Layer 1 and

Layer 3 are two other PCBs based on low-cost substrate with 0.254 mm thickness. They are attached to the center layer by either conductive bonding material such as Rogers COOLSPAN adhesive or by melted soldering paste. Metalized arc slots other than common metalized via are used as the cavity side walls. Another metalized slot in the center of Layer 3 aligns perfectly with the radiation slot on the cavity.

5.2.2 Dependency of resonating frequency on dimensions and structure, and cavity design procedure

The impact of the size of the air-filled region is further investigated. To this end, a parametric study with eigenmode simulator is performed by independently changing the outer and inner radius R_1 and R_2 of a closed cavity. The resultant curves in Fig. 5.6 show the variations of the resonating frequency (marked on the curves) of the TM_{010} mode and the frequency ratio of the first two modes. As R_1 increases, the frequency ratio $f_{TM_{110}}/f_{TM_{010}}$ increases, and on each curve, there is a certain value of R_2 that corresponds to a maximum of $f_{TM_{110}}/f_{TM_{010}}$.

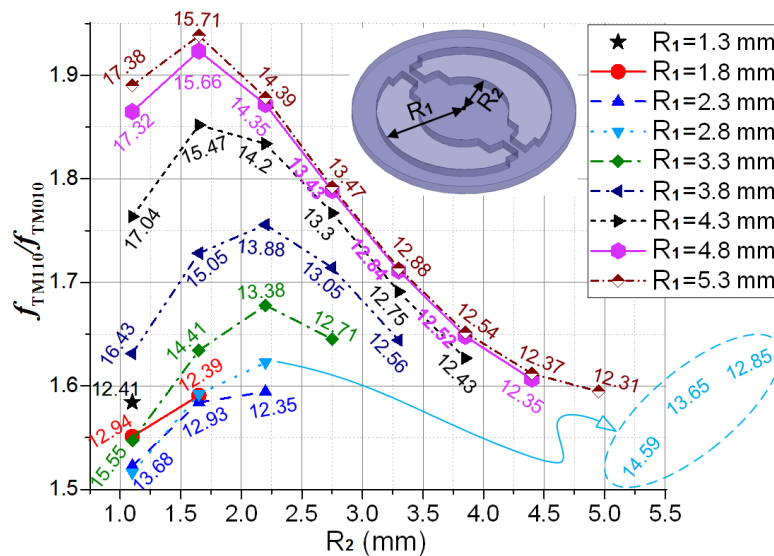


Figure 5.6: Ratio of the first two resonating mode frequencies and variation of the TM_{010} mode frequency (unit: GHz)

The radiation slot is equivalent to a capacitive loading on the TM_{110} mode of the cavity. So, with the slot, the resonating frequency of that mode becomes lower than without the slot. In other words, the effect of the slot is to translate the surface current in the center region of that mode into a displacement current which has a longer path, and the resonating frequency is in turn reduced because it is inversely proportional to the effective length of the current of the mode.

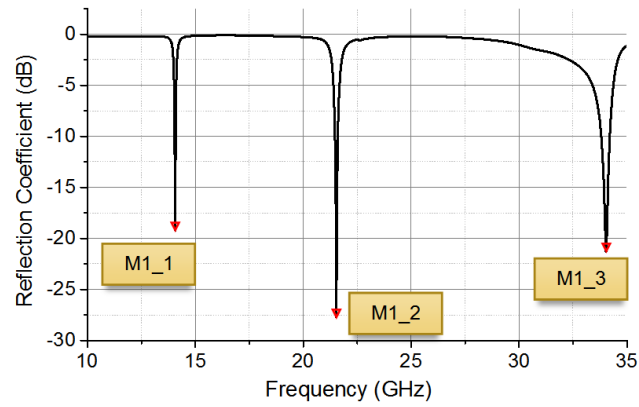


Figure 5.7: The simulated reflection coefficient at P2 of the designed tri-function SIW cavity.

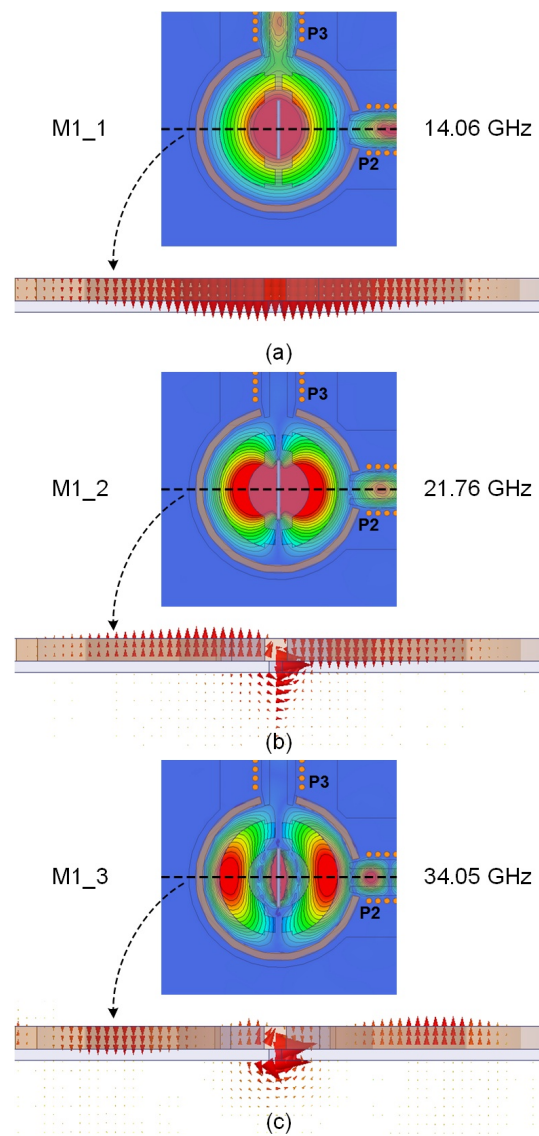


Figure 5.8: The electric field magnitude and vector of the first three modes, (a) TM_{010} , (b) TM_{110} and (c) hybrid, of the tri-function SIW cavity.

Fig. 5.7 shows the simulated reflection coefficient looking into P2 of the cavity with feedings and radiation slot. The markers of ‘M1_1’, ‘M1_2’ and ‘M1_3’ at the notches of the curves represent the first three modes of the cavity, at 14.06 GHz, 21.76 GHz, and 34.05 GHz, respectively. Fig. 5.8 illustrates their electric field density in the cavity as well as the electric field vector on the plane which is perpendicular to the longitudinal direction of the radiation slot. It can be seen that the first two are TM_{010} and TM_{110} modes, and the third one is a hybrid of TM_{110} , $TM_{11\frac{1}{2}0}$, and TM_{120} modes. Due to the relatively higher effective permittivity at the center portion of the cavity and the capacitive slot, the third mode profile in that region shrinks. Fig. 5.9 shows the simulated reflection coefficient and the electric field of the same cavity without a radiation slot. The first two modes, TM_{010} and TM_{110} , resonate at 14.04 GHz and 25.64 GHz, respectively. The third one at 30.77 GHz is the $TM_{11\frac{1}{2}0}$ mode, whose field distribution is not shown for its irrelevance to the discussion. Although the TM_{010} mode frequency is scarcely affected, the ratio $f_{TM_{110}}/f_{TM_{010}}$ is shifted from 1.83 to 1.55 by the slot. As mentioned in Section 5.2.1, a circular SIW cavity based on a homogeneous dielectric substrate has $f_{TM_{110}}/f_{TM_{010}} = 1.59$. Therefore, only using the air-filling technique cannot even compensate for the frequency ratio decreasing caused by the capacitive effect of the radiation slot, not to mention about increasing it to 2. So, it is necessary to introduce other techniques for mode and frequency tuning.

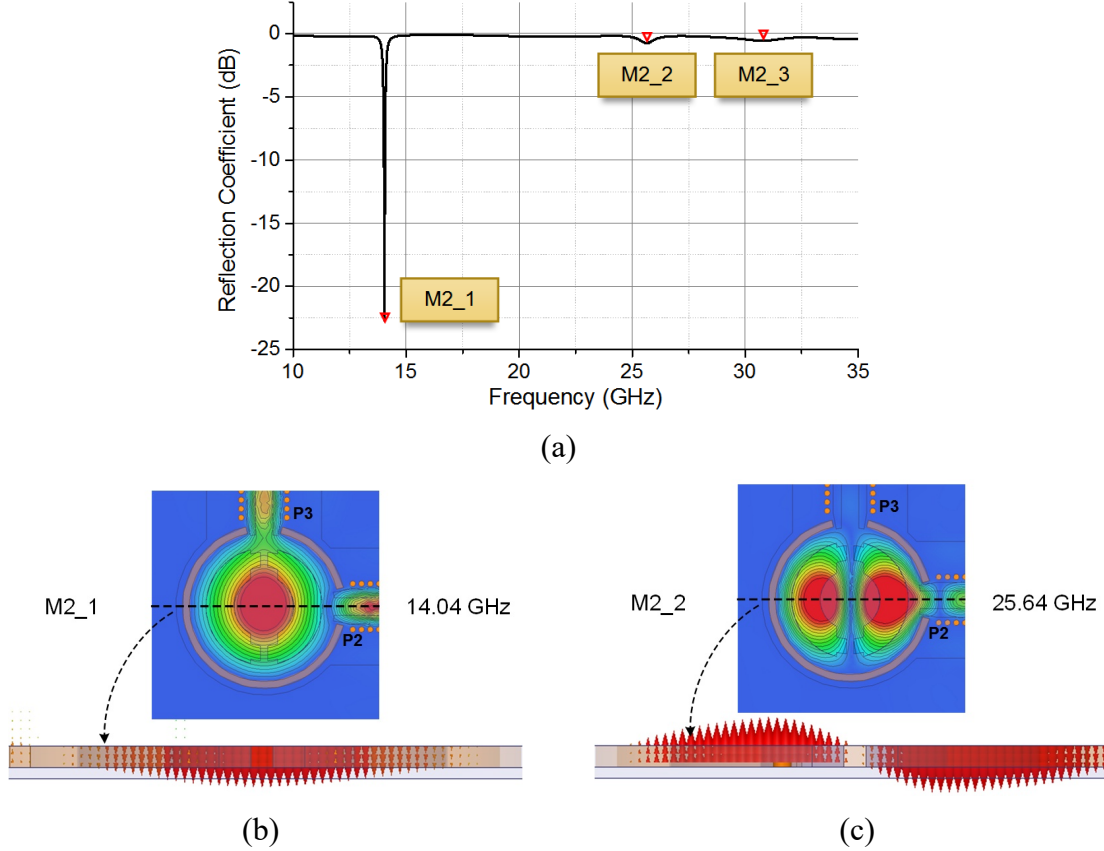


Figure 5.9: (a) The simulated reflection coefficient at P2 of the designed SIW cavity without a radiation slot; (b) and (c) The electric field magnitude and vector of TM₀₁₀ and TM₁₁₀ modes of the designed SIW cavity without a slot.

An observation of the field distribution of the hybrid mode in Fig. 5.8 (c) suggests that the field intensities at the substrate side and the air side of the radiation slot are almost the same. If a piece of dielectric material is attached to the slot on the air side, the outer field intensity will increase and the inner counterpart will decrease. Moreover, the field profile in the air-filled region will be extended and stretched towards the center of the cavity. Thus, the hybrid mode becomes almost pure TM₁₁₀ mode and its frequency is reduced accordingly. To validate the concept, a cylinder dielectric with the thickness $H_{res} = 2.54$ mm and the diameter $D_{res} = 6.858$ mm is attached on the slot, as shown in Fig. 5.10 (a). In the full-wave simulations, its relative permittivity varies from $\epsilon_r = 1$ to 6, and the resultant reflection coefficients, as well as the electric field vectors are shown in Fig. 5.10 (b) and Fig. 5.10 (c), respectively. As the permittivity increases, the electric field density in the center portion of the cavity is reduced and that in the dielectric bulk is increased. The field distribution becomes more similar to that of the TM₁₁₀ mode, compared with the hybrid mode

shown in Fig. 5.8 (c). As the permittivity goes high, the intensive field in the center is basically across the slot instead of within the cavity. Finally, the Rogers RT/duriod 6006 substrate with a relative permittivity of 6.15 and a thickness of 2.54 mm is selected to fabricate the dielectric resonator, and such a design presents the targeted radiation frequency at about 28 GHz. By comparing the curve corresponding to $\epsilon_r = 1$ with others in Fig. 5.10 (b), another benefit of the dielectric loading technique is that the impedance bandwidth of the antenna is broadened.

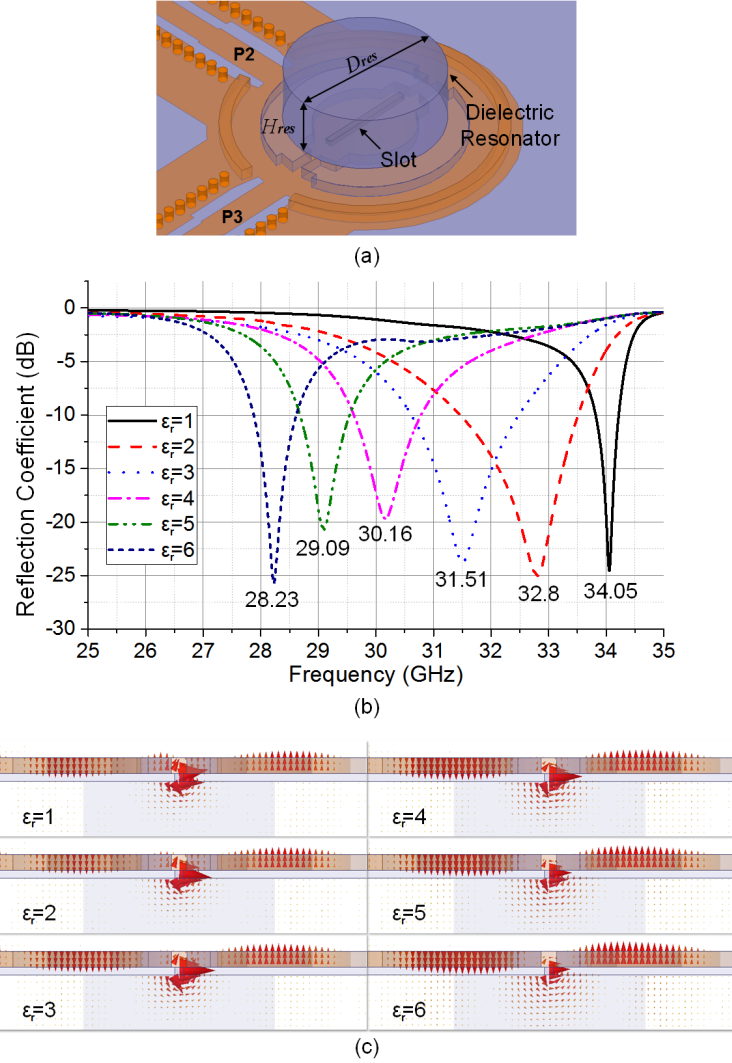


Figure 5.10: (a) A dielectric resonator is attached to the slot; (b) The simulated reflection coefficients at P2 of the designed tri-function SIW cavity with dielectric loading; (c) The electric field vectors of the cavity with ϵ_r changed from 1 to 6.

Based on the discussion above, a procedure of design for the tri-function SIW cavity and the methods of selecting its initial parameters are summarized as follows:

- (1) The design starts with choosing the substrate material for the SIW cavity. High frequency laminates such as RT/duriod 5880, 6002 and RO3003 from Rogers are few exemplary choices due to their low dielectric losses. A thicker substrate is preferred for reducing the conductor loss of SIW structures, but this would lead to a wider microstrip line which may generate high order modes at high frequency and cause difficulty of designing transition structures. Once the substrate is selected, the SIW cavity radius can be estimated using the closed-form equation for the TM_{010} mode given in [68], assuming a complete-dielectric-filled circular cavity and a resonating frequency at a half of the targeted radiation frequency.
- (2) The outer radius R_1 of the air-filled region is selected as close to the SIW cavity radius as possible, with the fabrication limitations in mind. According to the simulated curves in Fig. 5.6, a frequency ratio closer to 2 is then achieved.
- (3) The material for the dielectric resonator is selected. A critical parameter to consider is the dielectric loss, which should be as low as possible at the frequency of radiation. The relative permittivity should be more than 5 as a rule of thumb, so that the dielectric material plays a significant role in the mode and frequency tuning. But a high permittivity will bring a burden on the fabrication tolerance due to the size scaling down. Then the initial dimension of the cylinder dielectric resonator can be calculated based on the equation given in [162]. The fundamental mode $HEM_{11\delta}$ is selected. However, with a lower relative permittivity, the accuracy of the equation becomes worse and the real resonator may not operate with a perfect $HEM_{11\delta}$ mode.
- (4) The initial length of the radiation slot is selected to be a half of the wavelength in the dielectric material used for the dielectric resonator at the frequency of radiation, to guarantee an efficient energy coupling.
- (5) The inner radius R_2 of the air-filled region (refer to Fig. 5.5) is chosen to be slightly larger than a half of the length of the radiation slot, so as to accommodate the slot. Moreover, the curves in Fig. 5.6 should be taken into consideration, which suggests that under certain R_1 , there is an optimized R_2 that provides the highest frequency ratio.
- (6) Finally, a full-wave simulation is performed. By adjusting R_2 , a frequency ratio of 2 can be achieved. Normally, such a design will deviate from the targeted frequency, and this will be compensated by proportionally scaling the dimension of the whole structure. The size

of the dielectric resonator needs a further optimization for a maximized radiation efficiency and bandwidth.

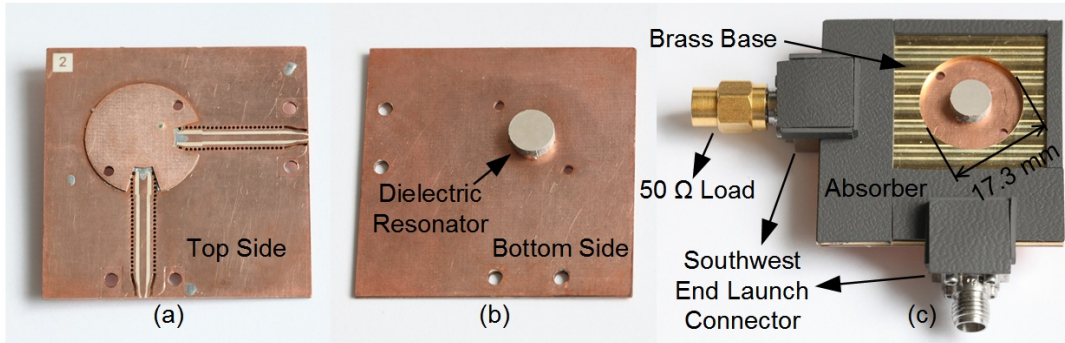


Figure 5.11: (a) The top and (b) the bottom side photo of the fabricated tri-function SIW cavity prototype with dielectric resonator loading. (c) The prototype with the based and connectors assembled, and covered with microwave absorber material.

Fig. 5.11 illustrates the fabricated and assembled tri-function SIW cavity. To perform two port S-parameter measurement and gain measurement, a base fabricated with brass is attached to the PCB and Southwest end launch connectors are used for coaxial cable connection. Microwave absorber ECCOSORB GDS/SS6M from Laird Technologies is used to cover the connector and the base to avoid the effect of extra ground plane and the connector surface reflection. The S-parameters are shown in Fig. 5.12. In the measurement, the effect of the connectors is removed by TRL calibration. The simulated and measured curves coincide with each other. The S21 curves around 14.06 GHz imply that the real structure has lower Q factor than the simulated counterpart. This is mainly due to the extra loss of the epoxy used to glue the dielectric resonator. The measured radiation center frequency is 28.39 GHz, slightly higher than the simulated one at 28.25 GHz. This difference is due to the simulation model using the nominal permittivity value of the dielectric substrate at 10 GHz. But the real permittivity becomes higher with the increase of frequency [163]. An isolation better than 25 dB at the frequency of radiation is achieved. This is the basic guarantee for the self-isolation characteristic of the proposed harmonic active radiator. When a signal in the free space at about 28 GHz is received, it will be only directed to the common port.

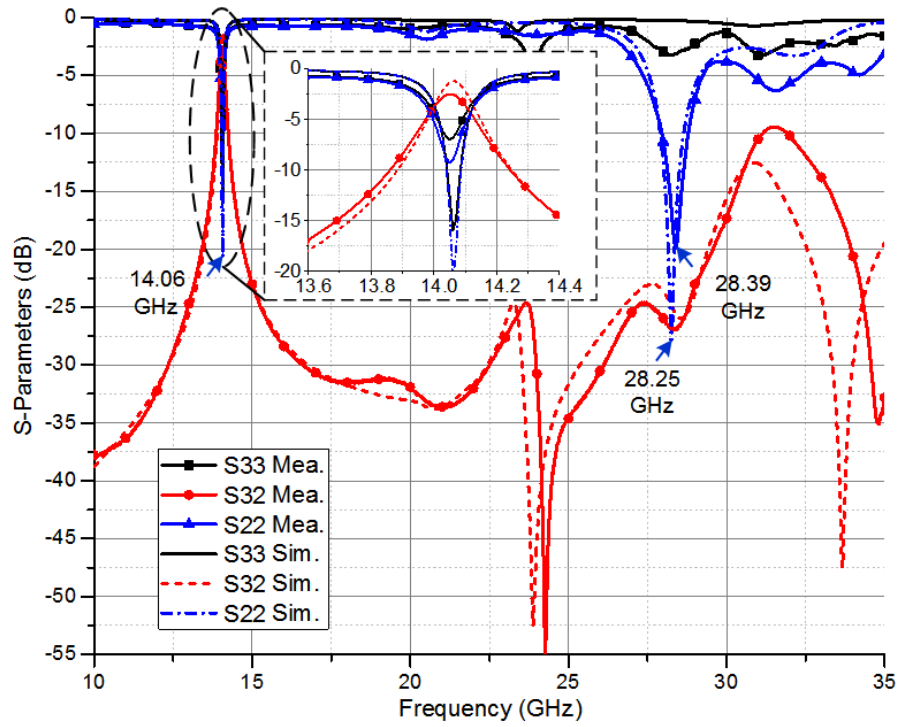


Figure 5.12: The simulated and measured S-parameters of the finalized tri-function SIW cavity design.

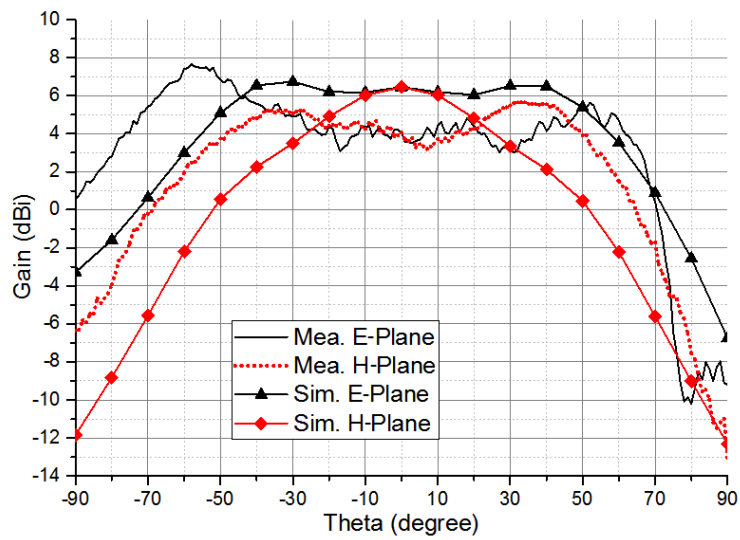


Figure 5.13: The simulated and measured gain of the finalized tri-function SIW cavity design.

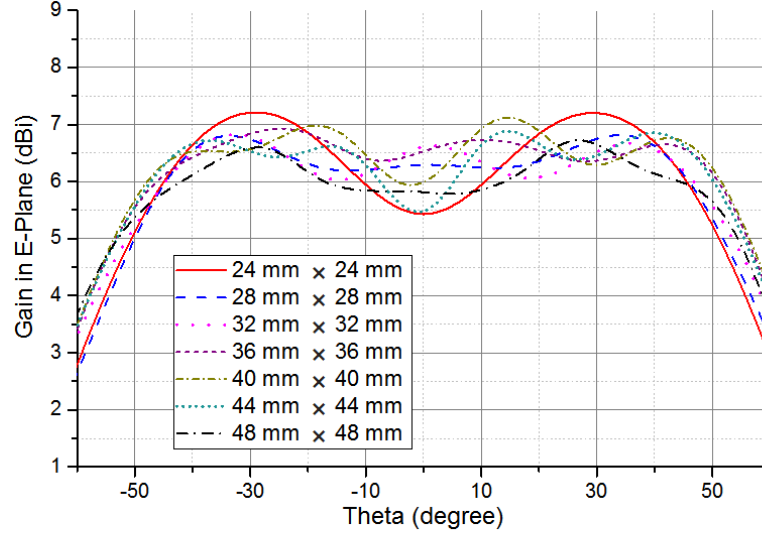


Figure 5.14: The simulated E-plane gain with different size of the ground plane.

The radiation performance is measured in the anechoic chamber of the Poly-Grames Research Center. The low frequency port which corresponds to the P3 feeding point in Fig. 5.5 is loaded with a $50\ \Omega$ terminal. The simulated and measured gain curves at the center radiation frequency are plotted in Fig. 5.13. In the simulation model, the size of the ground plane is set to be $30\ \text{mm} \times 30\ \text{mm}$. For the measured gain, 1.5 dB cable and connector loss is compensated. It can be seen that the maximum gain is not in the boresight direction and the patterns are unsymmetrical, which become more obvious in the measured results. This is caused by the ground plane effect and the reflection of the connectors, and the absorber is not perfect in eliminating the reflections. Such an explanation is validated by the simulated gain curves in Fig. 5.14, where the size of the ground plane changes from $24\ \text{mm} \times 24\ \text{mm}$ to $48\ \text{mm} \times 48\ \text{mm}$.

5.3 Fabricated Prototype, Tuning Technique and the Characterizations

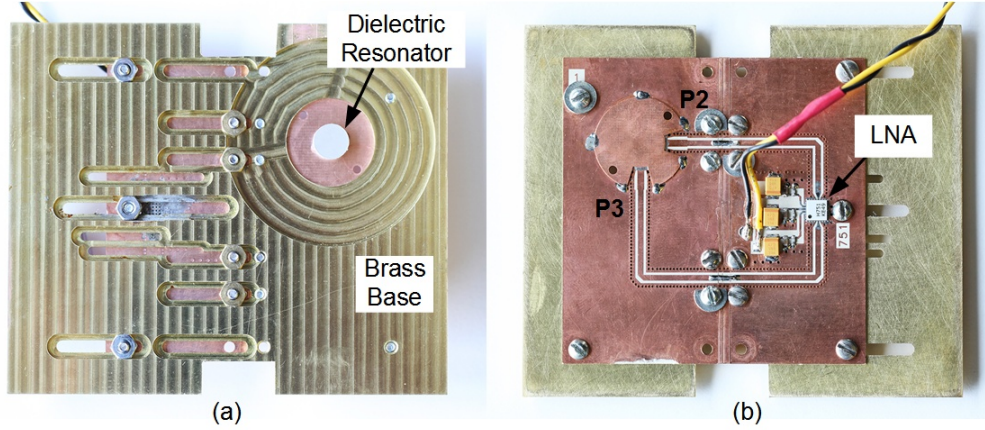


Figure 5.15: (a) The front and (b) the back sides of the fabricated self-isolated harmonic active radiator.

The designed and fabricated self-isolated harmonic active radiator is presented in Fig. 5.15. The LNA used in the loop is an HMC751LC4 chip from Hittite Microwave. It has a gain of no less than 24 dB, a noise figure lower than 2.5 dB and an output P1dB of 13 dBm in the 17~27 GHz frequency range. The design of the oscillation circuit is based on the Barkhausen criterion [91] at the fundamental frequency. The calibrated S-parameters of the LNA and the tri-function SIW cavity are measured separately. Therefore, the length of the loop can be adjusted to obtain a phase of $n \cdot 360$ degrees at the TM_{010} mode resonating frequency (about 14 GHz). Thus, the feedback loop oscillates at that frequency and the 2nd harmonic signal at about 28 GHz is generated from the LNA nonlinearity and transmitted by the antenna part. A base fabricated with brass is used to support the entire active radiator PCB, and also used to measure the independent S-parameters of the LNA and the SIW cavity with Southwest end launch connectors.

5.3.1 Frequency and power post-tuning technique

Caused by the fabrication tolerance and the inaccurate PCB characteristics, doubling the S21 first peak frequency may not be exactly the frequency that the tri-function cavity has its maximum radiation efficiency or the radiator has the maximum output power. Taking the fabricated prototype as an example, its narrow passband is at 14.06 GHz as shown in Fig. 5.12, while its radiation center frequency is 28.39 GHz. Thus, it is necessary to tune the resonator. Unlike the open structures such as microstrip circuits for which the impedance and the electrical length can be tuned by cutting the

lines, closed structures including SIW circuits cannot be tuned in an intuitive manner. Therefore, a post-tuning technique suitable for the SIW platform is required.

T. Martin *et al.* implemented movable metal pins in tuning the responses of air-filled SIW cavity filters [164]. A conductive pin with its axis parallel to the electric field of a mode is equivalent to an enhancement of the capacitance. Since a cavity resonates at a certain frequency where its capacitive and inductive reactance of the mode equal to each other, if an extra capacitance is introduced, the resonating frequency will be lowered to re-balance the two kinds of reactance. Fig. 5.16 (a) and Fig. 5.16 (b) are the photo and the simulation model of the tuning pins in the circuit. They are symmetrical about the slot, and at the place where the electric field of the TM_{110} mode has its maximum amplitude. The pins have a diameter of 0.508 mm and their stroke is the same as the thickness of the PCB. Metalized holes at the positions of the pins are made on Layer 1. Electric contact between the pins and Layer 1 is guaranteed by soldering. Using two pins instead of only one will improve the tuning range and field distribution symmetry for higher isolation between the low frequency port and the radiation mechanism. As the insertion depth of the pins is increased, the resonating frequency of both the two modes are reduced. But since the pins affect the TM_{110} mode at its peak electric field locations, while affect the TM_{010} mode at its fringe field, the frequency ratio of the two modes is reduced.

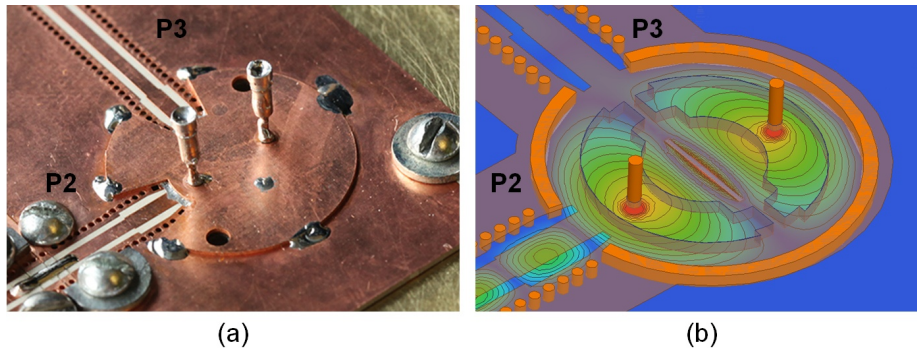


Figure 5.16: (a) and (b) are the photo and the simulation model of the cavity of the active radiator with tuning pins.

Fig. 5.17 (a) shows the simulated S_{21} and S_{22} curves as the insertion depth of the two tuning pins varies from 25.4 μm to 483 μm simultaneously. A frequency ratio tuning range of about 4.7% is achieved in the simulation. One drawback with such a tuning technique is it can only reduce the resonating frequency and the ratio, but not increase them. To overcome this, the pins with an insertion depth of a half of the substrate thickness is added to the simulation models in the design

phase. In the actual circuit tuning, the active radiator is fixed on a platform and the pins are attached to the head of a precise positioner, as shown in Fig. 5.17 (b). After the active radiator is powered on, a power meter or a spectrum analyzer connected to a horn antenna in the boresight of the radiator is used to track the radiation power variation during the tuning, until maximum receiving power is obtained.

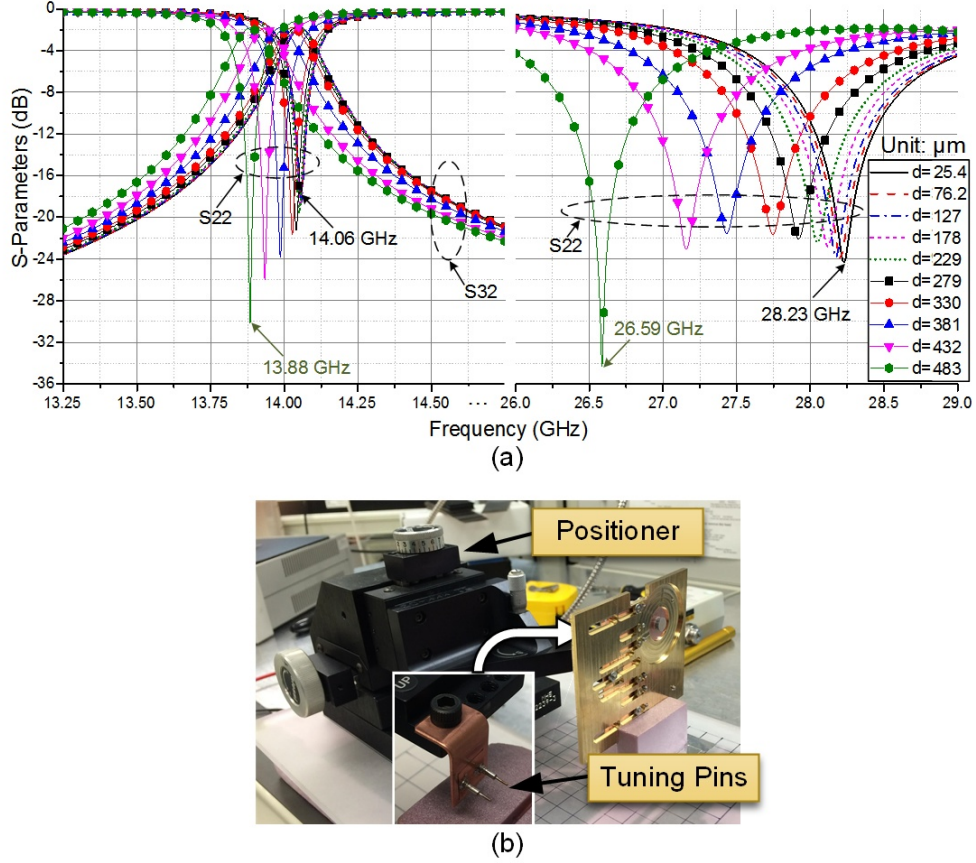


Figure 5.17: (a) The simulated S21 and S22 curves versus different pin insertion depth; (b) The frequency and power tuning setup.

5.3.2 Experimental characterizations of self-isolated active harmonic radiator prototype

The fabricated prototype (DUT) is characterized using the setup illustrated in Fig. 5.18. Absorbers are covered on the radiator for a reduced ground plane effect. The distance between the DUT and the phase center of the horn antenna (MI-12A-26 from MI Technologies, 26.4~40 GHz band) is 80 cm, which is about 75 wavelengths. The horn has a gain of 23.6 dBi at 28 GHz. The DUT is fixed on top of a wood pole and is adjusted to the same level as the center of the horn antenna aperture. The rotation table is used to change the angle of radiation so that the complete E or H cut

of the far field intensity can be captured. A signal analyzer N9030A from Agilent and a power meter ML2438A with a power sensor MA2474A both from Anritsu are used to measure the power received by the horn antenna.

Fig. 5.19 (a) shows the spectrum as the DUT boresight is pointing towards the horn antenna. Since the MI-12A-26 horn antenna cannot cover the frequency of the first three harmonics, another two horn antennas with a gain of 16.0 dBi at 14 GHz and 22.7 dBi at 42 GHz are used in turn to measure the spectrum, and the signal analyzer is switched to the maximum hold mode. With the assistance of the Friis equation, it can be calculated that the equivalent isotropic radiated power (EIRP) of the fundamental frequency signal and the 3rd harmonic is 22.4 dB and 24.7 dB lower than that of the 2nd harmonic, respectively. The phase noise is measured with the same configuration with a half of the distance and is shown in Fig. 5.19 (b), -108.46 dBc/Hz at 1 MHz offset is achieved. Since the power received by the signal analyzer is about -24 dBm, the limit to which the phase noise can be measured is -177 dBm/Hz $- (-24$ dBm) $= -153$ dBc/Hz, which is much lower than the measured phase noise of the DUT [165]. Therefore, the result is trustworthy.

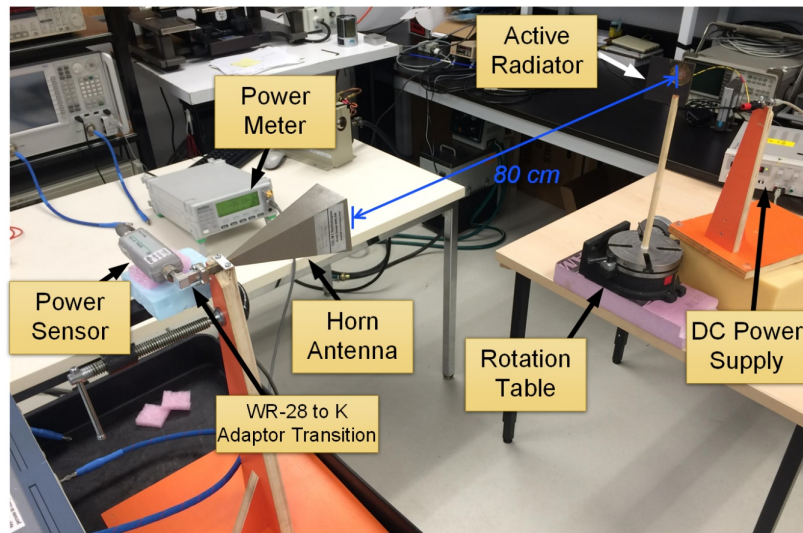
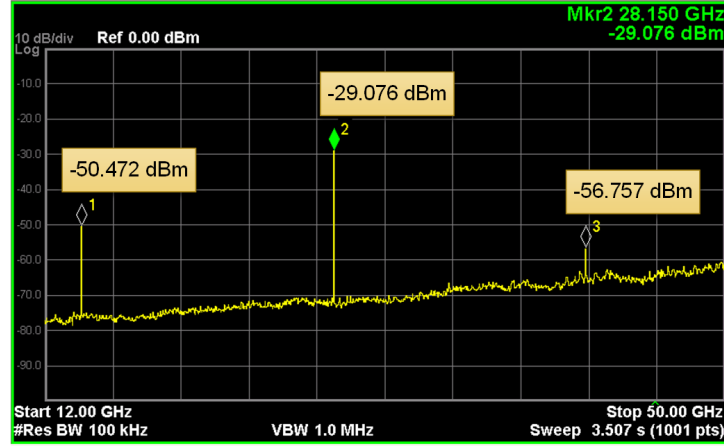
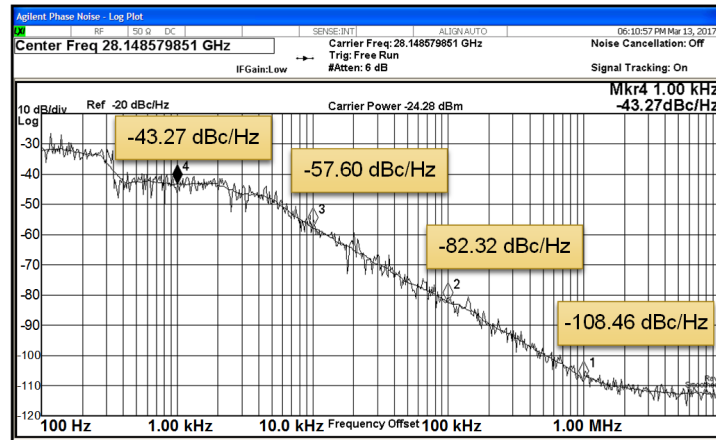


Figure 5.18: The measurement setup for characterization of the active radiator prototype.



(a)



(b)

Figure 5.19: (a) The measured spectrum in the boresight of the DUT; (b) The measured phase noise of the DUT.

To achieve a more accurate power level measurement, the calibrated power sensor is used. Since the waveguide to coaxial transition has a cutoff frequency of 21 GHz, the fundamental signal component at 14.08 GHz cannot reach the power sensor. Moreover, the 3rd and higher harmonics are 25 dB weaker than the main signal. So, the power reading of the 2nd harmonic signal is accurate and uncontaminated. Using the Friis equation, the EIRP is measured and plotted in Fig. 5.20 (a). Comparing the measured curves in Fig. 5.13 with those in Fig. 5.20 (a), the H-plane curves have similar shapes in the -90 to 90 degree range, but due to the ground plane effect, the E-plane curve of the EIRP has deeper notches than the gain curve at ± 40 degree directions. Fig. 5.20 (b) shows that the difference between the EIRP curve and the gain curve in H-plane has an average value of 8 dBm, which is the best estimation of the total radiated power (TRP) from the DUT. The dc power

supply provides a voltage of 4.7 V and current of 80 mA, and thus, 376 mW power consumption is achieved.

Table 5.1 compares the performance of the developed harmonic active radiator with the published active radiators as well as oscillators. Both the phase noise and the EIRP of the proposed structure enjoy superior advantages. The only obvious drawback is the power consumption. This is mainly because a pre-matched and packaged LNA is used in the feedback loop, so that the efficiency optimization is not taken into consideration during the design. If transistors are used, the power consumption and efficiency can be improved. Another shortcoming with the prototype is the deteriorated radiation pattern and EIRP pattern, especially in the E-plane. This could be solved by carefully adjusting the ground plane. To this end, the entire structure can be integrated using millimeter-wave integrated circuit (MMIC) technologies, then, the significantly reduced profile allows the ground plane to be reduced.

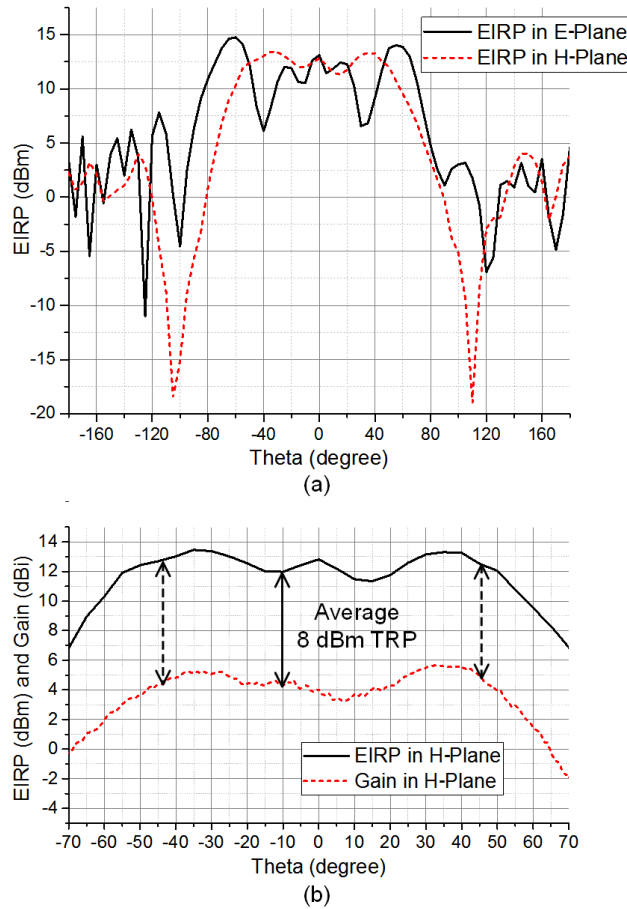


Figure 5.20: (a) The measured EIRP pattern in the E-plane and H-plane; (b) The TRP estimated by subtracting the gain curve from the EIRP curve.

Table 5.1: Performance Summary and Comparison with Published Active Radiators and Oscillators

Ref.	Frequency	Type	Technology	Phase Noise	EIRP/Output Power	Power Consumption
[166]	61.5 GHz	Active radiator	90 nm CMOS	-107.2 dBc/Hz @1 MHz	-3.6 dBm	99.0 mW
[167]	8.5 GHz	Active radiator	PCB, MS ¹ , HJ-FET	-87.5 dBc/Hz @100 KHz	11.2 dBm	27.0 mW
[157]	114 GHz	Active radiator	130 nm SiGe BiCMOS	-99.3 dBc/Hz @1 MHz	14.0 dBm	505 mW
[149]	5.25 GHz	Active radiator	PCB, MS, HJ-FET	-84.6 dBc/Hz @100 KHz	4.3 dBm	62.5 mW
[148]	12.3 GHz	Active radiator	PCB, SIW, HJ-FET	-107.0 dBc/Hz @1 MHz	6.5 dBm	18.0 mW
[168]	25.18 GHz	Push-push oscillator	PCB, SIW, GaAs HEMT	-120.3 dBc/Hz @1 MHz	-6.6 dBm	44.1 mW
[169]	29.5 GHz	Push-push oscillator	PCB, SIW, HJ-FET	-105.7 dBc/Hz @1 MHz	-14.7 dBm	18.0 mW
[170]	25.6 GHz	Oscillator	PCB, MS, GaAs HEMT	-108.0 dBc/Hz @ 1 MHz	-6.0 dBm	160 mW
[171]	18.1 GHz	Push-push oscillator	PCB, MS, GaAs FET	-93.2 dBc/Hz @100 KHz	1.9 dBm	120 mW
[172]	20 GHz	Oscillator	LTCC, SIW, GaAs HBT	-118.0 dBc/Hz @1 MHz	6.0 dBm	82.5 mW
This Work	28.15 GHz	Self-isolated harmonic active radiator	PCB, DR², Air-Filled SIW, GaAs LNA	-108.5 dBc/Hz @1 MHz	15.0 dBm	376 mW

¹ MS: Microstrip Line ² DR: Dielectric Resonator

5.3.3 Pulling effect mitigation experimental comparison with a fundamental frequency output active radiator

To validate the pulling effect mitigation performance of the proposed self-isolated harmonic active radiator, another active radiator with fundamental frequency output is designed and fabricated. It is shown in Fig. 5.21. It implements the same partially-air-filled SIW cavity, dielectric resonator and LNA as the harmonic active radiator. But the feeding at P3 is moved to P4, referring to Fig. 5.3. In this way, the cavity serves as a resonator and an antenna both using the TM₁₁₀ mode. In measurement, this active radiator transmits a fundamental frequency signal at 28.24 GHz with an EIRP of 8.2 dBm in the boresight direction.

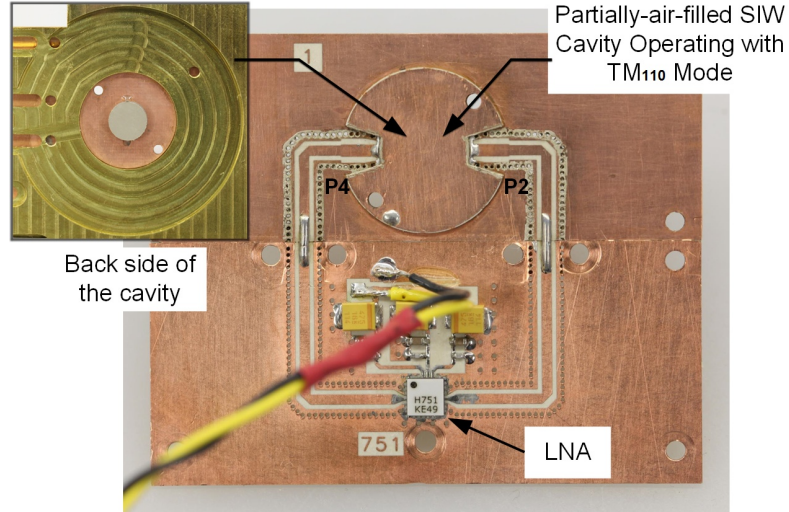


Figure 5.21: The fabricated active radiator with fundamental frequency output at 28.24 GHz, based on a partially-air-filled SIW cavity.

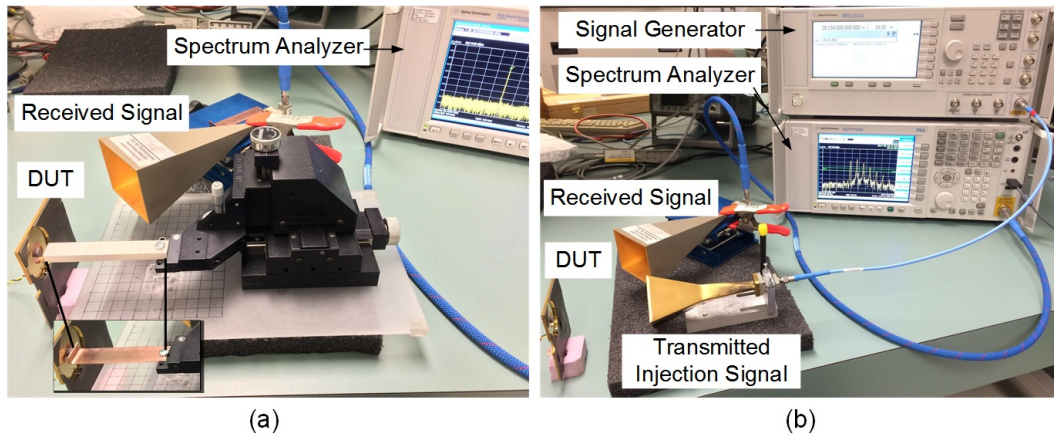


Figure 5.22: Measurement setups of (a) load pulling test and (b) injection pulling test.

Load pulling and injection pulling effects are tested using the setups shown in Fig. 5.22 (a) and Fig. 5.22 (b), respectively. The load pulling test uses a dielectric bar of Rogers RT/duriod 6010 substrate with a permittivity of 10.2 and a cross section dimension of 7.6 mm by 14 mm, as well as a copper bar with the same cross section dimension. They are mounted on a precise positioner and moved in a range of 0 to 10 mm away from the dielectric resonator. An MI-12A-26 horn antenna is connected to the spectrum analyzer to receive the radiated signal. Fig. 5.23 shows the variation of the radiated frequency of both radiators normalized by their respective open space radiation frequencies, and their phase noise at 1 MHz offset. It can be seen that the frequency pulling of the harmonic active radiator is about 10 times weaker than its fundamental counterpart. As the copper

bar is very close or touch the active radiators, the fundamental one stops operating, while the harmonic one is hardly affected. The phase noise relative variations are similar for both radiators. But the harmonic radiator has a lower absolute value.

The injection pulling test is carried out with the following conditions: the injection signal frequency is swept across an 80 MHz bandwidth about the respective free running frequencies of the two active radiators; the injection signal power is 15 dBm; a diagonal horn antenna FR6413 from ORBIT/FR with 17 dBi gain at 28 GHz is placed at 10 cm in front of the DUTs. The measured results are shown in Fig. 5.24. The harmonic radiator has about 17 times weaker frequency variation than its fundamental counterpart. Therefore, a significant frequency stability and phase noise improvement is achieved with the self-isolation concept and the tri-function cavity structure. Table 5.2 further summarized the characteristics of the two active radiators.

Table 5.2: Performance Summary of the Harmonic and Fundamental Active Radiators

	Harmonic	Fundamental
Frequency Output	28.15 GHz	28.24 GHz
Phase Noise at 1MHz offset	-108.5 dBc/Hz	-104 dBc/Hz
Boresight EIRP	13 dBm	8.2 dBm
Load Pulling Range (Normalized)	2.5×10^{-4}	2.4×10^{-3}
Injection Pulling Range (Normalized)	1.0×10^{-4}	1.7×10^{-3}

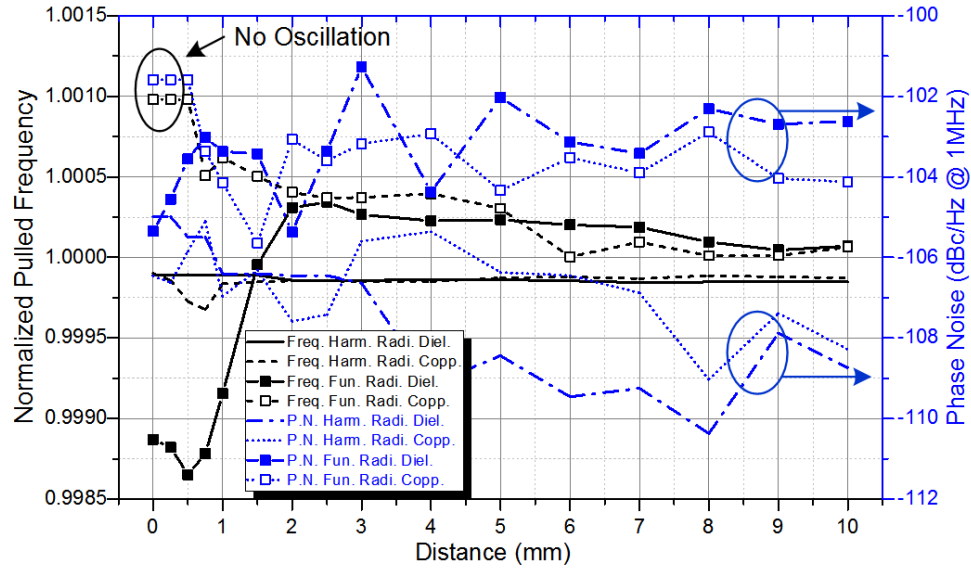


Figure 5.23: Measured normalized frequency and phase noise pulling of the harmonic radiator and the fundamental frequency radiator as the dielectric or the copper bar is positioned at different distance from the dielectric resonator.

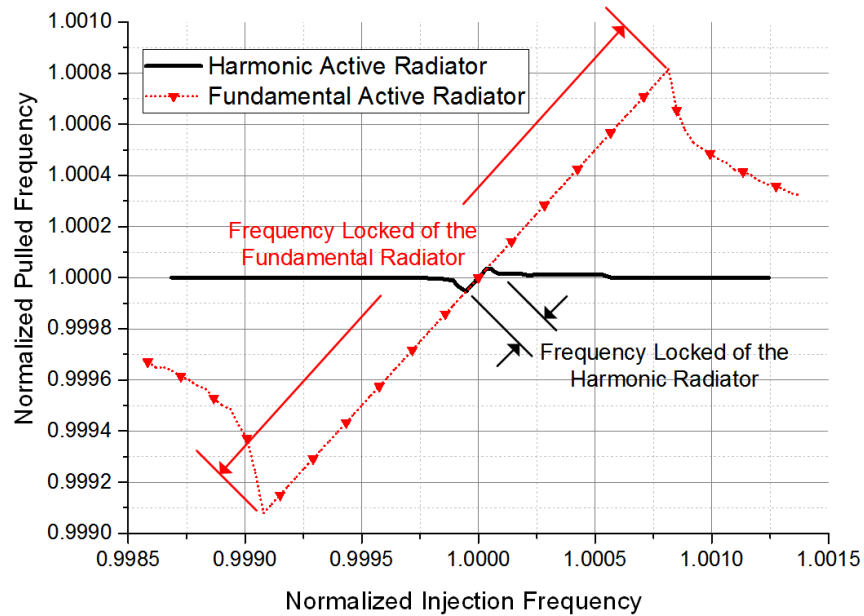


Figure 5.24: Measured normalized frequency of the signal from the active radiators with respect to the injection signal frequency.

5.4 Conclusion

This work proposed a self-isolated harmonic active radiator that oscillates at the fundamental frequency and radiates at the 2nd harmonic frequency of about 28 GHz simultaneously in the same structure. The achieved performance includes 15 dBm maximum EIRP, about 8 dBm TRP and -108.5 dBc/Hz phase noise at 1 MHz offset. Compared with an active radiator transmitting a fundamental frequency signal, the pulling effect caused by load variation or signal injection is significantly reduced. The radiator uses a partially-air-filled SIW cavity as a resonator, diplexer, and antenna concurrently, which provides characteristics of compact size, low pulling effects, and high power mmW signal generation. Such an active radiator topology is a promising candidate of low-cost signal source for mmW tag applications. Integration of such a structure on MMIC technologies is of much expectation for low-cost massive applications. The proposed tri-function cavity can be either realized out of the chip with printed technologies or on the chip with synthesized cavity structures reported by other researchers.

CHAPTER 6 ARTICLE 5: A MULTITARGET ACTIVE BACKSCATTERING 2-D POSITIONING SYSTEM WITH SUPER- RESOLUTION TIME SERIES POST-PROCESSING TECHNIQUE

Co-authored by Jian-Feng Gu, Fengchao Ren, and Ke Wu

Published in « *IEEE Transactions on Microwave Theory and Techniques* », 2017.

Abstract—An active backscattering two-dimensional (2-D) positioning system is studied and demonstrated in this work. The hardware is based on an investigated principle of switched injection phase-locking for wireless ranging. A new post-processing technique and system modeling for multiple-target time-of-arrival (TOA) and direction-of-arrival (DOA) estimations is proposed and studied. The technique features a joint singular value decomposition (SVD) based ESPRIT algorithm and a matrix diagonalization technique using Moore-Penrose pseudoinverse for model order estimation as well as the TOA/DOA extraction. They make use of the shift invariant property of a backscattered signal in the time-domain. The accuracy and resolution are studied and are shown to be superior to those of the conventional frequency-domain technique using a fast Fourier transform (FFT). Moreover, the proposed algorithms take full advantage of the chirp bandwidth and allow all the targets to operate at the same modulation frequency and arbitrary carrier frequency. These merits avoid a commonly exercised compromise of the FFT method among the resolution, target quantity, signal to noise ratio (SNR) and other critical specifications. The system is simulated, and the demonstrator is constructed for experimental verifications in both indoor and outdoor environments, with a bandwidth of 600 MHz centered at 5.6 GHz.

Index Terms—2-D positioning, active backscattering, multitarget, time-of-arrival, direction-of-arrival, ESPRIT, accuracy, resolution.

6.1 Introduction

Accurate indoor and outdoor physical positioning is one of the key enabling technologies for creating a unified wireless platform, which supports the functionality fusion of communication, sensing and powering. Future global and ubiquitous connectivity, internet of things (IoT) and eventually internet of space (IoS) are based on such a platform [173, 174]. Being aware of the position or location helps the nodes of an autonomous network (e.g. networks of industrial sensors, home appliances, and vehicles) to effectively interact and cooperate with each other [175] and also improves the communication throughput, latency, and robustness [176, 177]. With such an

application background in mind, researchers working on the wireless positioning technology are targeting at the exploration of technical features such as low cost, small footprint, real time, no/low power consumption, reduced demand for spectrum resources, high-density target deployment, and smart option for multi-function.

A large number of publications and documents have already contributed to this end and various theories and techniques of wireless positioning have been developed for different applications [2, 9]. The most commonly used positioning techniques are related to GPS, Galileo, GLONASS and BeiDou systems. They are all self-positioning oriented. Generally speaking, geometry information based system (e.g. measuring the angle-of-arrival) and propagation time based system are the two broad categories of remote or wireless positioning systems that enable achieving a sub-decimetre accuracy. The former needs a number of distributed base stations with prior-known coordinates for angle detection, based on which the distance is calculated through trigonometry. The latter requires absolute or relative time synchronization depending on specific architectures. The well-known and widely deployed frequency-modulated continuous-wave (FMCW) radar is a typical round-trip time-of-flight (TOF) positioning concept [17-19]. It has a relative time synchronization requirement fulfilled by the base station generating a highly linear and precise modulated waveform, which can easily be realized with VCO/PLL or DDS techniques [20]. Many researchers have been focusing on the development of the derivatives of FMCW system, thereby attempting to make breakthroughs with regards to longer range, lower bandwidth, higher sensitivity, multitarget identification and immunity to multipath. The essentials of some of these works can be concluded as adding modulation capabilities to the targets [21-23]. This move would be able to avoid low-frequency noise and passive clutter scattering. Moreover, data can be modulated on the backscattered signal of the targets. However, a major drawback is related to a heavy burden of dynamic range on the amplification stages of the targets and a limited link gain improvement. The signal has to travel through the round-trip distance, and the link loss is thus proportional to the 4th power of distance. On the other front, researchers have successfully implemented the concept of MIMO to realize a super-resolution FMCW system for dense multipath environment [24].

In recent years, a new positioning scheme based on switched injection-locked oscillator (SILO) has been brought to light. As it has been discussed in the literature [31-34], it extends the concept of conventional FMCW system and exhibits the advantages of simple structure, high precision, long range, and insensitive to clutter as well as the feasibility of simultaneous data transmission. It can be regarded as a discrete form of conventional FMCW radar. Since the signal out of the target

is spontaneous rather than a modulated/amplified duplicate of the interrogation signal, the link loss is solely proportional to the 2nd power of distance. For such a system, a fast Fourier transform (FFT) is usually employed to convert the baseband into the frequency-domain and the range is then calculated by $d = c \times \Delta f / 4\Omega$, in which c is the speed of light, Ω is the chirp rate (Hz/s), and Δf is the frequency difference between the two peaks centered around the modulation frequency of the target. Such a frequency-domain technique maintains a significant accuracy as long as only one single target is in the range of detection. As more targets come into play, their modulation frequency has to be appropriately staggered such that the corresponding characteristic peaks in the spectrum can be differentiated and the spectrum leakage issue can be minimized. At the same time, the pulse width of the targets has to be short enough for an increased peak sharpness so as to guarantee a low mean error [34] as well as to avoid a multitarget overlapping. However, the reduced pulse width would lower down the duty cycle and in turn the signal to noise ratio (SNR). In this work, a time-domain post-processing technique is proposed, developed and implemented with such a hardware architecture to overcome certain drawbacks and improve the system performance. Instead of using the orthogonal decomposition principle of the Fourier transform, the proposed method is based on a subspace decomposition, which has higher degrees of freedom and inherently enjoys the benefit of noise reduction. Without imposing any requirement on the pulse width and duty cycle, the proposed method is always valid whether the characteristic peaks of multitargets are aliased in the spectrum or not.

This paper is organized as follows. Section 6.2 introduces the system principle and architecture, based on which the generalized signal model taking into account multiple targets and antennae is developed. The Doppler effect is also included in the model. In Section 6.3, the methodology of parameter estimations including the number of targets, time-of-arrival (TOA) and direction-of-arrival (DOA) is presented in detail. The baseband signal in the base station is sampled and converted into a time series, and subsequently, matrix building and stacking techniques, as well as different solving methods are jointly used for the post-processing. In Section 6.4, the system performance is analyzed with a comparison between the proposed algorithm and the FFT technique for technical specifications, including the SNR, accuracy, resolution and others. The impact of sampling un-synchronization to the turn-on instant of the target is also studied. Simulations are performed to verify the analyses. Cramer-Rao lower bound (CRLB) and root mean square error (RMSE) are used to characterize the accuracy and resolution performances. Experimental demonstrations are carried out based on the designed and fabricated hardware which will be

presented in Section 6.5. The circuit design for both the base station and the targets are shown. Data acquired from indoor and outdoor measurements are processed by both the proposed methodology and the FFT method. The results are discussed and compared. Section 6.6 concludes the work with comments and prospects.

6.2 System Architecture and Signal Model

As introduced in [31], an active backscattering positioning system consists of a SILO based target and an FMCW radar base station. The base station transmits a chirp interrogation signal. The SILO is turned on/off by closing/opening the feedback loop at a fixed rate and duty cycle such that the target transmits a series of amplitude modulated (AM) pulses. Within the pulse durations, although the free-running oscillator operates at its eigenfrequency, at the turn-on instant leading each pulse, the phase of the oscillation signal is locked to that of the interrogation signal delayed by the TOF between the base station and the target. In the proposed system, the base station has one transmitting (Tx) and J receiving (Rx) channels with one antenna associated with each of them. K targets are in the range of detection. The system architecture and the Rx antennae configuration are illustrated in Fig. 6.1.

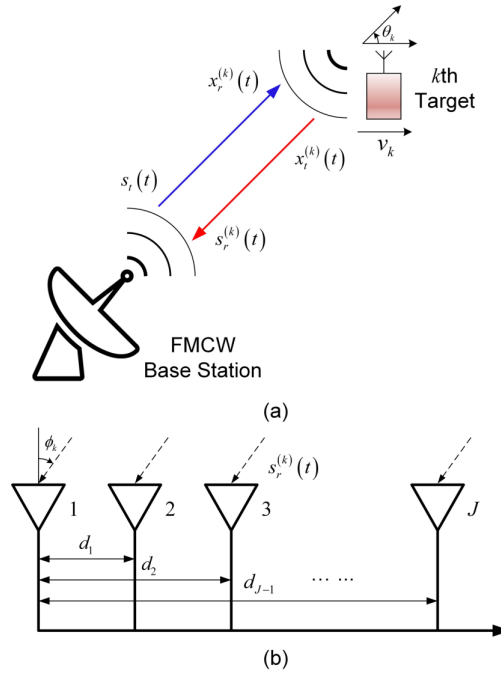


Figure 6.1: (a) System architecture and (b) Rx antennae array.

By using an antenna array with at least two uncorrelated elements ($J \geq 2$), the base station can detect not only the range but also the angle. Distances d_j are normalized with half of the free space

wavelength. $d_1 < 1$ is required to avoid ambiguity for the angular detection in a range of $-90^\circ \sim 90^\circ$ [178]. In the following sections, a mathematical model of the over-the-air and the processed signals is established. The signals are in complex form unless mentioned otherwise.

6.2.1 Transmitted FMCW interrogation waveform

A periodical linear chirp signal in the baseband of the base station's transmitter has the following expression

$$\bar{s}_t(t) = \exp\left[j2\pi \frac{g}{2}(t - mT_s)^2\right] q(t), \quad (6.1)$$

in which $m = 0, 1, 2, \dots$; and $g = \pm BW/T_s$ denotes the up/down chirp rate where T_s is the chirp period, and BW is the bandwidth. The amplitude is normalized for simplicity. The chirp duration window function $q(t)$ has the following expression:

$$q(t) = \begin{cases} 1 & t \in [mT_s, (m+1)T_s) \\ 0 & \text{otherwise} \end{cases}. \quad (6.2)$$

The baseband signal is then up-converted with carrier frequency f_c and is expressed by:

$$s_t(t) = \bar{s}_t(t) \exp(j2\pi f_c t). \quad (6.3)$$

Such an interrogation signal is received by the k th target with delay and Doppler shift:

$$x_r^{(k)}(t) = a_{xr}^{(k)} \bar{s}_t(t - \tau_k) \exp\left[j2\pi (f_c + f_d^{(k)})(t - \tau_k)\right], \quad (6.4)$$

in which $a_{xr}^{(k)}$ and τ_k are the transmission attenuation and the TOF between the base station and the k th target, respectively. The Doppler shift seen by the k th target referred to the base station is $f_d^{(k)}$.

With a narrow band approximation, it is expressed by:

$$f_d^{(k)} = v_k \cos(\theta_k) f_c / c, \quad (6.5)$$

in which v_k and θ_k are the speed and the direction of the k th target, respectively. The speed of light is c .

6.2.2 Backscattered signal from active targets

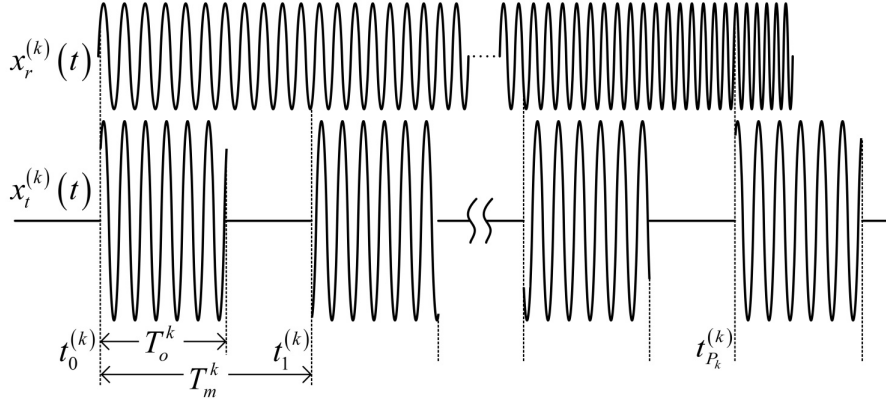


Figure 6.2: Backscattered waveform from the k th target.

Fig. 6.2 illustrates the waveform $x_t^{(k)}(t)$ transmitted by the k th target in a single chirp period with the existence of the interrogation signal $x_r^{(k)}(t)$. The turn-on instant is at:

$$t_{p_k}^{(k)} = t_0^{(k)} + p_k T_m^{(k)}, \quad (6.6)$$

in which $p_k = 0, 1, 2, \dots, P_k$; and $T_m^{(k)}$ is the pulse period of the k th target. $T_o^{(k)}$ is the on-duration of the k th target, and $t_0^{(k)}$ is the first phase synchronized turn-on instant in the first chirp period ($m=0$) of the k th target, $\tau_k \leq t_0^{(k)} < \tau_k + T_m^{(k)}$. At $t_{p_k}^{(k)}$ the phase of the backscattered signal is assumed to be perfectly locked to that of the interrogation signal, which is expressed by:

$$\phi_r^{(k)}(t_{p_k}^{(k)}) = 2\pi \left[(f_c + f_d^{(k)})(t_{p_k}^{(k)} - \tau_k) + \frac{g}{2}(t_{p_k}^{(k)} - \tau_k)^2 \right]. \quad (6.7)$$

As such, the backscattered signal from the k th target is:

$$x_t^{(k)}(t) = a_{xt}^{(k)} \sum_{p_k=0}^{P_k} \left\{ \bar{q}_{p_k}^{(k)}(t) \cdot \exp \left[j\phi_r^{(k)}(t_{p_k}^{(k)}) \right] \cdot \exp \left[j2\pi f_c^{(k)}(t - t_{p_k}^{(k)}) \right] \right\}, \quad (6.8)$$

where $a_{xt}^{(k)}$ is the transmitted amplitude, $f_c^{(k)}$ is the carrier frequency of the oscillator on the k th target, and $\bar{q}_{p_k}^{(k)}(t)$ is the pulse window function, expressed by:

$$\bar{q}_{p_k}^{(k)}(t) = \begin{cases} 1 & t \in [t_{p_k}^{(k)}, t_{p_k}^{(k)} + T_o^{(k)}] \\ 0 & \text{otherwise} \end{cases}. \quad (6.9)$$

Equation (6.8) can be regarded as a sampled interrogation signal modulated on carrier frequency $f_c^{(k)}$.

6.2.3 Received waveforms by base station

The backscattered signal from the k th target is received by one of the Rx channels of the base station, with delay and Doppler shift:

$$s_r^{(k)}(t) = a_{sr}^{(k)} a_{xt}^{(k)} \sum_{p_k=0}^{P_k} \left\{ \bar{q}_{p_k}^{(k)}(t - \tau_k) \cdot \exp \left[j\phi_r^{(k)}(t_{p_k}^{(k)}) \right] \cdot \exp \left[j2\pi \left(f_c^{(k)} + f_d^{(k)} \right) (t - t_{p_k}^{(k)} - \tau_k) \right] \right\}, \quad (6.10)$$

in which $a_{sr}^{(k)}$ is the transmission attenuation between the k th target and the base station. As such, the total signal received by the base station is simply the sum of (6.10) from $k=1$ to $k=K$. After the down-conversion by the carrier frequency f_c in the base station, the total received signal is:

$$\bar{s}_r(t) = \sum_{k=1}^K \bar{a}_k \sum_{p_k=0}^{P_k} \exp \left[j2\pi \left(f_{md}^{(k)} (t - t_{p_k}^{(k)} - \tau_k) + f_d^{(k)} t_{p_k}^{(k)} + \frac{g}{2} (t_{p_k}^{(k)} - \tau_k)^2 \right) \right] q_{p_k}^{(k)}(t), \quad (6.11)$$

where

$$\bar{a}_k = a_{sr}^{(k)} a_{xt}^{(k)} \exp \left[-j2\pi \left(2f_c + f_d^{(k)} \right) \tau_k - j2\pi\theta \right], \quad (6.12)$$

in which θ is the phase of the LO signal, and

$$f_{md}^{(k)} \triangleq f_d^{(k)} + \Delta f_c^{(k)}, \quad (6.13)$$

in which $\Delta f_c^{(k)}$ is the carrier frequency offset of the k th target defined by $\Delta f_c^{(k)} \triangleq f_c^{(k)} - f_c$. While

$$q_{p_k}^{(k)}(t) = \begin{cases} 1 & t \in \left[t_{p_k}^{(k)} + \tau_k, t_{p_k}^{(k)} + T_o^{(k)} + \tau_k \right] \\ 0 & \text{otherwise} \end{cases}. \quad (6.14)$$

The previously proposed frequency-domain approach in [31] estimates the TOF with two assumptions, the first requiring that the Doppler shift being negligible, and

$$\exp[j2\pi g t] q_{p_k}^{(k)}(t) \approx \exp \left[j2\pi g \left(t_{p_k}^{(k)} + \tau_k + \frac{T_o^{(k)}}{2} \right) \right], \quad (6.15)$$

$$\text{when } t \in \left[t_{p_k}^{(k)} + \tau_k, t_{p_k}^{(k)} + T_o^{(k)} + \tau_k \right].$$

The second assumption requires a narrow pulse width or a low duty cycle. As explained in section 6.4.1 with more details, this requirement reduces the SNR. Actually, our proposed technique doesn't rely on such assumptions.

The down-converted signal $\bar{s}_r(t)$ is then mixed with the baseband chirp signal in a single chirp period, producing:

$$\begin{aligned} \bar{z}_r(t) &= \bar{s}_t(t) \bar{s}_r^*(t) \\ &= \sum_{k=1}^K \bar{a}_k \sum_{p_k=0}^{P_k} \exp \left[j2\pi \left(\left(\frac{g}{2} (t - t_{p_k}^{(k)} - \tau_k) + g\tau_k - f_{md}^{(k)} \right) (t - t_{p_k}^{(k)} - \tau_k) + \right. \right. \\ &\quad \left. \left. \left(g(t - t_{p_k}^{(k)} - \tau_k) + 2g\tau_k - f_d^{(k)} \right) t_{p_k}^{(k)} \right) \right] \cdot \tilde{q}_{p_k}^{(k)}(t - t_{p_k}^{(k)} - \tau_k), \end{aligned} \quad (6.16)$$

in which

$$\tilde{q}_{p_k}^{(k)}(t) = \begin{cases} 1 & t \in [0, T_o^{(k)}] \\ 0 & \text{otherwise} \end{cases}, \quad (6.17)$$

and $*$ is the complex conjugate operation. Such a baseband signal from one of the Rx channels is then digitized with a sampling period of T by substituting t with $nT + T_{rd}$, in which T_{rd} is an unknown parameter representing the initial sampling instant, and $n=0, 1, 2, \dots$. If $T_m^{(k)} = T_m$ for $k=1, 2, \dots, K$, and T_m/T is an integer, then the following time series can be defined:

$$z_r(n) = \sum_{k=1}^K \bar{a}_k \sum_{p_k=0}^{P_k} \exp \left[j2\pi \left(\left(\frac{g}{2} (n_k T + T_{rd}^{(k)} - \tau_k) + g\tau_k - f_{md}^{(k)} \right) (n_k T + T_{rd}^{(k)} - \tau_k) + \right. \right. \\ \left. \left. \left(g(n_k T + T_{rd}^{(k)} - \tau_k) + 2g\tau_k - f_d^{(k)} \right) t_{p_k}^{(k)} \right) \right] \cdot \tilde{q}_{p_k}^{(k)}(n_k T + T_{rd}^{(k)} - \tau_k). \quad (6.18)$$

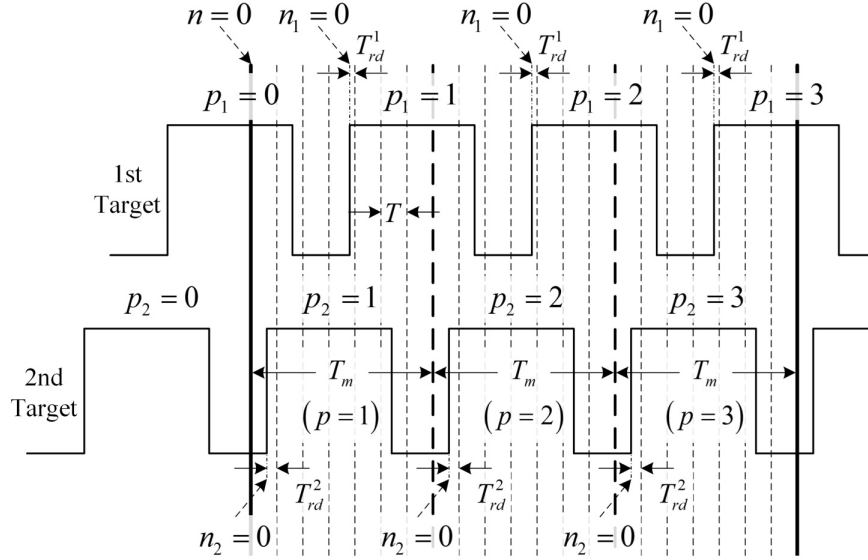


Figure 6.3: Timing diagram of the sampled baseband signal.

Fig. 6.3 illustrates the baseband signal sampling in case of two targets. To be clear, high/low levels are used in the diagram to represent the on/off states although the real baseband signals during the on states are short chirps, which can be seen from (6.16). As shown in Fig. 6.3 and (6.18), the global sampling points counted by n are divided into local sampling points counted by n_k which is repeated with the period of T_m . The time shift between the local sampling instant $n_k T$ and the actual sampling instant is represented by $T_{rd}^{(k)} \in [-T/2, T/2]$.

Such a shift is ignored for the time being and its effect on the parameter estimation accuracy is discussed in section 6.4.2 Then the time series is re-written as:

$$z_r(n) = \sum_{k \in \Omega_n} \sum_{p_k=0}^{P_k} \bar{a}_k \exp \left[j2\pi \left(\left(\frac{g}{2} n_k T + g\tau_k - f_{md}^{(k)} \right) n_k T + \left(g n_k T + 2g\tau_k - f_d^{(k)} \right) p_k T_m^{(k)} \right) \right], \quad (6.19)$$

where $\bar{a}_k = \bar{a}_k \exp[j2\pi(g n_k T + 2g\tau_k - f_d^{(k)})t_0^{(k)}]$ and $\Omega_n = \{k | 1 \leq k \leq K \text{ and } 0 \leq n_k T \leq T_o^{(k)}\}$ whose cardinality is assumed to be K_n . For the p th period of modulation, (6.19) can be simplified to:

$$z_r^{(p)}(n) = \sum_{k \in \Omega_n} a_k(n_k) \exp[jp\alpha_k(n_k)], \quad (6.20)$$

where $a_k(n_k) = \bar{a}_k \exp[j2\pi(g n_k T/2 + g\tau_k - f_{md}^{(k)})n_k T + j\hat{p}_k(n_k)\alpha_k(n_k)]$, $\alpha_k(n_k) = 2\pi(g n_k T + 2g\tau_k - f_d^{(k)})T_m^{(k)}$, and $\hat{p}_k(n_k) = p_k - p$ which only depends on n_k and is irrelevant to p or p_k .

6.2.4 Discussion

A few comments can be made by observing the constructed signal model. First of all, it can be seen that both a_k and α_k are constant for different p when n_k is fixed. Such a shift invariant property can be exploited for matrix construction and subspace-based parameter estimations. The expression of α_k suggests that to estimate the delay and the Doppler shift simultaneously, both up and down chirps have to be used, which is unnecessary under the scenario of static or low speed.

Secondly, the assumption of coherent pulse rate ($T_m^{(k)} = T_m$ for $k=1, 2, \dots, K$) relies on inter-target synchronization techniques or extremely accurate time references (e.g. rubidium clocks) for real implementation. However, none of the two techniques should be considered in the proposed system since they significantly increase the system complexity and cost. Actually, the pulse rate coherency can be relaxed so that the shift invariant property of a_k and α_k is satisfied with certain tolerance during every few pulse periods instead of the entire chirp period. In this way, the parameter estimations are carried out in each of the coherence duration, and the overall result is obtained by post-averaging. As such, off-the-shelf commercial oscillators (e.g. VCXO and TCXO) can be used.

Thirdly, a conventional subspace based parameter estimation method requires that the model order (number of targets) K_n has to be known in advance. However, this is not practical in real applications. Moreover, the number of targets seen by the base station varies from sample to sample, which can be interpreted from Fig. 6.3. Therefore, the model order has to be estimated sample by sample before other parameters can be estimated. Most existing techniques rely on the hypothesis test for an additive white noise and the method of information theoretic criteria [179-181]. To implement these methods, two terms have to be obtained. One is the postulated likelihood, and the other is the user-defined threshold or penalty term [180, 182], which are very hard to select in practice. In our proposed method, the signal model property such as the shift invariance is taken advantage of to avoid the procedure of penalty term selection [183, 184].

Finally, the transmitted signal from a single target is a monotone spectrum-spread by a *Sinc* function. Its bandwidth is much smaller than BW due to the low pulse rate (several MHz to tens of MHz). As such, if $f_c^{(k)}$ is roughly the center frequency of the chirp (e.g. $\Delta f_c^{(k)} \approx BW/2$), the baseband signal has a bandwidth of about $BW/2$. The frequency-domain approach is used to calculate τ_k by identifying the two lowest frequency peaks around $f = 1/T_m$ in the baseband

spectrum, and the majority of the spectrum is discarded by filtering. This is equivalent to using a chirp bandwidth of $4/T_m$ which is usually much smaller than BW . In other words, the chirp bandwidth cannot be fully exploited to obtain the expected resolution.

6.3 Algorithm Development of Model Order Detection and Parameter Estimation

In this section, the shift invariant property of the constructed signal model is used to develop the algorithm for detecting the model order (number of targets) and estimating the parameters including τ_k and $f_d^{(k)}$. Firstly, assuming the model order K_n is a known value, the method to estimate $\alpha_k(n_k)$ at a fixed n (or n_k) is developed in 6.3.1 based on a matrix construction technique. Then, in 6.3.2, the algorithm for estimating K_n is introduced based on the signal property and the constructed matrices. These two sections bring forward the mathematical foundations of parameter estimation using one single sample of the baseband signal from one Rx channel. To aggregate the information from multiple samples and multiple channels for an improved performance as well as a joint estimation of the TOA and the DOA, matrix stacking techniques are developed in 6.3.3 and 6.3.4. The technique of staking matrices associated with adjacent samples is introduced in 6.3.3 while that of staking matrices constructed from different channels is introduced in 6.3.4.

6.3.1 Principle of matrix construction and solution

If the coherence duration includes P pulse periods, a $(L+1)$ by $(P-L)$ Hankel matrix is constructed as follows:

$$\mathbf{Z}(n) = \begin{bmatrix} z_r^{(0)}(n) & z_r^{(1)}(n) & \cdots & z_r^{(P-L-1)}(n) \\ z_r^{(1)}(n) & z_r^{(2)}(n) & \cdots & z_r^{(P-L)}(n) \\ \vdots & \vdots & \ddots & \vdots \\ z_r^{(L)}(n) & z_r^{(L+1)}(n) & \cdots & z_r^{(P-1)}(n) \end{bmatrix}. \quad (6.21)$$

The data is assumed to be free of additive white noise. In practical applications, this assumption can be supported with forward and backward averaging operations by extending the matrix as:

$$\mathbf{Z} \rightarrow \begin{bmatrix} \mathbf{Z} & \mathbf{J}_{L+1} \mathbf{Z}^* \mathbf{J}_{P-L} \end{bmatrix}, \quad (6.22)$$

in which \mathbf{J}_a is a dimension unit anti-diagonal square matrix (exchange matrix), and symbol $*$ means the complex conjugate operation.

If K_n is known, matrix $\mathbf{Z}(n)$ has a Vandermonde decomposition:

$$\mathbf{Z}(n) = \mathbf{A}_{L+1}(n) \mathbf{\Delta}(n) \mathbf{A}_{P-L}^T(n), \quad (6.23)$$

in which

$$\mathbf{\Delta}(n) = \text{diag}(\boldsymbol{\delta}(n)), \quad (6.24)$$

is a K_n by K_n diagonal matrix where

$$\boldsymbol{\delta}(n) = \begin{bmatrix} a_{k1}(n_{k1}) & a_{k2}(n_{k2}) & \cdots & a_{kK_n}(n_{kK_n}) \end{bmatrix}^T, \quad (6.25)$$

and $k1, k2, \dots, kK_n \in \Omega_n$. Matrix $\mathbf{A}_a(n)$ is a Vandermonde matrix with the rotation-invariant property:

$$\mathbf{A}_a(n) = \begin{bmatrix} \gamma_a(\alpha_{k1}) & \gamma_a(\alpha_{k2}) & \cdots & \gamma_a(\alpha_{kK_n}) \end{bmatrix}, \quad (6.26)$$

in which $\gamma_a(\alpha_k) = [1 \exp[j\alpha_k] \cdots \exp[j(a-1)\alpha_k]]$. In (6.26), the argument n_k of $\alpha_k(n_k)$ is omitted. It can be verified that if $\alpha_{k1} \neq \alpha_{k2}$ for all $k1 \neq k2$ and $k1, k2 \in \Omega_n$, the rank of $\mathbf{Z}(n)$ is $\min\{K_n, L+1, P-L\}$. L results from a tradeoff among the array aperture of the matrix, the number of sampling points of each subarray and the computational burden [185]. The optimal performance is usually reached when the matrix $\mathbf{Z}(n)$ is as square as possible [186].

If $\min\{(L+1), (P-L)\} > K_n$, the singular value decomposition (SVD) of $\mathbf{Z}(n)$ can be expressed by:

$$\mathbf{Z} = \begin{bmatrix} \mathbf{E}_s & \mathbf{E}_n \end{bmatrix} \begin{bmatrix} \boldsymbol{\Sigma} & \mathbf{0} \\ \mathbf{0} & \mathbf{0} \end{bmatrix} \mathbf{U}^H. \quad (6.27)$$

The $(L+1)$ by K_n matrix \mathbf{E}_s and the $(L+1)$ by $(L+1-K_n)$ matrix \mathbf{E}_n correspond to nonzero and zero singular values, and are called the signal subspace and the noise subspace respectively. $\boldsymbol{\Sigma}$ is a K_n by K_n diagonal matrix with nonzero singular values, and \mathbf{U} is a $(P-L)$ by $(P-L)$ matrix of singular vectors. Operation H is the conjugate transpose. The signal and noise subspaces are orthogonal to each other, so the following equation can be obtained:

$$\mathbf{E}_n^H \mathbf{Z}(n) = \begin{bmatrix} \mathbf{E}_n^H \mathbf{E}_s & \mathbf{E}_n^H \mathbf{E}_n \end{bmatrix} \begin{bmatrix} \boldsymbol{\Sigma} & \mathbf{0} \\ \mathbf{0} & \mathbf{0} \end{bmatrix} \mathbf{U}^H = \mathbf{0}. \quad (6.28)$$

It can be verified that $\boldsymbol{\Delta}(n) \mathbf{A}_{p-L}^T(n)$ is a full row rank matrix, so (6.28) implies $\mathbf{E}_n^H \mathbf{A}_{L+1}(n) = \mathbf{0}$. Since both \mathbf{E}_s and $\mathbf{A}_{L+1}(n)$ are full column rank, and they are both orthogonal to \mathbf{E}_n , they are isomorphic. So, there is a K_n by K_n invertible matrix \mathbf{G} such that:

$$\mathbf{E}_s = \mathbf{A}_{L+1} \mathbf{G}. \quad (6.29)$$

On the other hand, it is easy to find the following relationship:

$$\mathbf{A}_{L+1}(1:L, :) = \mathbf{A}_{L+1}(2:L+1, :) \boldsymbol{\Phi}, \quad (6.30)$$

in which

$$\boldsymbol{\Phi} = \text{diag} \left[\exp(-j\alpha_{k1}) \quad \exp(-j\alpha_{k2}) \quad \cdots \quad \exp(-j\alpha_{kK_n}) \right]. \quad (6.31)$$

If $\mathbf{E}_s^{(1)} \triangleq \mathbf{E}_s(1:L, :)$ and $\mathbf{E}_s^{(2)} \triangleq \mathbf{E}_s(2:L+1, :)$, and considering (6.29) and (6.30), it can be verified that $\mathbf{E}_s^{(1)} = \mathbf{E}_s^{(2)} \mathbf{G}^{-1} \boldsymbol{\Phi} \mathbf{G} \triangleq \mathbf{E}_s^{(2)} \mathbf{C}$. By calculating the Moore-Penrose left pseudoinverse of $\mathbf{E}_s^{(2)}$, \mathbf{C} can be obtained:

$$\mathbf{C} = \left(\mathbf{E}_s^{(2)H} \cdot \mathbf{E}_s^{(2)} \right)^{-1} \cdot \mathbf{E}_s^{(2)H} \cdot \mathbf{E}_s^{(1)}, \quad (6.32)$$

which is essentially the least-squares (LS) solution of matrix \mathbf{C} . Since matrix \mathbf{C} and matrix $\boldsymbol{\Phi}$ are similar to each other, they have the same eigenvalues $\exp(-j\alpha_k)$ ($k \in \Omega_n$), so α_k can be obtained.

6.3.2 Algorithm for model order estimation

As was suggested by [184], without additive noise:

$$\boldsymbol{\Gamma}_P^V \triangleq \mathbf{P}_{\mathbf{A}_{L+1}^V}^\perp \boldsymbol{\Gamma}^V = \mathbf{0} \Leftrightarrow V = K_n, \quad (6.33)$$

in which V is the assumed model order (number of targets). Under this assumption, $\boldsymbol{\Gamma}^V \triangleq [\mathbf{E}_s^{(1)} \quad \mathbf{E}_s^{(2)}]$ is constructed, and \mathbf{A}_{L+1}^V is the left matrix in the Vandermonde decomposition of \mathbf{Z} . \mathbf{P}_Λ^\perp is the orthogonal complement of the projection of matrix $\boldsymbol{\Lambda}$, which is calculated as $\mathbf{I} - \boldsymbol{\Lambda}(\boldsymbol{\Lambda}^H \boldsymbol{\Lambda})^{-1} \boldsymbol{\Lambda}^H$. This criterion can be used for the model order estimation. However, it usually results in an under-estimation as the SNR is low in real applications. Because of this drawback, another criterion is introduced based on the fact that:

$$\mathbf{Z}_P^V \triangleq \mathbf{P}_{\mathbf{A}_{L+1}^V}^\perp \mathbf{Z} = 0 \Leftrightarrow V \geq K_n. \quad (6.34)$$

Using these two criteria, a generalized likelihood ratio test can be defined for the model order estimation:

$$\hat{K}_n = \arg \max_{k \in [1, \min(L+1, P-L)]} \frac{1}{\sigma(\mathbf{\Gamma}_P^V) \sigma(\mathbf{Z}_P^V)}, \quad (6.35)$$

in which $\sigma(\cdot)$ means the largest singular value.

6.3.3 Matrix stacking and joint SVD technique

The above-discussed signal model and algorithm are developed and presented in a sample-by-sample manner. In practical applications, certain adjacent sampling points comprise the backscattered signals from the same group of targets, such as the samples at $n=2\sim 3$ (from the 2nd target only) and the samples at $n=4\sim 5$ (from the 1st and the 2nd targets) in Fig. 6.3. These adjacent sampling points have similar properties and can be used for joint SVD for parameter estimations (pre-average). On the contrary, the sample-by-sample manner (post-average) will lose the correlations between those adjacent samples and will reduce the parameter estimation resolution as well as the efficiency.

It can be found that $\alpha_k(n_k)$ is divided into two parts:

$$\alpha_k(n_k) = \hat{\alpha}_k + \tilde{\alpha}(n_k), \quad (6.36)$$

where $\hat{\alpha}_k = 2\pi T_m^{(k)}(2g\tau_k - f_d^{(k)})$ is constant and $\tilde{\alpha}(n_k) = 2\pi T_m^{(k)}g n_k T$ depends on the sample number n_k . A new time series is defined as follows:

$$y_r^{(p)}(n+l_n) = z_r^{(p)}(n+l_n) \exp[-jp\tilde{\alpha}(l_n)] = \sum_{k \in \Omega_n} a_k(n_k+l_n) \exp[jp\alpha_k(n_k)]. \quad (6.37)$$

Similar to (6.21) and (6.23) of matrix construction and Vandermonde decomposition, a new matrix with $y_r^{(p)}(n+l_n)$ as the elements can be built and de-composited as:

$$\mathbf{Y}(n+l_n) = \mathbf{A}_{L+1}(n) \mathbf{\Delta}(n+l_n) \mathbf{A}_{P-L}^T(n). \quad (6.38)$$

Assuming L_n is the number of the adjacent sampling points following the n th sampling point in the p th period, a stacked matrix is defined and de-composited as:

$$\mathbf{Y}_{L_n}(n) = \begin{bmatrix} \mathbf{Y}^T(n) & \mathbf{Y}^T(n+2) & \cdots & \mathbf{Y}^T(n+L_n-1) \end{bmatrix}^T = [\hat{\Delta}(n) \circ \mathbf{A}_{L+1}(n)] \mathbf{A}_{P-L}^T(n). \quad (6.39)$$

In the 2nd line of this equation, the operator ‘ \circ ’ is the Khatri-Rao product defined as the stack of the Kronecker products (‘ \otimes ’) of the column vectors of matrices \mathbf{A} and \mathbf{B} , which have the same number of columns:

$$\mathbf{A} \circ \mathbf{B} = \begin{bmatrix} \mathbf{a}_1 \otimes \mathbf{b}_1 & \mathbf{a}_2 \otimes \mathbf{b}_2 & \cdots & \mathbf{a}_M \otimes \mathbf{b}_M \end{bmatrix},$$

and

$$\hat{\Delta}(n) \triangleq \begin{bmatrix} \delta(n) & \delta(n+1) & \cdots & \delta(n+L_n-1) \end{bmatrix}^T. \quad (6.40)$$

The SVD of the stacked matrix is expressed by:

$$\mathbf{Y}_{L_n} = \begin{bmatrix} \hat{\mathbf{E}}_s & \hat{\mathbf{E}}_n \end{bmatrix} \begin{bmatrix} \hat{\Sigma} & \mathbf{0} \\ \mathbf{0} & \mathbf{0} \end{bmatrix} \hat{\mathbf{U}}^H, \quad (6.41)$$

in which $\hat{\mathbf{E}}_s$ and $\hat{\mathbf{E}}_n$ are $(L+1)L_n$ by K_n and $(L+1)L_n$ by $(L+1)L_n - K_n$ matrices respectively. Similar to (6.28), and due to the fact that $\mathbf{A}_{P-L}^T(n)$ is a full row matrix, there is a K_n by K_n invertible matrix $\hat{\mathbf{G}}$ such that:

$$\hat{\mathbf{E}}_s = [\hat{\Delta}(n) \circ \mathbf{A}_{L+1}(n)] \hat{\mathbf{G}}. \quad (6.42)$$

Because of the following relationship:

$$\hat{\Delta}(n) \circ \mathbf{A}_{L+1}(1:L, :) = \hat{\Delta}(n) \circ \mathbf{A}_{L+1}(2:L+1, :) \Phi, \quad (6.43)$$

a similar conclusion as given by (6.32) will be drawn, by defining $\hat{\mathbf{E}}_s^{(1)} \triangleq \hat{\mathbf{E}}_s(1:L, :)$ and $\hat{\mathbf{E}}_s^{(2)} \triangleq \hat{\mathbf{E}}_s(2:L+1, :)$: α_k can be obtained by calculating the eigenvalues of $\hat{\mathbf{C}} = (\hat{\mathbf{E}}_s^{(2)H} \hat{\mathbf{E}}_s^{(2)})^{-1} \hat{\mathbf{E}}_s^{(2)H} \hat{\mathbf{E}}_s^{(1)}$.

6.3.4 Joint estimation of the TOA and DOA

In the proposed system, as shown in Fig. 6.1, the measurement of both the TOA and DOA is achieved by an antenna array which comprises J independent antennae associated with each of the Rx channels. J matrices with the same form of $\mathbf{Y}_{L_n}(n)$ in (6.39) can be expressed by:

$$\mathbf{Y}_{L_n}^{(j)}(n) = [\hat{\Delta}(n) \circ \mathbf{A}_{L+1}(n)] \Upsilon^{(j)} \mathbf{A}_{P-L}^T(n), \quad j=1, 2, \dots, J, \quad (6.44)$$

where $\Upsilon^{(j)} = \text{diag}[\exp(-jd_{j-1}\pi\sin\phi_{k1}) \exp(-jd_{j-1}\pi\sin\phi_{k2}) \dots \exp(-jd_{j-1}\pi\sin\phi_{kK_n})]$ and $d_0 = 0$, which means the first antenna element is the reference. The only difference between $\mathbf{Y}_{L_n}(n)$ in (6.39) and $\mathbf{Y}_{L_n}^{(j)}(n)$ is that in the latter ones, $a_k(n_k)$ is multiplied by a factor $\exp(-jd_{j-1}\pi\sin\phi_k)$. If the Moore-Penrose left/right pseudoinverse are denoted as $^\diamond$ and † , respectively, then:

$$\mathbf{Y}_{L_n}^{(1)\dagger}(n) = [\mathbf{A}_{P-L}^T(n)]^\dagger [\hat{\Delta}(n) \circ \mathbf{A}_{L+1}(n)]^\diamond. \quad (6.45)$$

And the correlation matrices with respect to the first antenna element can be defined as:

$$\mathbf{R}^{(j,1)} \triangleq \mathbf{Y}_{L_n}^{(j)}(n) \mathbf{Y}_{L_n}^{(1)\dagger}(n) = [\hat{\Delta}(n) \circ \mathbf{A}_{L+1}(n)] \Upsilon^{(j)} [\hat{\Delta}(n) \circ \mathbf{A}_{L+1}(n)]^\diamond. \quad (6.46)$$

It can be seen from (6.46) that the elements of $\Upsilon^{(j)}$ are the eigenvalues of $\mathbf{R}^{(j,1)}$, from which the DOA can be calculated. Moreover, the k th column vector of $\hat{\Delta}(n) \circ \mathbf{A}_{L+1}(n)$ is the k th eigenvector of $\mathbf{R}^{(j,1)}$, which can be used to obtain the TOA by solving the k th columns of the two sides of (6.43). In this way, $J-1$ independent estimations of the DOA and TOA can be obtained, and then a post-averaging with the LS method can be performed.

In order to take advantage of the data correlations between antennae and have a higher performance in the TOA estimation, a similar matrix construction technique as (6.39) is used to form a $JL_n(L+1)$ by $(P-L)$ matrix by stacking $\mathbf{Y}_{L_n}^{(j)}(n)$, $j=1,2,\dots,J$, such that:

$$\hat{\mathbf{Y}}_{J|L_n}(n) = \begin{bmatrix} \mathbf{Y}_{L_n}^{(1)T}(n) & \mathbf{Y}_{L_n}^{(2)T}(n) & \dots & \mathbf{Y}_{L_n}^{(J)T}(n) \end{bmatrix}^T = \mathbf{\Pi}_J \circ [\hat{\Delta}(n) \circ \mathbf{A}_{L+1}(n)] \mathbf{A}_{P-L}^T(n), \quad (6.47)$$

in which $\mathbf{\Pi}_J \triangleq [\beta(\phi_{k1}) \beta(\phi_{k2}) \dots \beta(\phi_{kK_n})]$ and $\beta(\phi_k) \triangleq [1 \exp(-jd_1\pi\sin\phi_k) \dots \exp(-jd_{J-1}\pi\sin\phi_k)]^T$. α_k can be obtained with the same procedures suggested by (6.39) ~ (6.43).

As a result, the overall procedure for estimating the number of targets, TOA and DOA can be summarized as:

- (1) Use the likelihood ratio test defined by (6.35) in 6.3.2 to obtain the model order K_n in a sample-by-sample manner throughout a number of pulse periods, with the sampled baseband signal from any Rx channel. To this end, calculate the eigenvalues of the matrix \mathbf{C} defined by (6.32) and construct the matrix \mathbf{A}_{L+1}^V using (6.26); then, calculate the largest singular values of the matrices $\mathbf{\Gamma}_P^V$ and \mathbf{Z}_P^V , which are defined by (6.33) and (6.34).

- (2) With the knowledge of the time series K_n , L_n defined in 6.3.3 can be obtained by counting the number of adjacent samples sharing the same K_n value. Then construct the stacked matrix $\mathbf{Y}_{L_n}^{(j)}(n)$ defined by (6.44) in 6.3.4 for each of the J antennae using (6.39) in 6.3.3. Finally calculate the correlation matrix $\mathbf{R}^{(j, 1)}$ and its eigenvalues to obtain the targets' DOAs.
- (3) There are three ways to estimate the TOAs of the targets, listed as follows with an order of low accuracy/computational burden to high accuracy/computational burden.
 - 1) Using the eigenvalues of matrix \mathbf{C} obtained in step (1), $\alpha_k(n_k)$ can be got immediately.
 - 2) Take advantage of the matrix stacking technique described in 6.3.3 and calculate the matrix $\hat{\mathbf{C}}$ as well as its eigenvalues. Or use the eigenvectors of $\mathbf{R}^{(j, 1)}$ (refer to 6.3.4) to solve (6.43) for Φ .
 - 3) Use the matrix (6.47) stacked with the adjacent samples from all the Rx channels to get $\alpha_k(n_k)$ with the procedures suggested by (6.39) ~ (6.43). This results in a pre-average throughout the whole acquired data but has the highest processing complexity.

Moreover, it should be noted that with the theory and equations developed in section 6.3, the number of the targets (as long as there are more than two) doesn't affect the execution procedure of the post-processing algorithms. Therefore, two targets are used for verifications in both simulations and measurements for conciseness. However, the computational burden may vary in the following two cases:

- 1) The searching range of the model order changes. In real applications, it is very rare that there is no a priori information about the range of the number of targets.
- 2) The number of targets is so large that the size of the matrix $\mathbf{Z}(n)$ has to be increased to satisfy $P/2 > K_n$.

6.4 System Performance Analysis and Simulation

6.4.1 Conventional FFT enabled FMCW and SILO positioning system

As summarized by [187], the theoretical distance resolution of a conventional FMCW radar when detecting a passive reflective target has the analytical expression $\Delta R = c/2BW$. This is due to the fact that the frequency resolution of an FFT is inversely proportional to the duration of observation, which is the same as the chirp period.

For the SILO positioning system implemented with FFT, the TOF between the base station and the target is calculated by $\tau_k = f_{beat}/(2g) - T_o^{(k)}/4$ ([31, 34]), in which f_{beat} is equivalent to the beat frequency of the conventional passive FMCW radar, as shown in Fig. 6.4.

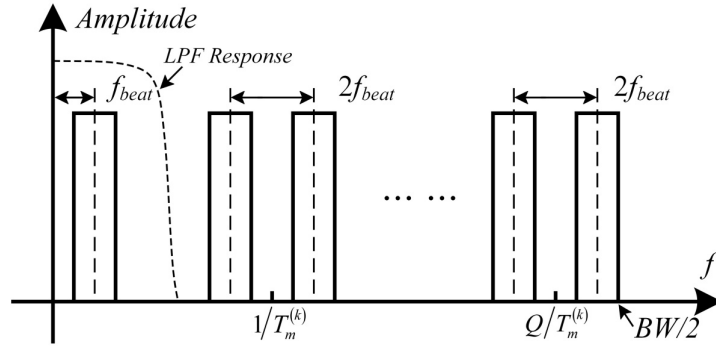


Figure 6.4: The real part of the baseband spectrum of the SILO positioning system with one target. The carrier frequency of the target is assumed to be the center frequency of the interrogation chip signal.

The modulation of the SILO can be regarded as another degree of sampling process besides the one performed at the rate of $1/T$ on the baseband signal in the base station. The effective number of points for the FFT is equal to the number of modulation pulses within one chirp period. So, the frequency resolution of the resulting spectrum is $(BW/2)/(T_s/T_m)$. Since there are $T_o^{(k)}/T$ sampling points in a single pulse, the final baseband spectrum of the k th target is a stitch of $T_o^{(k)}/T$ individual spectrums with a frequency shift of $1/T$ in between two adjacent ones. Such a ‘stitch’ process is equivalent to a post-average operation, which can increase the estimation accuracy but not the resolution. It means that the number of estimated positions in a circle around the real position can be increased, so that the averaged position gets closer to the real one. But the radius of such a circle cannot be reduced.

The above analysis is based on the noise-free assumption. In case of additive white noise, the standard deviation is used as an index of resolution of parameter estimations, which is calculated from the nominal distance resolution ΔR [188]:

$$|\sigma| = \Delta R / \sqrt{2 \cdot \text{SNR}} . \quad (6.48)$$

With this equation, the effect of the duty cycle $\xi^{(k)}$ of the k th target can be explained as follows: with a fixed chirp bandwidth and modulation frequency, the nominal resolution maintains the same, but the SNR is reduced by a factor of $\xi^{(k)}$. So, the standard deviation $|\sigma|$ is enlarged by $(1 - \sqrt{\xi^{(k)}}) / \sqrt{\xi^{(k)}}$.

When the FFT technique is implemented, a low pass filter (LPF) or equivalently a band pass filter (BPF) followed by down-sampling is used in the baseband. The latter case has the advantage of being exempt from significant low frequency noise. Both of the two filtering techniques will result in the loss of effective bandwidth. As shown in Fig. 6.4, an LPF is used to select the band around zero frequency. It implies that only a chirp bandwidth of $BW/(2Q+1)$ is in effect. Looking at the time-domain signal, the majority of the chirp period is seriously attenuated by the filter, which is equivalent to capturing a section of the baseband waveform and fill the rest with zeros (zero-padding). As it has been widely known, zero-padding cannot improve the frequency resolution although the number of points in the spectrum is increased.

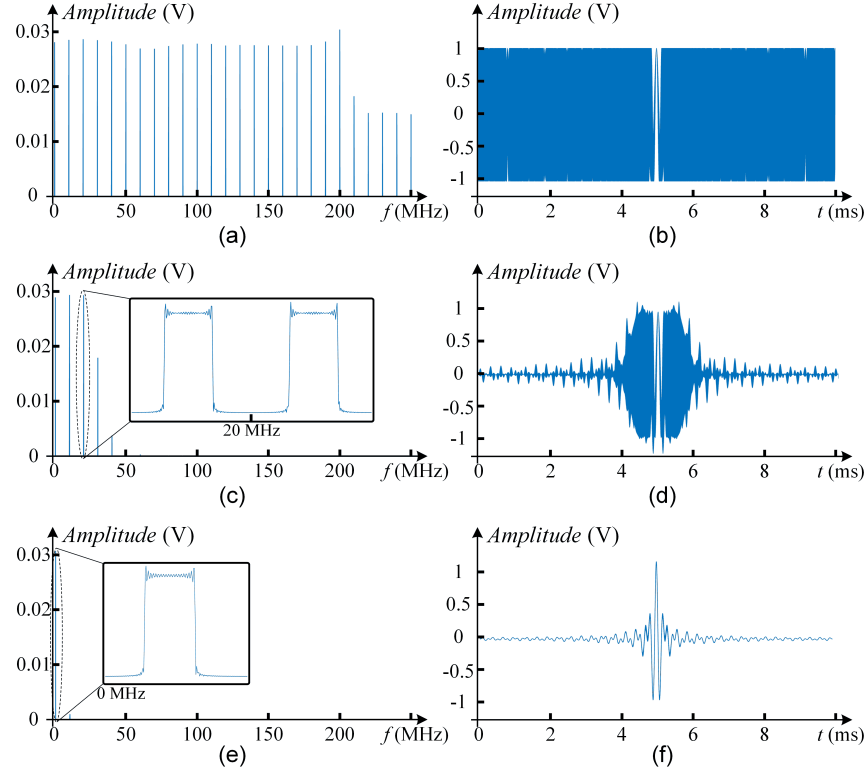


Figure 6.5: Simulated spectrum and time-domain waveforms of the baseband: (a), (c) and (d) are the spectrum of the un-filtered, 20 MHz low pass filtered and 5 MHz low pass filtered baseband; (b), (d) and (e) are the time-domain waveform of the un-filtered, 20 MHz low pass filtered and 5 MHz low pass filtered baseband.

Fig. 6.5 illustrates the simulated spectrum and time-domain waveforms of the baseband signal using Matlab, with the following parametric conditions: $BW=400$ MHz, $T_s=10$ ms, $\tau=40$ ns, $1/T_m=10$ MHz, duty cycle =75% and $1/T=500$ MHz. Fig. 6.5 (a) and (b) correspond to the signal without filtering, (c) and (d) are with a 20 MHz Butterworth LPF while (e) and (f) are with a 2 MHz Butterworth LPF. It can be seen from (d) and (e) that the effective bandwidth is reduced proportionally with a narrower LPF. In order to compensate for the bandwidth loss, Q has to be zero, which means that the modulation frequency of the target has to be at least $BW/2$. This is a challenge for circuit realization when BW is more than 1 GHz due to a limited speed of the modulator and relatively large time constant of the resonator in the SILO. Actually, as the target modulation frequency tends to be infinity, from (6.7) and (6.8), it can be seen that $t_{pk}^{(k)}$ is replaced with t , and the transmitted signal from the target becomes a delayed duplicate of the interrogation signal. So, the system tends to act in the same manner as the passive FMCW radar.

As a conclusion, to adopt the FFT technique for the SILO based positioning system with a higher resolution, the modulation frequency has to be increased. For a higher accuracy, it is the duty cycle that must be increased, but this has to be done carefully to avoid the spectrum of two targets getting overlapped with each other.

6.4.2 Effect of unsynchronized sampling

From (6.18) and (6.19), it can be seen that by ignoring the time difference between the local sampling instant and the actual sampling instant, a random systematic error of $T_{rd}^{(k)}/2$ between the real τ_k and its estimated value $\bar{\tau}_k$ appears. Since $T_{rd}^{(k)} < T/2$, it means that the system has an inherent uncertainty of less than a quarter sampling cycle. Actually, this uncertainty is not exclusive for our proposed algorithm but also exists in the frequency-domain approaches in [31, 34], which can be explained by Fig. 6.6.

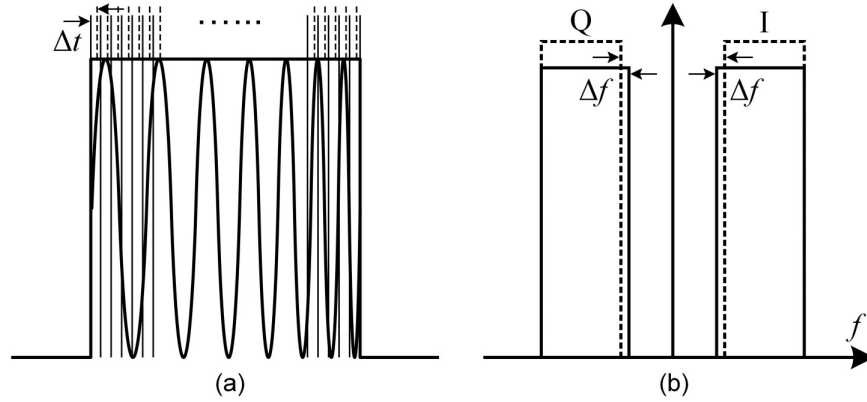


Figure 6.6: (a) Time-domain pulse in baseband and (b) its corresponding frequency-domain signal obtained by FFT.

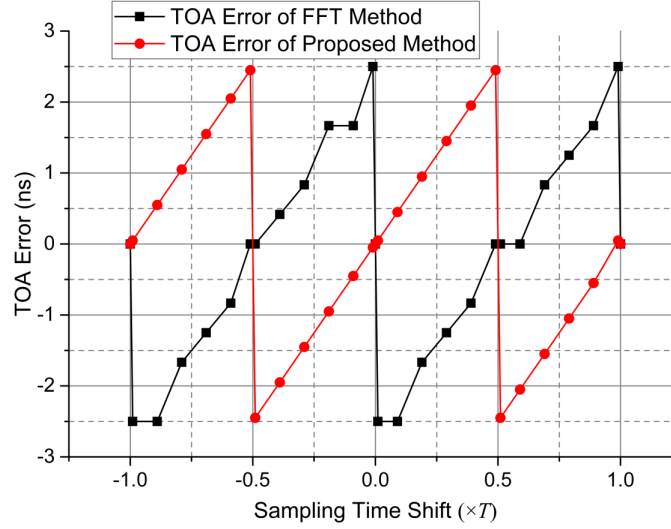


Figure 6.7: Simulated curves of the TOA estimation error due to unsynchronized sampling through both the FFT method and the proposed method.

As the actual sampling points (dashed lines in Fig. 6.6 (a)) are shifted by Δt from the ideal ones (solid lines in Fig. 6.6 (a)), and when $\Delta t \rightarrow T$ or 0^- , the corresponding I spectrum obtained by FFT is shifted towards higher frequency by $\Delta f/2$ with its upper shoulder fixed. Since $\Delta f = g\Delta t$, the estimation of τ_k is shifted by $\Delta t/4 \rightarrow T/4$. Similarly, when $\Delta t \rightarrow -T$ or 0^+ , τ_k is shifted by $\Delta t/4 \rightarrow -T/4$. So the uncertainty is within a quarter sampling period. To verify the analyses, the simulated error curves of the TOA estimation through both the FFT method and the proposed method are shown in Fig. 6.7, which are plotted as the sampling time shift is between $-T$ and T , and the sampling frequency is 100 MHz. In order to mitigate this problem, the following condition has to be satisfied: $T_o^{(k)} \cdot g < 1/T_s$. For the FFT technique, it means the frequency variation within one baseband pulse is less than the frequency resolution. For the proposed technique, it implies that there is only one sample in a baseband pulse.

6.4.3 Validate the proposed algorithm and comparison with the FFT technique by simulations

A series of simulations are performed to prove the proposed post-processing technique and to verify its resolution capability. First of all, the targets configuration as shown in Fig. 6.8 (a) is used for simulation. There are two targets for identification; one is fixed at a radial distance of 18 m and an angle of -0.5° , and the second is located at 18.3 m/ 0.5° . The second one moves along the radial

direction until 22.5 m/0.5° and stops at the position of 18.9 m and 21 m. Fig. 6.8 (b) illustrates the theoretical CRLB and RMSE simulated with the Monte Carlo method for the radial distance estimation.

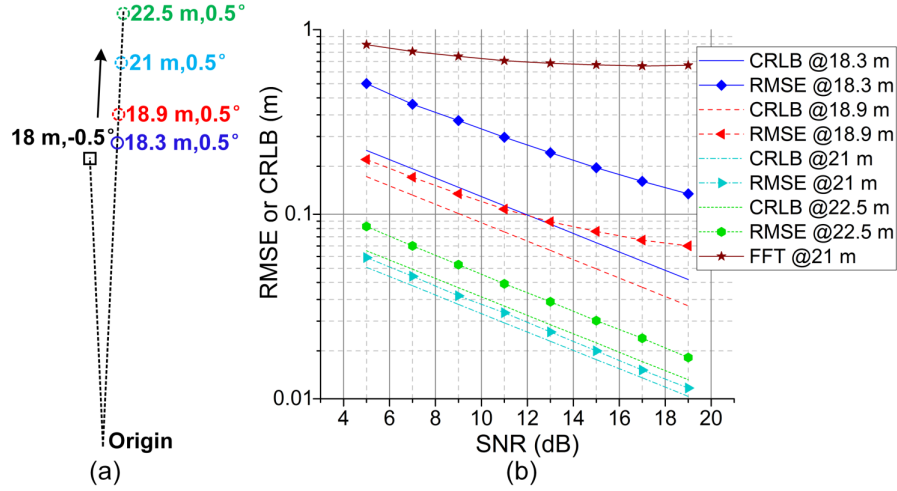


Figure 6.8: (a) Targets configuration for simulation; (b) Calculated and simulated CRLB and RMSE curves for radial distance estimations.

Both the proposed algorithm and the FFT technique are used and compared. Keysight SystemVue is utilized for the system simulation, and the data processing is done with Matlab. The system parameters are as follows: $f_c^{(1)}$ and $f_c^{(2)} = 5.6$ GHz, $BW = 60$ MHz, $T_s = 1$ ms, $T_m = 1$ μ s, $T = 1$ ns, $J = 2$ and $d_1 = 1$. There is no low pass filter applied to either the proposed or the FFT techniques.

From Fig. 6.8 (b), it can be seen that as the radial distance difference between the two targets gets larger, both the CRLB and the RMSE gets lower. This result is due to the effect of mutual disturbance and applies to any parametric or non-parametric method. The figure also shows the superiority of the proposed method over the FFT method regarding errors. The targets operate at 75% duty cycle, but only 2% of total sampling points are used to avoid the aliasing problem when implementing the FFT method.

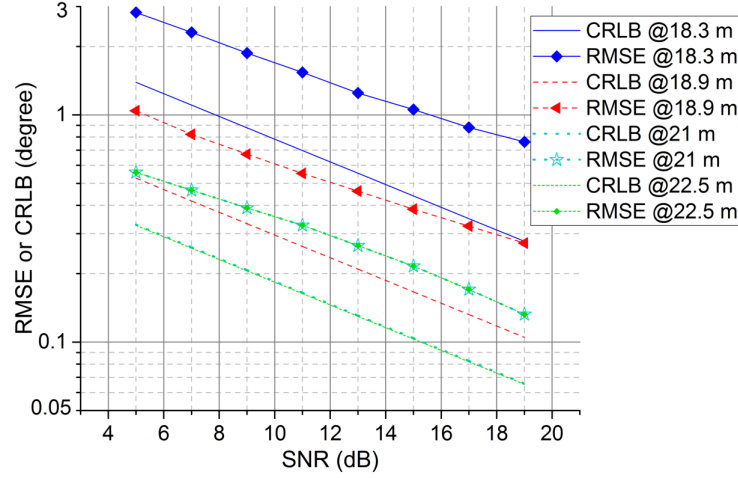


Figure 6.9: Calculated and simulated CRLB and RMSE curves for the DOA estimations.

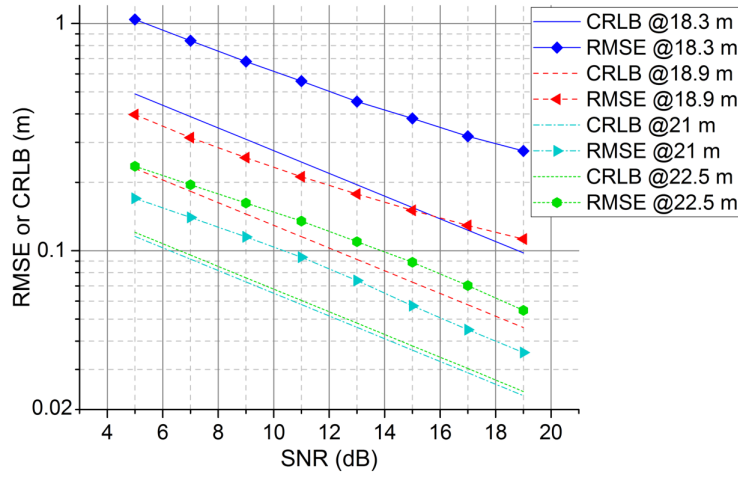


Figure 6.10: Calculated and simulated CRLB and RMSE curves for the vector estimations.

Fig. 6.9 shows the CRLB and RMSE curves for the angle estimations with the same target and system configurations. Fig. 6.10 shows CRLB and RMSE curves for the module of the error vectors of estimated values, which present whole pictures of the 2-D resolution.

In order to have an intuitive view of the resolution capability of the proposed algorithms, Fig. 6.11 plots all the individually estimated values by 2000 times Monte Carlo experiments at 10 dB SNR, as the space between the two targets changes. The same system configuration is used. It can be seen that as the targets get close to each other, the estimation becomes biased and less concentrated. This corresponds to the phenomenon observed in Fig. 6.8 to Fig. 6.10. It can also be found that the angular resolution is worse than the distance resolution. This is because only two antennae are used

for the DOA estimation, which means two spatial samples. While tens to hundreds of time-domain samples are used for the TOA estimation.

In order to validate the analysis of the relation between the modulation frequency and the resolution regarding the FFT technique, simulations are performed, and results are shown in Fig. 6.12. They are under the condition of 5% duty cycle, 5 dB SNR and 2000 times simulations. It can be seen that the resolution is improved as the modulation frequency increases.

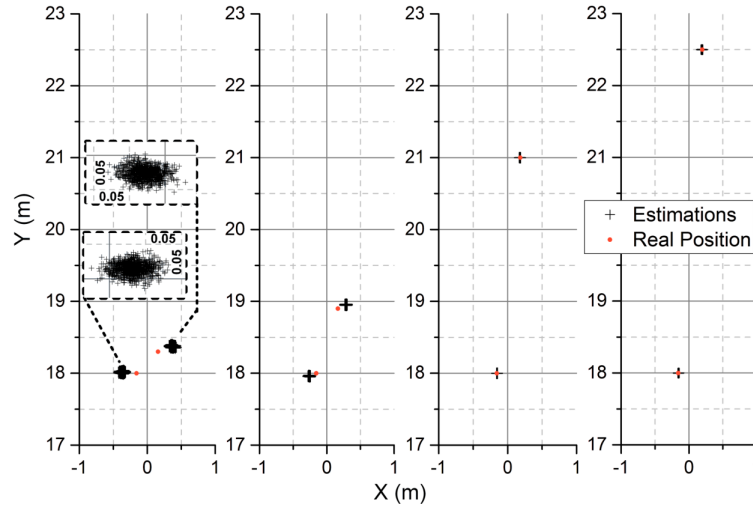


Figure 6.11: Simulated 2-D position estimations with different target spacing at 10 dB SNR, using the proposed algorithms.

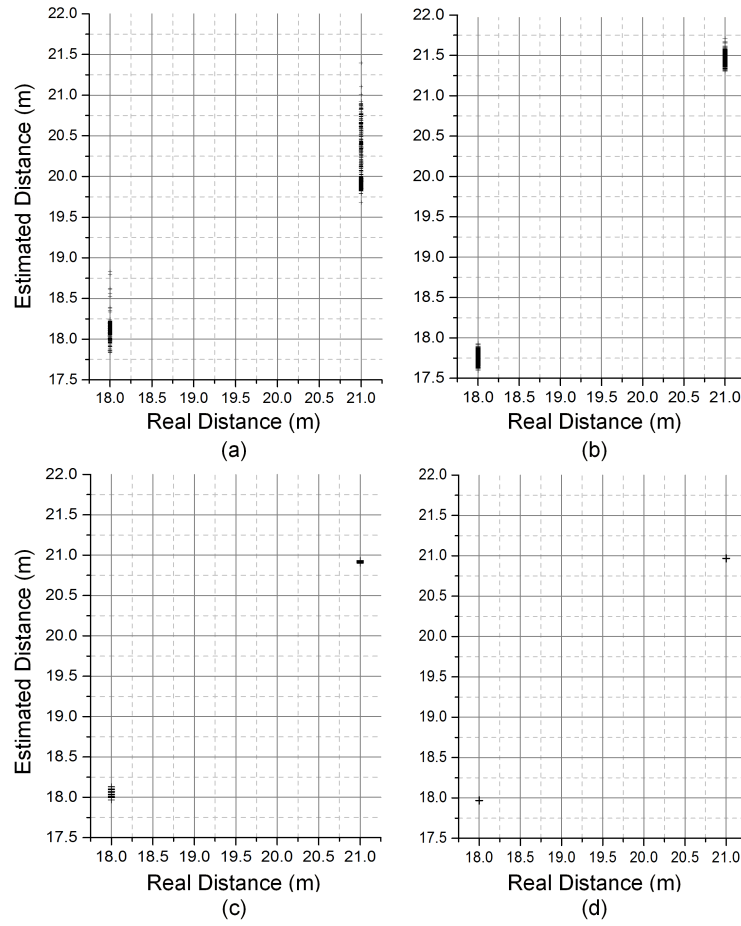


Figure 6.12: Resolution test of the FFT method at modulation frequency at (a) 1 MHz, (b) 5 MHz, (c) 10 MHz and (d) 20 MHz.

6.5 Experimental Demonstration and Measurement Results

6.5.1 Base station and target demonstrator

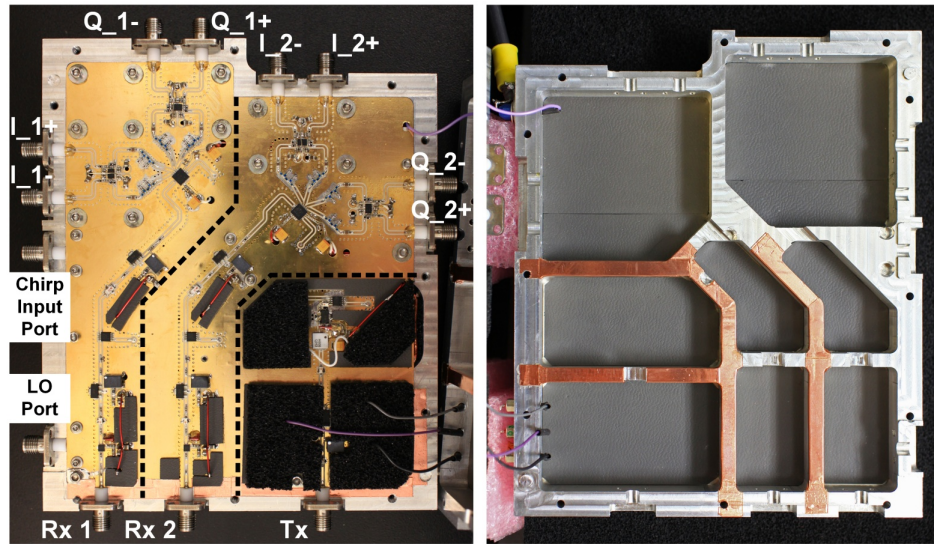
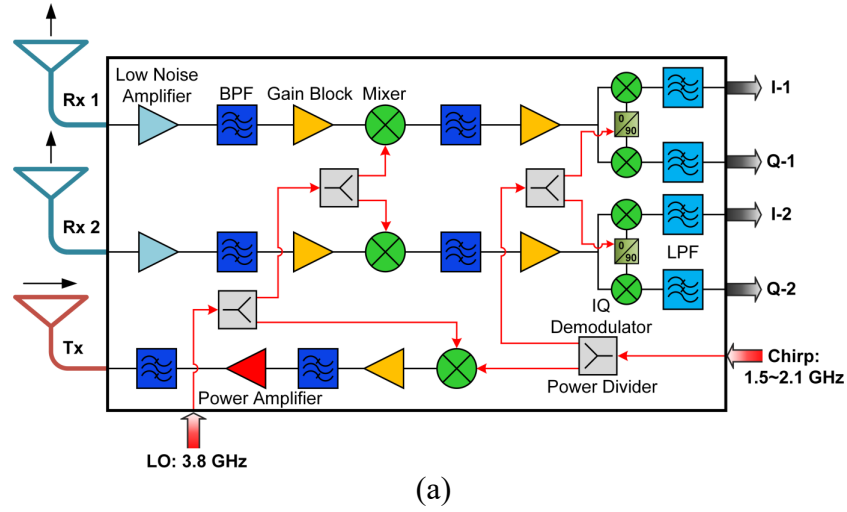


Figure 6.13: Description of the base station (a) system architecture and (b) fabricated demonstrator.

The base station system architecture is illustrated in Fig. 6.13 (a). It has one Tx channel with the direct up-conversion structure and two identical Rx channels with super-heterodyne structure. The base station has two input ports including one LO port at the frequency of 3.8 GHz and one chirp input port which can accept a maximum frequency range from 1.5 GHz to 2.1 GHz. The source of the chirp signal can be a VCO/PLL, a DDS or an arbitrary waveform generator (AWG). The largest

transmitting frequency range is 5.3 GHz to 5.9 GHz. The received signal is centered at 5.6 GHz. The baseband I and Q signals are taken differentially. The fabricated demonstrator embedded in shielding cavity is shown in Fig. 6.13 (b). It is prototyped with the commercial off-the-shelf components and standard PCB process with Rogers RO3003 substrate ($\epsilon=3$, $\tan\delta=0.0011$ and thickness=10 mil). The LO and chirp signal distribution networks are fabricated on a second PCB. The two pieces of circuits are stacked and connected together with an optimized interlayer transition structure. The measured noise figure of each of the two Rx channels is 5.6 dB. The maximum output power of the Tx is 25 dBm, at 6 dB back off from the output 1 dB compression point of the PA.

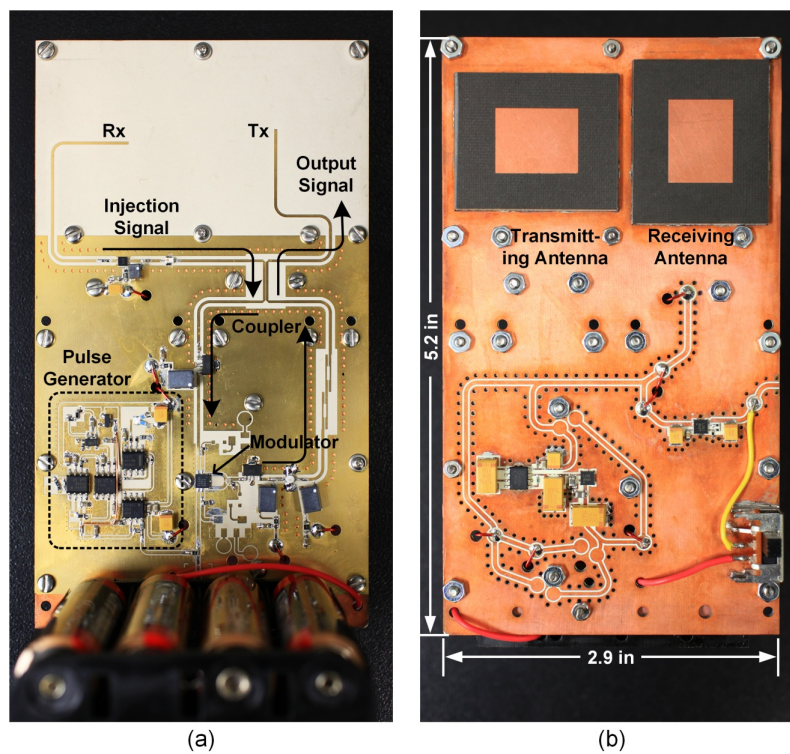


Figure 6.14: Fabricated active backscattering target demonstrator. (a) Front side and (b) back side.

The front and back sides of the fabricated target demonstrator are illustrated in Fig. 6.14 (a) and (b), respectively. The front side is fabricated on Rogers RO3003 substrate with 10 mil thickness. It consists of an oscillator with an injection signal path as well as a pulse generator with tunable frequency and duty cycle. As illustrated in Fig. 6.14 (a), the oscillator feedback loop consists of a bi-directional coupler such that the injection (interrogation) signal will join the loop with the maximum efficiency. A low noise amplifier is used after the Rx antenna to boost the interrogation

signal amplitude. A quad MOSFET array mixer is used as the modulator whose LO port is connected to the pulse generator. The oscillator has a free-running frequency of 5.6 GHz and a continuous wave power output of 5 dBm.

The back side of the target is fabricated on Rogers RO4350B substrate with a thickness of 60 mil. This board acts as the frame of the antennae as well as the dc distribution circuit with regulators and inverters. To improve the Tx and Rx isolation and to prevent unstable operations, the Tx antenna is designed to have a vertical polarization while the Rx antenna is designed to have a horizontal polarization. The microstrip feed lines are integrated on the front side layer, connecting to the input and output of the oscillator. The radiation patches are printed on one side of 120 mil thick Rogers RT/duroid® 5880 substrates, and the other side of copper cladding is removed. Such a thickness is selected for bandwidth enhancement. The patches are aperture-coupled to the microstrip open-ends with H-shape slots on the ground plane of the 10 mil substrate. The pair of patch elements are orthogonally arranged and embedded into the rectangle holes in the frames, and the inner walls of the holes are metalized to improve the isolation. The antennae structure is shown in Fig. 6.15 (a). The S_{11} and S_{22} parameters shown in Fig. 6.15 (b) indicate operation frequency and bandwidth. The S_{21} parameter shows the antennae isolation. The radiation patterns for the two antennae at different planes are shown in Fig. 6.15 (c). The base station uses the same antennae structure with orthogonal polarizations as the ones on the targets. However, its Rx antennae are vertically polarized, and the Tx antenna is horizontally polarized in order to match the targets. In some cases, the Tx antenna of the base station can adopt horn antenna to improve the isolation further.

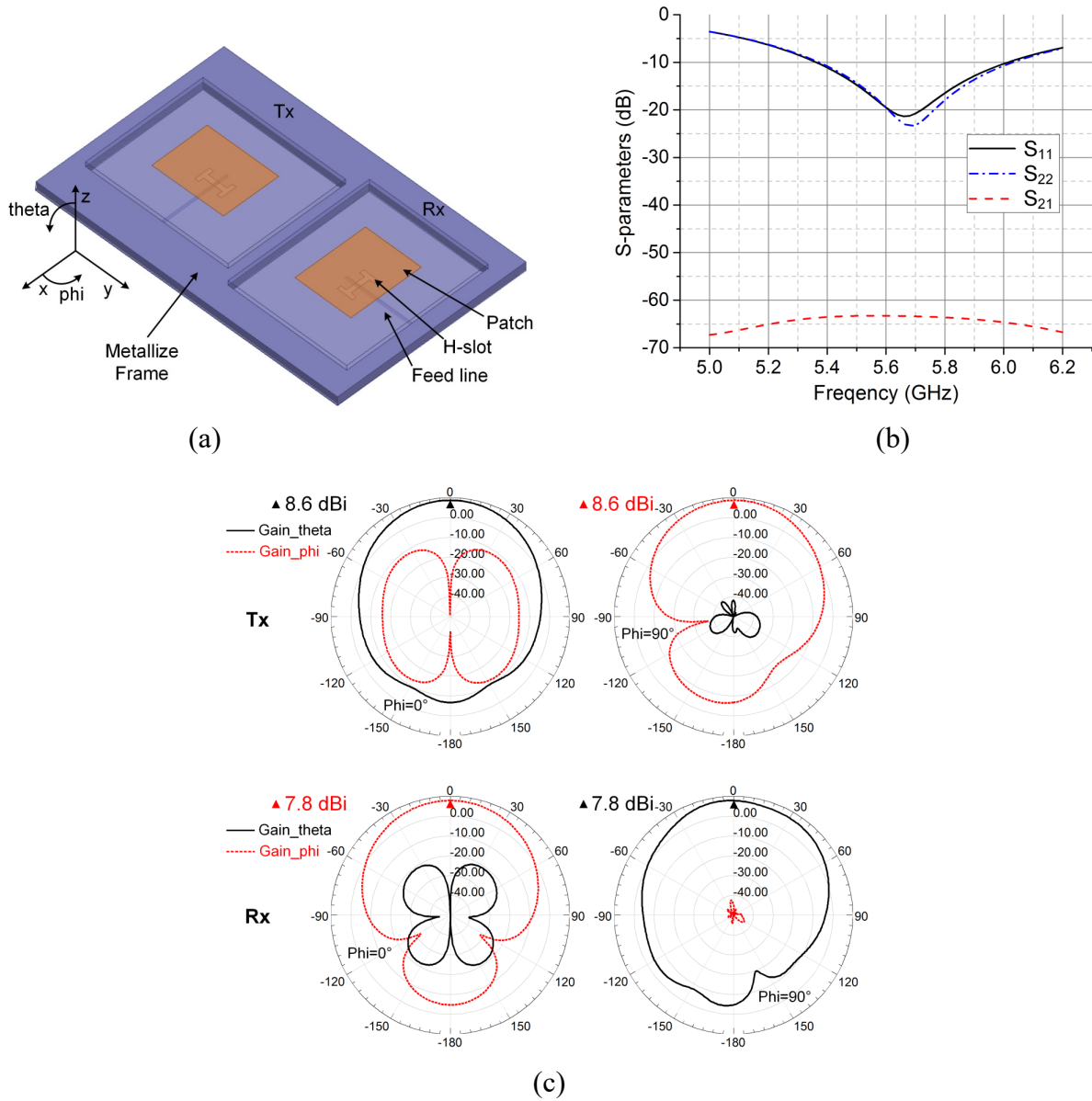
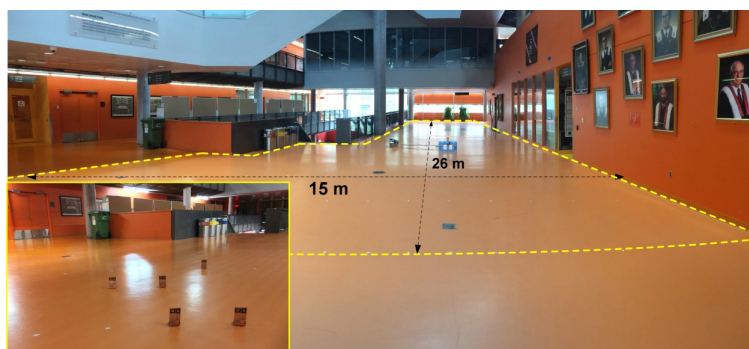


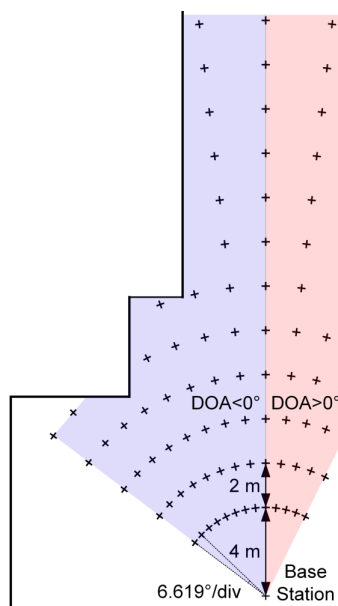
Figure 6.15: (a) Antennae structure for the base station and the targets, (b) S-parameters of a pair of Tx and Rx antennae and (c) radiation patterns.

If a target operates at a duty cycle of 75%, the average transmitted power is about 3.75 dBm. If the baseband sampling rate is at 1 GSa/s, the received SNR is about 15 dB when target is placed 100 m away from the base station.

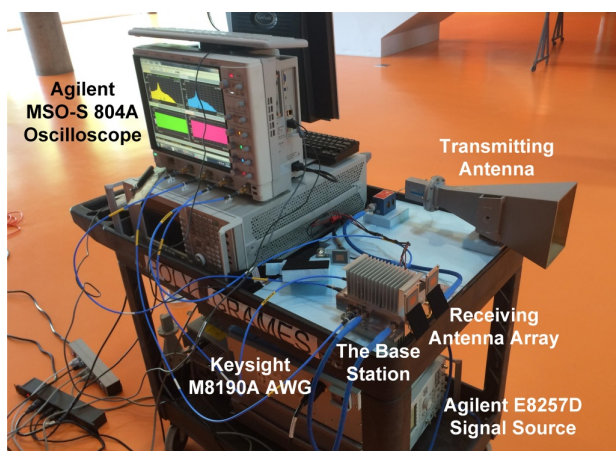
6.5.2 Indoor experiments and measured results



(a)



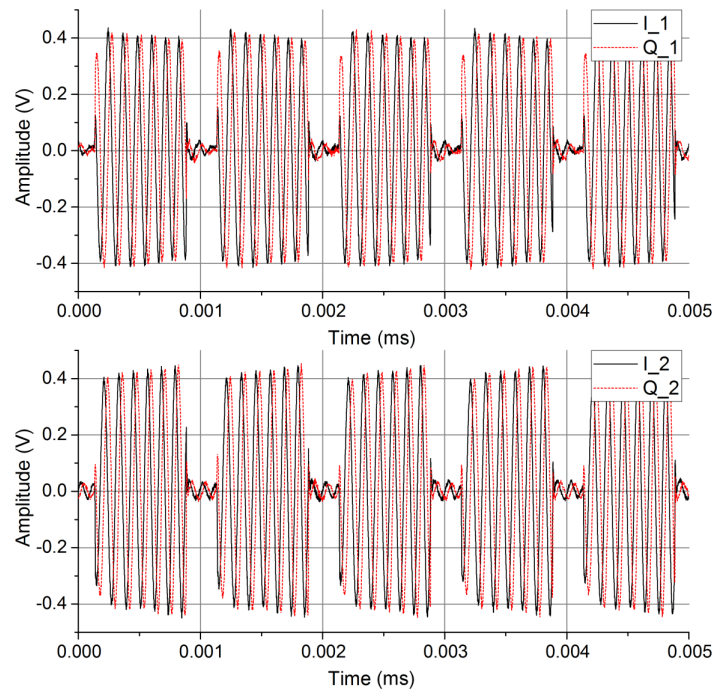
(b)



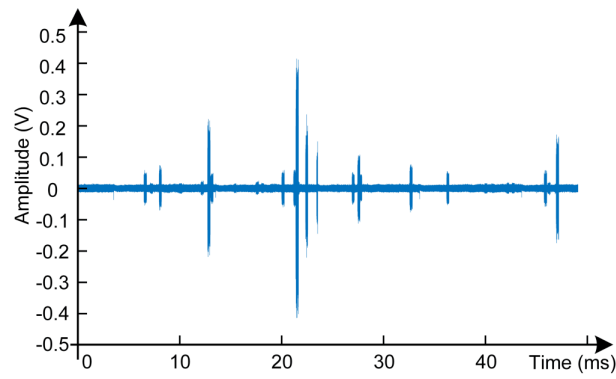
(c)

Figure 6.16: (a) The indoor measurement environment, (b) the layout plan of the test points and (c) the measurement setup.

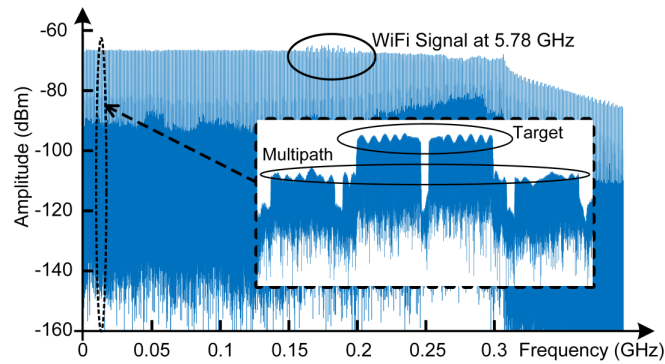
First of all, a real environment measurement is carried out in the lobby of the Lassonde Building of Polytechnique Montréal. Limited by the space, the area of test is within a 15 m by 26 m region, which is shown in Fig. 6.16 (a) and (b). The measurement setup is shown in Fig. 6.16 (c). The Keysight M8190A AWG is used to generate an up-chirp signal with a bandwidth of 600 MHz (1.5~2.1 GHz) and $T_s=10$ ms. The LO signal at the frequency of 3.8 GHz is generated by Agilent E8257D signal source. The demodulated baseband signal is digitized and recorded by Agilent MSO-S 804A oscilloscope which has 10bit vertical resolution, at a rate of 1 GSa/s. A rectangular horn antenna is used for transmitting, and a pair of designed patch antennae is used for receiving. The distance between the Rx array elements is 70 mm, which is 1.3 times of the free space wavelength at 5.6 GHz. Theoretically, this Rx antennae configuration will result in an ambiguity-free angular detecting range of $-22.6^\circ \sim 22.6^\circ$. The modulation frequency and the duty cycle of the targets are selected to be 1 MHz and 75%. 20% of the recorded sequence is used for post-processing.



(a)

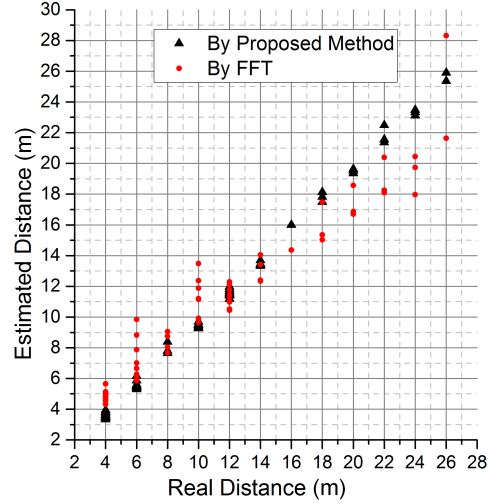


(b)

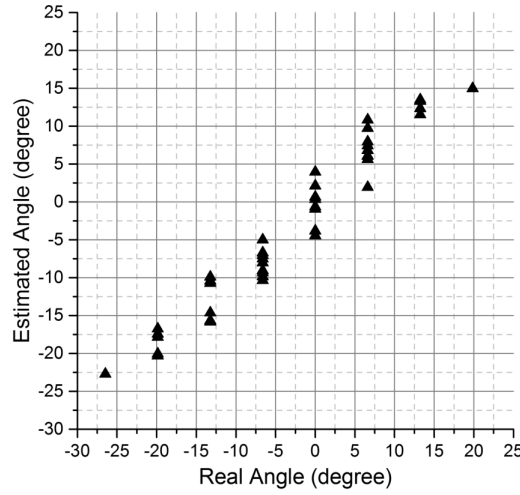


(c)

Figure 6.17: (a) A snapshot of the I/Q waveforms of a target at 4 m/13.238°. (b) An indoor interference waveform recorded in baseband. (c) The I₁ spectrum of the target at 4 m/13.238°.



(a)



(b)

Figure 6.18: Measured (a) distance and (b) angle of the indoor test.

Fig. 6.17 (a) is a snapshot of the recorded baseband I/Q waveform for both of the two Rx channels when the target is placed at 4 m/13.238°. Fig. 6.17 (b) shows a recording of the WiFi and other interference signals in the indoor environment with the same base station. It can be seen that the peaks of the interference have almost the same amplitude as the signal from the target. Fig. 6.17 (c) shows the baseband spectrum of the I signal of channel 1. The WiFi interference can be found. The spectrum consists of 300 pairs of bands, one of which is zoomed in with details. Not only the direct signal from the target but also the multipath products are shown. Fig. 6.18 illustrates the measured distance and the angle for the indoor setup. The distance measurement using the proposed estimation algorithm has obvious advantages over that using the FFT technique. From the layout plane, it can be seen that some of the points are out of the ambiguity-free detecting range of

$-22.6^\circ \sim 22.6^\circ$. Their AOA results are excluded from Fig. 6.18 (b). Similar to the results shown in Fig. 6.11, the angular resolution is worse than the distance resolution due to the limited number of spatial samples. The measured distance with the FFT method is also illustrated for comparison. Fig. 6.19 shows the measurement results of two pairs of targets, which are selected from the layout plan. They also exhibit the differences between the angular resolution and the distance resolution.

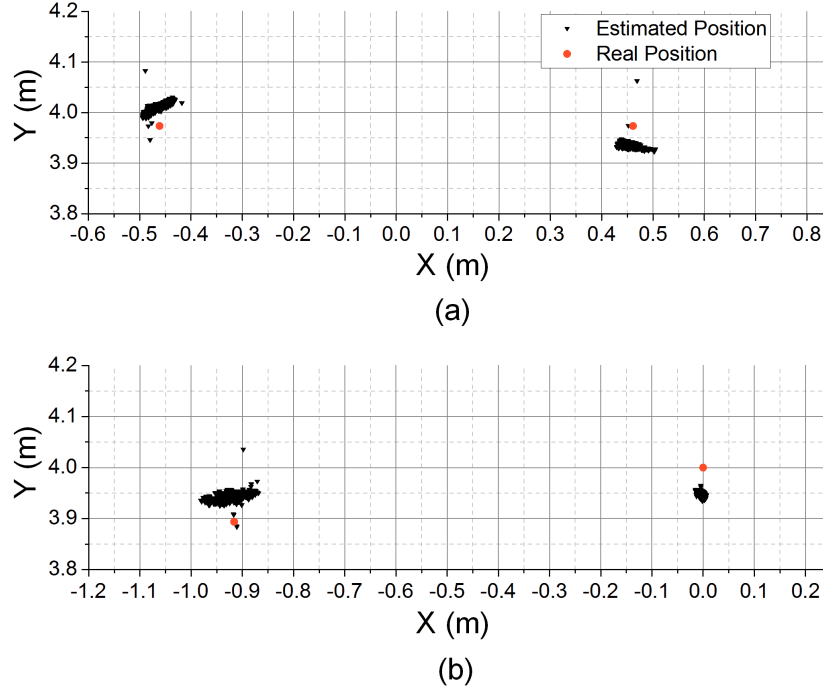
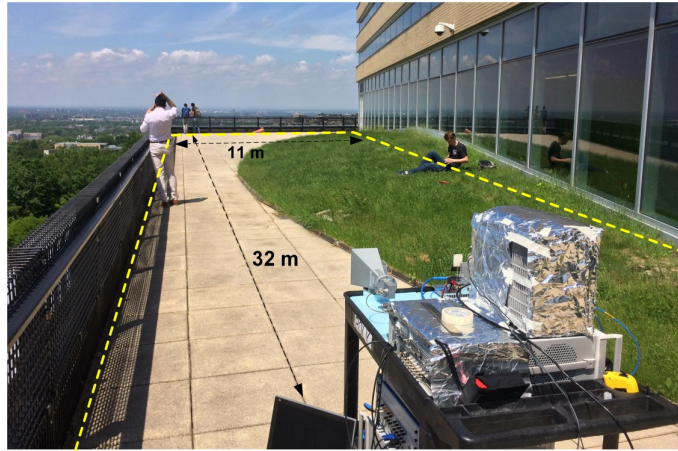


Figure 6.19: Measurement results for two targets located at (a) 4 m/ -6.619° and 4 m/ 6.619° as well as (b) 4 m/ -13.238° and 4 m/ 0° .

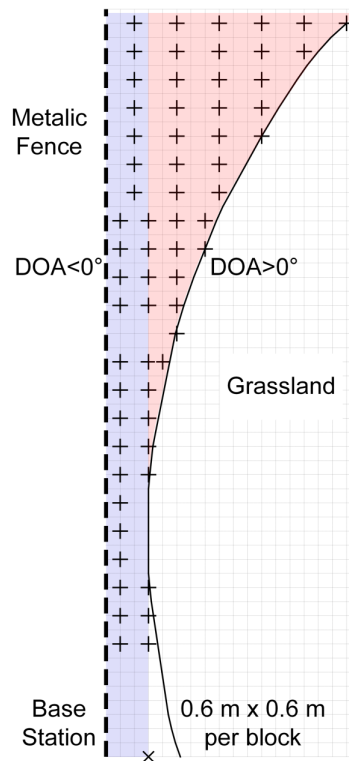
6.5.3 Outdoor experiments and measured results

The outdoor measurement setup is shown in Fig. 6.20 (a), and the layout plan of the test points is shown in Fig. 6.20 (b). The hardware configuration of the base station, the targets, and the instruments remain the same. Different from the indoor measurement, 40% of the recorded sequence is used for post-processing instead. Fig. 6.21 illustrates the measured results of the distance and the angle for the outdoor setup. It can be seen that the distance measurement has an outstanding accuracy. However, the angle measurement results are poor on most of the points. This is mainly due to the highly reflective metal fence and the protruding grassland, which create a multipath effect and block the signal since the targets are placed at a low height. The measured distance with the FFT method is also illustrated for comparison. In Fig. 6.22, the results for selected

two pairs of targets are illustrated. They show that as the targets get closer to the base station, the results of the angle estimations are more reliable.

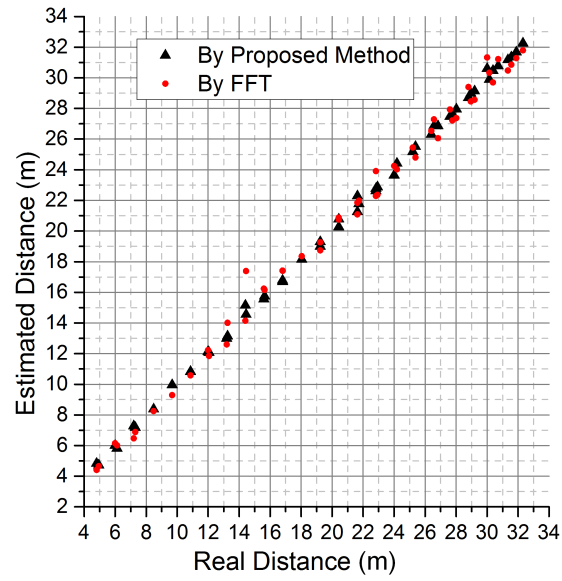


(a)

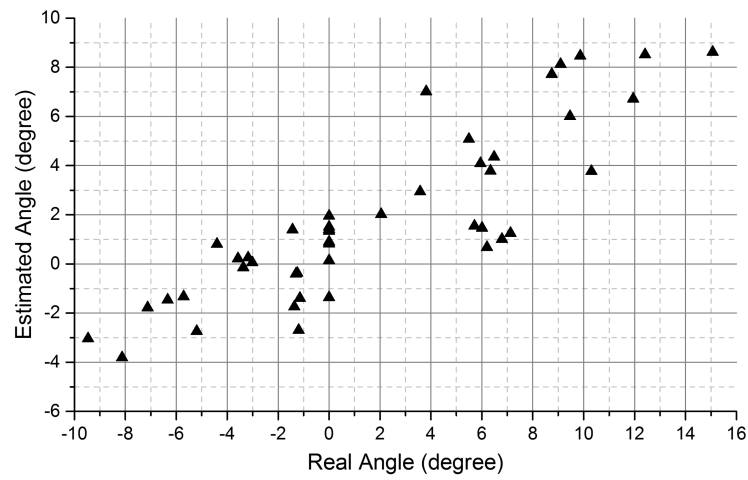


(b)

Figure 6.20: (a) The outdoor measurement environment and (b) the layout plan of the test points.



(a)



(b)

Figure 6.21: Measured (a) distance and (b) angle of the outdoor test.

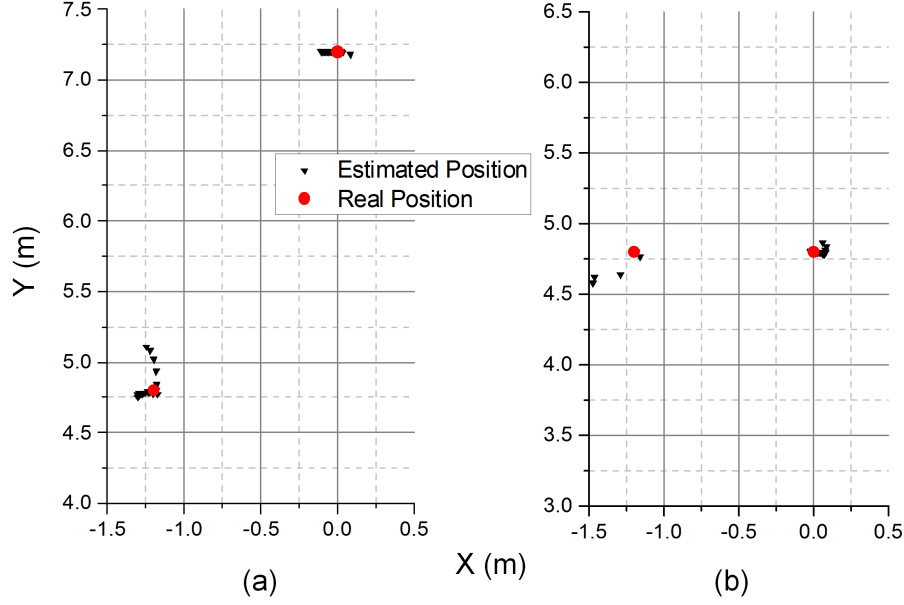


Figure 6.22: Measurement results for two targets located at (a) $(-1.2 \text{ m}, 4.8 \text{ m})$ and $(0 \text{ m}, 7.2 \text{ m})$ as well as (b) $(-1.2 \text{ m}, 4.8 \text{ m})$ and $(0 \text{ m}, 4.8 \text{ m})$.

6.6 Conclusion

This work introduces, investigates and demonstrates an active backscattering 2-D positioning system with innovative super-resolution time-domain post-processing techniques. The system hardware architecture is based on the SILO concept which was proposed in recent years and was demonstrated to enjoy the advantages of long range, low cost and high accuracy when the frequency-domain post-processing technique was implemented. The algorithms proposed in this paper overcome some drawbacks of the existing methods and the inherent compromise among the resolution, target quantity, SNR and other technical specifications. The theoretical limits of the resolution and accuracy for such an architecture with both the conventional and the proposed parameter estimation methods are presented. Simulations and abundant indoor and outdoor measurements have validated the proposed schemes and verified the hardware and algorithm performances. However, the proposed techniques still need improvement in terms of execution efficiency, angular resolution and self-interference cancellations. Moreover, multiple targets may have mutual interferences when they are close to each other. The proposed methods can be immediately extended to the 3-D positioning scenarios and may be enhanced by extra data transmission capability.

6.7 Acknowledgment

The authors are grateful to Keysight Technology for providing the key instruments and technical assistance for the measurement. The authors would like to thank Mini-Circuits, Analog Devices, Linear Technology, Coilcraft, Rogers Corporation and Larid for providing free samples. Also, the authors would like to acknowledge the technical support team of the Poly-Grames Research Center for their outstanding fabrication works and technical assistance.

CHAPTER 7 A MULTITARGET HARMONIC-BACKSCATTERING POSITIONING SYSTEM WITH ACTIVE TAGS BASED ON SELF- ISOLATED HARMONIC OSCILLATOR

Abstract—A harmonic-backscattering two-dimensional (2-D) wireless positioning system with active tags based on a class of self-isolated harmonic oscillator (SIHO) is proposed, studied and demonstrated in this work. Instead of using the same frequency band for transmitting and backscattering like a conventional frequency-modulated continuous-wave (FMCW) radar system or a switched injection phase-locking positioning system, our proposed system takes advantage of a 2nd harmonic emission from a tag which is based on a switched SIHO. Accordingly, the receiving band in the base station is centered at the 2nd harmonic frequency of the carrier of the transmitter. Time domain post-processing techniques, which are proved to be superior over the conventional frequency domain counterparts in multitarget time-of-arrival (TOA) and direction-of-arrival (DOA) estimations, are implemented. By leveraging the harmonics, the proposed system enjoys numerous advantages in terms of bandwidth, interferences, cluster scattering, load pulling of tags, and so on, compared to an architecture without resorting to harmonic signal components. The theory is introduced, and the design of a system prototype is presented. Experimental verification is then carried out in reflection-rich environments.

Index Terms—Active backscattering, direction-of-arrival (DOA), harmonic oscillator, multitarget, time-of-arrival (TOA), wireless positioning.

7.1 System Architecture and Signal Model

7.1.1 Architecture and advantages

Fig. 7.1 describes a simplified schematic that illustrates the operating principle of the proposed harmonic-backscattering positioning system with active tags (HPS-AT). The base station (BS) is comprised of a front-end sub-system including one transmitting channel (Tx) and J receiving channels (Rxs), as well as a back-end sub-system that digitizes and processes signals. The Tx sends a frequency-modulated continuous-wave (FMCW) periodical chirp interrogation signal generated by the voltage-controlled oscillator (VCO) through an antenna. The chirp signal has a bandwidth of BW and a frequency of the carrier (center frequency) of f_c . Also, the chirp signal is frequency-doubled and fed to the quadrature demodulator of each Rx. The frequency-mixing operation in the demodulators is equivalent to a de-chirp process of conventional FMCW radar system. The in-

phase and quadrature (I/Q) baseband signals are sampled by analog-to-digital converter (ADC) and then processed by a micro-controlling-unit (MCU), which also controls the VCO.

A self-isolated harmonic oscillator (SIHO) [189] is used on the tag. The SIHO is switched on/off by closing/opening the feedback loop at a certain rate and duty cycle so that the tag transmits a series of amplitude modulated (AM) pulses with carrier frequency designed at about $2f_c$. Between the diplexer and the switch in the SIHO, a power combiner which covers both frequencies f_c and $2f_c$ is used to introduce the interrogation signal received by the Rx antenna of the tag to the loop of the SIHO. In this way, at the turn-on instant of each pulse, the fundamental oscillation signal is triggered with the phase of the received interrogation signal with a delay of the time-of-flight (TOF) between the BS and the tag. Because of a nonlinearity of the saturated amplifier in the SIHO, the phase locked fundamental oscillation signal is converted to its 2nd harmonic, which is then sent back to the BS by the Tx antenna of the tag.

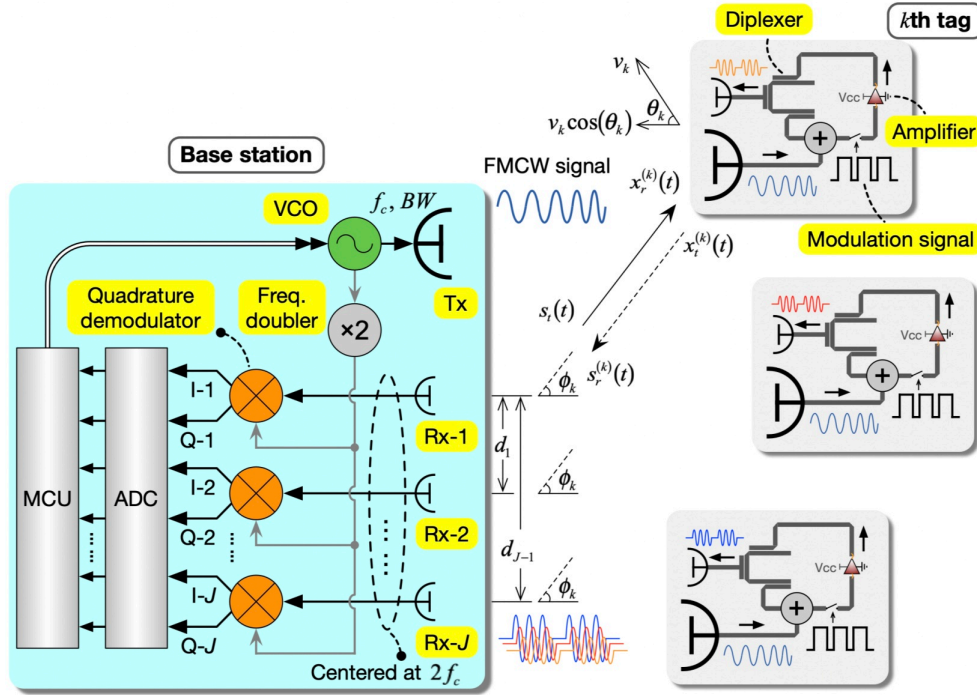


Figure 7.1: A simplified schematic of the proposed HPS-AT. The BS has one Tx and J Rxs, and the active tags are based on SIHO with fundamental signal injection phase-locking and on/off modulation.

Compared to a system without resorting to a harmonic from the tag as the backscattering signal [21, 31, 33, 76] (hereinafter referred to as a fundamental system), our proposed system has a number of advantages as follows:

- 1) 50% absolute bandwidth of interrogation signal is saved to achieve the same range resolution. This is because the effective bandwidth of an HPS-AT is equivalent to that of a fundamental system with the following configurations: the same Rx-1 to Rx- J of the HPS-AT, a Tx transmitting a chirp interrogation signal with $2BW$ bandwidth at $2f_c$ center frequency, and active tags transmitting and receiving in the same band centered at about $2f_c$. Generally, if the n th harmonic is used as a tag's backscattering signal, $(n-1)/n$ absolute bandwidth is saved.
- 2) Self-interference and cluster scattering are completely eliminated on both tag and BS. In both fundamental system and conventional FMCW radar, a signal coupling between the Tx and Rx antennas on a BS may severely compromise the system performance. A signal from a faraway tag may be jammed if it is weaker than a signal from a static reflector or directly coupled from the Tx to Rx. Therefore, the BS sensitivity is degraded. Cluster scatterings may be recognized as fake targets, not only giving a wrong information of location but also increasing the burden of computation especially when a search algorithm is used. Tx and Rx antenna coupling on the tag will significantly reduce the phase locking accuracy because the initial phase of some of the pulses may be unexpectedly locked to a transmitted signal from the tag itself. Because of this, circuit instability may also happen. Tx and Rx antennas with cross polarizations can be used to enhance the isolation between them [76], but usually, this technique can only mitigate the effect by no more than 20 dB. With the decreasing of the size of tags for ubiquitous sensing, reducing antenna coupling in a small form factor becomes even more difficult to achieve. Adaptive cancellation circuits in front-end systems are also widely used [190] for coupling reduction, but they may increase the noise, complexity, and cost.
- 3) Interference among the tags in a multitarget configuration is a hurdle of the fundamental systems. This is because, with respect to one tag, a transmitted signal from another tag may be much stronger than an interrogation signal from the BS. Because both signals share the same band, this may cause the phase of the first tag being completely ruined. When tags are deployed in a high density or in certain relative position (like face-to-face), this problem

may even hinder the operation. Synchronization techniques among the tags may be used to avoid the overlapping of their pulses. But this will inevitably increase the cost and decrease the signal to noise ratio (SNR) of each tag. An HPS-AT can perfectly avoid such an issue due to the frequency isolation between the Tx and Rx of tags.

- 4) The HPS-AT configuration is a favorable choice for wearable devices and applications in crowded spectrums thanks to the low pulling effect of the SIHOs on tags. This feature ensures that tags can work without being interrupted even with foreign objects in proximity or ambient signals at about $2f_c$ is received by the antennas of tags.
- 5) Low-cost integrated circuit process can be selected to design tags operating at millimeter-wave (mmW) frequency and above. This is because harmonic oscillators (including SIHO) can be designed to work at a frequency much higher than f_{\max} of transistors [136, 191], while fundamental oscillators with the same frequency output require a more expensive process.

7.1.2 Signal model and operation principle

Referring to Fig. 7.1 and Fig. 7.2 (a), the k th tag receives a signal with the following expression:

$$x_r^{(k)}(t) = a^{(k)} \bar{s}_t(t - \tau_k) \cdot \exp \left[j2\pi \left(f_c + f_d^{(k)} \right) (t - \tau_k) \right]. \quad (7.1)$$

Notations for this equation:

- $a^{(k)}$ and τ_k : path loss and TOF of radio frequency (RF) signal between the BS and the k th tag;
- $f_d^{(k)}$: Doppler shift seen by the k th tag having a velocity of v_k referred to the BS;
- $\bar{s}_t(t) = q(t) \cdot \exp \left[j\pi g(t - mT_s)^2 \right]$: baseband chirp signal of the BS with a normalized amplitude;
- $g = +/ - BW/T_s$: up/down chirp rate;
- T_s : chirp period;
- $q(t) = 1$ or 0 , if $t \in [mT_s, (m+1)T_s)$ or others: chirp duration windows function in which $m = 0, 1, 2, \dots$.

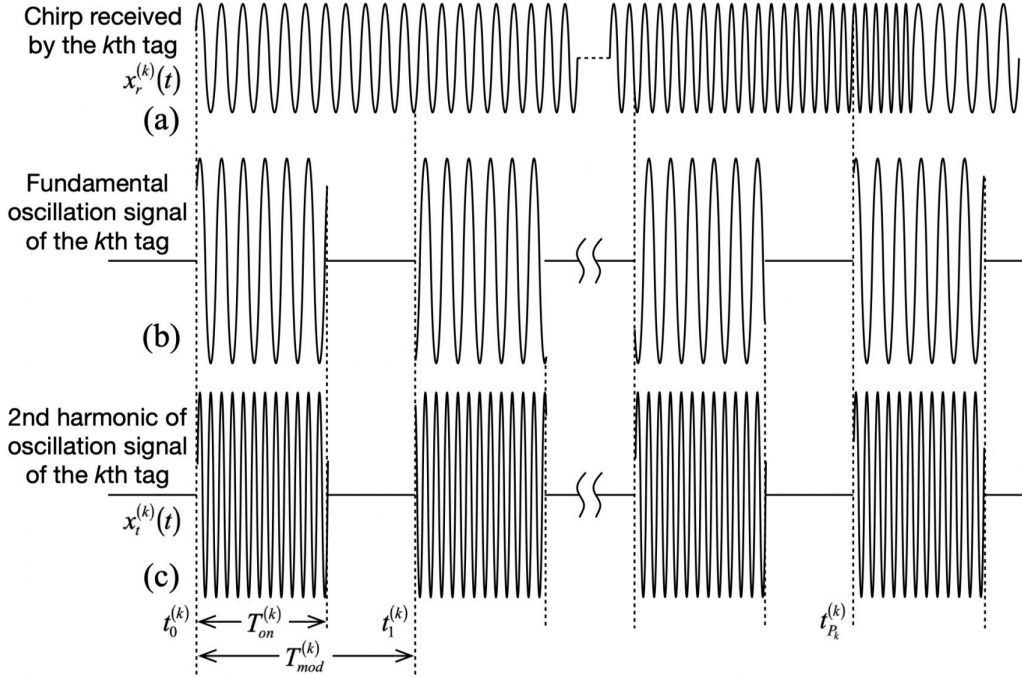


Figure 7.2: Illustrative waveforms of the k th tag: (a) received periodical chirp signal from the BS, (b) fundamental oscillation signal of SIHO phase-locked to signal in (a), and (c) 2nd harmonic of signal in (b), which is transmitted towards the BS.

As shown in Fig. 7.2 (b), the fundamental oscillation signal of the pulsed SIHO on the k th tag is phase-locked to $x_r^{(k)}(t)$. It has a period of $T_{mod}^{(k)}$ and a duty cycle of $\eta = T_{on}^{(k)} / T_{mod}^{(k)}$, and can be expressed as:

$$\hat{x}^{(k)}(t) = \sum_{p_k=0}^{P_k} \bar{q}_{p_k}^{(k)}(t) \cdot \exp \left[j2\pi f_c^{(k)}(t - t_{p_k}^{(k)}) + j\phi_r^{(k)}(t_{p_k}^{(k)}) \right]. \quad (7.2)$$

Notations in this equation:

- $f_c^{(k)} \approx f_c$: frequency of a fundamental oscillation signal;
- $\bar{q}_{p_k}^{(k)}(t) = 1$ or 0 , if $t \in [t_{p_k}^{(k)}, t_{p_k}^{(k)} + T_{on}^{(k)}]$ or others: pulse window function;
- $\phi_r^{(k)}(t_{p_k}^{(k)}) = 2\pi(f_c + f_d^{(k)})(t_{p_k}^{(k)} - \tau_k) + \pi g(t_{p_k}^{(k)} - \tau_k)^2$: initial phase of the p_k th pulse at each turn-on instant $t_{p_k}^{(k)}$;
- P_k : number of pulses of the k th tag in a chirp period.

Therefore, a series of transmitted pulses from the k th tag (Fig. 7.2 (c)), which is comprised of the 2nd harmonic of the fundamental pulses of (7.2), can be expressed as:

$$x_t^{(k)}(t) = a_{xt}^{(k)} \sum_{p_k=0}^{P_k} \bar{q}_{p_k}^{(k)}(t) \cdot \exp \left[j4\pi f_c^{(k)}(t - t_{p_k}^{(k)}) + j2\phi_r^{(k)}(t_{p_k}^{(k)}) \right], \quad (7.3)$$

in which the dc component is ignored and $a_{xt}^{(k)}$ is the transmitted amplitude. It should be noted that the fundamental signal and $\geq 3^{\text{rd}}$ order harmonics may also exist in $x_t^{(k)}(t)$ but have 30 dB lower amplitude than the 2nd harmonic one, if the SIHO on the tag is properly designed.

$s_r^{(k)}(t)$, which is the backscattered signal from the k th tag received by an Rx of the BS, is simply $a^{(k)} x_t^{(k)}(t - \tau_k)$ in which $f_c^{(k)}$ is replaced by $f_c^{(k)} + f_d^{(k)}$ to account for the Doppler effect. Therefore, the total signal from all the tags received by the Rx is:

$$s_r(t) = \sum_{k=1}^K s_r^{(k)} = \sum_{k=1}^K \bar{a}_k \sum_{p_k=0}^{P_k} q_{p_k}^{(k)}(t) \cdot \exp \left\{ j2\pi \left[g(t_{p_k}^{(k)} - \tau_k)^2 + 2f_{md}^{(k)}(t - t_{p_k}^{(k)} - \tau_k) + 2f_d^{(k)}t_{p_k}^{(k)} + 2f_c t \right] \right\}. \quad (7.4)$$

Notations in this equation:

- K : the number of tags in the range of detection;
- $q_{p_k}^{(k)}(t) = 1$ or 0 , if $t \in [t_{p_k}^{(k)} + \tau_k, t_{p_k}^{(k)} + T_{on}^{(k)} + \tau_k]$ or others: shifted pulse window function;
- $f_{md}^{(k)} = f_d^{(k)} + f_c^{(k)} - f_c$;
- $\bar{a}_k = a^{(k)} a_{xt}^{(k)} \exp[-j2\pi(4f_c + 2f_d^{(k)})\tau_k]$.

$s_r(t)$ is then demodulated by the frequency-doubled chirp signal and the following baseband signal is generated, whose real and imaginary parts are the I and Q signals in Fig. 7.1, respectively:

$$z_r(t) = s_t^2(t) s_r^*(t) = \sum_{k=1}^K \bar{a}_k \sum_{p_k=0}^{P_k} \exp \left\{ j2\pi \left[\left(g(t - t_{p_k}^{(k)} - \tau_k) + 2g\tau_k - 2f_{md}^{(k)} \right) \cdot \left(t - t_{p_k}^{(k)} - \tau_k \right) + \left(2g(t - t_{p_k}^{(k)} - \tau_k) + 4g\tau_k - 2f_d^{(k)} \right) t_{p_k}^{(k)} \right] \right\} \cdot q_{p_k}^{(k)}(t). \quad (7.5)$$

By doubling the parameters g , f_c , $f_d^{(k)}$ and $f_{md}^{(k)}$ in equation (16) of [76], we can get the same equation as (7.5). Therefore, an HPS-AT has the same baseband waveform and can be implemented with the same signal post-processing techniques for time-of-arrival (TOA) and direction-of-arrival (DOA) estimation as the fundamental system with a doubled bandwidth.

Both frequency domain and time domain methods can be used to solve τ_k , $f_d^{(k)}$ and the phase difference between the demodulated signals from different channels so that the spatial position and velocity can be obtained [76]. To understand the physical meaning of the signal model, we assume the modulation frequency of a tag is infinity. In this way, $t_{pk}^{(k)}$ becomes a continuous variable $t \cdot (f_c^{(k)} + f_d^{(k)}) / f_c^{(k)} - \tau_k$ and equations (7.4) and (7.5) become:

$$\tilde{s}_r(t) = \sum_{k=1}^K \tilde{s}_r^{(k)} \approx \sum_{k=1}^K a^{(k)} a_{xt}^{(k)} \exp \left\{ j2\pi \left[g(t - 2\tau_k)^2 + (2f_c + 4f_d^{(k)})(t - 2\tau_k) \right] \right\}, \quad (7.6)$$

and

$$\tilde{z}_r(t) = s_t^2(t) \tilde{s}_r^*(t) \approx \sum_{k=1}^K a^{(k)} a_{xt}^{(k)} \exp \left[j2\pi (4g\tau_k - 4f_d^{(k)})t + \theta \right], \quad (7.7)$$

respectively, in which the phase constant θ is negligible. As such, the system is simply an FMCW radar with carrier frequency $2f_c$, bandwidth $2BW$, and beat frequency $4g\tau_k - 4f_d^{(k)}$. So, an HPS-AT can be regarded as a discretized FMCW radar embedded with frequency doubling techniques.

7.2 Hardware Design of System Demonstrator

A wideband super-heterodyne structure is selected for the Rx design of a BS front-end to achieve a high linearity, dynamic range, and spurious rejection as well as a low noise figure (NF). The Tx design of a BS front-end uses a simple direct up-conversion structure. A SIHO with a loop switch and an injection signal path is designed for the tag. The loop switch is comprised of a pair of complementary switches based on pin diode (PD) featuring low insertion loss (IL) at on-state, high isolation at off-state and fast switching speed. Both tag and BS front-end prototypes are integrated with a printed circuit board (PCB) technology and off-the-shelf components. The back-end subsystem of a BS uses commercially available instruments and development boards. In this section, the frequency planning and link budget are analyzed first. Subsequently, detailed tag and BS front-end designs are explained.

7.2.1 Frequency planning and link budget

We propose a hardware system that aims at demonstrating the concept and theory in a controllable indoor environment. Prioritizing the system performance and considering the cost and availability of components, the selected operating frequency may not meet spectrum allocation regulations by government departments such as FCC. Nevertheless, we have to avoid radiating at frequencies

occupied by normal devices around the location-of-test. To this end, a spectrum survey is carried out using a WR137 waveguide antenna connected to an Agilent N9030A signal analyzer. Four 90° sectors in the azimuth plane are detected in both vertical and horizontal polarization. For each of the 8 measurements, maximum-hold is used for one hour. Measured spectrums are superposed and plotted in Fig. 7.3. The first two peaks are WiFi signals, and the one at 9.34 GHz may be from satellite broadcasting.

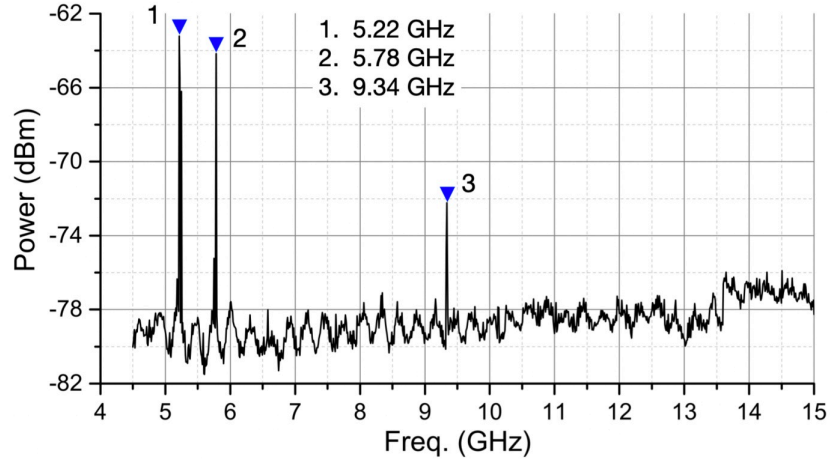


Figure 7.3: Occupied frequencies in 4 GHz ~ 15 GHz band around the location of indoor HPS-AT demonstration.

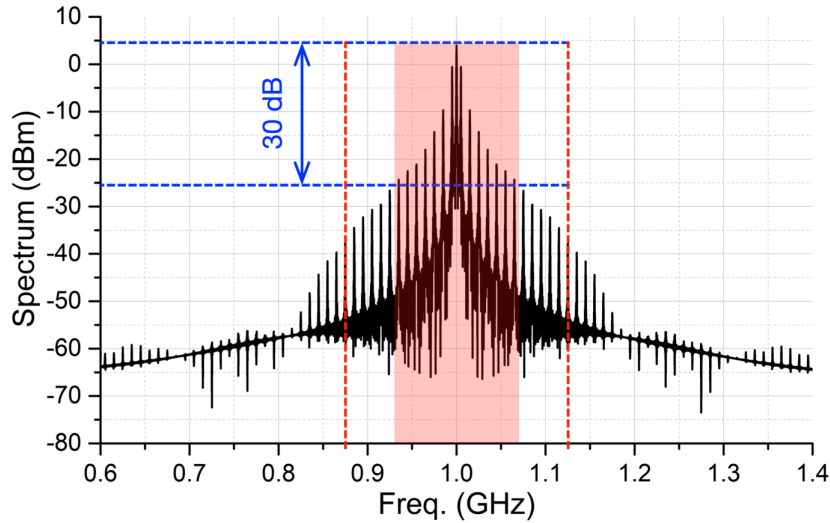


Figure 7.4: Tag output spectrum with 5 MHz modulation frequency and 8 ns rise/fall time. Carrier frequency is normalized to 1 GHz.

From Fig. 7.4, it can be seen that the output spectrum of a tag with 5 MHz modulation frequency and 8 ns rise/fall time of pulses has about 150 MHz 30-dB bandwidth. Considering the fact that

carrier frequencies of multiple tags may have slight differences because of fabrication tolerance, and to make sure that backscattered signals from all the tags are well collected, we define the Rx bandwidth of the BS front-end to be 250 MHz. To guarantee a 0.1 m standard deviation of distance estimation at 5 dB SNR, 800 MHz equivalent bandwidth is required [188], so the interrogation chirp bandwidth is 400 MHz.

According to the above information and using typical off-the-shelf mixer specifications, spurious and intermodulation products (IMs) of BS Tx and Rx are simulated and shown in Fig. 7.5, together with a frequency planning in this connection. The RF signals for Tx and Rx are center at 6.3 GHz and its 2nd harmonic frequency 12.6 GHz, respectively. The intermediate frequency (IF) signal of the Tx is a 400 MHz chirp whose carrier frequency is restricted below 1.2 GHz because of the limited capability of the direct digital synthesizer (DDS) or arbitrary waveform generator (AWG) we used in this work. Referring to Fig. 7.5 (b), the frequencies of the Tx local oscillator (LO) and IFt are adjusted subject to the requirements that spurious and IM which fall into the Tx band should be 50 dB lower than the desired signal, and those out of Tx band should be kept far enough in the spectrum so as to be effectively attenuated by a Tx band-pass filter (BPF) with achievable side-band response. The low side band signal $-IFt+LO1t$ has a similar amplitude as the desired one at the mixer output and may interfere the tags and other devices if it is not filtered out. A higher IFt frequency makes the $2\times IFt+LO1t$ band and $LO1t$ farther from the Tx band and easier to get filtered out. Spurious and IM components around 12.6 GHz can block BS Rx through antenna coupling if they are not filtered out, because the backscattering signal received by a BS Rx can be as low as -70 dBm or less. When we carry out a frequency planning, strong spurious and IM components around the frequencies shown in Fig. 7.3 should be avoided, too. And Tx BPF rejections at those bands have to be guaranteed.

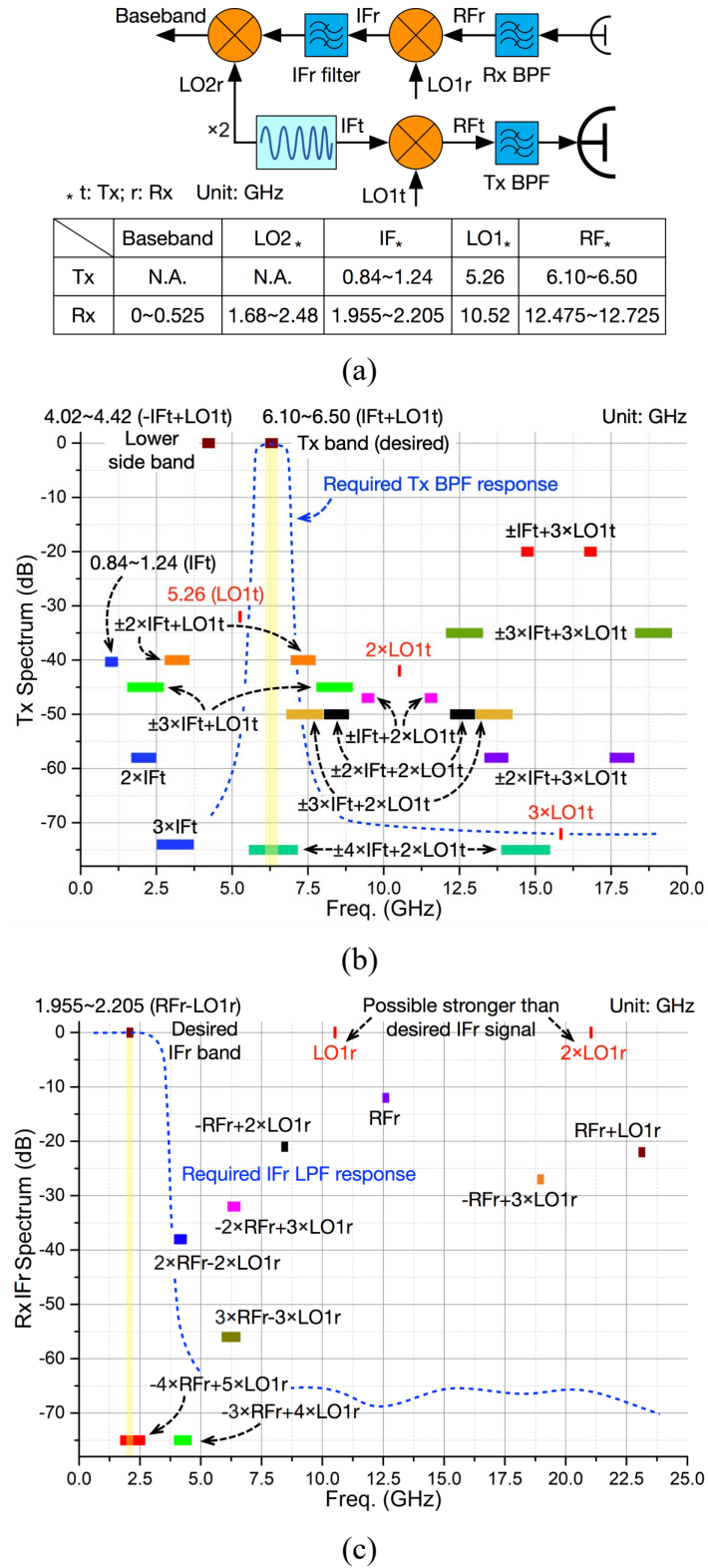


Figure 7.5: (a) Proposed frequency planning of the BS front-end demonstrator. (b) Output spectrum of the Tx mixer in the BS front-end. (c) Output spectrum of the IF mixer of the Rx in the BS front-end.

In Fig. 7.5 (c), the IFR spectrum of an Rx is plotted. The desired IFR band can be selected by a low-pass filter (LPF) or BPF. Spurious, IM and their harmonics may mix with the leaked LO2r and its harmonics in the baseband demodulator and contaminate the baseband signal. Therefore, we have to make sure that the spurious and IM are properly located by a careful frequency planning and they can be effectively filtered out. The amplitude of LO1r in the IFR spectrum is only determined by the LO power of a mixer, therefore it may be stronger than the desired IFR signal. And LO1r may mix with the 5th harmonic of LO2r at the baseband demodulator to produce a non-negligible spurious within 0 to 0.525 GHz band. As such, the IFR filter should have 60 dB or higher rejection at 10.52 GHz. Moreover, components $-2 \times \text{RFR} + 3 \times \text{LO1r}$, $-\text{RFR} + 2 \times \text{LO1r}$ and RFR can be converted to baseband when mixed with the 3rd or 5th harmonics of LO2r. Considering their amplitude and distance to the $\text{RFR} - \text{LO1r}$ band, they all can be handled by the IF filter to achieve a -50 dBc spurious level in the baseband. In addition, Rx BPF has to be designed with two factors in mind, namely the spurious and IM from BS Tx, and the occupied bands shown in Fig. 7.3.

Table 7.1: System Demonstrator Link Budget and Key Specs

	Path loss		Antenna gain		Power	
	Tx (100 m)	Tx (4 m)	Tx	Rx	Tx	Rx
BS	-88.4 dB	-60.5 dB	12 dBi	10 dBi	25 dBm	-72.5~-44.5 dBm
Tag	-94.5 dB	-66.5 dB	7 dBi	7 dBi	5 dBm	-44.4~-16.5 dBm

	Bandwidth (input)	Noise floor (input)	Min SNR (input)	Min SNR equiv. (output)	Allowed NF max
BS Rx	150 MHz	-92.1 dBm	19.6 dB	10 dB	9.2 dB

Link budget and key specifications of the proposed demonstrator are given in Table 7.1. Moderate antenna gain and transmitted power for both BS and tag are used. A single tag with $2f_c^{(k)} = 12.6$ GHz is assumed when calculating the NF. Therefore, the input signal has a bandwidth of 150 MHz. If LO2r is a monotone, the baseband signal also has a bandwidth of 150 MHz. Since LO2r is a chirp, the power of the baseband signal is distributed into a bandwidth of 475 MHz. As such, the equivalent minimum SNR for the desired 0.1 m standard deviation of distance estimation is $5 + 10 \cdot \log_{10} \frac{475}{150} = 10$ dB, which can be used to correlate the normal NF definition using the same input and output bandwidth. It comes out that BS Rx needs to achieve an

NF better than 9.2 dB to realize a maximum range coverage of 100 m. It should be noted that an NF margin of more than 4 dB is reserved [76, 192]. Therefore, a range of at least 260 m should be feasible in the best case. The requirement of minimum range of 4 m decides the BS Rx compression performance and spurious level. The BS front-end should have a high enough spurious-free dynamic range such that the farthest and closet tags can be handled simultaneously. A tag with an adaptive transmitted power control based on a received signal strength is favorable because it may improve the BS-received SNR of a distant tag and increase the ratio of maximum and minimum range, although this function is not implemented in this demonstration system.

7.2.2 Tag analysis and schematic

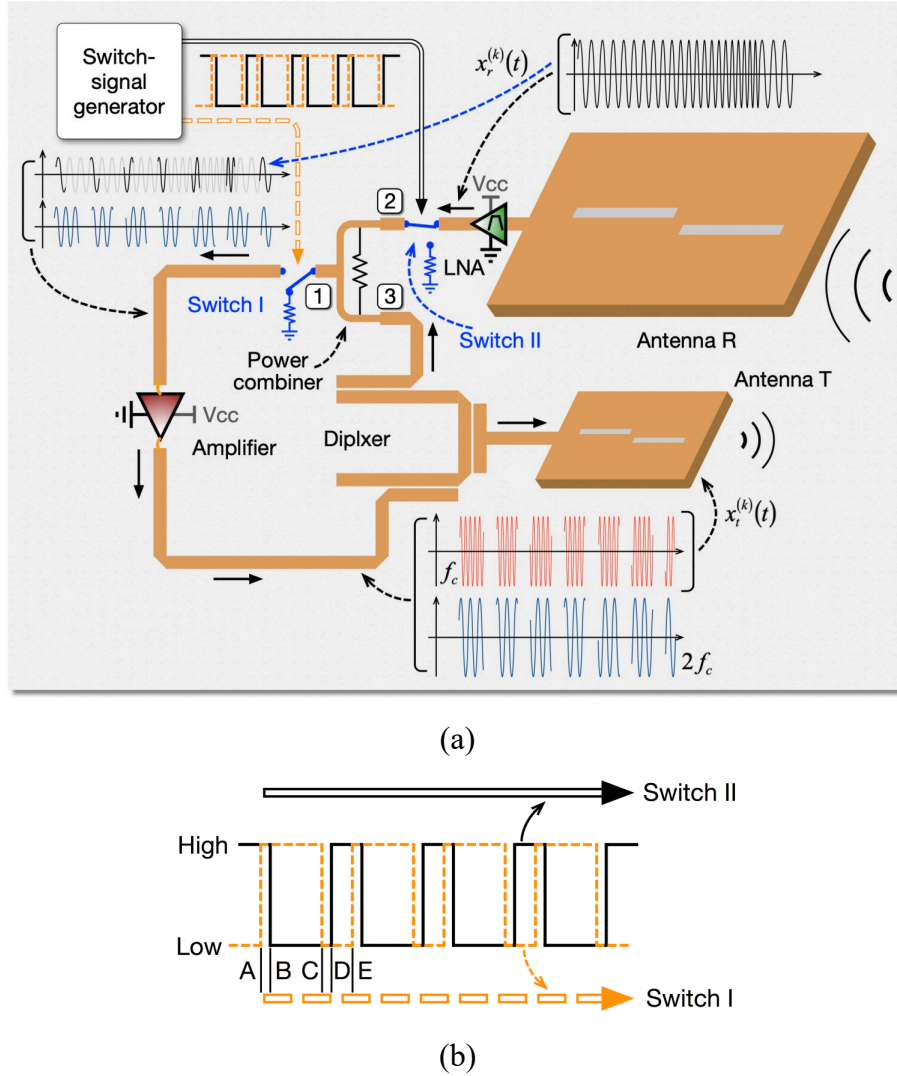


Figure 7.6: (a) Operation principle of active tag with a switched SIHO, antennas, and switch-signal generator. (b) Timing diagram of switch control signals.

Fig. 7.6 (a) illustrates the operation principle and key components of a tag of HPS-AT. Antenna R for receiving operates at f_c with a bandwidth of BW and Antenna T for transmitting operates at $2f_c^{(k)}$ with a bandwidth of 150 MHz. A power combiner is added between the diplexer and amplifier of a standard SIHO to introduce an injection signal $x_r^{(k)}(t)$ from Antenna R. A low noise amplifier (LNA) is used immediately after Antenna R, followed by a BPF. A loop switch is comprised of Switch I and Switch II, at port 1 and port 2 of the combiner, respectively. Both switches are single-pole-double-throw (SPDT) type. When a signal path is connected by a switch, we say that the switch is at on-state, otherwise, we say that it is at off-state. The lower throws of both switches are connected to matched loads. In this way, a signal reflection is minimized no matter a switch is at on-state or off-state, as Fig. 7.6 (a) suggests.

The two switches are controlled by a pair of quasi-complementary signals, whose timing diagram is shown in Fig. 7.6 (b). At the high-level of a control signal, the corresponding switch is at on-state. During AB segment, both switches are at on-state, SIHO loop takes the injected signal, with whose phase oscillation starts to build up. During BC segment, Switch II is at off-state so that the injection signal is prohibited, and the loop keeps oscillating and outputting a pulse at frequency $2f_c^{(k)}$. AB segment is so short that after oscillation is built, the injection signal stops pulling the SIHO frequency. This feature is critical especially when as strong as a single-digit-dBm of injection signal (after being amplified by the LNA of a tag at a distance of 4 m) may be introduced to the loop, which is at a similar magnitude as the output power of a tag, as suggested by our link budget. Accordingly, at off-state, Switch II should have an enhanced isolation which can suppress the injected signal to a level negligible for the SIHO oscillating dynamics. Moreover, Switch II has to ensure port 2 of the power combiner always sees a matched condition, such that for the entire AC segment, the loop has a stable characteristic. Both switches are at off-state during CD segment, which can be designed as short as possible. In this segment, Switch I only needs to create an isolation high enough to offset the loop gain of the SIHO. During the entire BD segment, an open circuit can be seen by the output of the LNA, so the injection signal reflection happens among antenna, LNA, and filters, resulting in an unwanted standing wave with phase ambiguity. In DE segment, Switch I and II are at off- and on-state, respectively. In this way, the standing wave is flushed out to the matched load of Switch I and an injection signal with the desired phase is prepared for next cycle.

In the following paragraphs, the key components of a tag are designed to fulfill the required functions and specifications. Unless otherwise stated, all the components are designed and realized with a Taconic TSM-DS3 substrate with 0.508 mm thickness.

7.2.3 Tag components and complete design

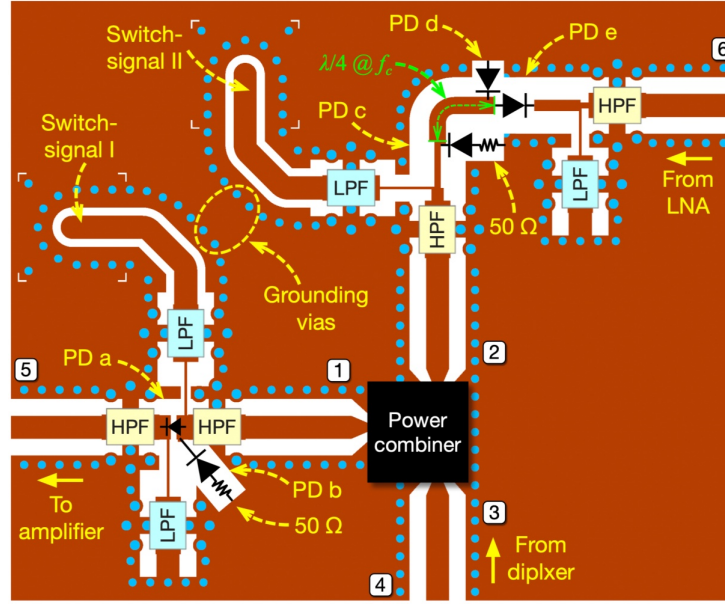


Figure 7.7: Layout of switch circuits on an HPS-AT tag.

Fig. 7.7 illustrates the designed layout of Switch I and Switch II. A broad band power combiner EP2C+ from Mini-Circuits is used. It can cover 1.8 GHz to 13 GHz band. All the 5 PDs are MA4AGP907 from MACOM, they have an RC product of 0.1 ps and a switching speed of 2 ns. The LPFs are LFCN-3800, which has a 3-dB corner frequency of 4.8 GHz with about 25 dB and 20 dB IL at 6.3 GHz and 12.6 GHz, respectively. The high-pass filters (HPFs) are HFCN-5500 which has a 3-dB corner frequency of 5.5 GHz and more than 33 dB IL below 4 GHz. Both types of filter are from Mini-Circuits, and they are used to isolate the control signal path and the isolation loop. The LPF can support a rising edge of less than 0.3 ns which is much shorter than the PD switching time.

When switch signal I is at high-level (1.4 V), PD a is forward-biased (turned on) and PD b is reverse-biased (turned off). When switch signal I is at low-level (−1.4 V), PD a is turned off and PD b is turned on so that port 1 of the combiner is terminated with 50 Ω. When switch signal II is at high-level (1.4 V), PD e is turned on and PD c & d are turned off so Switch II is a through. When switch signal II is at low-level (1.4 V), PD c & d are turned on and PD e is turned off. Therefore,

the microstrip line (MSL) is shorted to the ground at PD d. Since the MSL between PD c and PD d is about 90° at f_c , PD c can see an open condition at its cathode towards PD d, which enhances the isolation and ensures port 2 of the combiner is always terminated with $50\ \Omega$ at the fundamental oscillating frequency.

The layout is designed, optimized and fabricated. The measured S-parameters of a loop switch corresponding to the layout in Fig. 7.7 are shown in Fig. 7.8. It can be seen that as Switch I is at on-state, the IL and phase between ports 4 and 5 at 6.3 GHz are about 5 dB and 30° , respectively, regardless of the state of Switch II. When Switch II is at on-state, S₆₆ is always below -20 dB regardless of the state of Switch I. Isolations (IL difference between on-state and off-state) of Switch I and II at 6.3 GHz are about 17 dB and 32 dB, respectively. Considering the 3.7 dB IL of the power combiner and 1~2 dB IL of a diplexer, the loop gain will fall below 0 dB if an amplifier of 20 dB gain is used. On the other hand, assuming a tag receives -16.5 dBm injection power and the LNA has a gain of 20 dB, the injection power that joins the oscillating loop during BD segment will be less than -30 dBm. Since the SIHO is expected to output 5 dBm of its 2nd harmonic, the injected signal is too weak to have a frequency pulling. Therefore, the loop switch design fulfills our requirements.

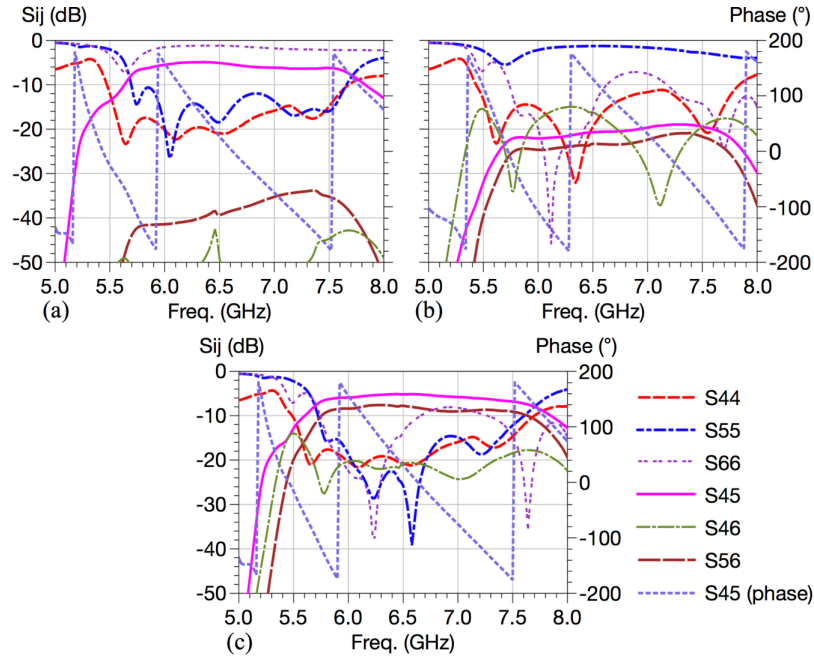


Figure 7.8: Measured S-parameters of loop switch at (a) Switch I is at on-state and Switch II is at off-state; (b) Switch I is at off-state and Switch II is at on-state; (c) Both Switch I and Switch II are at on-state.

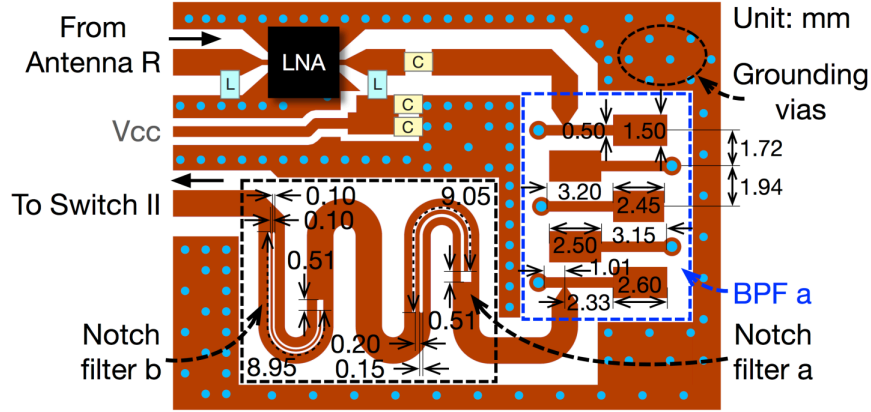
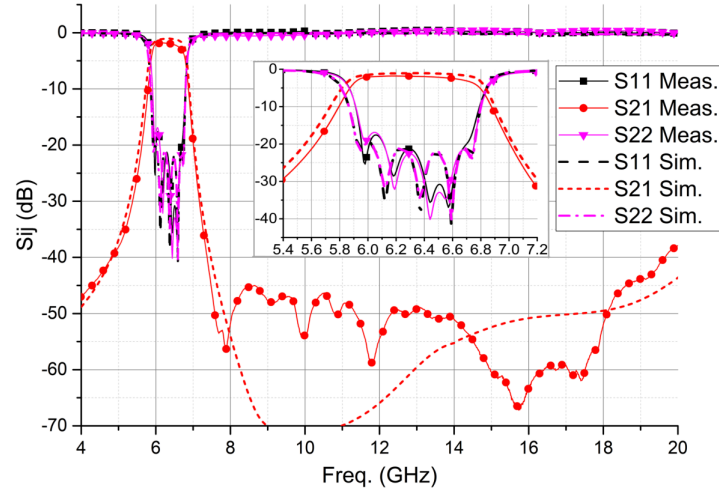
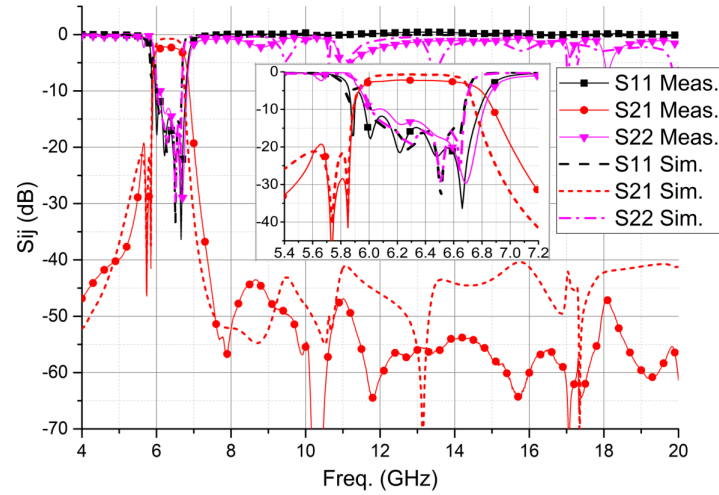


Figure 7.9: Layout and dimensions of tag input filters following the LNA.

Fig. 7.9 shows the layout of the filters following the LNA that amplifies the received interrogation signal. The selected LNA is a PMA3-83LN+ from Mini-Circuits which has a gain of 21.3 dB, NF of 1.56 dB and input P1dB of 0 dBm, all at 6.3 GHz. The same component is also used as the amplifier in the SIHO loop (Fig. 7.6 (a)). BPF a is a stepped-impedance resonator (SIR) filter with symmetrical input and output arrangement [193], covering the 6.1 GHz to 6.5 GHz band. It has a good harmonic band rejection but lacks a steep side-band response. To enhance a rejection of the 5.8 GHz Wi-Fi band, BPF a is cascaded with notch filters a and b with quarter wavelength open stubs embedded in MSL [194], which work at 5.74 GHz and 5.85 GHz, respectively. The simulated and measured responses of BPF a and the complete input filter chain are shown in Fig. 7.10. We can see the Wi-Fi bands are attenuated by more 25 dB and the 12.6 GHz band is rejected by more than 55 dB. IL in the pass-band is about 1.8 dB.



(a)



(b)

Figure 7.10: Simulated and measured S-parameters of (a) BPF a, and (b) BPF a cascaded with notch filter a and notch filter b.

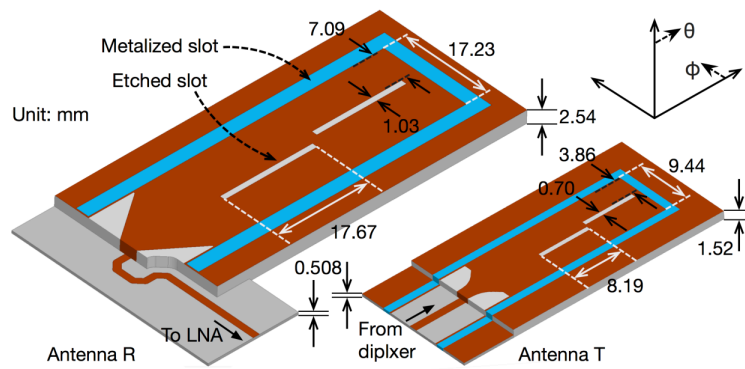


Figure 7.11: Perspective view and dimensions of Rx and Tx antennas of an HPS-AT tag.

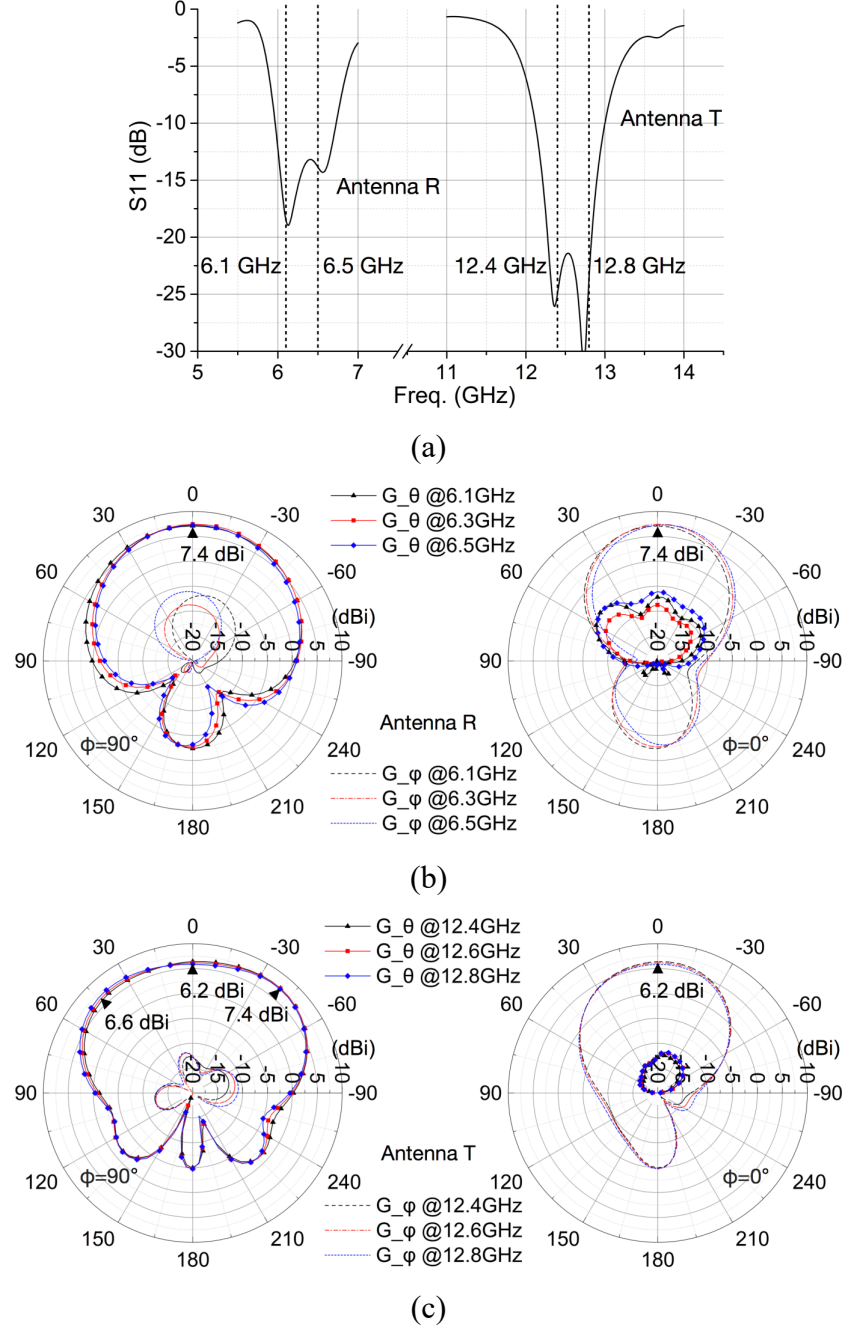


Figure 7.12: (a) Measured S_{11} of Rx and Tx antennas of tag. (b) radiation patterns of Rx antenna. (c) radiation patterns of Tx antenna.

Fig. 7.11 is the perspective view of antennas of a tag design. Both Tx and Rx antennas make use of substrate integrated waveguide (SIW) technology which has the superiority of compact size, low mutual-coupling and self-shielding [138, 195]. Also, the Tx SIW antenna is designed to have a cutoff frequency higher than $f_c + BW/2$ such that the interrogation signal has minimum

unintentional interference to the SIHO through the output. To satisfy a bandwidth requirement, Rogers RT/duroid® 6002 substrates with thicknesses of 2.54 mm and 1.52 mm are used for the two antennas, respectively. Step transitions to MSL on the same 0.508 mm Taconic substrate of other components are optimized to ensure a low IL. The measured input reflection coefficients and radiation patterns are shown in Fig. 7.12. Antenna T and R have a boresight gain of 6.2 dBi and 7.4 dBi, respectively. Antennas are designed to have narrower H-plane 3-dB beamwidth (70° for T and 59° for R) and wider E-plane 3-dB beamwidth (135° for T and 103° for R) to reduce scattering in elevation and to have sufficient coverage in azimuth.

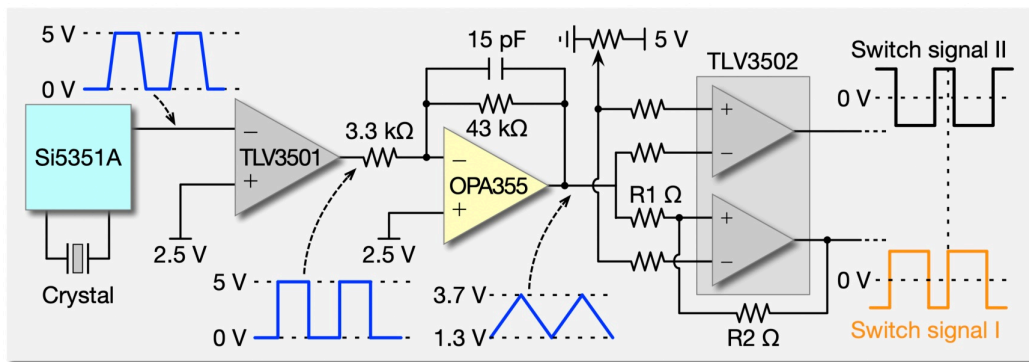


Figure 7.13: Simplified schematic of switch-signal generator of tag.

A simplified schematic of switch-signal generator designed for the tag is shown in Fig. 7.13. A low-cost programmable clock generator Si5351A from Silicon Labs is used to generate a square wave. It has a very low jitter (70 ps, peak-peak) such that a coherence duration can cover a complete chirp period [76]. High-speed operational amplifier (Op-Amp) and comparators all from Texas Instruments are used to shape the clock signal. Among them, a comparator TLV3501 shortens rise and fall time of the square wave, an Op-Amp OPA355 is used to turn the square wave into a triangle wave, based on that, a comparator pair TLV3502 with tunable reference voltage generators antipodal square waves with tunable duty cycle. A tiny shift between the two switch signals is realized by adding a hysteresis with appropriate resistors R1 and R2.

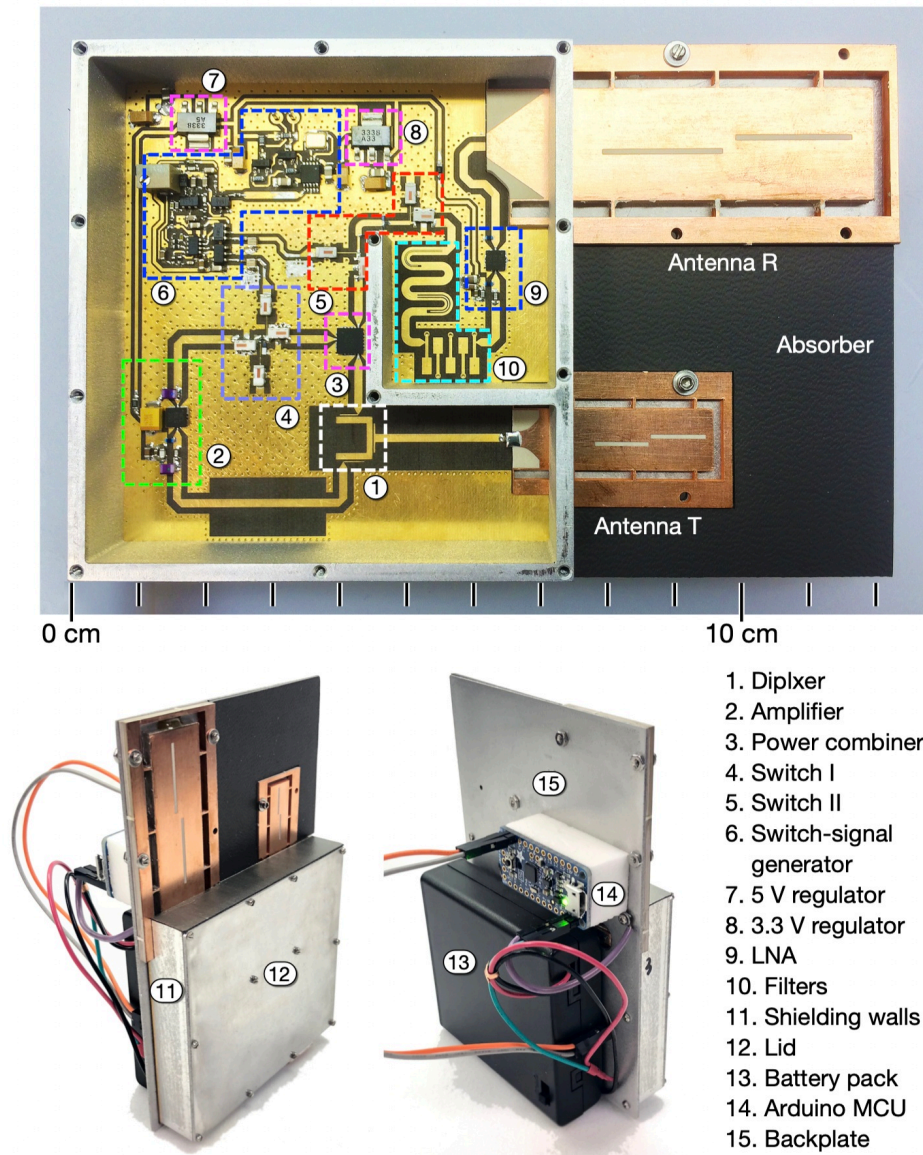


Figure 7.14: Photos of the PCB and complete unit of a tag for HPS-AT.

The complete PCB and assembled HPS-AT tag unit are shown in Fig. 7.14. The diplexer and SIHO are designed with reference to the theory and method presented in [189]. Aluminum shielding walls and backplate sandwich the antennas and PCB. Grooves are cut on the walls to fit the position and thickness of the antennas, creating a perfect contact with the broadside of SIWs. An Arduino microcontroller board is used to automatically program the Si5351A chip to a predefined switching frequency each time a tag is powered up by a 6 V battery pack.

7.2.4 BS front-end analysis and schematic

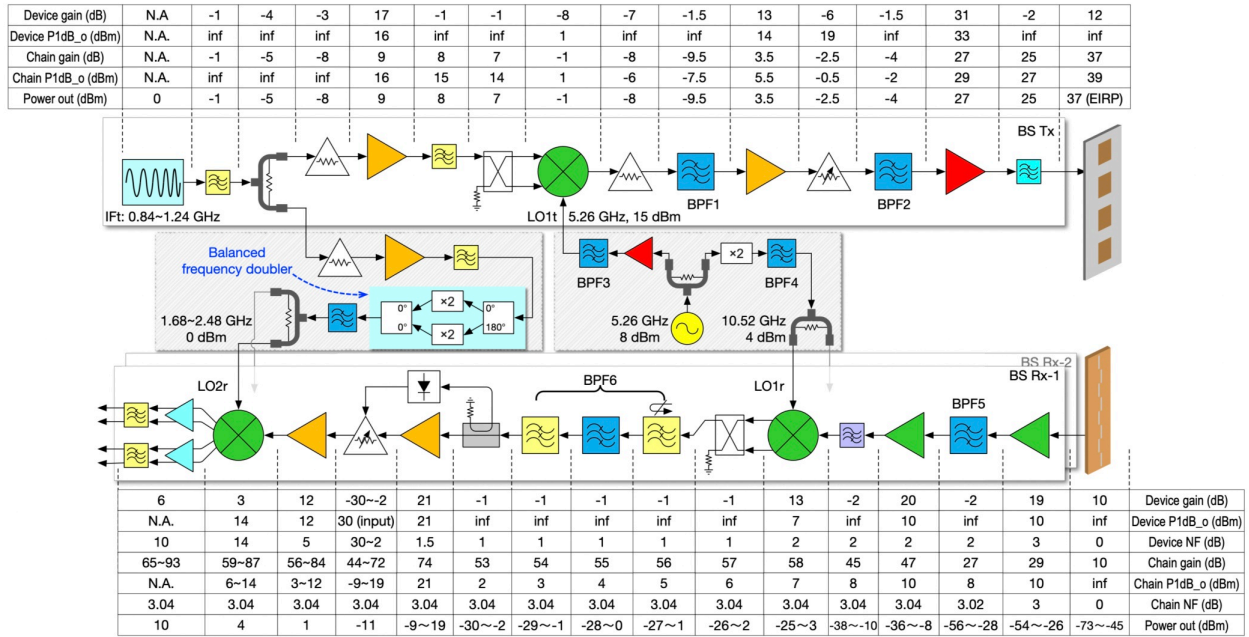


Figure 7.15: Detailed schematic and chain budget of the proposed BS Front-end

A detailed schematic of the BS front-end design in compliance with the function, frequency, spurious and power requirement discussed in the previous sections is illustrated in Fig. 7.15. Data of chain budget is also shown. There are one Tx and two Rx's. Adaptive gain control circuits are used in Rx's for a fixed baseband output level, which makes it convenient to digitize with ADC or oscilloscope. Baseband demodulators output balanced I/Q signals which are then conditioned by Op-Amps and LPFs.

IFt signal, which is a chirp from 0.84 GHz to 1.24 GHz, has about 40% of fractional bandwidth. Therefore, after it is processed by a frequency doubler, unwanted harmonics may have very close frequencies to the desired ones (LO2r) and makes an effective filtering impossible. For example, the triple of 0.84 GHz is very close to the double of 1.24 GHz. To prevent the baseband spurious and IM components caused by this effect, we implement a balanced frequency doubler which comprises a pair of identical doubler units, a 180° power divider and a 0° power combiner both having excellent balance performance. In this way, odd harmonics outputs are canceled out, and the closest unwanted even harmonic outputs can be easily suppressed by filters.

Since the LO signals for the IF mixers of Tx and Rx's are generated from the same source, and the LO for the baseband demodulator of Rx's is a doubled IFt, signal isolation performance of LO

distribution networks becomes critical. The amplitude of signals in Tx may be much stronger than that of Rx, a weak coupling or feed through of such a signal may result in a significant interference in Rx. In the IFt distribution circuit, amplifiers following the power divider adopt ones with a high reverse isolation (low S_{12}). In the LO1t feed path, a high isolation power amplifier is used. BPF3 for LO1t is a narrow band filter only allowing a 5.25 GHz signal to pass, blocking IFt, RFt and harmonics of LO1t. In the LO1r feed path, BPF4 is also a narrow band one, allowing a 10.52 GHz signal to pass and blocking other harmonics of 5.26 GHz as well as IFt and RFt. To avoid coupling issues, we also use independent dc power supply units for different channels.

As stated in section 7.3.1, the IF filter BPF6 of an Rx is critical for an excellent system performance. It is designed as a cascade of three filters. The first one from the right is a reflectless LPF. Although the stop-band attenuation of this type of filter usually is not as high as its reflect type counterpart, it can absorb undesired high-frequency components generated by the mixer instead of reflecting and re-feeding them back to the mixer, creating more interferences unintentionally. In this way, output signal quality can be improved. Moreover, when cascading reflectless LPF with other filters, we can avoid standing waves, which may deteriorate pass-band performance. The rest two filters in BPF6 helps to further enhance stop-band attenuation.

The IF mixers for Tx and Rx use single side band structure and image rejection structure, respectively, for a lower spurious and a less sophisticated filter design. Some of the filters and passive components in the system are in-house designed with single- or two-layer planar topologies and fabricated together with the BS front-end PCB, therefore ensuring a low cost and high reliability. The Tx and Rx antennas are designed and fabricated separately and assembled with the system.

7.2.5 BS front-end filters and complete design

Design and verification of the filters of the BS front-end are presented in this section. The complete BS front-end prototype is illustrated and explained in the last.

BPF1 and BPF2 use the same design as BPF a of the tag design. Referring to Fig. 7.10 (a) and Fig. 7.5 (b), we can find that BPF1 satisfies the discussed requirement of suppression. At 5.26 GHz (LO1t frequency) and 4.42 GHz (lower side band), S_{21} of BPF1 is -35 dB and -45 dB, respectively. In addition, the mixer provides extra lower side band rejection. S_{21} of BPF1 at the low end of $2 \times \text{IFt} + \text{LO1t}$ band is -15 dB. BPF1 and BPF2 together provides about 100 dB of suppression of any signal in the Rx band centered at 12.6 GHz.

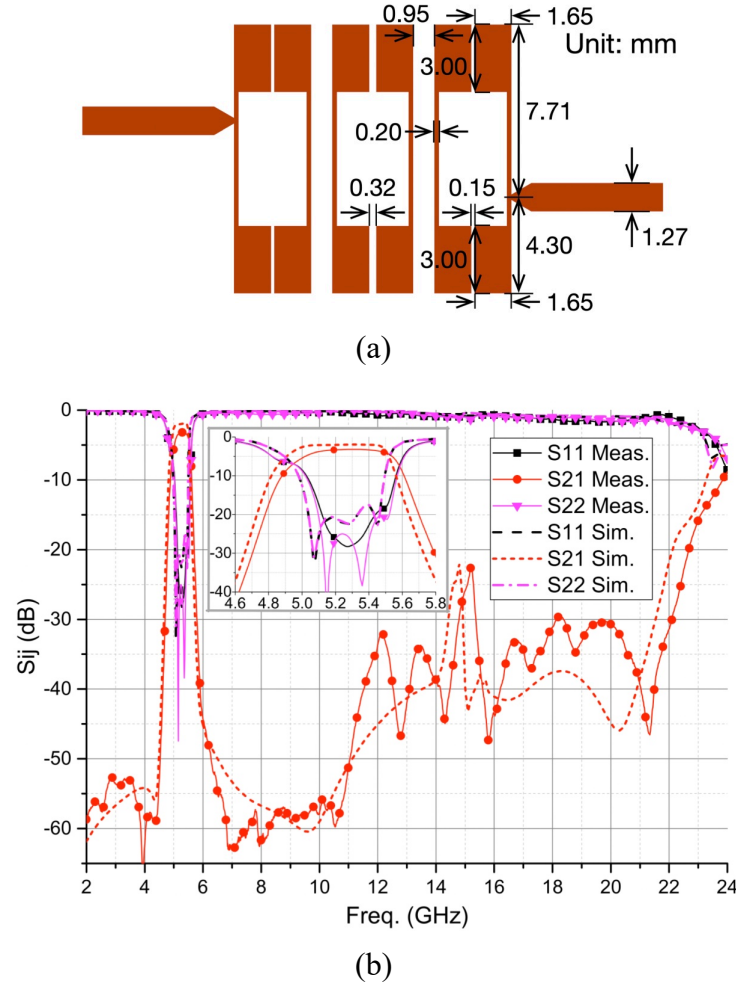


Figure 7.16: (a) Layout of BPF3 with dimensions. (b) Simulated and measured S-parameters of BPF3.

Fig. 7.16 shows the layout and S-parameters of BPF3, which is a narrow band filter with an extended stop-band employing high quality factor half-wavelength SIRs [196, 197]. It has identical resonators and is axisymmetric. Fig. 7.17 shows the layout and S-parameters of BPF4, the filter of LO1r. It is a cascade of an MSL LPF and an SIW cavity filter [198] with wide stop-band using corner cavities. The MSL LPF is employed to suppress the parasitic pass-band of the SIW filter at about $2 \times \text{LO1r}$ frequency.

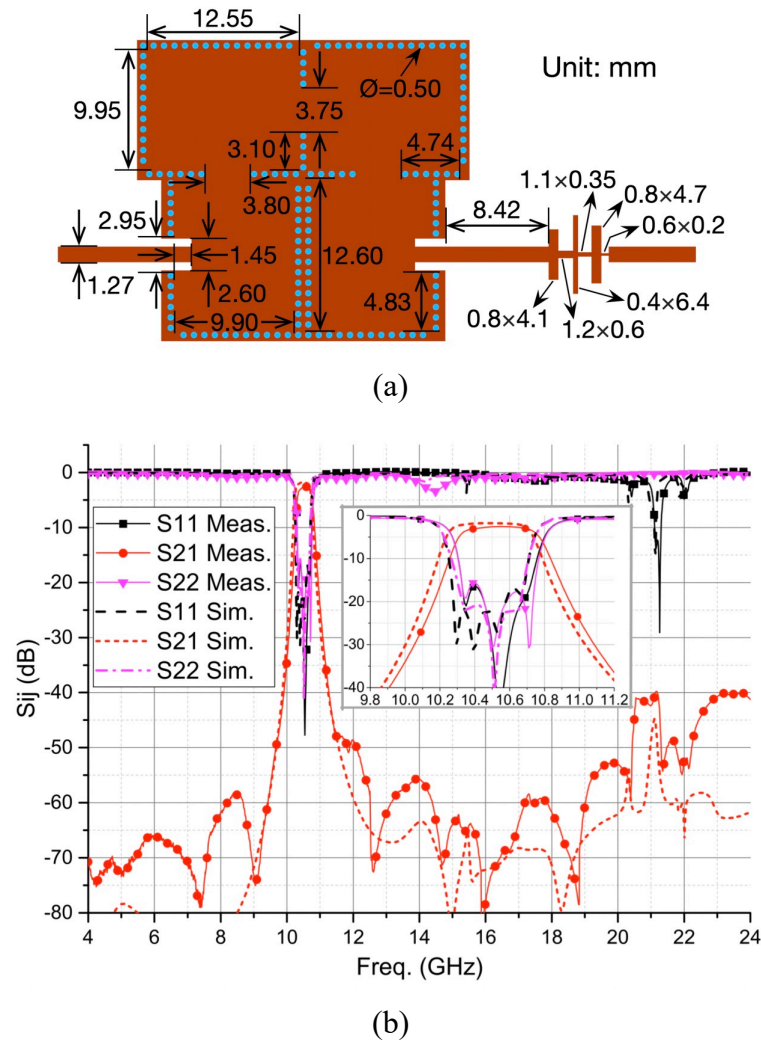


Figure 7.17: (a) Layout of BPF4 with dimensions. (b) Simulated and measured S-parameters of BPF4.

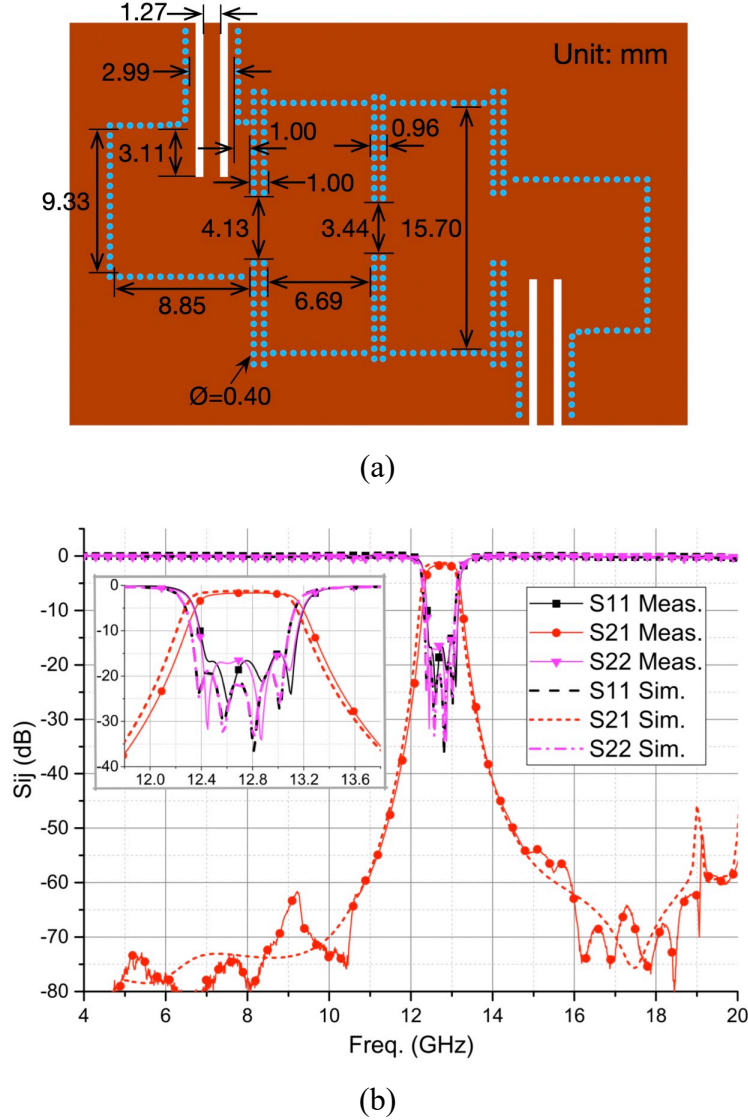


Figure 7.18: (a) Layout of BPF5 with dimensions. (b) Simulated and measured S-parameters of BPF5.

Fig. 7.18 is the layout and S-parameters of BPF5 at the input of an Rx. It utilizes corner cavities at the input and output as well as large-aspect-ratio central cavities to realize a steep upper side-band response and a high attenuation at 17.5 GHz, which is the 2nd order cavity mode frequency. Therefore, BPF5 can further suppress the transmitted spurious components. In addition, BPF5 has more than 70 dB rejection below 10 GHz, where occupied bands (Fig. 7.3) and the image band at about 8.44 GHz of Rx exist. Fig. 7.19 (a) shows an LPF design with elliptical response [100] for BPF6. The reflectless LPF and the BPF for BPF 6 are XLF-252+ and SXBP-2150+, respectively, both from Mini-Circuits. Fig. 7.19 (b) shows the simulated and measured S-parameters of BPF6.

It can be seen that almost all the spurious and IM components from the Rx IF mixer fall in the absorption band of the reflectless LPF. The photo of all the fabricated filter is shown in Fig. 7.20.

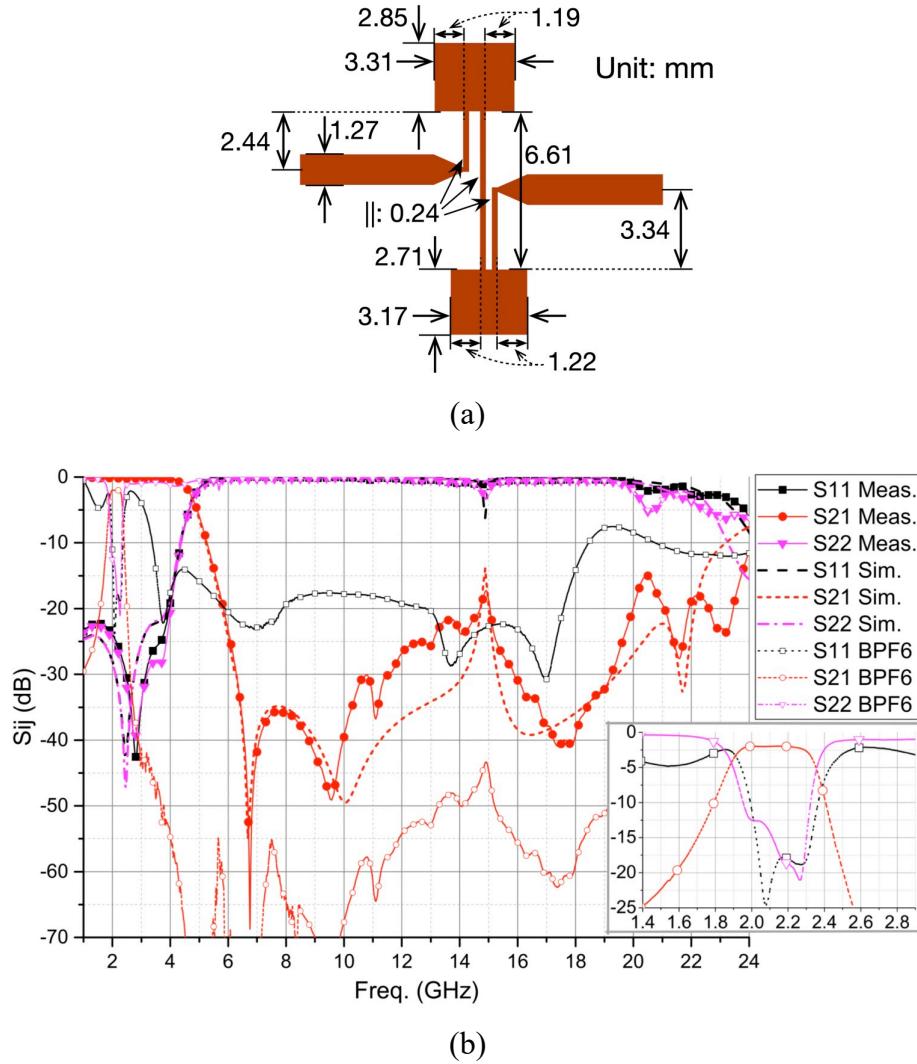


Figure 7.19: (a) Layout of LPF in BPF6 with dimensions. (b) Simulated and measured S-parameters of LPF of (a) and BPF6.

Fig. 7.21 is the photo of the assembled BS front-end prototype. The entire sub-system is fabricated on one piece of 6-layer PCB. Metal layers at the top and bottom sides are for RF signal. The two metal layers in the middle are for dc signal. Grounding and signal interconnections between layers are realized with metalized through holes. The PCB is sandwiched by two pieces of shielding frames. Cells of the frames are designed to prevent coupling. In the areas of the PCB corresponding to the walls of the frames, solder mask is avoided and sufficient grounding vias are placed to make sure a perfect grounding between the PCB and frames. For each of the frame, we also made a metal

lid with inner side covered by microwave absorber material QR-13AF/SS3 from Laird Technologies.

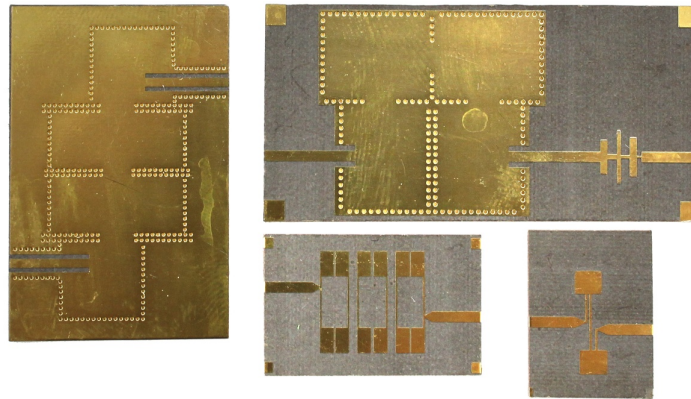


Figure 7.20: Photo of the fabricated filters for BS front-end.

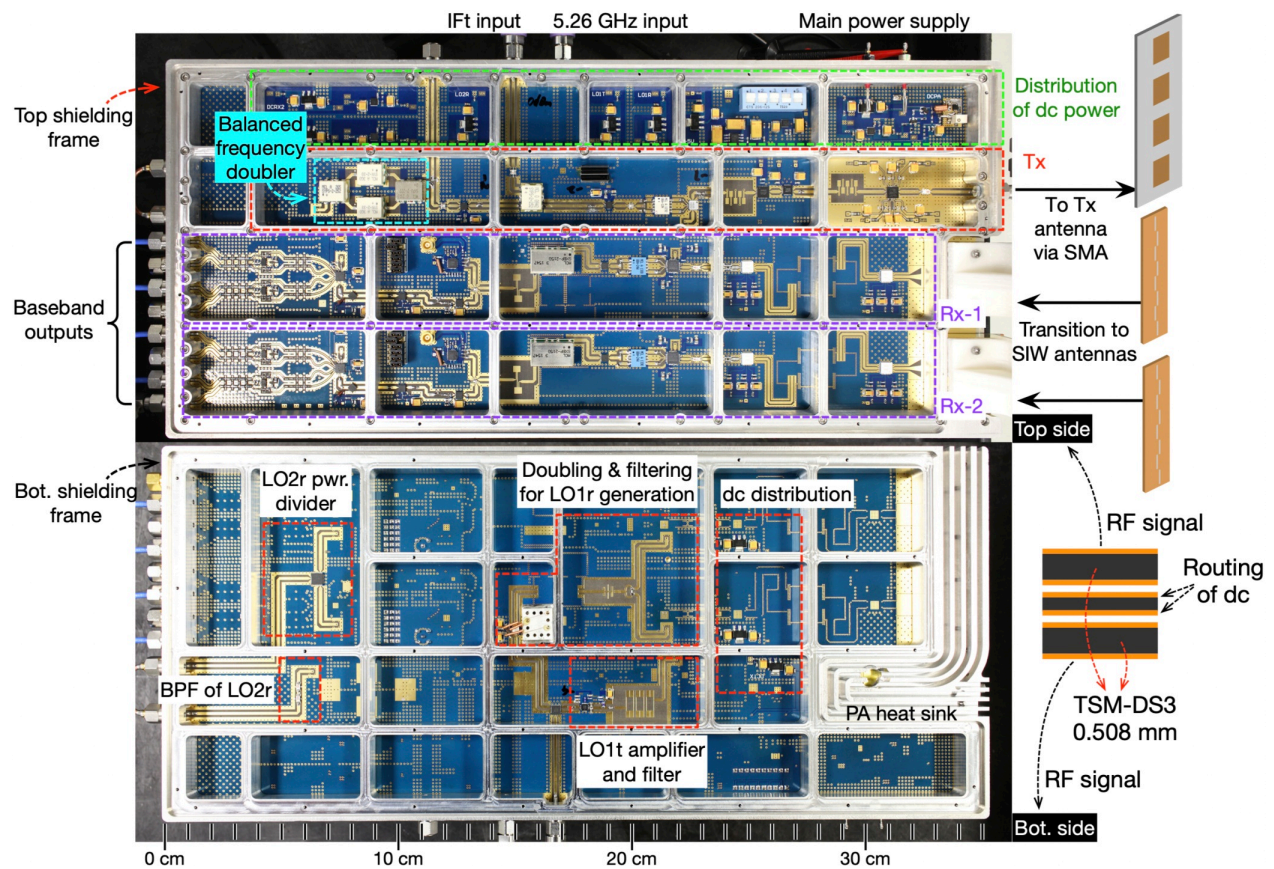


Figure 7.21: Photo of the BS front-end prototype.

7.2.6 BS antennas and replaceable transition

A linear rectangular patch array antenna with tapering is designed for Tx of the BS, as shown in Fig. 7.22 (a). Radiation elements are etched on a Rogers RT/duroid® 5880 substrate with a thickness of 3.18 mm. The MSL feeding network is designed on a Taconic TSM-DS3 substrate with 0.508 mm thickness. Patches are fed by the MSL open-ends through H-shape slots on the ground plane. Aperture feeding at the backside minimizes the radiation pattern tilting due to a parasitic effect of the feeding network. The antenna has an SMA port to connect with the Tx. Coupled power to 1~4 patch elements relative to the antenna input is -12.22 dB, -3.92 dB, -3.92 dB, and -12.22 dB, respectively, for a low sidelobe. As shown in Fig. 7.22 (b) and (c), both impedance bandwidth and pattern bandwidth can cover the interrogation signal band. Fig. 7.22 (c) also shows that a gain of 12.5 dBi in the boresight can be obtained. 3-dB beamwidth of E-plane (azimuth) and H-plane (elevation) are 66° and 24° , respectively.

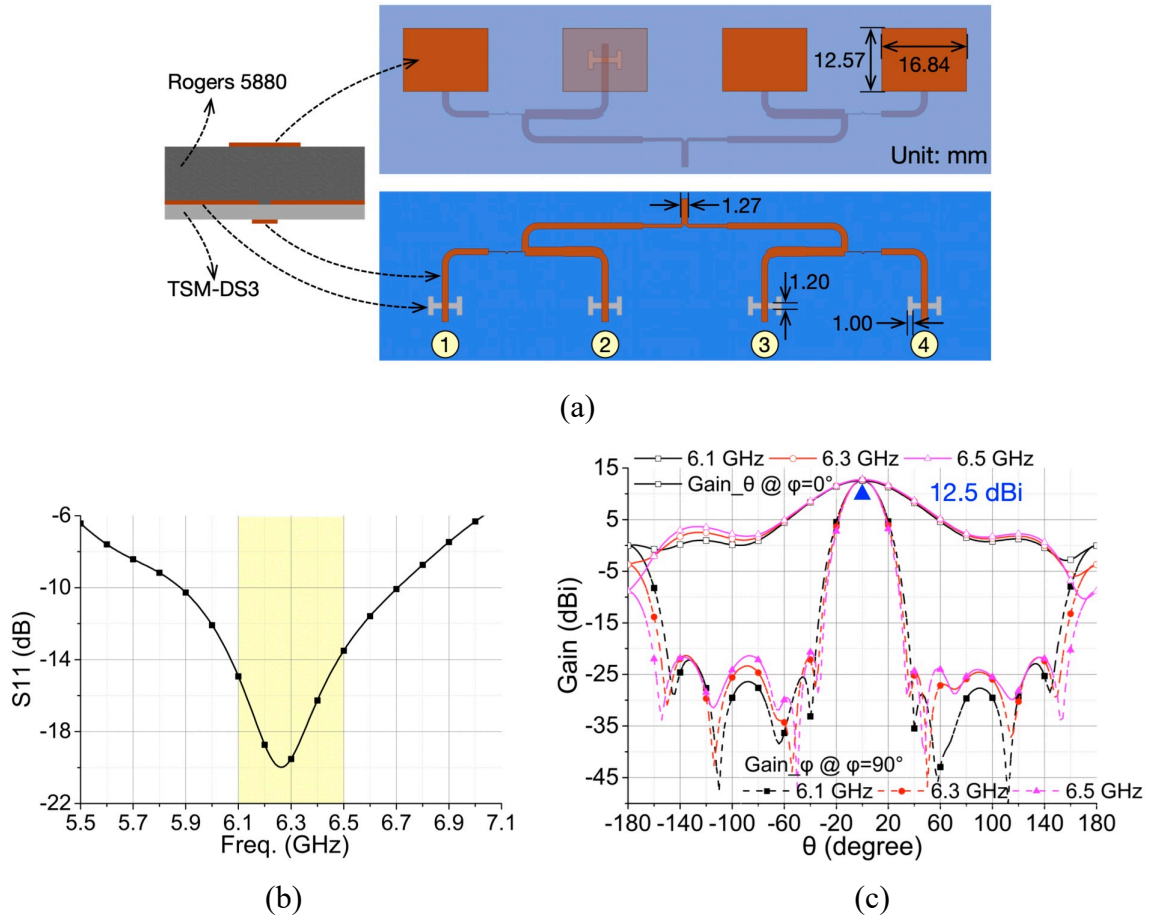
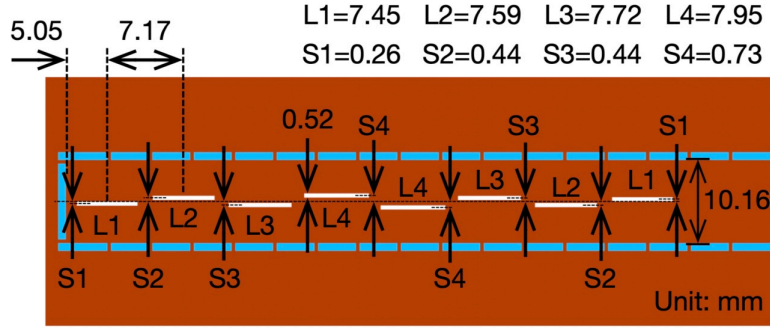
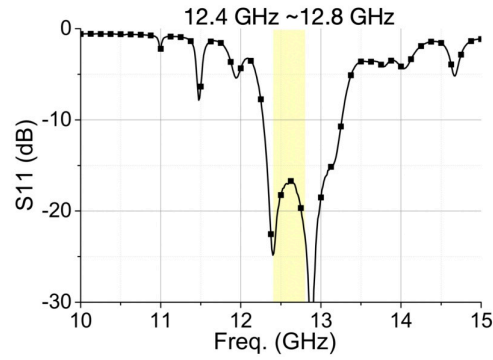


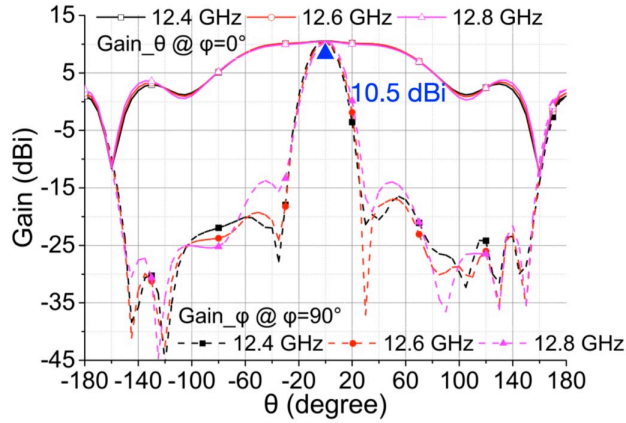
Figure 7.22: Aperture feed patch array antenna for BS Tx, (a) structure and dimensions, (b) S11, and (c) radiation pattern.



(a)



(b)



(c)

Figure 7.23: SIW slot array antenna for BS Rx, (a) structure and dimensions, (b) S11, and (c) radiation pattern.

Fig. 7.23 (a) is the structure and dimensions of an SIW antenna with evenly distributed slots in the longitudinal direction for BS Rx. L1~L4 are the lengths of slots and S1~S4 are the distances between the centers of slots and SIW. The antenna is designed and fabricated with a Rogers RT/duroid® 6002 substrate with a 1.52 mm thickness. Input reflection coefficient and radiation

patterns of the antenna are plotted in Fig. 7.23 (b) and (c). It can achieve a gain of 9.8 dBi in the boresight of radiation, and its 3-dB beamwidth of E-plane (azimuth) and H-plane (elevation) are 134° and 21° , respectively.

The Tx and Rx antennas are fabricated and assembled on the BS front-end demonstrator, as shown in Fig. 7.24 (a). The Tx antenna is connected with SMA adaptors. The Rx antennas are connected through a 90° bend and an SIW interlayer transition, as shown in Fig. 7.24 (b). The bend is formed by an Rx antenna and another SIW line with the same width, thickness and substrate material for a good impedance matching. The interlayer SIW transition is formed between the thick (1.52 mm) SIW line and a thin (0.508 mm) SIW line on the system PCB extended from a gap on the top shielding frame. Usually, an interlayer transition of two SIW lines with the same width and thickness can be simply designed using a transversal slot at about a half wavelength from the shortening end of each line. The larger the thickness difference is, the more substantial the impedance mismatch and the narrower the bandwidth will be. In the thick SIW close to the paired transition slots, we introduce a notch taper, which reduces the local thickness, increases the capacitance and enables a smooth field conversion. The notch taper of 0.76 mm deep on the thick SIW is realized by milling the taper shape and mount a wedge made on a brass block, as shown in Fig. 7.24 (c). Unit_1 is the thin SIW extended from the system PCB and Unit_2 is thick SIW with the notch taper. Electric field is plotted at the transition portion and the bend. The notch taper can also be realized by cutting-through the taper shape on the thick SIW and fill it with a piece of dielectric with the same shape and 0.76 mm thickness. Using such a transition instead of connecting both the BS Rx and antenna to SMA connectors and then mating them can reduce the interconnection loss at high frequency, therefore reducing the NF. The structure of Unit_1 can also be built independently as a BS test interface to cables, as shown in Fig. 7.24 (b). Two identical test interface blocks are connected back-to-back and measured. The Unit_1 to Unit_2 transition followed by a 90° bend is also measured. S-parameters for both measurements are shown in Fig. 7.24 (d). The minimum IL of the first case is 0.9 dB, for which a calibration is performed at the SMA ports; in the second case, a TRL calibration to SIW cross-sections is used and the minimum IL is 0.65 dB.

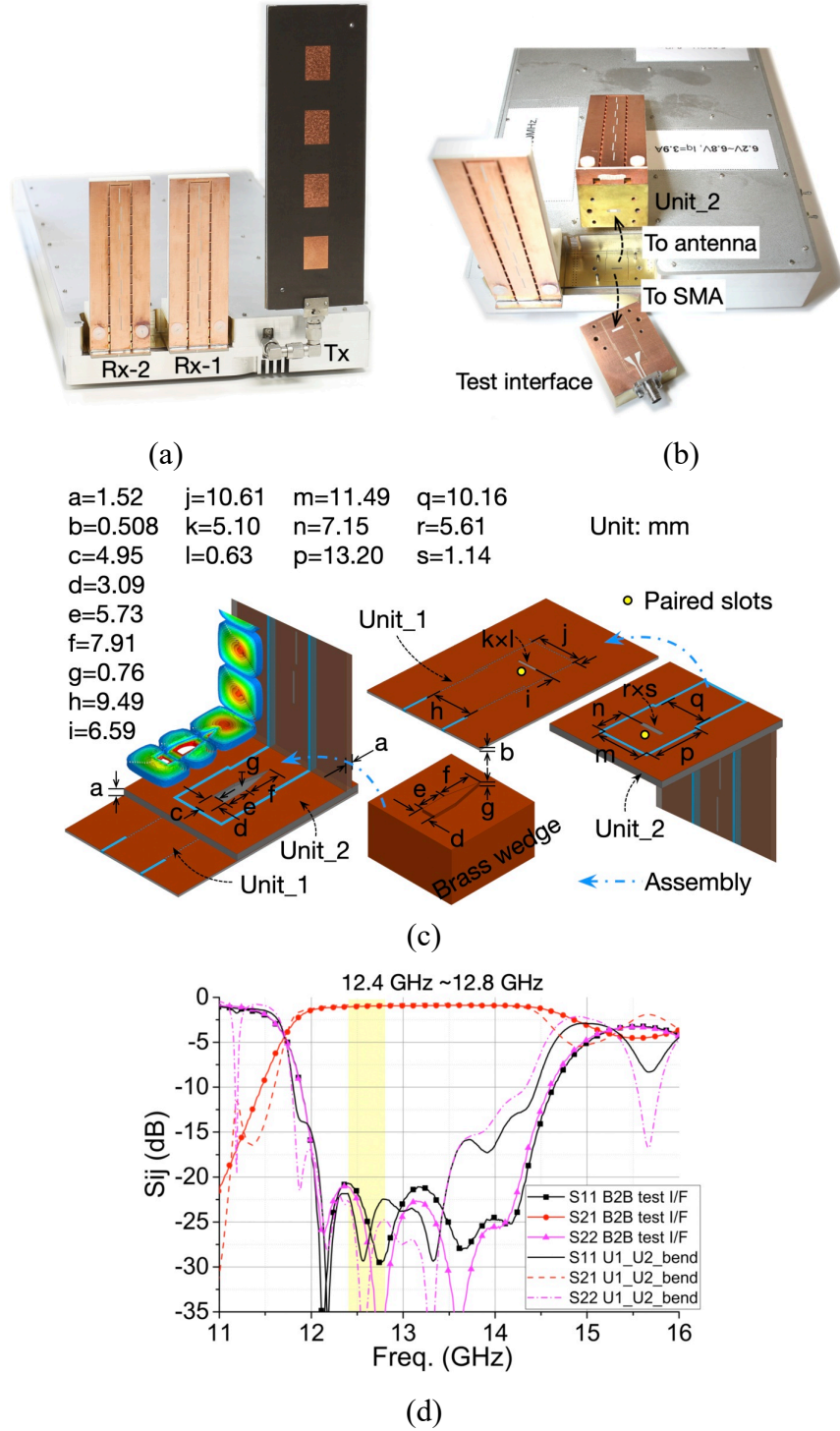


Figure 7.24: (a) Fabricated antennas assembled on a BS front-end demonstrator. (b) SIW replaceable transition to an Rx antenna with 90° bend or to an SMA connector. (c) Structure and dimensions of an SIW transition between thin and thick SIW units using an impedance matching wedge. (d) Measured S-parameters of two test interface blocks in back-to-back connection, and thin to thick SIW transition followed by a 90° bend.

7.3 Measurement and System Demonstration

7.3.1 Function measurement of tag and BS front-end

Three tags are fabricated for the HPS-AT demonstration. An output waveform from a tag-under-test (TUT) at 5 MHz modulation frequency without an interrogation signal is shown in Fig. 7.25 (a), a close-in look of the waveform is shown in Fig. 7.25 (b). The rise (10% to 90% maximum amplitude) and fall (90% to 10% maximum amplitude) time of a pulse is 11.67 ns and 2.42 ns, respectively. The waveform is over-the-air (OTA) measured by an Agilent DSO81204B oscilloscope connected with an ETS-Lindgren 3160-8 horn antenna at 1 m from the TUT. Using the Friis transmission equation, we can find the output power of SIHO on the TUT is about 6.5 dBm if running at a 100% duty cycle.

Fig. 7.26 illustrates the measured spectrums when the TUT is set in a continuous-wave mode for which Switch I is at on-state and Switch II is at off-state. The TUT receives an injection signal at frequency f_{inj} from 6.24 GHz to 6.33 GHz, and at power of -16 dBm, which is about the same level as what the closest tag (at 4 m) receives from the BS. Due to the strong injection signal, IMs at frequencies $2f_c^{(k)} \pm (f_c^{(k)} - f_{inj})$ and about 45 dB lower than the main signal are produced from the TUT. At the same time, the main output signal maintains a stable frequency of 12.5664 GHz, thanks to the excellent isolation of Switch II. Thereafter, we can find that if Switch II is at on-state, the injected signal may contribute more than a half part of the TUT output, hence inevitably pulling the frequency of the TUT.

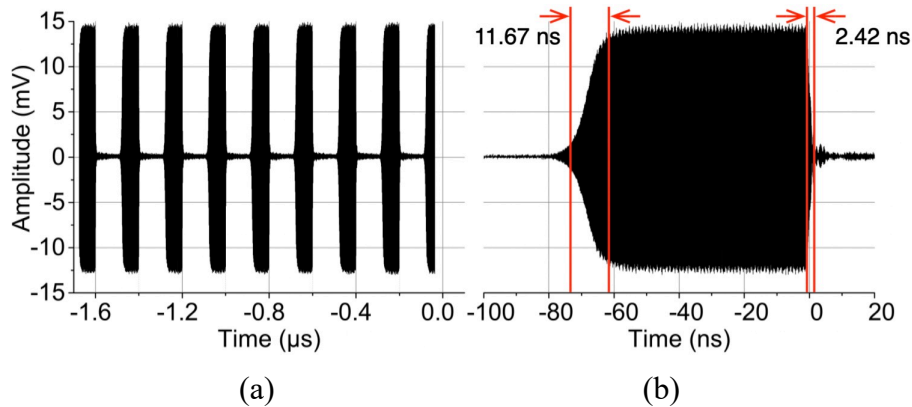


Figure 7.25: (a) OTA measured waveform of a tag. (b) Close-in view of a pulse in the measured waveform.

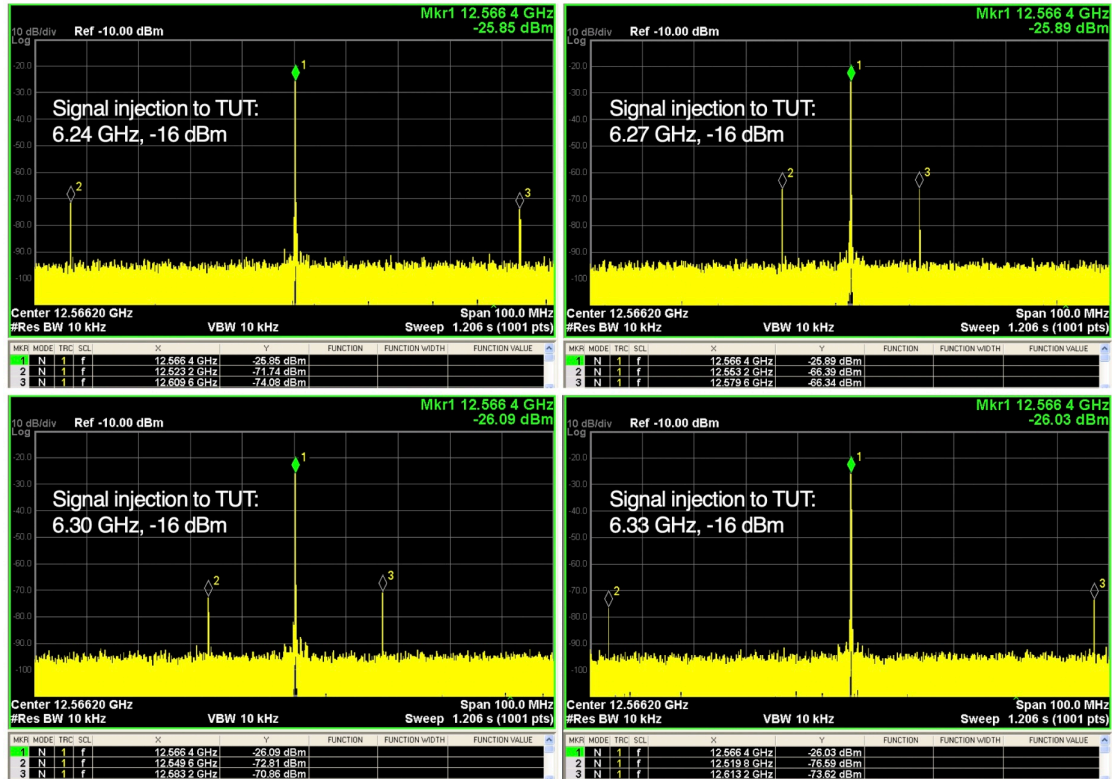


Figure 7.26: OTA measured output spectrum of a TUT under frequency pulling test. The TUT is in continuous-wave mode, subject to signal injection with different frequency.

The phase locking phenomenon of a tag is also evaluated. The same TUT is set to operate with a switching signal of 5 MHz and 50% duty cycle. The oscilloscope is set to use 256 times average on the captured signal and trigger at 1.6 mV. Therefore, the central pulse that the trigger acts on keeps the same amplitude as when averaging is off, but because the rest of pulses have random initial phases, they exhibit a reduced amplitude as a result of canceling. With infinite times of average, we are supposed to see only one pulse. However, if the initial phase of each pulse is locked to an injection signal, the entire train of pulses become repeatable and all the pulses will have the same amplitude no matter they are triggered or not. The stronger the injection signal is, the higher the probability of phase locking will be and the flatter the pulse train will be. The experimental results are shown in Fig. 7.27. An injection signal has a frequency of 6.5 GHz, whose 2nd harmonic has the maximum frequency difference with reference to the output frequency of the TUT in the interrogation chip bandwidth. The injection power is gradually increased from Fig. 7.27 (a) to (g). As the tag-received injection signal power is lower than -54 dBm, the phase locking is compromised. From -44 dBm to -16 dBm, we can see that the initial phases are fully locked. With a higher injection power level, the initial signal amplitude to induce the SIHO start is higher,

therefore the settling time is shorter. This phenomenon can be verified by the close-in views on the right. Especially for Fig. 7.27 (e) to (g), the 2nd harmonic of the injected signal starts to emerge in the AB segment that leads each pulse, and continuously increases up to a half of the main signal. With a reference to Fig. 7.6, this segment is where both switches are at on-state. At the instant B, Switch II is toggled off and the injection signal in the loop is damped. Segment AC is 100 ns, which is exactly the on-time of a 50% duty cycle 5 MHz square waves. By comparing Fig. 7.27 (a) with (g), we can see the settling time is about 40 ns.

The BS front-end performance is also characterized. Fig. 7.28 is the spectrum of the Tx when IFt is a monotone at 1.02 GHz or a stepped frequency wave from 0.84 GHz to 1.24 GHz, measured by an Agilent N9030A signal analyzer connected to the Tx with an SMA cable. We can find the output power is about 24 dBm and the only detectable spurious is the $-4 \times \text{IFt} + 2 \times \text{LO1t}$ component which is 62 dB lower than the desired signal. The in-band spectrum flatness is about 2 dB. Fig. 7.29 (a) and (b) are the baseband spectrums of an Rx output when LO2r is at 2.28 GHz or from 1.68 GHz to 2.48 GHz, and the input RF signal is a monotone at 12.6 GHz with a power of -72.5 dBm and -44.5 dBm, respectively. The highest spurious is less than -50 dBc for the case of a higher input power. The output power difference between Fig. 7.28 (a) and (b) is due to the non-ideal logarithmic response of the power detector in the gain control circuit. Fig. 7.29 (a) also shows that better than 1 dB of baseband flatness is achieved as LO2r is swept from 1.68 GHz to 2.48 GHz. With -72.5 dBm input power, the input SNR for a 150 MHz bandwidth is 19.6 dB. The baseband noise power for the same bandwidth is -12.6 dBm, measured by the band power function of the signal analyzer. As a result, the baseband SNR is 15.9 dB. Therefore, the NF of Rx is about 3.7 dB.

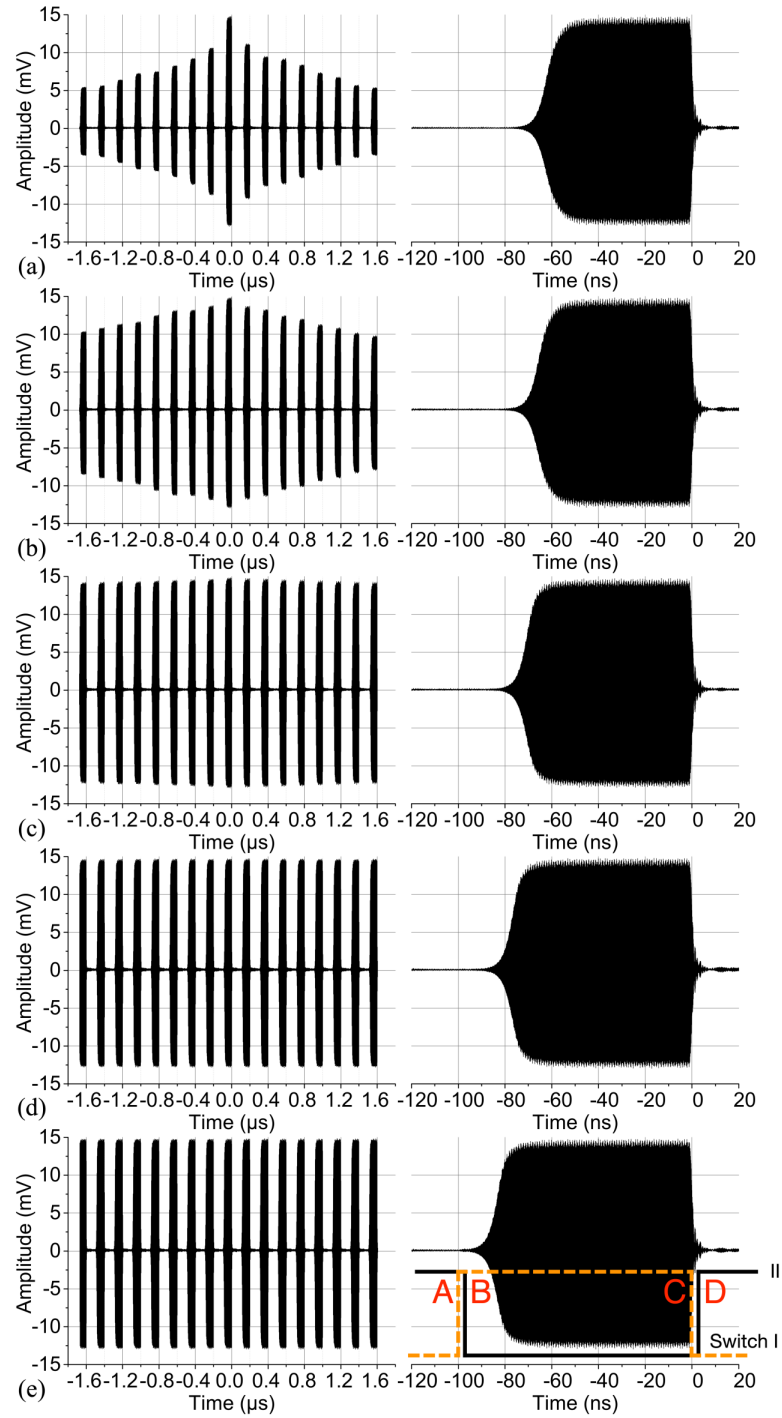


Figure 7.27: Phase locking test results of a TUT. Waveforms of a tag are OTA measured with an injection signal at 6.5 GHz and with power of (a) -74 dBm, (b) -64 dBm, (c) -54 dBm, (d) -44 dBm, (e) -34 dBm, (f) -29 dBm, and (g) -16 dBm.

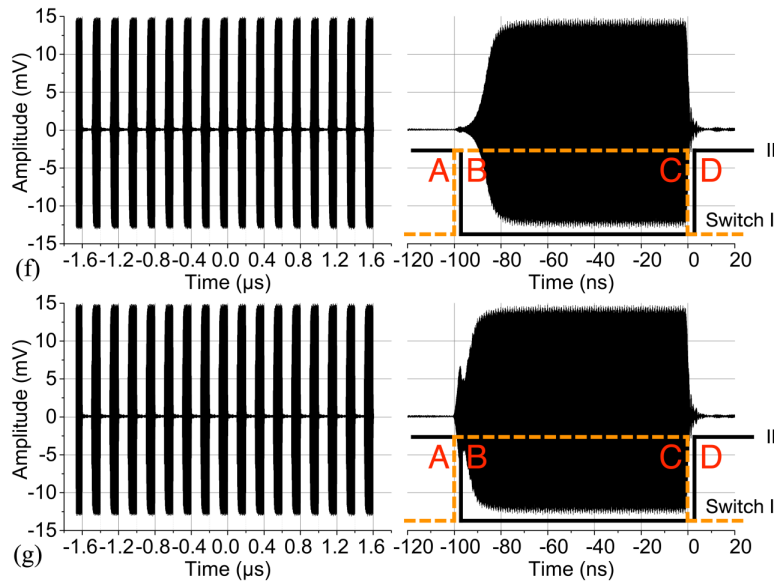


Figure 7.27 (cont.)

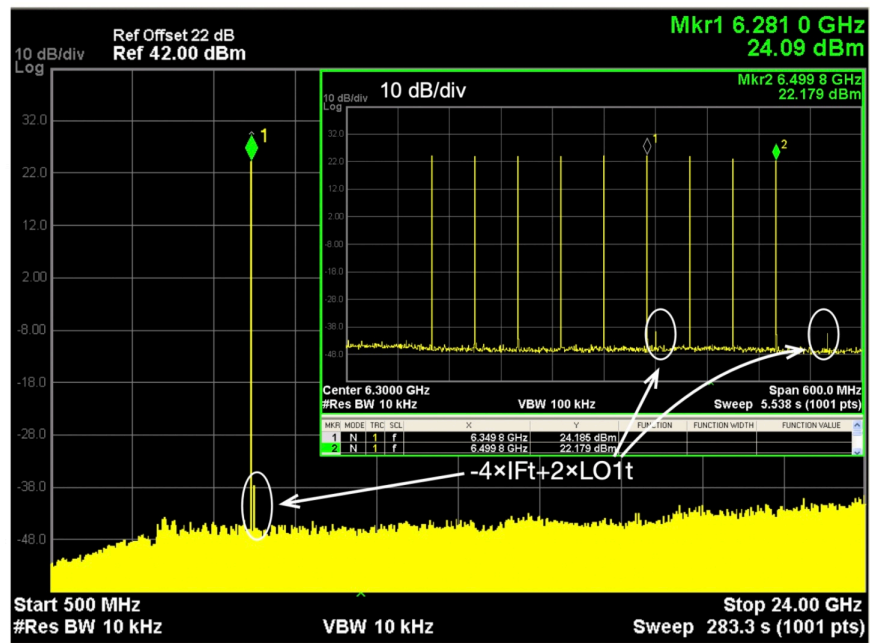
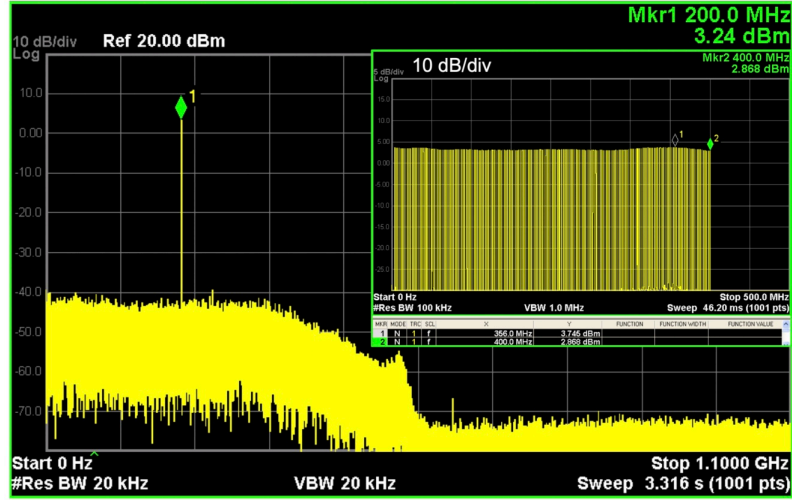
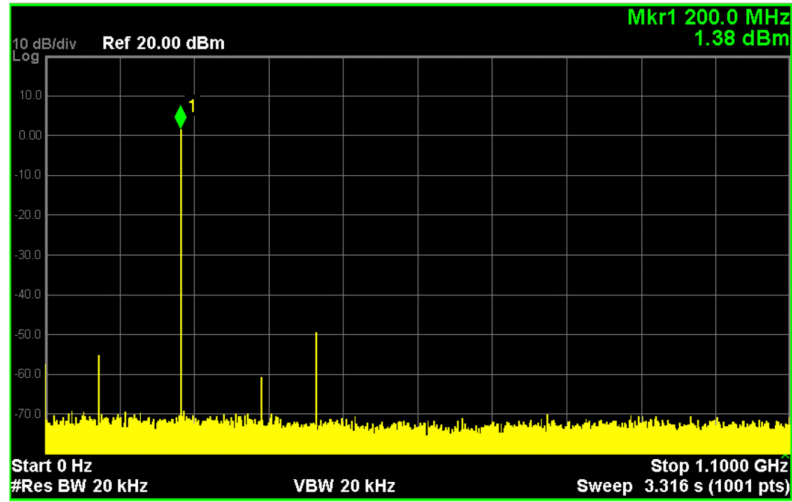


Figure 7.28: Output spectrum of Tx of the BS demonstrator.



(a)



(b)

Figure 7.29: Baseband spectrum of Rx when RF input power is (a) -72.5 dBm, and (b) -44.5 dBm.

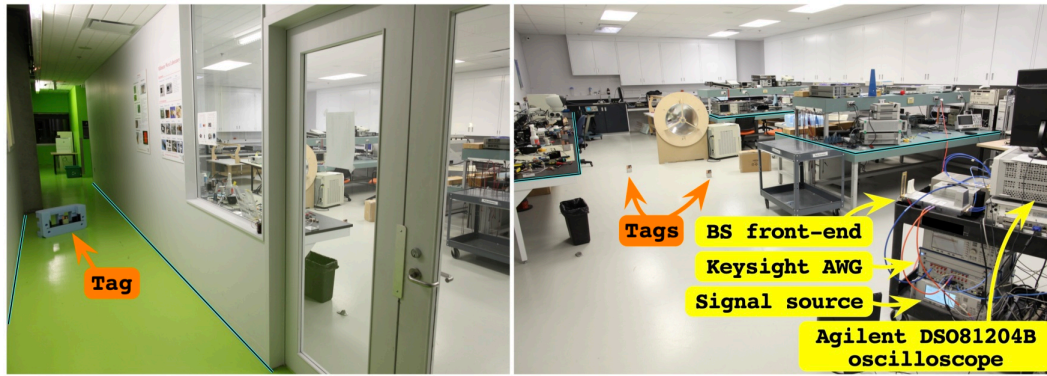
7.3.2 Positioning test in two indoor scenarios

Indoor positioning tests and evaluations of the HPS-AT demonstrator are performed. Parameters of the experimental setup are listed in Table 7.2. There are two testing scenarios. The first is a laboratory of the Poly-Grames Research Center, as shown in Fig. 7.30. There are numerous metal objects such as the table bases, steel cart, steel cabinets on the wall, instruments and so on, creating an environment with rich signal reflection. Fig. 7.30 (a) shows the photo of the test environment and the setup. Fig. 7.30 (b) shows the measured positions of the targets and the real ones obtained with measuring tape. For each position, 100 measurements are carried out, and each measurement

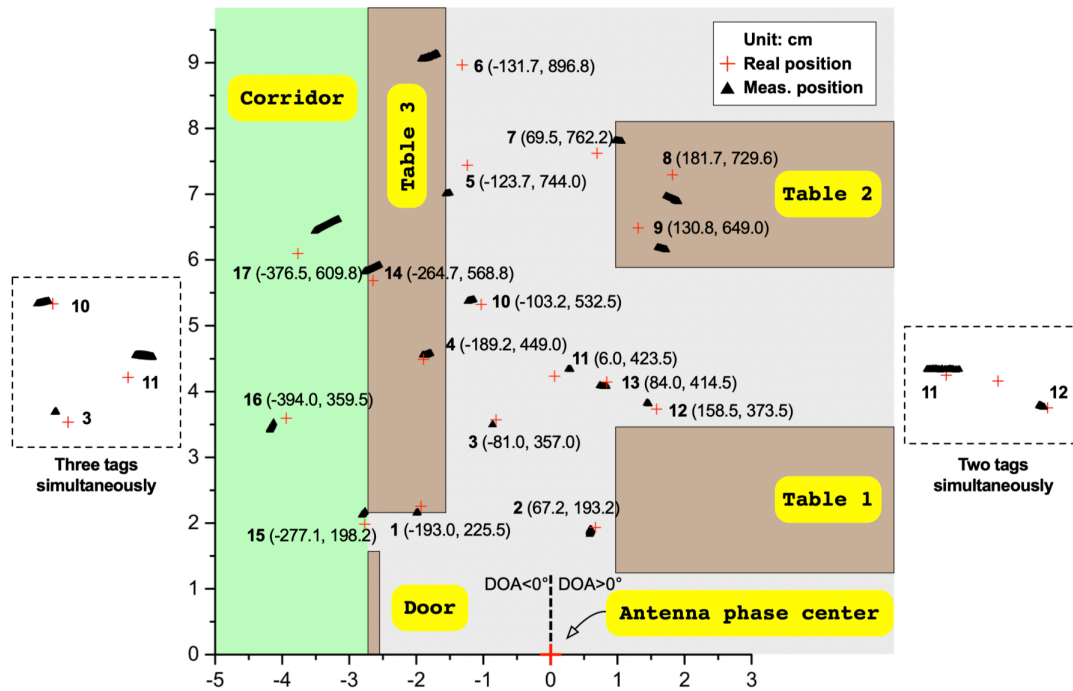
uses the baseband samples extracted from the same location of different pulses. By doing so, the effect of multipath can be observed from the variation of the measured positions. Fig. 7.30 (c) shows the measured angle and range versus their respective real values, taking into account all the measurements of all the positions. Stress tests are carried out with close tags within 4 m to the BS, for which a strong injection to tags and a signal compression of Rx are expected. System calibration can be performed either with a tag at known positions inside an anechoic chamber or with a connectorized tag coupled to the BS through cables and attenuators with known delays. Algorithms and procedure summarized in [76] are used to process the recorded baseband signals. Matrix stacking techniques using data from both Rxs are implemented for DOA and TOA extraction. Results for the first scenario are summarized in Table 7.3. It can be seen that the close tags are measured accurately. The first reason is an Rx compression happens in the stages before the baseband demodulator and the generated harmonics are outside the demodulator input bandwidth. Secondly, the compression point of the input LNA of a tag is not reached and Switch II provides a high enough isolation to prevent a pulling of the SIHO frequency. Root-mean-square-error (RMSE) is calculated with the coordinates of a real position and the 100 measured ones. Relatively large RMSE for some positions are mainly due to multipath effects and accumulated errors when using measuring tapes.

Table 7.2: Parameters of the Experimental Setup

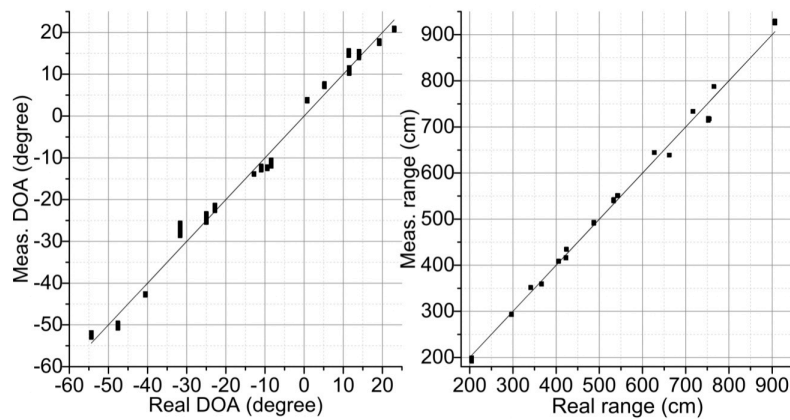
BW	400 MHz
T_s	0.5 ms
Chirp	Up and down interleaved
Chirp generator	Keysight M8190A AWG
Baseband digitizer	Agilent DSO81204B
Sampling freq.	2 GSa/s
Recorded length	1.5 ms
Tag modulation	5 MHz, 50% duty cycle
Target quantity	≤ 5



(a)



(b)



(c)

Figure 7.30: (a) Photo of the first test environment and setup. (b) Layout plan and target distribution. (c) Error bar of angle and range measurements.

Table 7.3: Result of the First Test Scenario with a Single Target

Pos. index	Real range (cm)	Real angle (°)	Meas. range avg. (cm)	Meas. angle avg. (°)	RMSE range (cm)	RMSE angle (°)
1	296.8	-40.6	292.8	-42.6	4.0	2.0
2	204.6	19.2	196.4	17.7	8.3	1.5
3	366.1	-12.8	359.5	-13.8	6.6	1.1
4	487.2	-22.8	491.8	-21.7	4.6	1.2
5	754.2	-9.4	717.6	-12.4	36.6	2.9
6	906.4	-8.4	926.4	-11.3	20.0	3.0
7	765.4	5.2	787.6	7.2	22.2	2.0
8	751.9	14.0	715.1	15.2	36.8	1.3
9	662.1	11.4	639.3	15.1	22.7	3.7
10	542.4	-11.0	551.4	-12.5	9.0	1.6
11	423.5	0.8	434.6	3.8	11.0	3.0
12	405.7	23.0	408.5	20.8	2.8	2.2
13	422.9	11.5	415.6	10.8	7.3	0.8
14	627.4	-25.0	644.6	-24.9	17.2	0.6
15	340.7	-54.4	351.6	-52.2	11.0	2.3
16	533.4	-47.6	540.8	-50.4	7.5	2.8
17	716.7	-31.7	733.5	-27.4	16.9	4.5

Fig. 7.31 (a) shows a snapshot of the baseband I/Q waveforms from a tag at position No. 12. In such a single target case, multipath components can be easily identified during the off-time. We also find that the on-time is less than 50% of a period, due to the fact of the injection signal amplitude observed in Fig. 7.27. Fig. 7.31 (b) is the baseband spectrum related to the same target during a chirp period. The spectrum starts to roll off at about 370 MHz because its carrier frequency $2f_c^{(k)}$ deviates from 12.6 GHz by about 30 MHz. A zoom-in of one of the peaks in the spectrum is also shown, in which multipath components are reflected as sidelobes with a lower amplitude.

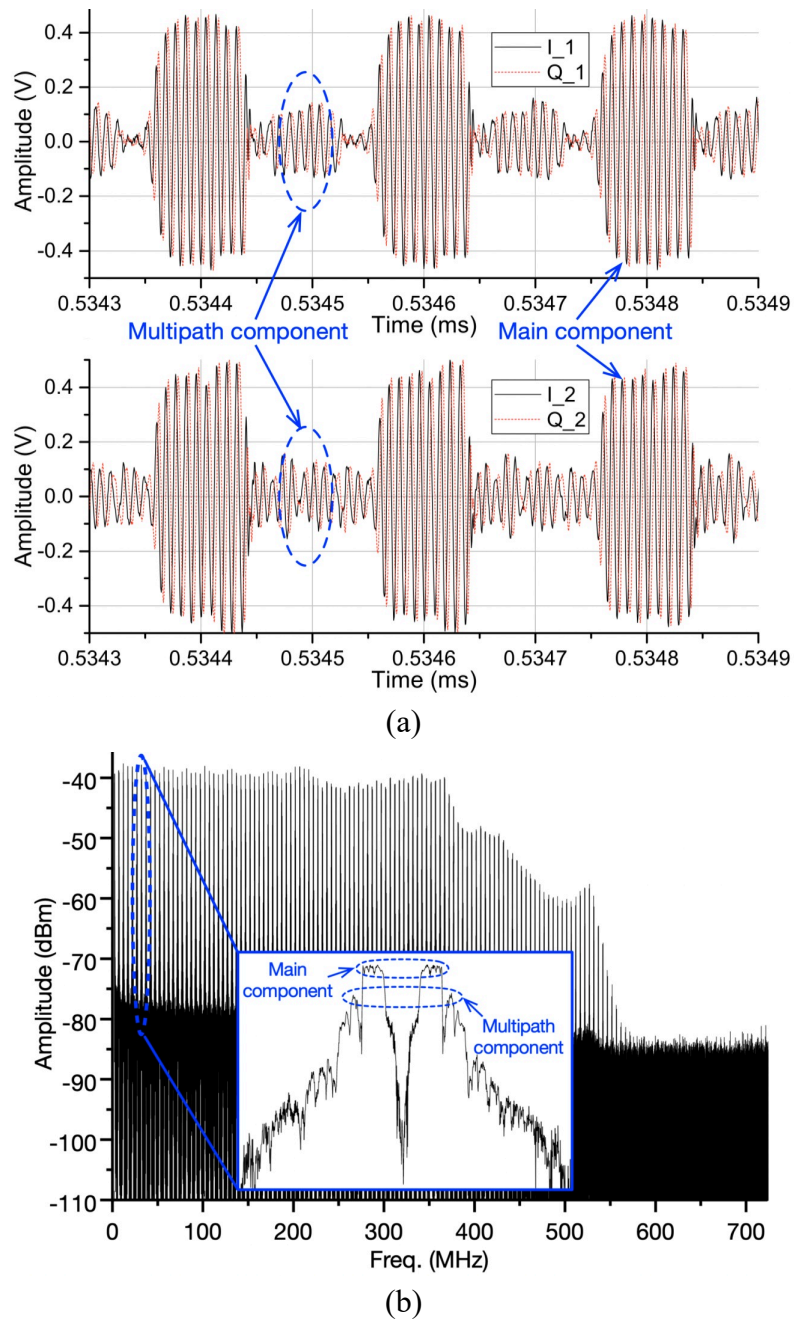
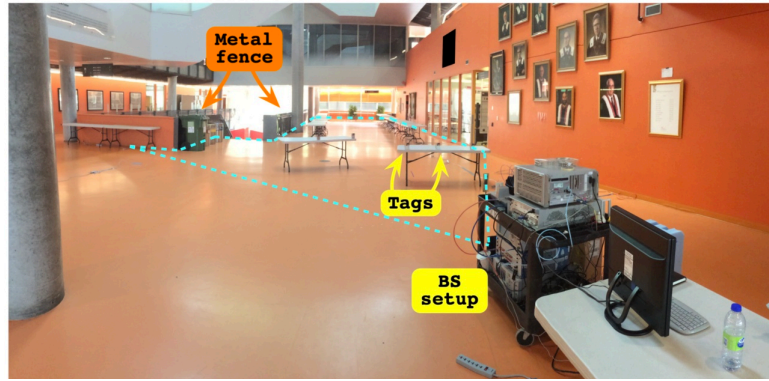
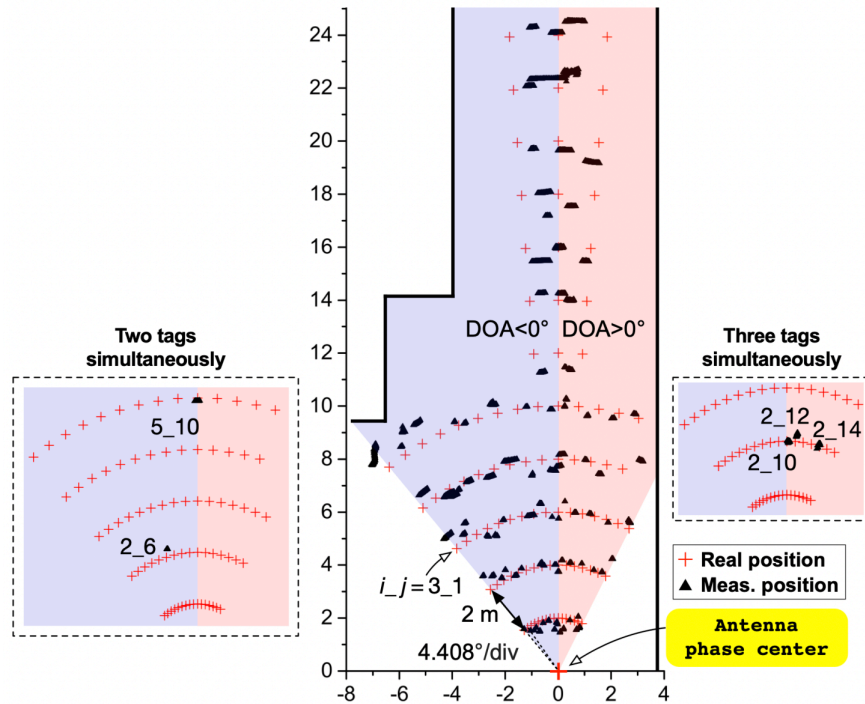


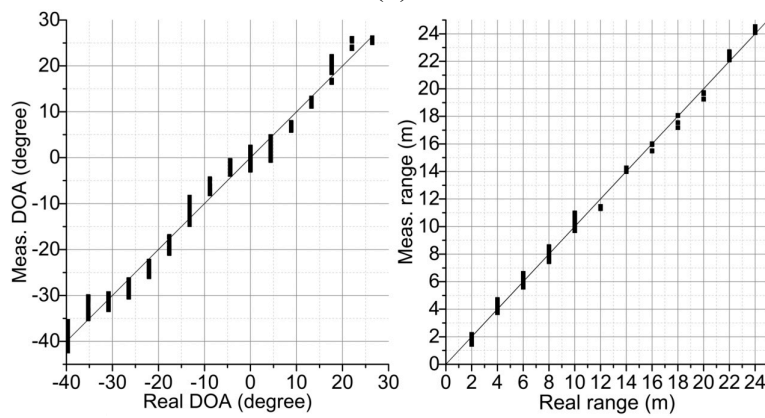
Figure 7.31: (a) A snapshot of the baseband I/Q waveforms related to a tag at position No. 12. (b) Spectrum of the recorded baseband I_1 signal during a chirp period.



(a)



(b)

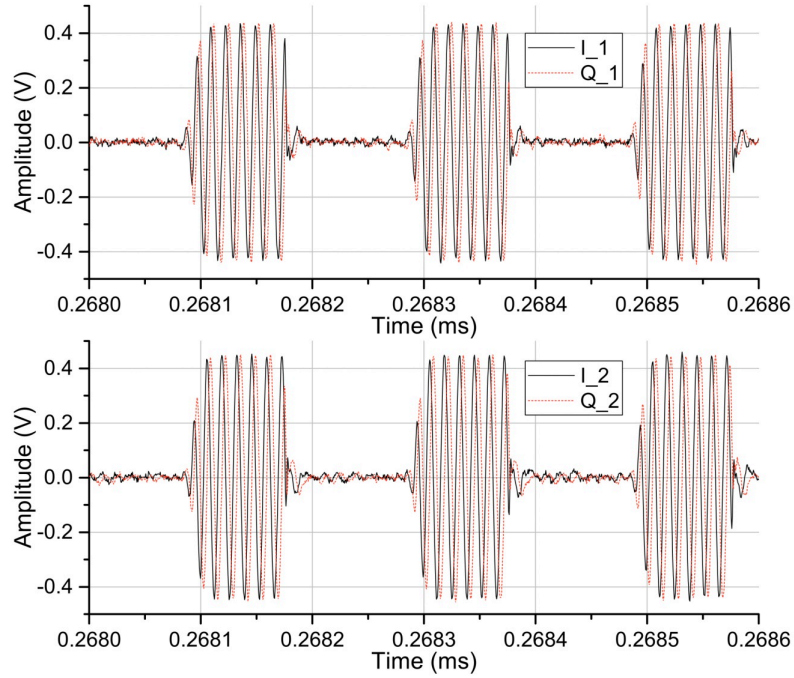


(c)

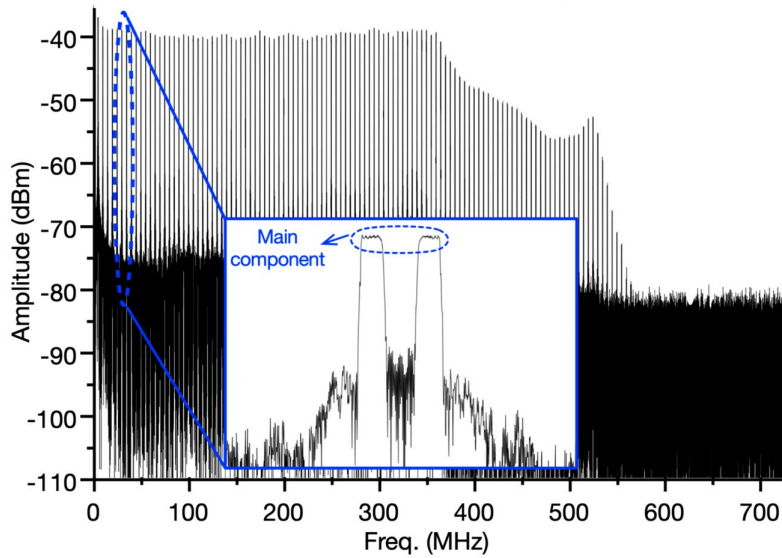
Figure 7.32: (a) Photo of the second test environment and setup. (b) Layout plan and target distribution. (c) Error bar of angle and range measurement.

Table 7.4: RMSE of the Second Test Scenario with a Single Target

Pos. index	RMSE range (m)	RMSE angle (°)	Pos. index	RMSE range (m)	RMSE angle (°)	Pos. index	RMSE range (m)	RMSE angle (°)
1_1	0.045	0.7	3_2	0.277	0.6	5_5	0.190	0.5
1_2	0.154	0.8	3_3	0.602	1.4	5_6	0.009	3.1
1_3	0.221	0.4	3_4	0.277	1.0	5_7	0.351	0.5
1_4	0.162	0.2	3_5	0.392	2.4	5_8	0.041	1.9
1_5	0.349	2.7	3_6	0.061	2.2	5_9	0.134	3.0
1_6	0.104	0.4	3_7	0.044	4.1	5_10	0.011	1.4
1_7	0.062	2.6	3_8	0.351	2.8	5_11	0.259	2.6
1_8	0.435	4.1	3_9	0.181	2.2	5_12	0.311	2.3
1_9	0.165	2.9	3_10	0.251	0.2	5_13	0.250	1.1
1_10	0.248	0.4	3_11	0.404	2.1	5_14	0.122	1.0
1_11	0.547	1.7	3_12	0.013	2.8	6_1	0.711	1.2
1_12	0.409	1.4	3_13	0.057	1.9	6_2	0.533	1.4
1_13	0.035	0.3	3_14	0.090	0.9	6_3	0.619	2.1
1_14	0.193	2.6	3_15	0.283	3.0	7_1	0.271	2.0
1_15	0.299	1.8	3_16	0.228	0.6	7_2	0.243	0.8
1_16	0.182	0.3	4_1	0.466	3.1	7_3	0.016	2.6
2_1	0.575	1.5	4_2	0.166	4.4	8_1	0.517	2.2
2_2	0.367	0.5	4_3	0.298	1.0	8_2	0.021	0.4
2_3	0.101	0.3	4_4	0.190	2.2	8_3	0.500	0.7
2_4	0.300	1.1	4_5	0.076	3.1	9_1	0.811	3.0
2_5	0.053	2.0	4_6	0.220	1.3	9_2	0.061	1.8
2_6	0.116	2.1	4_7	0.161	0.9	9_3	0.450	2.8
2_7	0.110	4.2	4_8	0.548	1.2	10_1	0.272	1.6
2_8	0.021	1.3	4_9	0.432	3.4	10_2	0.348	0.8
2_9	0.007	3.2	4_10	0.274	0.4	10_3	0.762	0.6
2_10	0.255	0.5	4_11	0.178	3.1	11_1	0.103	1.6
2_11	0.184	2.5	4_12	0.040	1.4	11_2	0.368	1.4
2_12	0.113	2.5	4_13	0.396	1.2	11_3	0.609	3.1
2_13	0.147	0.9	4_14	0.542	3.9	12_1	0.312	2.1
2_14	0.048	1.8	5_1	0.820	1.1	12_2	0.084	0.4
2_15	0.085	2.0	5_2	0.336	0.4	12_3	0.530	3.1
2_16	0.698	0.7	5_3	0.765	2.1			
3_1	0.589	1.1	5_4	0.774	3.4			



(a)



(b)

Figure 7.33: (a) A snapshot of baseband I/Q waveforms related to a tag at position 2_8. (b) Spectrum of the recorded baseband I_1 signal during a chirp period.

Fig. 7.32 (a) illustrates the second test environment, which is the six-story-height lobby of Lassonde building of Polytechnique Montreal. It has a more pronounced maximum multipath delay

compared with the space of the first test. The same setup parameters as shown in Table 7.2 are used. Fig. 7.32 (b) presents the real positions as well as the extracted ones. Position i_j is the j th one from the left in the i th row from the BS. The distance between adjacent rows is 2 m and the angle between adjacent positions in a row is 4.408° . There are 100 measured results for each position. Fig. 7.32 (c) shows the measured angle and range versus their respective real values. It can be seen that both parameters extracted from the second test have a larger variation compared to the first test due to the multipath delay in the magnitude of a few hundred ns. Calculated RMSE values are shown in Table 7.4. Fig. 7.33 (a) and (b) are the baseband I/Q waveform snapshots and spectrum related to a single tag at position 2_8 of the second test. For this specific case, a multipath effect can be hardly observed in both time and frequency domain.

CHAPTER 8 GENERAL DISCUSSIONS

From the results of the presented indoor and outdoor tests of the developed fundamental and harmonic positioning systems in this thesis research, it can be seen that the multipath effects have to be further investigated and dealt with for a robust operation under all environments. To this end, three aspects are considered:

First, the coding of active backscattering tags. As suggested by [29, 30], a CDMA coding enables a real-time processing and identifying multiple targets simply by modulating the transponder with a CDMA scheme. This technique is very attractive for our proposed system due to the following reasons. a) Baseband computation burden can be greatly reduced. Specifically, the model order estimation can be skipped, or the searching space can be shrunk, so that the multitarget signal is reduced to a single or a much smaller number of targets before processing. b) Coding the tags can solve the problem of matching the estimated TOA and DOA. c) The multipath issue will become easier to resolve, which can be seen from the analysis of the next paragraph. d) It can be realized with the current tag hardware simply by controlling the switch signal generator for a pulse width modulation.

Second, the adaptive re-configurability and hybrid digital/analog beamforming scheme. Currently, we attempt to enhance the antenna coverage in the azimuth plane on both tag and BS to prevent loss of any target. By doing so, interrogation multipath components may be received by tags. This can be more fatal than in the case of passive frequency doubling tags. This is because the active tags only respond to the phase front it sensed, either from the line-of-sight main component or from a superposed line-of-sight and non-line-of-sight component. If it is the second case, BS cannot make correction or compensation no matter how sophisticated the hardware or algorithm is. We can use a scanning technique in the azimuth plane with a narrower interrogation beam to solve this issue. But this may only be effective with the help of coding (e.g. CDMA), because otherwise, an over-estimation or ambiguity issue may emerge. On the BS Rx side, a larger array is expected to enhance the angular resolution. For the interrogation signal, an analog beamforming is preferred because adding extra Tx will significantly increase PA power consumption, while for the receiving side, a hybrid beamforming by adding an analog phased array for each of the two Rxs might be a balanced choice.

We have proposed a phase shifter solution based on SIW and liquid crystal. It has very promising features of extremely low loss at high frequency (e.g. mmW), seamless integration with other

components on SIW (e.g. antennas with feeding network), and zero power consumption. The phase shifter prototype is shown in Fig. 8.1. We have shown that, with the best nematic liquid crystal material for RF applications, a single dB of IL can support more than 100° of phase shift.

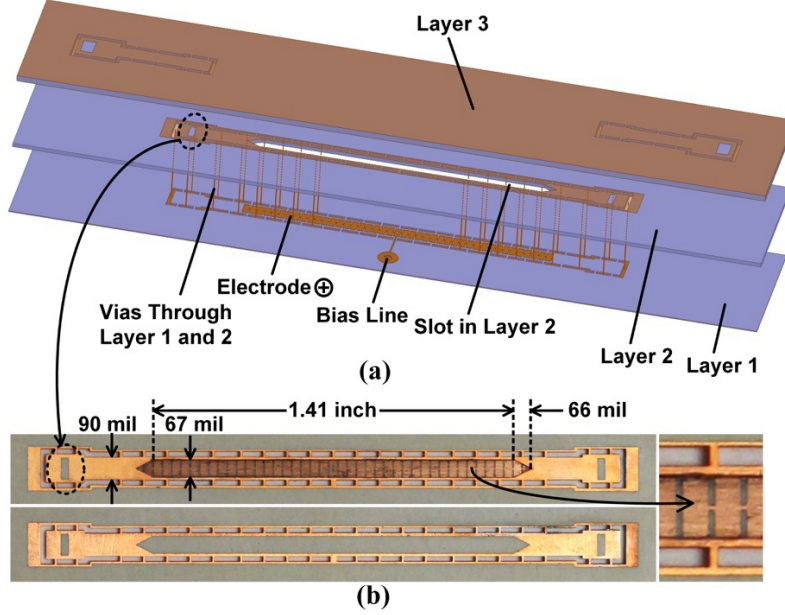


Figure 8.1: (a) The perspective view of an SIW liquid crystal phase shifter. (b) The fabricated assembly showing the liquid crystal cell and electrode.

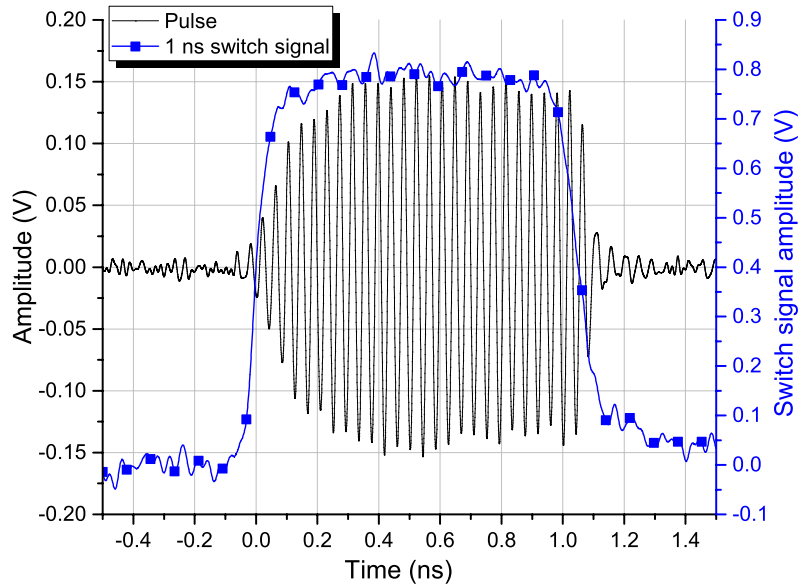


Figure 8.2: A waveform of mmW switched SIHO on CMOS technology.

Third, reduction of the post-processing computational burden with harmonic receivers. By observing the baseband spectrum of either the fundamental system or the harmonic system, we can

find that useful information is constrained within narrow bands centered at harmonics of the tag modulation frequency. As the modulation frequency increases, the number of such bands is reduced. With CMOS technology, SIHO on a harmonic tag can be designed with a rise and fall time as short as 100~200 ps, as shown in Fig. 8.2. Therefore, the modulation frequency can be as high as 500 MHz. In this way, for a BS interrogation bandwidth of 500 MHz, only two sub-bands can be seen in the baseband signal. We can implement harmonic receivers such as the ones in [36, 37] to concurrently receive the two narrow sub-bands, instead of digitizing the entire few hundred MHz wide baseband and overload the processor with useless samples.

CHAPTER 9 CONCLUSIONS AND FUTURE WORK

9.1 Conclusions

In this thesis, the theory, technology and experiments of an active backscattering positioning system with innovative harmonic oscillator tags are presented. The main features of such a system can be summarized as harmonic frequency diversity, time-series multitarget post-processing and immunity to commonly exercised frequency pulling. At the same time, the favorable characteristics of systems in the literature are maintained.

To this end, we have discovered a new class of harmonic oscillator, namely the self-isolated harmonic oscillator (SIHO) which enjoys the advantage of harmonic output and low pulling effect. As the experiments suggested, load pulling and frequency pulling are reduced by 15 to 20 times. Such an oscillator can be designed with the X-parameter nonlinear model of an amplifier extracted with a large signal network analyzer (LSNA) and can be also designed in a more convenient way with our developed harmonic-measurement-and-design (HMD) system, which is based on the concept of experimental waveform optimization and design automation. As the general theoretical and experimental foundations for nonlinear circuit (including the SIHO) analysis and design, an X-parameter based modeling technique and an LSNA verification device are developed and presented in this thesis.

An SIHO-antenna fusion harmonic active radiator structure has been proposed and demonstrated at millimeter wave (mmW) frequency. The radiator employs a circular substrate integrated waveguide (SIW) cavity to achieve the functions of diplexer, resonator, and antenna concurrently. Therefore, it transmits the second harmonic of the oscillating signal to free space and at the same time and maintains the advantages of low pulling effect and simple design of the SIHO topology. Although the structure is not implemented for the positioning system of this thesis, it may become essential and indispensable for low-cost Internet of Things (IoT) devices including the positioning system in the mmW band that represents an overwhelming advancement for an integration with the mmW 5th generation (5G) wireless technology in the future.

In terms of the post-processing algorithms of the proposed positioning system, we give up the conventional frequency domain methods such as a fast Fourier transformation (FFT) which has obvious drawbacks when implemented with the switched injection phase locking principle. Our developed time-domain post-processing techniques feature a joint singular value decomposition

(SVD) based ESPRIT algorithm and a matrix diagonalization technique using Moore-Penrose pseudoinverse for model order estimation as well as the time-of-arrival (TOA) and direction-of-arrival (DOA) extractions. These techniques allow us to differentiate multiple tags even though their spectrums are overlapped in the demodulated baseband signal. Our developed algorithms also reduce the commonly exercised restrictions of tag design when a low mean error is desired. We have verified the function and performance of the techniques on a developed 2-D positioning system in which both up- and down-link are in the same fundamental frequency band, which is regarded as the fundamental system to get distinguished from the other developed system with harmonic frequency diversity. Nevertheless, we have to acknowledge that, this is only an initial step towards a robust algorithm and a mature cooperation with the hardware platform.

Based on the above-mentioned works, the ultimate objective of this thesis, namely a multitarget harmonic backscattering positioning system with active tags (HPS-AT) has been developed and presented. The concept of collaborated advantages of the switched injection phase locking principle, our proposed time-domain post-processing technique and the harmonic diversity has been verified. Table 9.1 summarizes the main features of our developed fundamental and harmonic systems.

Table 9.1: Comparison of the Fundamental and Harmonic Positioning Systems Developed in this Thesis

	Fundamental 2-D active backscattering multitarget positioning system	2 nd harmonic 2-D active backscattering multitarget positioning system
Interrogation signal from the base station	Linear FMCW with bandwidth BW at f_0	Linear FMCW with bandwidth BW at f_0
Backscattering signal from the tags	Phase-locked AM pulses with carrier frequency f_0	Phase-locked AM pulses with carrier frequency $2f_0$
Ideal resolution limit	$c/2BW$	$c/4BW$
Tag operation principle	Switched injection locked oscillator	Switched injection locked oscillator
Oscillator on the tag	Fundamental frequency feedback-loop oscillator	Self-isolated harmonic oscillator
Base station self-interference	Yes	No
Interference from cluster reflection	Yes	No
Tag self-interference	Yes	No
Tag frequency locking	Strong	Weak
Tag robustness under pulling	Low	High
Cost of mmW tag SoC	High	Low

In the wireless community, many harmonic systems for different applications have come into view in recent years. However, a frequency planning in compliance with regulations is still a bottleneck. With such a limitation, the systems may only operate with ultra-low power or in a strictly confined environment. As regulation authorities are in the process of establishing new 5G standards, more mmW bands become available. Those harmonic system concepts will get a better chance to be implemented and applied in real life together with the future wireless platforms.

9.2 Prospects of Future Work

1. CMOS technology is the best solution for an integration of the harmonic active tags for low-cost ubiquitous location awareness. A CMOS self-isolated harmonic radiator with switching capability at mmW frequency has been demonstrated in our lab, with an external diplexer-resonator-antenna structure fabricated with a ceramic substrate. This is still costly and bulky for mass applications. CMOS integrated cavity, which has been reported in the literature, can be seen as a very promising technology to achieve a fully integrated positioning tag system-on-chip (SoC).
2. Larger scale beamforming is indispensable for an improved accuracy, resolution, and robustness, especially in complex application scenarios with significant multipath effect. A hybrid digital and analog beamforming should be considered for both transmitter and receiver of the base station (BS). Moreover, a beamforming on the tag is also worth considering. But this has to be achieved with unconventional techniques for a reasonable complexity, cost and power consumption.
3. A wireless powered battery-free tag is highly desired as the number of connected objects grows explosively. Such a concept has been demonstrated on mmW CMOS by other researchers.
4. Positioning tag with other functions is also a promising direction of research. If sensors and data transmitting function are integrated, people can construct truly smart networks of data acquiring and situated communication. Considering a limited power availability, such an integration also should not be done in a conventional way.

All in all, our proposed HPS-AT at mmW frequency using a single BS together with above mentioned future accomplishments is expected to achieve a coverage of 100 m and 120°, a

range resolution/accuracy of 1 cm, an angular resolution/accuracy of 1° , tag overall power efficiency of 20% (with wireless charging), single tag cost of less than 1 US dollar (with a quantity of 10,000). As such, the system may become a extremely competitive choice for industrial, robotic and logistic applications.

REFERENCES

- [1] J. Hightower and G. Borriello, "Location Systems for Ubiquitous Computing," *Computer*, vol. 34, no. 8, pp. 57-66, 2001.
- [2] M. Vossiek, L. Wiebking, P. Gulden, J. Wiegardt, C. Hoffmann, and P. Heide, "Wireless Local Positioning," *IEEE Microw. Mag.*, vol. 4, no. 4, pp. 77-86, Dec. 2003.
- [3] F. Boccardi, R. W. Heath, A. Lozano, T. L. Marzetta, and P. Popovski, "Five Disruptive Technology Directions for 5G," *IEEE Commun. Mag.*, vol. 52, no. 2, pp. 74-80, Feb. 2014.
- [4] M. Shafi, A. F. Molisch, P. J. Smith, T. Haustein, P. Zhu, P. D. Silva, F. Tufvesson, A. Benjebbour, and G. Wunder, "5G: A Tutorial Overview of Standards, Trials, Challenges, Deployment, and Practice," *IEEE J. Sel. Areas Commun.*, vol. 35, no. 6, pp. 1201-1221, 2017.
- [5] S. B. Baker, W. Xiang, and I. Atkinson, "Internet of Things for Smart Healthcare: Technologies, Challenges, and Opportunities," *IEEE Access*, vol. 5, pp. 26521-26544, 2017.
- [6] A. Zanella, N. Bui, A. Castellani, L. Vangelista, and M. Zorzi, "Internet of Things for Smart Cities," *IEEE IoT-J*, vol. 1, no. 1, pp. 22-32, 2014.
- [7] M. Wollschlaeger, T. Sauter, and J. Jasperneite, "The Future of Industrial Communication: Automation Networks in the Era of the Internet of Things and Industry 4.0," *IEEE Ind. Electron. Mag.*, vol. 11, no. 1, pp. 17-27, 2017.
- [8] J. Lin, W. Yu, N. Zhang, X. Yang, H. Zhang, and W. Zhao, "A Survey on Internet of Things: Architecture, Enabling Technologies, Security and Privacy, and Applications," *IEEE IoT-J*, vol. 4, no. 5, pp. 1125-1142, 2017.
- [9] N. Iliev and I. Paprotny, "Review and Comparison of Spatial Localization Methods for Low-Power Wireless Sensor Networks," *IEEE Sensors J.*, vol. 15, no. 10, pp. 5971-5987, Oct. 2015.
- [10] R. Miesen, R. Ebelt, F. Kirsch, T. Schäfer, G. Li, H. Wang, and M. Vossiek, "Where is the Tag?," *IEEE Microw. Mag.*, vol. 12, no. 7, pp. S49-S63, 2011.
- [11] Y. Dobrev, M. Vossiek, M. Christmann, I. Bilous, and P. Gulden, "Steady Delivery: Wireless Local Positioning Systems for Tracking and Autonomous Navigation of Transport Vehicles and Mobile Robots," *IEEE Microw. Mag.*, vol. 18, no. 6, pp. 26-37, 2017.
- [12] C. Feng, W. S. A. Au, S. Valaee, and Z. Tan, "Received-Signal-Strength-Based Indoor Positioning Using Compressive Sensing," *IEEE Trans. Mobile Comput.*, vol. 11, no. 12, pp. 1983-1993, 2012.
- [13] A. Yassin, Y. Nasser, M. Awad, A. Al-Dubai, R. Liu, C. Yuen, R. Raulefs, and E. Aboutanios, "Recent Advances in Indoor Localization: A Survey on Theoretical Approaches and Applications," *IEEE Commun. Surveys Tuts.*, vol. 19, no. 2, pp. 1327-1346, 2017.
- [14] S. He and S. G. Chan, "Wi-Fi Fingerprint-Based Indoor Positioning: Recent Advances and Comparisons," *IEEE Commun. Surveys Tuts.*, vol. 18, no. 1, pp. 466-490, 2016.

- [15] M. Kok, J. D. Hol, and T. B. Schön, "Indoor Positioning Using Ultrawideband and Inertial Measurements," *IEEE Trans. Veh. Tech.*, vol. 64, no. 4, pp. 1293-1303, 2015.
- [16] A. Cazzorla, G. D. Angelis, A. Moschitta, M. Dionigi, F. Alimenti, and P. Carbone, "A 5.6-GHz UWB Position Measurement System," *IEEE Trans. Instrum. Meas.*, vol. 62, no. 3, pp. 675-683, 2013.
- [17] A. G. Stove, "Linear FMCW Radar Techniques," *IEE Proc. F - Radar Signal Process.*, vol. 139, no. 5, pp. 343-350, Oct. 1992.
- [18] A. Stelzer, K. Pourvoyeur, and A. Fischer, "Concept and Application of LPM - A Novel 3-D Local Position Measurement System," *IEEE Trans. Microw. Theory Tech.*, vol. 52, no. 12, pp. 2664-2669, Dec. 2004.
- [19] S. Ayhan, S. Scherr, A. Bhutani, B. Fischbach, M. Pauli, and T. Zwick, "Impact of Frequency Ramp Nonlinearity, Phase Noise, and SNR on FMCW Radar Accuracy," *IEEE Trans. Microw. Theory Tech.*, vol. 64, no. 10, pp. 3290-3301, Oct. 2016.
- [20] L. Han and K. Wu, "24-GHz Integrated Radio and Radar System Capable of Time-Agile Wireless Communication and Sensing," *IEEE Trans. Microw. Theory Tech.*, vol. 60, no. 3, pp. 619-631, March 2012.
- [21] M. Vossiek, R. Roskosch, and P. Heide, "Precise 3-D Object Position Tracking using FMCW Radar," in *1999 29th Eur. Microw. Conf.*, Munich, Germany, 1999, vol. 1, pp. 234-237.
- [22] F. Wang, C. Fang, T. Horng, K. Peng, J. Li, and C. Chen, "Concurrent Vital Sign and Position Sensing of Multiple Individuals Using Self-Injection-Locked Tags and Injection-Locked I/Q Receivers with Arctangent Demodulation," *IEEE Trans. Microw. Theory Tech.*, vol. 61, no. 12, pp. 4689-4699, Dec. 2013.
- [23] J. Lorenzo, A. Lazaro, R. Villarino, and D. Girbau, "Active Backscatter Transponder for FMCW Radar Applications," *IEEE Antennas Wireless Propag. Lett.*, vol. 14, pp. 1610-1613, 2015.
- [24] R. Gierlich, J. Huettner, A. Ziroff, R. Weigel, and M. Huemer, "A Reconfigurable MIMO System for High-Precision FMCW Local Positioning," *IEEE Trans. Microw. Theory Tech.*, vol. 59, no. 12, pp. 3228-3238, Dec. 2011.
- [25] N. E. Agroudy, M. El-Shennawy, N. Joram, and F. Ellinger, "Design of a 24 GHz Frequency Divider-by-10 in 45 nm-Silicon-on-Insulator as an Active Reflector Tag," *Electron. Lett.*, vol. 53, no. 23, pp. 1546-1548, 2017.
- [26] D. Psychoudakis, W. Moulder, C. Chen, H. Zhu, and J. L. Volakis, "A Portable Low-Power Harmonic Radar System and Conformal Tag for Insect Tracking," *IEEE Antennas Wireless Propag. Lett.*, vol. 7, pp. 444-447, 2008.
- [27] Z. Tsai, P. Jau, N. Kuo, J. Kao, K. Lin, F. Chang, E. Yang, and H. Wang, "A High-Range-Accuracy and High-Sensitivity Harmonic Radar Using Pulse Pseudorandom Code for Bee Searching," *IEEE Trans. Microw. Theory Tech.*, vol. 61, no. 1, pp. 666-675, 2013.
- [28] Y. Ma and E. C. Kan, "Accurate Indoor Ranging by Broadband Harmonic Generation in Passive NLTL Backscatter Tags," *IEEE Trans. Microw. Theory Tech.*, vol. 62, no. 5, pp. 1249-1261, 2014.

- [29] X. Hui, Y. Ma, and E. C. Kan, "Code Division Multiple Access in Centimeter Accuracy Harmonic RFID Locating System," *IEEE J. Radio Freq. Identification*, vol. 1, no. 1, pp. 51-58, 2017.
- [30] X. Hui and E. C. Kan, "Collaborative Reader Code Division Multiple Access in the Harmonic RFID System," *IEEE J. Radio Freq. Identification*, vol. 2, no. 2, pp. 86-92, 2018.
- [31] M. Vossiek and P. Gulden, "The Switched Injection-Locked Oscillator: A Novel Versatile Concept for Wireless Transponder and Localization Systems," *IEEE Trans. Microw. Theory Tech.*, vol. 56, no. 4, pp. 859-866, April 2008.
- [32] S. Wehrli, R. Gierlich, J. Huttner, D. Barras, F. Ellinger, and H. Jackel, "Integrated Active Pulsed Reflector for an Indoor Local Positioning System," *IEEE Trans. Microw. Theory Tech.*, vol. 58, no. 2, pp. 267-276, Feb. 2010.
- [33] C. Carlowitz, M. Vossiek, A. Strobel, and F. Ellinger, "Precise Ranging and Simultaneous High Speed Data Transfer Using mm-Wave Regenerative Active Backscatter Tags," in *2013 IEEE Int. Conf. RFID* Penang, 2013, pp. 253-260.
- [34] A. Strobel, C. Carlowitz, R. Wolf, F. Ellinger, and M. Vossiek, "A Millimeter-Wave Low-Power Active Backscatter Tag for FMCW Radar Systems," *IEEE Trans. Microw. Theory Tech.*, vol. 61, no. 5, pp. 1964-1972, May 2013.
- [35] S. Appel, D. Berges, D. Mueller, A. Ziroff, and M. Vossiek, "MIMO FMCW Reader Concept for Locating Backscatter Transponders," *IEEE Trans. Microw. Theory Tech.*, vol. 64, no. 9, pp. 2955-2967, 2016.
- [36] P. Cheong, K. Wu, and K. Tam, "Nonlinear Communication System with Harmonic Diversity," *IEEE Trans. Microw. Theory Tech.*, vol. 63, no. 12, pp. 4130-4149, 2015.
- [37] F. Zhu, K. Wang, and K. Wu, "A Fundamental-and-Harmonic Dual-Frequency Doppler Radar System for Vital Signs Detection Enabling Radar Movement Self-Cancellation," *IEEE Trans. Microw. Theory Tech.*, pp. 1-13, 2018.
- [38] J. Verspecht, "Large-Signal Network Analysis," *IEEE Microw. Mag.*, vol. 6, no. 4, pp. 82-92, 2005.
- [39] G. Simpson, J. Horn, D. Gunyan, and D. E. Root, "Load-Pull + NVNA = Enhanced X-Parameters for PA Designs with High Mismatch and Technology-Independent Large-Signal Device Models," in *2008 72nd Microw. Meas. Symp.*, 2008, pp. 88-91.
- [40] C. Baylis, R. J. Marks, J. Martin, H. Miller, and M. Moldovan, "Going Nonlinear," *IEEE Microw. Mag.*, vol. 12, no. 2, pp. 55-64, Apr. 2011.
- [41] M. Rajabi, D. A. Humphreys, G. Avolio, P. Barmuta, K. R. Łukasik, T. S. Nielsen, and D. M. M. Schreurs, "Design and Evaluation of Nonlinear Verification Device for Nonlinear Vector Network Analyzers," *IEEE Trans. Microw. Theory Tech.*, vol. 66, no. 2, pp. 1121-1130, 2018.
- [42] V. Gillet, J. Teyssier, T. Reveyard, S. Laurent, M. Prigent, and R. Quéré, "A Fully Calibrated NVNA Set-Up for Linearity Characterization of RF Power Devices Using Unequally Spaced Multi-Tone Signal Through IM3 & IM5 Measurements," in *2018 91st Microw. Meas. Conf.*, 2018, pp. 1-4.

- [43] M. Salter, L. Stant, K. Buisman, and T. Nielsen, "An Inter-Laboratory Comparison of NVNA Measurements," in *2018 Int. Workshop Integr. Nonlinear Microw. Millim. wave Circuits (INMMIC)*, 2018, pp. 1-3.
- [44] A. Pelaez-Perez, S. Woodington, J. Alonso, M. Fernandez-Barciela, and P. Tasker, "X-parameters-Based Closed-Form Expressions for Evaluating Power-Dependent Fundamental Negative and Positive Real Impedance Boundaries in Oscillator Design," *IET Microw., Antennas & Propag.*, vol. 6, no. 8, pp. 835-840, June 2012.
- [45] A. Pelaez-Perez, S. Woodington, M. Fernandez-Barciela, P. J. Tasker, and J. Alonso, "Large-Signal Oscillator Design Procedure Utilizing Analytical X-Parameters Closed-Form Expressions," *IEEE Trans. Microw. Theory Tech.*, vol. 60, no. 10, pp. 3126-3136, Oct. 2012.
- [46] A. Rodriguez-Testera, O. Mojon, A. S. Boaventura, M. Fernandez-Barciela, N. B. Carvalho, M. V. Bossche, and G. Pailloncy, "Diode Power Detector X-Parameters Model Extraction Using LSNA-Based Measurement System," *Electron. Lett.*, vol. 49, no. 3, pp. 196-198, 2013.
- [47] W. Dementroux, C. Maziere, E. Gatard, S. Dellier, M. Campovecchio, and R. Quere, "Multiharmonic Volterra Model Dedicated to the Design of Wideband and Highly Efficient GaN Power Amplifiers," *IEEE Trans. Microw. Theory Tech.*, vol. 60, no. 6, pp. 1817-1828, 2012.
- [48] R. Essaadali, A. Jarndal, A. B. Kouki, and F. M. Ghannouchi, "A New GaN HEMT Equivalent Circuit Modeling Technique Based on X-Parameters," *IEEE Trans. Microw. Theory Tech.*, vol. 64, no. 9, pp. 2758-2777, 2016.
- [49] H. G. Joujili, M. Mivehchy, and M. Habibi, "A Novel Analytical Design Approach for Determining the Optimum Load to Minimize Harmonic Output Power Based on X-Parameters," *IEEE Trans. Microw. Theory Tech.*, vol. 64, no. 11, pp. 3492-3500, 2016.
- [50] C. Lee, Y. Lin, and W. Lin, "Investigation of Time-Domain Locus of SiGe HBTs in the Avalanche Region by Using the X-Parameter Measurement under Large-Signal Drive," *IEEE Microw. Wireless Compon. Lett.*, vol. 27, no. 5, pp. 464-466, 2017.
- [51] W. Akstaller, C. Musolff, R. Weigel, and A. Hagelauer, "X-Parameter Characterization of TC SAW Filters with Enhanced Dynamic Range," *IEEE Trans. Microw. Theory Tech.*, vol. 65, no. 11, pp. 4541-4549, 2017.
- [52] K. Kurokawa, "Power Waves and the Scattering Matrix," *IEEE Trans. Microw. Theory Tech.*, vol. 13, no. 2, pp. 194-202, Mar. 1965.
- [53] Keysight Technology, "An Evaluation of X-Parameter, P2D and S2D Models for Characterizing Nonlinear Behavior in Active Devices," *Application Note 5990-8732EN*, Aug. 2014.
- [54] D. Vye, "Fundamentally Changing Nonlinear Microwave Design," *Microw. J.*, vol. 53, no. 3, pp. 22-24, Mar. 2010.
- [55] D. E. Root, J. Verspecht, D. Sharrit, J. Wood, and A. Cognata, "Broad-Band Poly-Harmonic Distortion (PHD) Behavioral Models from Fast Automated Simulations and Large-Signal Vectorial Network Measurements," *IEEE Trans. Microw. Theory Tech.*, vol. 53, no. 11, pp. 3656-3664, Nov. 2005.

- [56] D. Root, "Polyharmonic Distortion Modeling," *IEEE Microw. Mag.*, vol. 7, no. 3, pp. 44-57, June 2006.
- [57] J. Verspecht, D. Gunyan, J. Horn, J. Xu, A. Cognata, and D. E. Root, "Multi-Tone, Multi-Port, and Dynamic Memory Enhancements to PHD Nonlinear Behavioral Models from Large-Signal Measurements and Simulations," in *2007 IEEE MTT-S Int. Microw. Symp. Dig.*, Honolulu, HI, 2007, pp. 969-972.
- [58] P. Roblin, *Nonlinear RF Circuits and Nonlinear Vector Network Analyzers: Interactive Measurement and Design Techniques*. Cambridge University Press, 2011, pp. 160 -179.
- [59] J. Wood and D. E. Root, Eds. *Fundamentals of Nonlinear Behavioral Modeling for RF and Microwave Design*. Artech House Publishers, 2005.
- [60] Introduction [Online]. Available: <http://www.openwaveforum.org>
- [61] D. Williams, P. Hale, and K. A. Remley, "The Sampling Oscilloscope as a Microwave Instrument," *IEEE Microw. Mag.*, vol. 8, no. 4, pp. 59-68, Aug. 2007.
- [62] K. A. Remley, "The Impact of Internal Sampling Circuitry on the Phase Error of the Nose-to-Nose Oscilloscope Calibration," Technical Note (NIST TN)-1528, Aug. 2003.
- [63] NVNA Calibration and Verification at Mesuro [Online]. Available: http://www.arftg.org/lsna/2011_spring_Baltimore_nvna_users.html
- [64] Overview and Notes [Online]. Available: http://www.arftg.org/lsna/2011_spring_Baltimore_nvna_users.html
- [65] S. Adhikari, A. Ghiotto, K. Wang, and K. Wu, "Development of a Large-Signal-Network-Analyzer Round-Robin Artifact," *IEEE Microw. Mag.*, vol. 14, no. 1, pp. 140-145, Jan.-Feb. 2013.
- [66] A. Toccafondi, D. Zampilli, C. D. Giovampaola, and V. Tesi, "Low-Power UWB Transmitter for RFID Transponder Applications," in *2012 IEEE Int. Conf. RFID-Tech. Appl. (RFID-TA)*, 2012, pp. 234-238.
- [67] Y. Cassivi and K. Wu, "Low Cost Microwave Oscillator Using Substrate Integrated Waveguide Cavity," *IEEE Microw. Wireless Compon. Lett.*, vol. 13, no. 2, pp. 48-50, Feb. 2003.
- [68] D. M. Pozar, *Microwave Engineering*, 3rd ed. New Jersey, USA: John Wiley & Sons, 2004.
- [69] J. Obregon and A. Khanna, "Exact Derivation of the Nonlinear Negative-Resistance Oscillator Pulling Figure," *IEEE Trans. Microw. Theory Tech.*, vol. 30, no. 7, pp. 1109-1111, July 1982.
- [70] B. Razavi, "A Study of Injection Locking and Pulling in Oscillators," *IEEE J. Solid-State Circuits*, vol. 39, no. 9, pp. 1415-1424, Sept. 2004.
- [71] F. Okada, K. Ohwi, and Y. Yokochi, "YIG Resonator Circuit with Isolator Property and its Application to a Gunn Diode Oscillator," *IEEE Trans. Microw. Theory Tech.*, vol. 26, no. 12, pp. 1035-1039, Dec. 1978.
- [72] C.-F. Chen, T.-Y. Huang, C.-P. Chou, and R.-B. Wu, "Microstrip Diplexers Design with Common Resonator Sections for Compact Size, but High Isolation," *IEEE Trans. Microw. Theory Tech.*, vol. 54, no. 5, pp. 1945-1952, May 2006.

- [73] R. Bhattacharyya, C. Floerkemeier, and S. Sarma, "Low-Cost, Ubiquitous RFID-Tag-Antenna-Based Sensing," *Proc. IEEE*, vol. 98, no. 9, pp. 1593-1600, Sept. 2010.
- [74] J. Lu, H. Okada, T. Itoh, T. Harada, and R. Maeda, "Toward the World Smallest Wireless Sensor Nodes with Ultralow Power Consumption," *IEEE Sensors J.*, vol. 14, no. 6, pp. 2035-2041, June 2014.
- [75] P. Burasa, T. Djerafi, N. G. Constantin, and K. Wu, "High-Data-Rate Single-Chip Battery-Free Active Millimeter-Wave Identification Tag in 65-nm CMOS Technology," *IEEE Trans. Microw. Theory Tech.*, vol. 64, no. 7, pp. 2294-2303, July 2016.
- [76] K. Wang, J.-F. Gu, F. Ren, and K. Wu, "A Multitarget Active Backscattering 2-D Positioning System with Superresolution Time Series Post-Processing Technique," *IEEE Trans. Microw. Theory Tech.*, vol. 65, no. 5, pp. 1751-1766, May 2017.
- [77] C.-H. Hsiao, C.-T. Chen, T.-S. Horng, and K.-C. Peng, "Design of a Direct Conversion Transmitter to Resist Combined Effects of Power Amplifier Distortion and Local Oscillator Pulling," *IEEE Trans. Microw. Theory Tech.*, vol. 60, no. 6, pp. 2000-2009, June 2012.
- [78] I. Bashir, R. B. Staszewski, O. Eliezer, B. Banerjee, and P. T. Balsara, "A Novel Approach for Mitigation of RF Oscillator Pulling in a Polar Transmitter," *IEEE J. Solid-State Circuits*, vol. 46, no. 2, pp. 403-415, Feb. 2011.
- [79] J. Dominguez, A. Suarez, and S. Sancho, "Semi-Analytical Formulation for the Analysis and Reduction of Injection-Pulling in Front-End Oscillators," in *2009 IEEE MTT-S Int. Microw. Symp. Dig.*, Boston, MA, USA, 2009, pp. 1589-1592.
- [80] Y. Chen and Z. Chen, "A Dual-Gate FET Subharmonic Injection-Locked Self-Oscillating Active Integrated Antenna for RF Transmission," *IEEE Microw. Wireless Compon. Lett.*, vol. 13, no. 6, pp. 199-201, June 2003.
- [81] M. Pelissier, J. Jantunen, B. Gomez, J. Arponen, G. Masson, S. Dia, J. Varteva, and M. Gary, "A 112 Mb/s Full Duplex Remotely-Powered Impulse-UWB RFID Transceiver for Wireless NV-Memory Applications," *IEEE J. Solid-State Circuits*, vol. 46, no. 4, pp. 916-927, Apr. 2011.
- [82] K. Sengupta and A. Hajimiri, "Mutual Synchronization for Power Generation and Beam-Steering in CMOS with On-Chip Sense Antennas Near 200 GHz," *IEEE Trans. Microw. Theory Tech.*, vol. 63, no. 9, pp. 2867-2876, Sept. 2015.
- [83] Y. Tousi and E. Afshari, "A High-Power and Scalable 2-D Phased Array for Terahertz CMOS Integrated Systems," *IEEE J. Solid-State Circuits*, vol. 50, no. 2, pp. 597-609, Feb. 2015.
- [84] Z. Hu, M. Kaynak, and R. Han, "High-Power Radiation at 1 THz in Silicon: a Fully Scalable Array Using a Multi-Functional Radiating Mesh Structure," *IEEE J. Solid-State Circuits*, vol. 53, no. 5, pp. 1313-1327, May 2018.
- [85] S. Pellerano, J. Alvarado, and Y. Palaskas, "A mm-Wave Power-Harvesting RFID Tag in 90 nm CMOS," *IEEE J. Solid-State Circuits*, vol. 45, no. 8, pp. 1627-1637, Aug. 2010.
- [86] S. Jeon, S. Jung, D. Lee, and H. Lee, "A Fully Integrated CMOS LC VCO and Frequency Divider for UHF RFID Reader," in *2006 IEEE North-East Workshop Circuits Syst.*, Gatineau, QC, CA, 2006, pp. 117-120.

- [87] B.-E. Seow, S.-T. Lin, T.-H. Huang, and H.-R. Chuang, "Injection Pulling Mitigation in CMOS Voltage Controlled Oscillator Using a Novel Honeycomb-Shaped Planar Inductor," *IEEE Trans. Circuits Syst. II: Exp. Briefs.*, DOI: 10.1109/TCSII.2018.2826138.
- [88] K. W. Kobayashi, A. K. Oki, L. T. Tran, J. C. Cowles, A. Gutierrez-Aitken, F. Yamada, T. R. Block, and D. C. Streit, "A 108-GHz InP-HBT Monolithic Push-Push VCO with Low Phase Noise and Wide Tuning Bandwidth," *IEEE J. Solid-State Circuits*, vol. 34, no. 9, pp. 1225-1232, Sept. 1999.
- [89] R. Wanner, H. Schafer, R. Lachner, G. R. Olbrich, and P. Russer, "A Fully Integrated 70 GHz SiGe Low Phase Noise Push-Push Oscillator," in *2005 IEEE MTT-S Int. Microw. Symp. Dig.*, Long Beach, CA, USA, 2005, pp. 1523-1526.
- [90] G. Gonzalez, *Microwave Transistor Amplifiers: Analysis and Design*. New Jersey, USA: Prentice Hall, 1997.
- [91] K. Wang, A. Ghiotto, and K. Wu, "Harmonic Feedback-Loop Oscillator for Pulling Effect Reduction and Improved Phase Noise," in *2014 IEEE MTT-S Int. Microw. Symp. Dig.*, Tampa, FL, USA, 2014, pp. 1-4.
- [92] Z. Li, R. Zeng, Z. Li, and J. Bao, "Design of Low Phase Noise Feedback-Type Harmonic Oscillator Using SIW-CMSRR Diplexer," in *2017 47th Eur. Microw. Conf.*, Nuremberg, BY, DE, 2017, pp. 759-762.
- [93] K. Wang, A. Ghiotto, and K. Wu, "A Millimeter-Wave Self-Isolated Harmonic Active Radiator for Identification, Sensing, Tracking and Communication Applications," *IEEE Trans. Antennas Propag.*, Submitted.
- [94] R. Adler, "A Study of Locking Phenomena in Oscillators," *Proc. IEEE*, vol. 61, no. 10, pp. 1380-1385, Oct. 1973.
- [95] A. K. Poddar, U. L. Rohde, and A. M. Apte, "How Low Can They Go?: Oscillator Phase Noise Model, Theoretical, Experimental Validation, and Phase Noise Measurements," *IEEE Microw. Mag.*, vol. 14, no. 6, pp. 50-72, Sept.-Oct. 2013.
- [96] H. J. Tang, W. Hong, J.-X. Chen, G. Q. Luo, and K. Wu, "Development of Millimeter-Wave Planar Diplexers Based on Complementary Characters of Dual-Mode Substrate Integrated Waveguide Filters with Circular and Elliptic Cavities," *IEEE Trans. Microw. Theory Tech.*, vol. 55, no. 4, pp. 776-782, Apr. 2007.
- [97] N. Athanasopoulos, D. Makris, and K. Voudouris, "Development of a 60 GHz Substrate Integrated Waveguide Planar Diplexer," in *2011 IEEE MTT-S Int. Microw. Workshop Series mmW Integr. Tech.*, Sitges, Spain, 2011, pp. 128-131.
- [98] W.-F. Liang, W. Hong, and J.-X. Chen, "Analysis and Design of a Voltage-Current Transformer Feedback Neutralization Network with an Arbitrarily Chosen Coupling-Factor," *IEEE Trans. Microw. Theory Tech.*, vol. 61, no. 11, pp. 3892-3904, Nov. 2013.
- [99] J. Verspecht and P. Van Esch, "Accurately Characterizing Hard Nonlinear Behavior of Microwave Components with the Nonlinear Network Measurement System: Introducing 'Nonlinear Scattering Functions'," in *Proc. 5th Int. Workshop Integr. Nonlinear Microw. mmW Circuits*, 1998, pp. 17-26.
- [100] J.-S. G. Hong and M. J. Lancaster, *Microstrip Filters for RF/Microwave Applications*. New York, NY, USA: John Wiley & Sons, 2001.

- [101] L.-H. Hsieh and K. Chang, "Equivalent Lumped Elements G, L, C, and Unloaded Q's of Closed-and Open-Loop Ring Resonators," *IEEE Trans. Microw. Theory Tech.*, vol. 50, no. 2, pp. 453-460, Feb. 2002.
- [102] R. Hopkins and C. Free, "Equivalent Circuit for the Microstrip Ring Resonator Suitable for Broadband Materials Characterisation," *IET Microw., Antennas & Propag.*, vol. 2, no. 1, pp. 66-73, Feb. 2008.
- [103] A. M. Pelaez-Perez, S. Woodington, M. Fernandez-Barciela, P. J. Tasker, and J. I. Alonso, "Application of an NVNA-Based System and Load-Independent X-Parameters in Analytical Circuit Design Assisted by an Experimental Search Algorithm," *IEEE Trans. Microw. Theory Tech.*, vol. 61, no. 1, pp. 581-586, Jan. 2013.
- [104] K. Wang, S. Adhikari, A. Ghiotto, and K. Wu, "Multiharmonic Generator for Large-Signal-Network-Analyzer Verification," *IEEE Microw. Mag.*, vol. 15, no. 1, pp. 120-128, Jan.-Feb. 2014.
- [105] J. Jeong and D. Jang, "Design Technique for Harmonic-Tuned RF Power Oscillators for High-Efficiency Operation," *IEEE Trans. Ind. Electron.*, vol. 62, no. 1, pp. 221-228, Jan. 2015.
- [106] D. Barataud, C. Arnaud, B. Thibaud, M. Campovecchio, J.-M. Nebus, and J. P. Villotte, "Measurements of Time-Domain Voltage/Current Waveforms at RF and Microwave Frequencies Based on the Use of a Vector Network Analyzer for the Characterization of Nonlinear Devices-Application to High-Efficiency Power Amplifiers and Frequency-Multipliers Optimization," *IEEE Trans. Instrum. Meas.*, vol. 47, no. 5, pp. 1259-1264, Oct. 1998.
- [107] Maury Microwave, "Active Harmonic Load-Pull with Realistic Wideband Communications Signals," *Application Note 5A-044*, June 2010.
- [108] S. Gustafsson, M. Thorsell, and C. Fager, "A Novel Active Load-Pull System with Multi-Band Capabilities," in *2013 81st Microw. Meas. Conf.*, Seattle, WA, USA, 2013, pp. 1-4.
- [109] S. Gustafsson, M. Thorsell, J. Stenarson, and C. Fager, "An Oscilloscope Correction Method for Vector-Corrected RF Measurements," *IEEE Trans. Instrum. Meas.*, vol. 64, no. 9, pp. 2541-2547, Sept. 2015.
- [110] S. Gustafsson, C. Fager, K. Buisman, and M. Thorsell, "Wideband RF Characterization Setup with High Dynamic Range Low Frequency Measurement Capabilities," in *2016 87th Microw. Meas. Conf.*, San Francisco, CA, USA, 2016, pp. 1-4.
- [111] P. J. Tasker, "Practical Waveform Engineering," *IEEE Microw. Mag.*, vol. 10, no. 7, Dec. 2009.
- [112] M.-Q. Lee, S.-J. Yi, S. Nam, Y. Kwon, and K.-W. Yeom, "High-Efficiency Harmonic Loaded Oscillator with Low Bias Using a Nonlinear Design Approach," *IEEE Trans. Microw. Theory Tech.*, vol. 47, no. 9, pp. 1670-1679, Sept. 1999.
- [113] M. D. Janezic and J. A. Jargon, "Complex Permittivity Determination from Propagation Constant Measurements," *IEEE Microw. Guided Wave Lett.*, vol. 9, no. 2, pp. 76-78, Feb. 1999.
- [114] Y. Zhao, S. Hemour, T. Liu, and K. Wu, "Non-Uniformly Distributed Electronic Impedance Synthesizer," *IEEE Trans. Microw. Theory Tech.*, DOI: 10.1109/TMTT.2018.2868941.

- [115] H.-Y. Chang, C.-H. Lin, Y.-C. Liu, W.-P. Li, and Y.-C. Wang, "A K-band High Efficiency High Power Monolithic GaAs Power Oscillator Using Class-E Network," *IEEE Microw. Wireless Compon. Lett.*, vol. 27, no. 1, pp. 55-57, Jan. 2017.
- [116] E. W. Bryerton, W. A. Shiroma, and Z. B. Popovic, "A 5-GHz High-Efficiency Class-E Oscillator," *IEEE Microw. Guided Wave Lett.*, vol. 6, no. 12, pp. 441-443, Dec 1996.
- [117] Y. Iyama, A. Iida, T. Takagi, and S. Urasaki, "Second-Harmonic Reflector Type High-Gain FET Frequency Doubler Operating in K-Band," in *1989 IEEE MTT-S Int. Microw. Symp. Dig.*, Long Beach, CA, USA, 1989, pp. 1291-1294.
- [118] D. G. Thomas and G. Branner, "Optimization of Active Microwave Frequency Multiplier Performance Utilizing Harmonic Terminating Impedances," *IEEE Trans. Microw. Theory Tech.*, vol. 44, no. 12, pp. 2617-2624, Dec. 1996.
- [119] D. G. Thomas and G. Branner, "Single-Ended HEMT Multiplier Design Using Reflector Networks," *IEEE Trans. Microw. Theory Tech.*, vol. 49, no. 5, pp. 990-993, May 2001.
- [120] J.-J. Hung, T. M. Hancock, and G. M. Rebeiz, "High-Power High-Efficiency SiGe Ku-and Ka-Band Balanced Frequency Doublers," *IEEE Trans. Microw. Theory Tech.*, vol. 53, no. 2, pp. 754-761, Feb. 2005.
- [121] I. Ju, C. D. Cheon, and J. D. Cressler, "A Compact Highly Efficient High-Power Ka-Band SiGe HBT Cascode Frequency Doubler with Four-Way Input Transformer Balun," *IEEE Trans. Microw. Theory Tech.*, vol. 66, no. 6, pp. 2879-2887, June 2018.
- [122] M. D. Weiss and Z. Popovic, "An X/K-Band Class-E High-Efficiency Frequency Doubler," in *2001 31st Eur. Microw. Conf.*, London, UK, 2001, pp. 1-4.
- [123] E. Sandhiya, D. Denis, and I. C. Hunter, "Novel Design Methodology for High Efficiency Class E Microwave Frequency Triplers," in *2006 IEEE MTT-S Int. Microw. Symp. Dig.*, San Francisco, CA, USA, 2006, pp. 1825-1828.
- [124] R. Zulinski and J. Steadman, "Idealized Operation of Class E Frequency Multipliers," *IEEE Trans. Circuits Syst.*, vol. 33, no. 12, pp. 1209-1218, Dec. 1986.
- [125] S. C. Cripps, *RF Power Amplifiers for Wireless Communications*, 2nd ed. Norwood, MA, USA: Artech House, 2006.
- [126] K. Wu, P. Burasa, T. Djerafi, and N. Constantin, "Millimeter-Wave Identification for Future Sensing, Tracking, Positioning and Communicating Systems," in *Proc. IEEE Millim. Waves (GSMM) Global Symp. ESA Workshop Millimeter-Wave Techn. Appl.*, 2016, pp. 1-4, Espoo, Finland.
- [127] F. C. Commission, "Report and Order and Second Further Notice of Proposed Rulemaking," *Washington, D.C., USA, Rep. & Ord. FCC 16-89*, Jul. 14, 2016.
- [128] W. Li and J. Yao, "Investigation of Photonic Assisted Microwave Frequency Multiplication Based on External Modulation," *IEEE Trans. Microw. Theory Tech.*, vol. 58, no. 11, pp. 3259-3268, 2010.
- [129] A. Maestrini, J. S. Ward, J. J. Gill, C. Lee, B. Thomas, R. H. Lin, G. Chattopadhyay, and I. Mehdi, "A Frequency-Multiplied Source with More Than 1 mW of Power Across the 840–900-GHz Band," *IEEE Trans. Microw. Theory Tech.*, vol. 58, no. 7, pp. 1925-1932, 2010.

- [130] J. Stake, A. Malko, T. Bryllert, and J. Vukusic, "Status and Prospects of High-Power Heterostructure Barrier Varactor Frequency Multipliers," *Proc. IEEE*, vol. 105, no. 6, pp. 1008-1019, 2017.
- [131] G. Chattopadhyay, E. Schlecht, J. S. Ward, J. J. Gill, H. H. S. Javadi, F. Maiwald, and I. Mehdi, "An All-Solid-State Broad-Band Frequency Multiplier Chain at 1500 GHz," *IEEE Trans. Microw. Theory Tech.*, vol. 52, no. 5, pp. 1538-1547, May 2004.
- [132] T. Djurhuus, V. Krozer, J. Vidkjaer, and T. K. Johansen, "Nonlinear Analysis of a Cross-Coupled Quadrature Harmonic Oscillator," *IEEE Trans. Circuits Syst. I, Reg. Papers*, vol. 52, no. 11, pp. 2276-2285, Nov. 2005.
- [133] F. Huang, C. Lin, and Y. Chan, "V-Band GaAs pHEMT Cross-Coupled Sub-Harmonic Oscillator," *IEEE Microw. Wireless Compon. Lett.*, vol. 16, no. 8, pp. 473-475, Aug. 2006.
- [134] J. Grzyb, Y. Zhao, and U. R. Pfeiffer, "A 288-GHz Lens-Integrated Balanced Triple-Push Source in a 65-nm CMOS Technology," *IEEE J. Solid-State Circuits*, vol. 48, no. 7, pp. 1751-1761, Jul. 2013.
- [135] Z. Zong, M. Babaie, and R. B. Staszewski, "A 60 GHz Frequency Generator Based on a 20 GHz Oscillator and an Implicit Multiplier," *IEEE J. Solid-State Circuits*, vol. 51, no. 5, pp. 1261-1273, May 2016.
- [136] R. Kananizadeh and O. Momeni, "High-Power and High-Efficiency Millimeter-Wave Harmonic Oscillator Design, Exploiting Harmonic Positive Feedback in CMOS," *IEEE Trans. Microw. Theory Tech.*, vol. 65, no. 10, pp. 3922-3936, 2017.
- [137] W. R. Deal, N. Kaneda, J. Sor, Y. Qian, and T. Itoh, "A New Quasi-Yagi Antenna for Planar Active Antenna Arrays," *IEEE Trans. Microw. Theory Tech.*, vol. 48, no. 6, pp. 910-918, June 2000.
- [138] M. Bozzi, A. Georgiadis, and K. Wu, "Review of Substrate-Integrated Waveguide Circuits and Antennas," *IET Microw., Antennas & Propag.*, vol. 5, no. 8, pp. 909-920, June 2011.
- [139] A. Dierck, H. Rogier, and F. Declercq, "A Wearable Active Antenna for Global Positioning System and Satellite Phone," *IEEE Trans. Antennas Propag.*, vol. 61, no. 2, pp. 532-538, Feb. 2013.
- [140] B. Goettel, P. Pahl, C. Kutschker, S. Malz, U. R. Pfeiffer, and T. Zwick, "Active Multiple Feed On-Chip Antennas with Efficient In-Antenna Power Combining Operating at 200–320 GHz," *IEEE Trans. Antennas Propag.*, vol. 65, no. 2, pp. 416-423, Feb. 2017.
- [141] C. Young Jun, K. Ki Hak, C. Dong Hyuk, L. Seung Sik, and P. Seong-Ook, "A Miniature UWB Planar Monopole Antenna with 5-GHz Band-Rejection Filter and the Time-Domain Characteristics," *IEEE Trans. Antennas Propag.*, vol. 54, no. 5, pp. 1453-1460, May 2006.
- [142] G. Q. Luo, W. Hong, H. J. Tang, J. X. Chen, X. X. Yin, Z. Q. Kuai, and K. Wu, "Filtenna Consisting of Horn Antenna and Substrate Integrated Waveguide Cavity FSS," *IEEE Trans. Antennas Propag.*, vol. 55, no. 1, pp. 92-98, Jan. 2007.
- [143] O. A. Nova, J. C. Bohorquez, N. M. Pena, G. E. Bridges, L. Shafai, and C. Shafai, "Filter-Antenna Module Using Substrate Integrated Waveguide Cavities," *IEEE Antennas Wireless Propag. Lett.*, vol. 10, pp. 59-62, Jan. 2011.

- [144] A. J. Martinez-Ros, J. L. Gómez-Tornero, and G. Goussetis, "Multifunctional Angular Bandpass Filter SIW Leaky-Wave Antenna," *IEEE Antennas Wireless Propag. Lett.*, vol. 16, pp. 936-939, Oct. 2017.
- [145] C. E. Saavedra, B. R. Jackson, and S. S. K. Ho, "Self-Oscillating Mixers: A Natural Fit for Active Antennas," *IEEE Microw. Mag.*, vol. 14, no. 6, pp. 40-49, Sept.-Oct. 2013.
- [146] P. Burasa, N. G. Constantin, and K. Wu, "Low-Power Injection-Locked Zero-IF Self-Oscillating Mixer for High Gbit/s Data-Rate Battery-Free Active μ Rfid Tag at Millimeter-Wave Frequencies in 65-nm CMOS," *IEEE Trans. Microw. Theory Tech.*, vol. 64, no. 4, pp. 1055-1065, Apr. 2016.
- [147] K. Chang, R. A. York, P. S. Hall, and T. Itoh, "Active Integrated Antennas," *IEEE Trans. Microw. Theory Tech.*, vol. 50, no. 3, pp. 937-944, Mar. 2002.
- [148] F. Giuppi, A. Georgiadis, A. Collado, and M. Bozzi, "A Compact, Single-Layer Substrate Integrated Waveguide (SIW) Cavity-Backed Active Antenna Oscillator," *IEEE Antennas Wireless Propag. Lett.*, vol. 11, pp. 431-433, Apr. 2012.
- [149] Y. Lin and T. Ma, "Frequency-Reconfigurable Self-Oscillating Active Antenna with Gap-Loaded Ring Radiator," *IEEE Antennas Wireless Propag. Lett.*, vol. 12, pp. 337-340, Mar. 2013.
- [150] C. Wu and T. Ma, "Self-Oscillating Semi-Ring Active Integrated Antenna with Frequency Reconfigurability and Voltage-Controllability," *IEEE Trans. Antennas Propag.*, vol. 61, no. 7, pp. 3880-3885, Jul. 2013.
- [151] C. Wu and T. Ma, "Pattern-Reconfigurable Self-Oscillating Active Integrated Antenna with Frequency Agility," *IEEE Trans. Antennas Propag.*, vol. 62, no. 12, pp. 5992-5999, Dec. 2014.
- [152] E. H. Lim and K. W. Leung, "Novel Utilization of the Dielectric Resonator Antenna as an Oscillator Load," *IEEE Trans. Antennas Propag.*, vol. 55, no. 10, pp. 2686-2691, Oct. 2007.
- [153] P. Liao and R. A. York, "A New Phase-Shifterless Beam-Scanning Technique Using Arrays of Coupled Oscillators," *IEEE Trans. Microw. Theory Tech.*, vol. 41, no. 10, pp. 1810-1815, Oct. 1993.
- [154] K. Sengupta and A. Hajimiri, "Distributed Active Radiation for THz Signal Generation," in *2011 IEEE Int. Solid-State Circuits Conf.*, San Francisco, CA, 2011, pp. 288-289.
- [155] K. Sengupta and A. Hajimiri, "Designing Optimal Surface Currents for Efficient On-Chip mm-Wave Radiators with Active Circuitry," *IEEE Trans. Microw. Theory Tech.*, vol. 64, no. 7, pp. 1976-1988, Jul. 2016.
- [156] K. Sengupta and A. Hajimiri, "A 0.28 THz Power-Generation and Beam-Steering Array in CMOS Based on Distributed Active Radiators," *IEEE J. Solid-State Circuits*, vol. 47, no. 12, pp. 3013-3031, Dec. 2012.
- [157] P. Nazari, S. Jafarlou, and P. Heydari, "A Fundamental-Frequency 114GHz Circular-Polarized Radiating Element with 14dBm EIRP, -99.3 dBc/Hz Phase-Noise at 1MHz Offset and 3.7% Peak Efficiency," in *2017 IEEE Int. Solid-State Circuits Conf.*, CA, 2017, pp. 322-323.

- [158] F. Parment, A. Ghiotto, T. Vuong, J. Duchamp, and K. Wu, "Low-Loss Air-Filled Substrate Integrated Waveguide (SIW) Band-Pass Filter with Inductive Posts," in *2015 45th Eur. Microw. Conf.*, Paris, France, 2015, pp. 761-764.
- [159] F. Parment, A. Ghiotto, T. Vuong, J. Duchamp, and K. Wu, "Air-Filled Substrate Integrated Waveguide for Low-Loss and High Power-Handling Millimeter-Wave Substrate Integrated Circuits," *IEEE Trans. Microw. Theory Tech.*, vol. 63, no. 4, pp. 1228-1238, Apr. 2015.
- [160] F. Parment, A. Ghiotto, T. Vuong, J. Duchamp, and K. Wu, "Double Dielectric Slab-Loaded Air-Filled SIW Phase Shifters for High-Performance Millimeter-Wave Integration," *IEEE Trans. Microw. Theory Tech.*, vol. 64, no. 9, pp. 2833-2842, Sept. 2016.
- [161] Z. Li and K. Wu, "24-GHz Frequency-Modulation Continuous-Wave Radar Front-End System-on-Substrate," *IEEE Trans. Microw. Theory Tech.*, vol. 56, no. 2, pp. 278-285, Feb. 2008.
- [162] R. K. Mongia and P. Bhartia, "Dielectric Resonator Antennas—A Review and General Design Relations for Resonant Frequency and Bandwidth," *Int. J. Microw. Millim. Wave Comput. - Aided Eng.*, vol. 4, no. 3, pp. 230-247, 1994.
- [163] A. Horn, "Dielectric Constant and Loss of Selected Grades of Rogers High Frequency Circuit Substrates from 1-50 GHz," *Rogers Corp., Rogers, CT, USA, Tech. Rep. 5788*, Sept. 19, 2003.
- [164] T. Martin, A. Ghiotto, T. Vuong, F. Lotz, and P. Monteil, "High Performance Air-Filled Substrate Integrated Waveguide Filter Post-Process Tuning Using Capacitive Post," in *2017 IEEE MTT-S Int. Microw. Symp. Dig.*, Honolulu, HI, 2017, pp. 196-199.
- [165] K. Gheen. Phase Noise Measurement Methods and Techniques [Online]. Available: www.keysight.com/upload/cmc_upload/All/PhaseNoise_webcast_19Jul12.pdf?&cc=CA&lc=eng
- [166] Y. Chen and T. Chu, "2-D Direct-Coupled Standing-Wave Oscillator Arrays," *IEEE Trans. Microw. Theory Tech.*, vol. 61, no. 12, pp. 4472-4482, Dec. 2013.
- [167] C. H. Mueller, R. Q. Lee, R. R. Romanofsky, C. L. Kory, K. M. Lambert, F. W. V. Keuls, and F. A. Miranda, "Small-Size X-Band Active Integrated Antenna with Feedback Loop," *IEEE Trans. Antennas Propag.*, vol. 56, no. 5, pp. 1236-1241, May 2008.
- [168] Z. Chen, W. Hong, J. Chen, and L. Li, "Design of A Push-Push and Push-Pull Oscillator Based on SIW/SICL Technique," *IEEE Microw. Wireless Compon. Lett.*, vol. 24, no. 6, pp. 397-399, Jun. 2014.
- [169] A. Georgiadis, S. Via, A. Collado, and F. Mira, "Push-Push Oscillator Design Based on a Substrate Integrated Waveguide (SIW) Resonator," in *2009 39th Eur. Microw. Conf.*, Rome, Italy, 2009, pp. 1231-1234.
- [170] W. T. Khan, S. Bhattacharya, S. Horst, J. D. Cressler, and J. Papapolymerou, "Low Phase Noise K-Band Oscillator on Organic Liquid Crystal Polymer (LCP) Substrate," in *2010 IEEE MTT-S Int. Microw. Symp. Dig.*, Anaheim, CA, 2010, pp. 1186-1189.
- [171] H. Lee, K. Yoon, B. Jeon, Y. Kim, H. Nam, and J. Lee, "Design of a New K-band Push-Push Oscillator Using Miniaturized Hairpin Resonator," in *2009 Asia Pacific Microw. Conf.*, Singapore, 2009, pp. 1675-1678.

- [172] T. Baras and A. F. Jacob, "Vertically Integrated Voltage-Controlled Oscillator in LTCC at K-Band," in *2008 IEEE MTT-S Int. Microw. Symp. Dig.*, Atlanta, GA, 2008, pp. 359-362.
- [173] F. Kirsch, R. Miesen, and M. Vossiek, "Precise Local-Positioning for Autonomous Situation Awareness in the Internet of Things," in *2014 IEEE MTT-S Int. Microw. Symp. Dig.*, Tampa, FL, 2014, pp. 1-4.
- [174] K. Witrisal, S. Hinteregger, J. Kulmer, E. Leitingner, and P. Meissner, "High-Accuracy Positioning for Indoor Applications: RFID, UWB, 5G, and Beyond," in *2016 IEEE Int. Conf. RFID* Orlando, FL, 2016, pp. 1-7.
- [175] G. Ding, J. Wang, Q. Wu, F. Song, and Y. Chen, "Spectrum Sensing in Opportunity-Heterogeneous Cognitive Sensor Networks: How to Cooperate?," *IEEE Sensors J.*, vol. 13, no. 11, pp. 4247-4255, Nov. 2013.
- [176] R. D. Taranto, S. Muppirisetty, R. Raulefs, D. Slock, T. Svensson, and H. Wymeersch, "Location-Aware Communications for 5G Networks: How Location Information Can Improve Scalability, Latency, and Robustness of 5G," *IEEE Signal Process. Mag.*, vol. 31, no. 6, pp. 102-112, Nov. 2014.
- [177] H. Celebi, I. Güvenç, S. Gezici, and H. Arslan, "Cognitive-Radio Systems for Spectrum, Location, and Environmental Awareness," *IEEE Antennas Propag. Mag.*, vol. 52, no. 4, pp. 41-61, Aug. 2010.
- [178] J. Gu, W. Zhu, and M. N. S. Swamy, "Joint 2-D DOA Estimation via Sparse L-Shaped Array," *IEEE Trans. Signal Process.*, vol. 63, no. 5, pp. 1171-1182, March 2015.
- [179] M. Wax and T. Kailath, "Detection of Signals by Information Theoretic Criteria," *IEEE Trans. Acoust., Speech, Signal Process.*, vol. 33, no. 2, pp. 387-392, Apr. 1985.
- [180] P. Stoica and Y. Selen, "Model-Order Selection: A Review of Information Criterion Rules," *IEEE Signal Process. Mag.*, vol. 21, no. 4, pp. 36-47, July 2004.
- [181] S. Kritchman and B. Nadler, "Non-Parametric Detection of the Number of Signals: Hypothesis Testing and Random Matrix Theory," *IEEE Trans. Signal Process.*, vol. 57, no. 10, pp. 3930-3941, Oct. 2009.
- [182] B. Nadler and A. Kontorovich, "Model Selection for Sinusoids in Noise: Statistical Analysis and a New Penalty Term," *IEEE Trans. Signal Process.*, vol. 59, no. 4, pp. 1333-1345, April 2011.
- [183] S. D. Silverstein, "A New Use of ESPRIT for Detection and Model Order Estimation," *IEEE Signal Process. Lett.*, vol. 1, no. 10, pp. 147-149, Oct. 1994.
- [184] J. Papy, L. D. Lathauwer, and S. V. Huffel, "A Shift Invariance-Based Order-Selection Technique for Exponential Data Modelling," *IEEE Signal Process. Lett.*, vol. 14, no. 7, pp. 473-476, July 2007.
- [185] D. W. Tufts and R. Kumaresan, "Estimation of Frequencies of Multiple Sinusoids: Making Linear Prediction Perform Like Maximum Likelihood," *Proc. IEEE*, vol. 70, no. 9, pp. 975-989, Sept. 1982.
- [186] B. D. Rao and K. S. Arun, "Model Based Processing of Signals: A State Space Approach," *Proc. IEEE*, vol. 80, no. 2, pp. 283-309, Feb. 1992.

- [187] Y. Mao, "FMCW Radar Receiver Front-End Design," M.S. Thesis, Dept. Microelectron., TU Delft, Delft, Netherlands, 2009.
- [188] R. Aljasmi, "FMCW-Radar Signal Processing and Parameter Estimation," Swedish Defense Res. Agency, FOI, , Linköping, Sweden Feb. 2002.
- [189] K. Wang, A. Ghiotto, F. Zhu, and K. Wu, "Large Signal Modeling and Experimental Design Automation of Self-Isolated Harmonic Oscillator for Pulling Effect Reduction," *IEEE Trans. Microw. Theory Tech.*, 2018.
- [190] K. Lin, Y. E. Wang, C. Pao, and Y. Shih, "A Ka-Band FMCW Radar Front-End with Adaptive Leakage Cancellation," *IEEE Trans. Microw. Theory Tech.*, vol. 54, no. 12, pp. 4041-4048, 2006.
- [191] O. Momeni and E. Afshari, "High Power Terahertz and Millimeter-Wave Oscillator Design: A Systematic Approach," *IEEE J. Solid-State Circuits*, vol. 46, no. 3, pp. 583-597, 2011.
- [192] A. H. Aljuhani, T. Kanar, S. Zehir, and G. M. Rebeiz, "A Scalable Dual-Polarized 256-Element Ku-Band Phased-Array SATCOM Receiver with $\pm 70^\circ$ Beam Scanning," in *2018 IEEE MTT-S Int. Microw. Symp. Dig.*, Philadelphia, PA, USA, 2018, pp. 1203-1206.
- [193] P. Chu, W. Hong, L. Dai, H. Tang, Z. Hao, J. Chen, and K. Wu, "Wide Stopband Bandpass Filter Implemented with Spur Stepped Impedance Resonator and Substrate Integrated Coaxial Line Technology," *IEEE Microw. Wireless Compon. Lett.*, vol. 24, no. 4, pp. 218-220, 2014.
- [194] W. Qin, H. Wei, H. J. Tang, and J. Wang, "Design and Implementation of UWB Bandpass Filter with a Frequency Notch for Choking Back the Interference from Narrow Band Wireless Communication Systems," in *2009 IEEE Int. Conf. Ultra-Wideband*, 2009, pp. 521-524.
- [195] Y. Li, H. Wei, H. Guang, C. Jixin, W. Ke, and C. Tie Jun, "Simulation and Experiment on SIW Slot Array Antennas," *IEEE Microw. Wireless Compon. Lett.*, vol. 14, no. 9, pp. 446-448, 2004.
- [196] Y. Zhang and Z. Song, "A Compact Substrate Integrated Coaxial Line Bandpass Filter with Extended Rejection Bandwidth," *Microw. Opt. Tech. Lett.*, vol. 56, no. 2, pp. 415-418, Feb. 2014.
- [197] J. Kuo and E. Shih, "Microstrip Stepped Impedance Resonator Bandpass Filter with an Extended Optimal Rejection Bandwidth," *IEEE Trans. Microw. Theory Tech.*, vol. 51, no. 5, pp. 1554-1559, 2003.
- [198] F. Zhu, W. Hong, J. X. Chen, and K. Wu, "Wide Stopband Substrate Integrated Waveguide Filter Using Corner Cavities," *Electron. Lett.*, vol. 49, no. 1, pp. 50-52, 2013.

APPENDIX A – PUBLICATIONS AND PATENTS

Published Papers:

- [1] **K. Wang**, A. Ghiotto and K. Wu, "Harmonic Feedback-Loop Oscillator for Pulling Effect Reduction and Improved Phase Noise," in *2014 IEEE MTT-S Int. Microw. Symp. Dig.*, Tampa, FL, USA, 2014, pp. 1-4.
- [2] **K. Wang**, S. Adhikari, A. Ghiotto and K. Wu, "Multiharmonic Generator for Large-Signal-Network-Analyzer Verification," *IEEE Microw. Mag.*, vol. 15, no. 1, pp. 120-128, Jan.-Feb. 2014.
- [3] **K. Wang** and K. Wu, "Liquid Crystal Enabled Substrate Integrated Waveguide Variable Phase Shifter for Millimeter-wave Application at 60GHz and beyond," in *2015 IEEE MTT-S Int. Microw. Symp. Dig.*, Phoenix, AZ, USA, 2015, pp. 1-4.
- [4] **K. Wang**, J. Gu, F. Ren and K. Wu, "A Multitarget Active Backscattering 2-D Positioning System with Superresolution Time Series Post-Processing Technique," *IEEE Trans. Microw. Theory Tech.*, vol. 65, no. 5, pp. 1751-1766, May 2017.
- [5] S. Adhikari, A. Ghiotto, **K. Wang** and K. Wu, "Development of a Large-Signal-Network-Analyzer Round-Robin Artifact," *IEEE Microw. Mag.*, vol. 14, no. 1, pp. 140-145, Jan.-Feb. 2013.
- [6] P. Chu, W. Hong, **K. Wang**, H. Tang, Z. Hao, J. Chen and K. Wu, "Balanced Substrate Integrated Waveguide Filter," *IEEE Trans. Microw. Theory Tech.*, vol. 62, no. 4, pp. 824-831, April 2014.
- [7] J. Moghaddasi, **K. Wang** and K. Wu, "Parametric Characterization of Six-Port Interferometer Demodulator through Mixer Modeling," in *2015 Eur. Microw. Conf.*, Paris, France, 2015, pp. 526-529.
- [8] P. Barmuta, D. Ribeiro, **K. Wang**, G. Avolio, M. Rajabi, A. Lewandowski, G. Gibiino, J. Szatkowski, D. Schreurs, P. Hale, K. Remley, and D. Williams, "Comparing LSNA Calibrations: Large-Signal Network Analyzer Round Robin," *IEEE Microw. Mag.*, vol. 17, no. 2, pp. 59-64, Feb. 2016.

- [9] H. Jin, **K. Wang**, J. Guo, S. Ding and K. Wu, "Slow-Wave Effect of Substrate Integrated Waveguide Patterned with Microstrip Polyline," *IEEE Trans. Microw. Theory Tech.*, vol. 64, no. 6, pp. 1717-1726, June 2016.
- [10] J. Gu, **K. Wang** and K. Wu, "System Architecture and Signal Processing for Frequency-Modulated Continuous-Wave Radar using Active Backscatter Tags," *IEEE Trans. Signal Process.*, vol. 66, no. 9, pp. 2258-2272, Nov. 2017.
- [11] F. Zhu, **K. Wang** and K. Wu, "A Fundamental-and-Harmonic Dual-Frequency Doppler Radar System for Vital Signs Detection Enabling Radar Movement Self-Cancellation," *IEEE Trans. Microw. Theory Tech.*, vol. 66, no. 11, pp. 5106-5118, Nov. 2018.

Submitted Papers:

- [1] **K. Wang**, A. Ghiotto, L. Guo, F. Zhu and K. Wu, "A Millimeter-Wave Self-Isolated Harmonic Active Radiator for Identification, Sensing, Tracking and Communication Applications," submitted to *IEEE Trans. Antennas Propag.*, 2018.
- [2] **K. Wang**, A. Ghiotto, F. Zhu and K. Wu, "Large Signal Modeling and Experimental Design Automation of Self-Isolated Harmonic Oscillator for Pulling Effect Reduction," submitted to *IEEE Trans. Microw. Theory Tech.*, 2018.
- [3] F. Zhu, **K. Wang**, and K. Wu, "A Reconfigurable Low-Voltage and Low-Power Millimeter-Wave Dual-Band Mixer in 65-nm CMOS," submitted to *IEEE Trans. Microw. Theory Tech.*, 2018.
- [4] F. Zhu, **K. Wang**, and K. Wu, "Design Considerations for Image Rejection Enhancement of Quadrature Mixer," submitted to *IEEE Microw. Wireless Compon. Lett.*, 2018.

Granted Patents:

- [1] **K. Wang**, H. Jin, K. Wu and T. Djerafi, "System and Method for Variable Microwave Phase Shifter," US9755286B2, 2014, Granted.
- [2] L. Li, J. Moghaddasi, **K. Wang** and K. Wu, "Reconfigurable Multi-Mode and Multi-Bands Radio Architecture and Transceiver," US9992722B2, 2015, Granted.
- [3] T. Djerafi, K. Wu, A. Guntupalli and **K. Wang**, "Apparatus and Method for a High Aperture Efficiency Broadband Antenna Element with Stable Gain," US9548541B2, 2015, Granted.